

Planck 2015 results

XX. Constraints on inflation

Planck Collaboration: P. A. R. Ade⁹⁹, N. Aghanim⁶⁶, M. Arnaud⁸², F. Arroja^{74,88}, M. Ashdown^{78,6}, J. Aumont⁶⁶, C. Baccigalupi⁹⁷, M. Ballardini^{54,56,37}, A. J. Banday^{112,11}, R. B. Barreiro⁷³, N. Bartolo^{36,74}, E. Battaner^{114,115}, K. Benabed^{67,111}, A. Benoît⁶⁴, A. Benoit-Lévy^{28,67,111}, J.-P. Bernard^{112,11}, M. Bersanelli^{40,55}, P. Bielewicz^{92,11,97}, J. J. Bock^{75,13}, A. Bonaldi⁷⁶, L. Bonavera⁷³, J. R. Bond¹⁰, J. Borrill^{16,104}, F. R. Bouchet^{67,102}, F. Boulanger⁶⁶, M. Bucher^{1,*}, C. Burigana^{54,38,56}, R. C. Butler⁵⁴, E. Calabrese¹⁰⁷, J.-F. Cardoso^{83,1,67}, A. Catalano^{84,81}, A. Challinor^{70,78,14}, A. Chaballu^{82,18,66}, R.-R. Chary⁶³, H. C. Chiang^{32,7}, P. R. Christensen^{93,43}, S. Church¹⁰⁶, D. L. Clements⁶², S. Colombi^{67,111}, L. P. L. Colombo^{27,75}, C. Combet⁸⁴, D. Contreras²⁶, F. Couchot⁸⁰, A. Coullais⁸¹, B. P. Crill^{75,13}, A. Curto^{73,6,78}, F. Cuttaia⁵⁴, L. Danese⁹⁷, R. D. Davies⁷⁶, R. J. Davis⁷⁶, P. de Bernardis³⁹, A. de Rosa⁵⁴, G. de Zotti^{51,97}, J. Delabrouille¹, F.-X. Désert⁶⁰, J. M. Diego⁷³, H. Dole^{66,65}, S. Donzelli⁵⁵, O. Doré^{75,13}, M. Douspis⁶⁶, A. Ducout^{67,62}, X. Dupac⁴⁶, G. Efstathiou⁷⁰, F. Elsner^{28,67,111}, T. A. Enblin⁸⁹, H. K. Eriksen⁷¹, J. Fergusson¹⁴, F. Finelli^{54,56,*}, O. Forni^{112,11}, M. Frailis⁵³, A. A. Fraisse³², E. Franceschi⁵⁴, A. Frejse⁹³, A. Frolov¹⁰¹, S. Galeotta⁵³, S. Galli⁷⁷, K. Ganga¹, C. Gauthier^{1,88}, M. Giard^{112,11}, Y. Giraud-Héraud¹, E. Gjerløw⁷¹, J. González-Nuevo^{23,73}, K. M. Górski^{75,116}, S. Gratton^{78,70}, A. Gregorio^{41,53,59}, A. Gruppiso⁵⁴, J. E. Gudmundsson^{109,95,32}, J. Hamann^{110,108}, W. Handley^{78,6}, F. K. Hansen⁷¹, D. Hanson^{90,75,10}, D. L. Harrison^{70,78}, S. Henrot-Versillé⁸⁰, C. Hernández-Monteagudo^{15,89}, D. Herranz⁷³, S. R. Hildebrandt^{75,13}, E. Hivon^{67,111}, M. Hobson⁶, W. A. Holmes⁷⁵, A. Hornstrup¹⁹, W. Hovest⁸⁹, Z. Huang¹⁰, K. M. Huffmanberger³⁰, G. Hurier⁶⁶, A. H. Jaffe⁶², T. R. Jaffe^{112,11}, W. C. Jones³², M. Juvela³¹, E. Keihänen³¹, R. Keskitalo¹⁶, J. Kim⁸⁹, T. S. Kisner⁸⁶, R. Kneissl^{145,8}, J. Knoché⁸⁹, M. Kunz^{20,66,3}, H. Kurki-Suonio^{31,50}, G. Lagache^{5,66}, A. Lähteenmäki^{2,50}, J.-M. Lamarre⁸¹, A. Lasenby^{6,78}, M. Lattanzi³⁸, C. R. Lawrence⁷⁵, R. Leonardi⁹, J. Lesgourgues^{68,110}, F. Levrier⁸¹, A. Lewis²⁹, M. Liguori^{36,74}, P. B. Lilje⁷¹, M. Linden-Vørnle¹⁹, M. López-Caniego^{46,73}, P. M. Lubin³⁴, Y.-Z. Ma^{26,76}, J. F. Macías-Pérez⁸⁴, G. Maggio⁵³, D. Maino^{40,55}, N. Mandolesi^{54,38}, A. Mangilli^{66,80}, M. Maris⁵³, P. G. Martin¹⁰, E. Martínez-González⁷³, S. Masi³⁹, S. Matarrese^{36,74,48}, P. McGehee⁶³, P. R. Meinhold³⁴, A. Melchiorri^{39,57}, L. Mendes⁴⁶, A. Mennella^{40,55}, M. Migliaccio^{70,78}, S. Mitra^{61,75}, M.-A. Miville-Deschênes^{66,10}, D. Molinari^{73,54}, A. Moneti⁶⁷, L. Montier^{112,11}, G. Morgante⁵⁴, D. Mortlock⁶², A. Moss¹⁰⁰, M. Münchmeyer⁶⁷, D. Munshi⁹⁹, J. A. Murphy⁹¹, P. Naselsky^{94,44}, F. Nati³², P. Natoli^{38,4,54}, C. B. Netterfield²⁴, H. U. Nørgaard-Nielsen¹⁹, F. Novello⁷⁶, D. Novikov⁸⁷, I. Novikov^{93,87}, C. A. Oxborrow¹⁹, F. Paci⁹⁷, L. Pagano^{39,57}, F. Pajot⁶⁶, S. Paladini⁶³, S. Pandolfi²¹, D. Paoletti^{54,56}, F. Pasian⁵³, G. Patanchon¹, T. J. Pearson^{13,63}, H. V. Peiris²⁸, O. Perdereau⁸⁰, L. Perotto⁸⁴, F. Perrotta⁹⁷, V. Pettorino⁴⁹, F. Piacentini³⁹, M. Piat¹, E. Pierpaoli²⁷, D. Pietrobon⁷⁵, S. Plaszczynski⁸⁰, E. Pointecouteau^{112,11}, G. Polenta^{4,52}, L. Popa⁶⁹, G. W. Pratt⁸², G. Prézeau^{13,75}, S. Prunet^{67,111}, J.-L. Puget⁶⁶, J. P. Rachen^{25,89}, W. T. Reach¹¹³, R. Rebolo^{72,17,22}, M. Reinecke⁸⁹, M. Remazeilles^{76,66,1}, C. Renault⁸⁴, A. Renzi^{42,58}, I. Ristorcelli^{112,11}, G. Rocha^{75,13}, C. Rosset¹, M. Rossetti^{40,55}, G. Roudier^{1,81,75}, M. Rowan-Robinson⁶², J. A. Rubiño-Martín^{72,22}, B. Rusholme⁶³, M. Sandri⁵⁴, D. Santos⁸⁴, M. Savelainen^{31,50}, G. Savini⁹⁶, D. Scott²⁶, M. D. Seiffert^{75,13}, E. P. S. Shellard¹⁴, M. Shiraishi^{36,74}, L. D. Spencer⁹⁹, V. Stolyarov^{6,105,79}, R. Stompor¹, R. Sudiwala⁹⁹, R. Sunyaev^{89,103}, D. Sutton^{70,78}, A.-S. Suur-Uski^{31,50}, J.-F. Sygnet⁶⁷, J. A. Tauber⁴⁷, L. Terenzi^{98,54}, L. Toffolatti^{23,73,54}, M. Tomasi^{40,55}, M. Tristram⁸⁰, T. Trombetti⁵⁴, M. Tucci²⁰, J. Tuovinen¹², L. Valenziano⁵⁴, J. Valiviita^{31,50}, B. Van Tent⁸⁵, P. Vielva⁷³, F. Villa⁵⁴, L. A. Wade⁷⁵, B. D. Wandelt^{67,111,35}, I. K. Wehus^{75,71}, M. White³³, D. Yvon¹⁸, A. Zacchei⁵³, J. P. Zibin²⁶, and A. Zonca³⁴

(Affiliations can be found after the references)

Received 14 February 2015 / Accepted 3 March 2016

ABSTRACT

We present the implications for cosmic inflation of the *Planck* measurements of the cosmic microwave background (CMB) anisotropies in both temperature and polarization based on the full *Planck* survey, which includes more than twice the integration time of the nominal survey used for the 2013 release papers. The *Planck* full mission temperature data and a first release of polarization data on large angular scales measure the spectral index of curvature perturbations to be $n_s = 0.968 \pm 0.006$ and tightly constrain its scale dependence to $dn_s/d\ln k = -0.003 \pm 0.007$ when combined with the *Planck* lensing likelihood. When the *Planck* high- ℓ polarization data are included, the results are consistent and uncertainties are further reduced. The upper bound on the tensor-to-scalar ratio is $r_{0.002} < 0.11$ (95% CL). This upper limit is consistent with the *B*-mode polarization constraint $r < 0.12$ (95% CL) obtained from a joint analysis of the BICEP2/Keck Array and *Planck* data. These results imply that $V(\phi) \propto \phi^2$ and natural inflation are now disfavoured compared to models predicting a smaller tensor-to-scalar ratio, such as R^2 inflation. We search for several physically motivated deviations from a simple power-law spectrum of curvature perturbations, including those motivated by a reconstruction of the inflaton potential not relying on the slow-roll approximation. We find that such models are not preferred, either according to a Bayesian model comparison or according to a frequentist simulation-based analysis. Three independent methods reconstructing the primordial power spectrum consistently recover a featureless and smooth $\mathcal{P}_R(k)$ over the range of scales $0.008 \text{ Mpc}^{-1} \lesssim k \lesssim 0.1 \text{ Mpc}^{-1}$. At large scales, each method finds deviations from a power law, connected to a deficit at multipoles $\ell \approx 20\text{--}40$ in the temperature power spectrum, but at an unconvincing statistical significance owing to the large cosmic variance present at these multipoles. By combining power spectrum and non-Gaussianity bounds, we constrain models with generalized Lagrangians, including Galileon models and axion monodromy models. The *Planck* data are consistent with adiabatic primordial perturbations, and the estimated values for the parameters of the base Λ cold dark matter (Λ CDM) model are not significantly altered when more general initial conditions are admitted. In correlated mixed adiabatic and isocurvature models, the 95% CL upper bound for the non-adiabatic contribution to the observed CMB temperature variance is $|\alpha_{\text{non-adi}}| < 1.9\%$, 4.0% , and 2.9% for CDM, neutrino density, and neutrino velocity isocurvature modes, respectively. We have tested inflationary models producing an anisotropic modulation of the primordial curvature power spectrum finding that the dipolar modulation in the CMB temperature field induced by a CDM isocurvature perturbation is not preferred at a statistically significant level. We also establish tight constraints on a possible quadrupolar modulation of the curvature perturbation. These results are consistent with the *Planck* 2013 analysis based on the nominal mission data and further constrain slow-roll single-field inflationary models, as expected from the increased precision of *Planck* data using the full set of observations.

Key words. cosmic background radiation – cosmology: theory – early Universe – inflation

* Corresponding author: Martin Bucher, e-mail: bucher@apc.univ-paris7.fr; Fabio Finelli, e-mail: finelli@iasfbo.inaf.it

1. Introduction

The precise measurements by *Planck*¹ of the cosmic microwave background (CMB) anisotropies covering the entire sky and over a broad range of scales, from the largest visible down to a resolution of approximately $5'$, provide a powerful probe of cosmic inflation, as detailed in the *Planck* 2013 inflation paper (Planck Collaboration XXII 2014, hereafter *PCI13*). In the 2013 results, the robust detection of the departure of the scalar spectral index from exact scale invariance, i.e., $n_s < 1$, at more than 5σ confidence, as well as the lack of the observation of any statistically significant running of the spectral index, were found to be consistent with simple slow-roll models of inflation. Single-field inflationary models with a standard kinetic term were also found to be compatible with the new tight upper bounds on the primordial non-Gaussianity parameters f_{NL} reported in Planck Collaboration XXVI (2014). No evidence of isocurvature perturbations as generated in multi-field inflationary models (*PCI13*) or by cosmic strings or topological defects was found (Planck Collaboration XXV 2014). The *Planck* 2013 results overall favoured the simplest inflationary models. However, we noted an amplitude deficit for multipoles $\ell \lesssim 40$ whose statistical significance relative to the six-parameter base Λ cold dark matter (Λ CDM) model is only about 2σ , as well as other anomalies on large angular scales but also without compelling statistical significance (Planck Collaboration XXIII 2014). The constraint on the tensor-to-scalar ratio, $r < 0.12$ at 95% CL, inferred from the temperature power spectrum alone, combined with the determination of n_s , suggested models with concave potentials.

This paper updates the implications for inflation in the light of the *Planck* full mission temperature and polarization data. The *Planck* 2013 cosmology results included only the nominal mission, comprising the first 14 months of the data taken, and used only the temperature data. However, the full mission includes the full 29 months of scientific data taken by the cryogenically cooled high frequency instrument (HFI; which ended when the $^3\text{He}/^4\text{He}$ supply for the final stage of the cooling chain ran out) and the approximately four years of data taken by the low frequency instrument (LFI), which covered a longer period than the HFI because the LFI did not rely on cooling down to 100 mK for its operation. For a detailed discussion of the new likelihood and a comparison with the 2013 likelihood, we refer the reader to Planck Collaboration XI (2016) and Planck Collaboration XIII (2016), but we mention here some highlights of the differences between the 2013 and 2015 data processing and likelihoods: (1) improvements in the data processing such as beam characterization and absolute calibration at each frequency result in a better removal of systematic effects and (2) the 2015 temperature high- ℓ likelihood uses half-mission cross-power spectra over more of the sky, owing to less aggressive Galactic cuts. The use of polarization information in the 2015 likelihood release contributes to the constraining power of *Planck* in two principal ways: (1) the measurement of the E-mode polarization at large angular scales (presently based on the 70 GHz channel) constrains the reionization optical depth, τ , independently of other estimates using ancillary data; and (2) the measurement of the

TE and *EE* spectra at $\ell \geq 30$ at the same frequencies used for the *TT* spectra (100, 143, and 217 GHz) helps break parameter degeneracies, particularly for extended cosmological models (beyond the baseline six-parameter model). A full analysis of the *Planck* low- ℓ polarization is still in progress and will be the subject of another forthcoming set of *Planck* publications.

The *Planck* 2013 results have sparked a revival of interest in several aspects of inflationary models. We mention here a few examples without the ambition to be exhaustive. A lively debate arose on the conceptual problems of some of the inflationary models favoured by the *Planck* 2013 data (Ijjas et al. 2013, 2014; Guth et al. 2014; Linde 2014). The interest in the R^2 inflationary model originally proposed by Starobinsky (1980) increased, since its predictions for cosmological fluctuations (Mukhanov & Chibisov 1981; Starobinsky 1983) are compatible with the *Planck* 2013 results (*PCI13*). It has been shown that supergravity motivates a potential similar to the Einstein gravity conformal representation of the R^2 inflationary model in different contexts (Ellis et al. 2013a,b; Buchmüller et al. 2013; Farakos et al. 2013; Ferrara et al. 2013b). A similar potential can also be generated by spontaneous breaking of conformal symmetry (Kallosh & Linde 2013b).

The constraining power of *Planck* also motivated a comparison between large numbers of inflationary models (Martin et al. 2014) and stimulated different perspectives on how best to compare theoretical inflationary predictions with observations based on the parameterized dependence of the Hubble parameter on the scale factor during inflation (Mukhanov 2013; Binétruy et al. 2015; Garcia-Bellido & Roest 2014). The interpretation of the asymmetries on large angular scales (Planck Collaboration XXIII 2014) also prompted a reanalysis of the primordial dipole modulation (Lyth 2013; Liddle & Cortés 2013; Kanno et al. 2013) of curvature perturbations during inflation.

Another recent development has been the renewed interest in possible tensor modes generated during inflation, sparked by the BICEP2 results (BICEP2 Collaboration 2014a,b). The BICEP2 team suggested that the *B*-mode polarization signal detected at $50 < \ell < 150$ at a single frequency (150 GHz) might be of primordial origin. However, a crucial step in this possible interpretation was excluding an explanation based on polarized thermal dust emission from our Galaxy. The BICEP2 team put forward a number of models to estimate the likely contribution from dust, but at the time relevant observational data were lacking, and this modelling involved a high degree of extrapolation. If dust polarization were negligible in the observed patch of 380 deg^2 , this interpretation would lead to a tensor-to-scalar ratio of $r = 0.2^{+0.07}_{-0.05}$ for a scale-invariant spectrum. A value of $r \approx 0.2$, as suggested by BICEP2 Collaboration (2014b), would have obviously changed the *Planck* 2013 perspective according to which slow-roll inflationary models are favoured, and such a high value of r would also have required a strong running of the scalar spectral index, or some other modification from a simple power-law spectrum, to reconcile the contribution of gravitational waves to temperature anisotropies at low multipoles with the observed *TT* spectrum.

The interpretation of the *B*-mode signal in terms of gravitational waves *alone* presented in BICEP2 Collaboration (2014b) was later cast in doubt by *Planck* measurements of dust polarization at 353 GHz (Planck Collaboration Int. XIX 2015; Planck Collaboration Int. XX 2015; Planck Collaboration Int. XXI 2015; Planck Collaboration Int. XXII 2015). The *Planck* measurements characterized the frequency dependence of intensity and polarization of the Galactic dust emission, and moreover showed that the polarization fraction is higher than expected

¹ *Planck* (<http://www.esa.int/Planck>) is a project of the European Space Agency (ESA) with instruments provided by two scientific consortia funded by ESA member states and led by Principal Investigators from France and Italy, telescope reflectors provided through a collaboration between ESA and a scientific consortium led and funded by Denmark, and additional contributions from NASA (USA).

in regions of low dust emission. With the help of the *Planck* measurements of Galactic dust properties (Planck Collaboration Int. XIX 2015), it was shown that the interpretation of the B -mode polarization signal in terms of a primordial tensor signal plus a lensing contribution was not statistically preferred to an explanation based on the expected dust signal at 150 GHz plus a lensing contribution (see also Flauger et al. 2014a; Mortonson & Seljak 2014). Subsequently, Planck Collaboration Int. XXX (2016) extrapolated the *Planck* B -mode power spectrum of dust polarization at 353 GHz over the multipole range $40 < \ell < 120$ to 150 GHz, showing that the B -mode polarization signal detected by BICEP2 could be entirely due to dust.

More recently, a BICEP2/Keck Array-*Planck* (BKP) joint analysis (BICEP2/Keck Array and Planck Collaborations 2015, hereafter BKP) combined the high-sensitivity B -mode maps from BICEP2 and Keck Array with the *Planck* maps at higher frequencies where dust emission dominates. A study of the cross-correlations of all these maps in the BICEP2 field found the absence of any statistically significant evidence for primordial gravitational waves, setting an upper limit of $r < 0.12$ at 95% CL (BKP). Although this upper limit is numerically almost identical to the *Planck* 2013 result obtained combining the nominal mission temperature data with WMAP polarization to remove parameter degeneracies (Planck Collaboration XVI 2014; Planck Collaboration XXII 2014), the BKP upper bound is much more robust against modifications of the inflationary model, since B modes are insensitive to the shape of the predicted scalar anisotropy pattern. In Sect. 13 we explore how the recent BKP analysis constrains inflationary models.

This paper is organized as follows. Section 2 briefly reviews the additional information on the primordial cosmological fluctuations encoded in the polarization angular power spectrum. Section 3 describes the statistical methodology as well as the *Planck* and other likelihoods used throughout the paper. Sections 4 and 5 discuss the *Planck* 2015 constraints on scalar and tensor fluctuations, respectively. Section 6 is dedicated to constraints on the slow-roll parameters and provides a Bayesian comparison of selected slow-roll inflationary models. In Sect. 7 we reconstruct the inflaton potential and the Hubble parameter as a Taylor expansion of the inflaton in the observable range without relying on the slow-roll approximation. The reconstruction of the curvature perturbation power spectrum is presented in Sect. 8. The search for parameterized features is presented in Sect. 9, and combined constraints from the *Planck* 2015 power spectrum and primordial non-Gaussianity derived in Planck Collaboration XVII (2016) are presented in Sect. 10. The analysis of isocurvature perturbations combined and correlated with curvature perturbations is presented in Sect. 11. In Sect. 12 we study the implications of relaxing the assumption of statistical isotropy of the primordial fluctuations. We discuss two examples of *anisotropic* inflation in light of the tests of isotropy performed in Planck Collaboration XVI (2016). Section 14 presents some concluding remarks.

2. What new information does polarization provide?

This section provides a short theoretical overview of the extra information provided by polarization data over that of temperature alone. (More details can be found in White et al. 1994; Ma & Bertschinger 1995; Bucher 2015, and references therein.) In Sect. 2 of the *Planck* 2013 inflation paper (PCI13), we gave an overview of the relation between the inflationary potential and the three-dimensional primordial scalar and tensor power spectra, denoted as $\mathcal{P}_{\mathcal{R}}(k)$ and $\mathcal{P}_t(k)$, respectively. (The scalar

variable \mathcal{R} is defined precisely in Sect. 3.) We shall not repeat the discussion there, instead referring the reader to PCI13 and references therein.

Under the assumption of statistical isotropy, which is predicted in all simple models of inflation, the two-point correlations of the CMB anisotropies are described by the angular power spectra C_{ℓ}^{TT} , C_{ℓ}^{TE} , C_{ℓ}^{EE} , and C_{ℓ}^{BB} , where ℓ is the multipole number. (See Kamionkowski et al. 1997; Zaldarriaga & Seljak 1997; Seljak & Zaldarriaga 1997; Hu & White 1997; Hu et al. 1998 and references therein for early discussions elucidating the role of polarization.) In principle, one could also envisage measuring C_{ℓ}^{BT} and C_{ℓ}^{BE} , but in theories where parity symmetry is not explicitly or spontaneously broken, the expectation values for these cross spectra (i.e., the theoretical cross spectra) vanish, although the observed realizations of the cross spectra are not exactly zero because of cosmic variance.

The CMB angular power spectra are related to the three-dimensional scalar and tensor power spectra via the transfer functions $\Delta_{\ell,\mathcal{A}}^s(k)$ and $\Delta_{\ell,\mathcal{A}}^t(k)$, so that the contributions from scalar and tensor perturbations are

$$C_{\ell}^{\mathcal{AB},s} = \int_0^{\infty} \frac{dk}{k} \Delta_{\ell,\mathcal{A}}^s(k) \Delta_{\ell,\mathcal{B}}^s(k) \mathcal{P}_{\mathcal{R}}(k) \quad (1)$$

and

$$C_{\ell}^{\mathcal{AB},t} = \int_0^{\infty} \frac{dk}{k} \Delta_{\ell,\mathcal{A}}^t(k) \Delta_{\ell,\mathcal{B}}^t(k) \mathcal{P}_t(k), \quad (2)$$

respectively, where $\mathcal{A}, \mathcal{B} = T, E, B$. The scalar and tensor primordial perturbations are uncorrelated in the simplest models, so the scalar and tensor power spectra add in quadrature, meaning that

$$C_{\ell}^{\mathcal{AB},\text{tot}} = C_{\ell}^{\mathcal{AB},s} + C_{\ell}^{\mathcal{AB},t}. \quad (3)$$

Roughly speaking, the form of the linear transformations encapsulated in the transfer functions $\Delta_{\ell,\mathcal{A}}^s(k)$ and $\Delta_{\ell,\mathcal{A}}^t(k)$ probe the late time physics, whereas the primordial power spectra $\mathcal{P}_{\mathcal{R}}(k)$ and $\mathcal{P}_t(k)$ are solely determined by the primordial Universe, perhaps not so far below the Planck scale if large-field inflation turns out to be correct.

To better understand this connection, it is useful to plot and compare the shapes of the transfer functions for representative values of ℓ and characterize their qualitative behavior. Referring to Fig. 1, we emphasize the following qualitative features:

1. For the scalar mode transfer functions, of which only $\Delta_{\ell,T}^s(k)$ and $\Delta_{\ell,E}^s(k)$ are non-vanishing (because to linear order, a three-dimensional scalar mode cannot contribute to the B mode of the polarization), both transfer functions start to rise at more or less the same small values of k (due to the centrifugal barrier in the Bessel differential equation), but $\Delta_{\ell,E}^s(k)$ falls off much faster at large k and thus smooths sharp features in $\mathcal{P}_{\mathcal{R}}(k)$ to a lesser extent than $\Delta_{\ell,T}^s(k)$. This means that polarization is more powerful than temperature for reconstructing possible sharp features in the scalar primordial power spectrum provided that the required signal-to-noise is available.
2. For the tensor modes, $\Delta_{\ell,T}^t(k)$ starts rising at about the same small k as $\Delta_{\ell,T}^s(k)$ and $\Delta_{\ell,E}^s(k)$ but falls off faster with increasing k than $\Delta_{\ell,T}^s(k)$. On the other hand, the polarization components, $\Delta_{\ell,E}^t(k)$ and $\Delta_{\ell,B}^t(k)$, have a shape completely different from any of the other transfer functions. The shape of

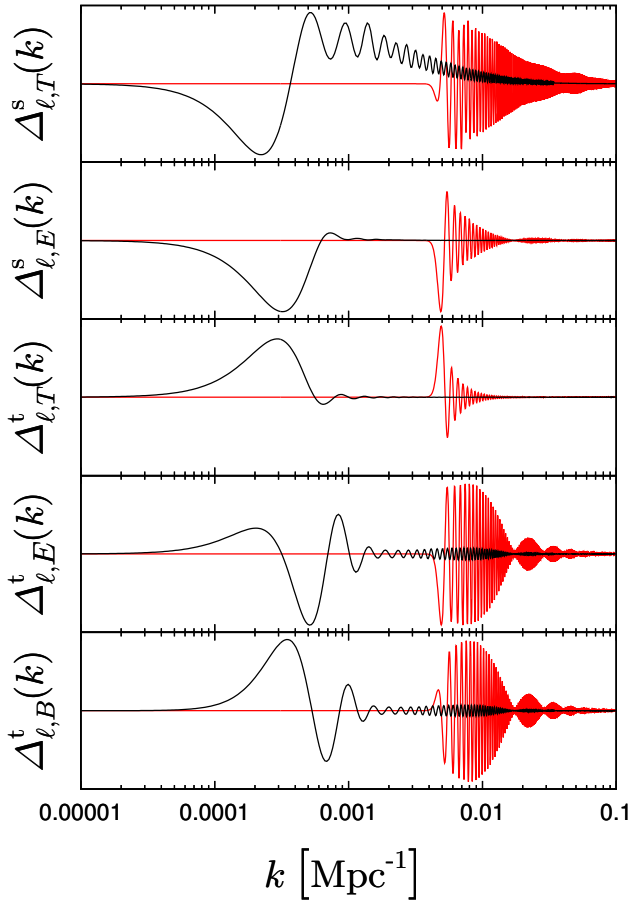


Fig. 1. Comparison of transfer functions for the scalar and tensor modes. The CMB transfer functions $\Delta_{\ell,\mathcal{A}}^s(k)$ and $\Delta_{\ell,\mathcal{A}}^t(k)$, where $\mathcal{A} = T, E, B$, define the linear transformations mapping the primordial scalar and tensor cosmological perturbations to the CMB anisotropies as seen by us on the sky today. These functions are plotted for two representative values of the multipole number: $\ell = 2$ (in black) and $\ell = 65$ (in red).

$\Delta_{\ell,E}^t(k)$ and $\Delta_{\ell,B}^t(k)$ is much wider in $\ln(k)$ than the scalar polarization transfer function, with a variance ranging from 0.5 to 1.0 decades. These functions exhibit several oscillations with a period smaller than that for scalar transfer functions, due to the difference between the sound velocity for scalar fluctuations and the light velocity for gravitational waves (Polarski & Starobinsky 1996; Lesgourgues et al. 2000).

Regarding the scalar primordial cosmological perturbations, the power spectrum of the E-mode polarization provides an important consistency check. As we explore in Sects. 8 and 9, to some extent the fit of the temperature power spectrum can be improved by allowing a complicated form for the primordial power spectrum (relative to a simple power law), but the C_ℓ^{TE} and C_ℓ^{EE} power spectra provide independent information. Moreover, in multi-field inflationary models, in which isocurvature modes may have been excited (possibly correlated amongst themselves as well as with the adiabatic mode), polarization information provides a powerful way to break degeneracies (see, e.g., Bucher et al. 2001).

The inability of scalar modes to generate *B*-mode polarization (apart from the effects of lensing) has an important consequence. For the primordial tensor modes, polarization information, especially information concerning the *B*-mode polarization, offers powerful potential for discovery or for establishing upper bounds. *Planck* 2013 and WMAP established upper bounds on

a possible tensor mode contribution using C_ℓ^{TT} alone, but these bounds crucially relied on assuming a simple form for the scalar primordial power spectrum. For example, as reported in PCI13, when a simple power law was generalized to allow for running, the bound on the tensor contribution degraded by approximately a factor of two. The new joint BICEP2/Keck Array-*Planck* upper bound (see Sect. 13), however, is much more robust and cannot be avoided by postulating baroque models that alter the scale dependence of the scalar power spectrum.

3. Methodology

This section describes updates to the formalism used to describe cosmological models and the likelihoods used with respect to the *Planck* 2013 inflation paper (PCI13).

3.1. Cosmological model

The cosmological models that predict observables such as the CMB anisotropies rely on inputs specifying the conditions and physics at play during different epochs of the history of the Universe. The primordial inputs describe the power spectrum of the cosmological perturbations at a time when all the observable modes were situated outside the Hubble radius. The inputs from this epoch consist of the primordial power spectra, which may include scalar curvature perturbations, tensor perturbations, and possibly also isocurvature modes and their correlations. The late time (i.e., $z \lesssim 10^4$) cosmological inputs include parameters such as ω_b , ω_c , Ω_Λ , and τ , which determine the conditions when the primordial perturbations become imprinted on the CMB and also the evolution of the Universe between last scattering and today, affecting primarily the angular diameter distance. Finally, there is a so-called “nuisance” component, consisting of parameters that determine how the measured CMB spectra are contaminated by unsubtracted Galactic and extragalactic foreground contamination. The focus of this paper is on the primordial inputs and how they are constrained by the observed CMB anisotropy, but we cannot completely ignore the other non-primordial parameters because their presence and uncertainties must be dealt with in order to correctly extract the primordial information of interest here.

As in PCI13, we adopt the minimal six-parameter spatially flat base Λ CDM cosmological model as our baseline for the late time cosmology, mainly altering the primordial inputs, i.e., the simple power-law spectrum parameterized by the scalar amplitude and spectral index for the adiabatic growing mode, which in this minimal model is the only late time mode excited. This model has four free non-primordial cosmological parameters (ω_b , ω_c , θ_{MC} , τ ; for a more detailed account of this model, we refer the reader to Planck Collaboration XIII 2016). On occasion, this assumption will be relaxed in order to consider the impact of more complex alternative late time cosmologies on our conclusions about inflation. Some of the commonly used cosmological parameters are defined in Table 1.

3.2. Primordial spectra of cosmological fluctuations

In inflationary models, comoving curvature (\mathcal{R}) and tensor (h) fluctuations are amplified by the nearly exponential expansion from quantum vacuum fluctuations to become highly squeezed states resembling classical states. Formally, this quantum mechanical phenomenon is most simply described by the evolution in conformal time, η , of the mode functions for

Table 1. Primordial, baseline, and optional late-time cosmological parameters.

Parameter	Definition
A_s	Scalar power spectrum amplitude (at $k_* = 0.05 \text{ Mpc}^{-1}$)
n_s	Scalar spectral index (at $k_* = 0.05 \text{ Mpc}^{-1}$ unless otherwise stated)
$dn_s/d\ln k$	Running of scalar spectral index (at $k_* = 0.05 \text{ Mpc}^{-1}$ unless otherwise stated)
$d^2n_s/d\ln k^2$	Running of running of scalar spectral index (at $k_* = 0.05 \text{ Mpc}^{-1}$)
r	Tensor-to-scalar power ratio (at $k_* = 0.05 \text{ Mpc}^{-1}$ unless otherwise stated)
n_t	Tensor spectrum spectral index (at $k_* = 0.05 \text{ Mpc}^{-1}$)
$\omega_b \equiv \Omega_b h^2$	Baryon density today
$\omega_c \equiv \Omega_c h^2$	Cold dark matter density today
θ_{MC}	Approximation to the angular size of sound horizon at last scattering
τ	Thomson scattering optical depth of reionized intergalactic medium
N_{eff}	Effective number of massive and massless neutrinos
Σm_ν	Sum of neutrino masses
Y_P	Fraction of baryonic mass in primordial helium
Ω_K	Spatial curvature parameter
w_{de}	Dark energy equation of state parameter (i.e., $p_{\text{de}}/\rho_{\text{de}}$) (assumed constant)

the gauge-invariant inflaton fluctuation, $\delta\phi$, and for the tensor fluctuation, h :

$$(ay_k)'' + \left(k^2 - \frac{x''}{x}\right) ay_k = 0, \quad (4)$$

with $(x, y) = (a\dot{\phi}/H, \delta\phi)$ for scalars and $(x, y) = (a, h)$ for tensors. Here a is the scale factor, primes indicate derivatives with respect to η , and $\dot{\phi}$ and $H = \dot{a}/a$ are the proper time derivative of the inflaton and the Hubble parameter, respectively. The curvature fluctuation, \mathcal{R} , and the inflaton fluctuation, $\delta\phi$, are related via $\mathcal{R} = H\delta\phi/\dot{\phi}$. Analytic and numerical calculations of the predictions for the primordial spectra of cosmological fluctuations generated during inflation have reached high standards of precision, which are more than adequate for our purposes, and the largest uncertainty in testing specific inflationary models arises from our lack of knowledge of the history of the Universe between the end of inflation and the present time, during the so-called “epoch of entropy generation”.

This paper uses three different methods to compare inflationary predictions with *Planck* data. The first method consists of a phenomenological parameterization of the primordial spectra of scalar and tensor perturbations according to:

$$\begin{aligned} \mathcal{P}_{\mathcal{R}}(k) &= \frac{k^3}{2\pi^2} |\mathcal{R}_k|^2 \\ &= A_s \left(\frac{k}{k_*}\right)^{n_s - 1 + \frac{1}{2} \frac{dn_s}{d\ln k} \ln(k/k_*) + \frac{1}{6} \frac{d^2n_s}{d\ln k^2} (\ln(k/k_*))^2 + \dots} \end{aligned} \quad (5)$$

$$\mathcal{P}_t(k) = \frac{k^3}{2\pi^2} (|h_k^+|^2 + |h_k^\times|^2) = A_t \left(\frac{k}{k_*}\right)^{n_t + \frac{1}{2} \frac{dn_t}{d\ln k} \ln(k/k_*) + \dots} \quad (6)$$

where A_s (A_t) is the scalar (tensor) amplitude and n_s (n_t), $dn_s/d\ln k$ ($dn_t/d\ln k$), and $d^2n_s/d\ln k^2$ are the scalar (tensor) spectral index, the running of the scalar (tensor) spectral index, and the running of the running of the scalar spectral index, respectively. $h^{+,\times}$ denotes the amplitude of the two polarization states (+, \times) of gravitational waves and k_* is the pivot scale. Unless otherwise stated, the tensor-to-scalar ratio,

$$r = \frac{\mathcal{P}_t(k_*)}{\mathcal{P}_{\mathcal{R}}(k_*)}, \quad (7)$$

is fixed to $-8n_t$, which is the relation that holds when inflation is driven by a single slow-rolling scalar field with a standard kinetic

term². We will use a parameterization analogous to Eq. (5) with no running for the power spectra of isocurvature modes and their correlations in Sect. 11.

The second method exploits the analytic dependence of the slow-roll power spectra of primordial perturbations in Eqs. (5) and (6) on the values of the Hubble parameter and the hierarchy of its time derivatives, known as the Hubble flow functions (HFF): $\epsilon_1 = -\dot{H}/H^2$, $\epsilon_{i+1} \equiv \dot{\epsilon}_i/(H\epsilon_i)$, with $i \geq 1$. We will use the analytic power spectra calculated up to second order using the Green’s function method (Gong & Stewart 2001; Leach et al. 2002; see Habib et al. 2002; Martin & Schwarz 2003; and Casadio et al. 2006 for alternative derivations). The spectral indices and the relative scale dependence in Eqs. (5) and (6) are given in terms of the HFFs by:

$$n_s - 1 = -2\epsilon_1 - \epsilon_2 - 2\epsilon_1^2 - (2C + 3) \epsilon_1 \epsilon_2 - C\epsilon_2\epsilon_3, \quad (8)$$

$$dn_s/d\ln k = -2\epsilon_1\epsilon_2 - \epsilon_2\epsilon_3, \quad (9)$$

$$n_t = -2\epsilon_1 - 2\epsilon_1^2 - 2(C + 1) \epsilon_1 \epsilon_2, \quad (10)$$

$$dn_t/d\ln k = -2\epsilon_1\epsilon_2, \quad (11)$$

where $C \equiv \ln 2 + \gamma_E - 2 \approx -0.7296$ (γ_E is the Euler-Mascheroni constant). See the Appendix of PCI13 for more details. Primordial spectra as functions of the ϵ_i will be employed in Sect. 6, and the expressions generalizing Eqs. (8) to (11) for a general Lagrangian $p(\phi, X)$, where $X \equiv -g^{\mu\nu} \partial_\mu \phi \partial_\nu \phi / 2$, will be used in Sect. 10. The good agreement between the first and second method as well as with alternative approximations of slow-roll spectra is illustrated in the Appendix of PCI13.

The third method is fully numerical, suitable for models where the slow-roll conditions are not well satisfied and analytical approximations for the primordial fluctuations are not available. Two different numerical codes, the inflation module of Lesgourgues & Valkenburg (2007) as implemented in CLASS (Lesgourgues 2011; Blas et al. 2011) and ModeCode (Adams et al. 2001; Peiris et al. 2003; Mortonson et al. 2009; Easther & Peiris 2012), are used in Sects. 7 and 10, respectively.³

Conventions for the functions and symbols used to describe inflationary physics are defined in Table 2.

² When running is considered, we fix $n_t = -r(2 - r/8 - n_s)/8$ and $dn_t/d\ln k = r(r/8 + n_s - 1)/8$.

³ <http://class-code.net>, <http://modecode.org>

Table 2. Conventions and definitions for inflation physics.

Parameter	Definition
ϕ	Inflaton
$V(\phi)$	Inflaton potential
a	Scale factor
t	Cosmic (proper) time
δX	Fluctuation of X
$\dot{X} = dX/dt$	Derivative with respect to proper time
$X' = dX/d\eta$	Derivative with respect to conformal time
$X_\phi = \partial X/\partial\phi$	Partial derivative with respect to ϕ
M_{pl}	Reduced Planck mass ($=2.435 \times 10^{18}$ GeV)
\mathcal{R}	Comoving curvature perturbation
$h^{+,\times}$	Gravitational wave amplitude of (+, \times)-polarization component
X_*	X evaluated at Hubble exit during inflation of mode with wavenumber k_*
X_e	X evaluated at end of inflation
$\epsilon_V = M_{\text{pl}}^2 V_\phi^2 / (2V^2)$	First slow-roll parameter for $V(\phi)$
$\eta_V = M_{\text{pl}}^2 V_{\phi\phi} / V$	Second slow-roll parameter for $V(\phi)$
$\xi_V^2 = M_{\text{pl}}^4 V_\phi V_{\phi\phi\phi} / V^2$	Third slow-roll parameter for $V(\phi)$
$\varpi_V^3 = M_{\text{pl}}^6 V_\phi^2 V_{\phi\phi\phi\phi} / V^3$	Fourth slow-roll parameter for $V(\phi)$
$\epsilon_1 = -\dot{H}/H^2$	First Hubble hierarchy parameter
$\epsilon_{n+1} = \dot{\epsilon}_n / (H\epsilon_n)$	$(n+1)$ st Hubble hierarchy parameter (where $n \geq 1$)
$N(t) = \int_t^{t_e} dt H$	Number of e -folds to end of inflation

3.3. Planck data

The *Planck* data processing proceeding from time-ordered data to maps has been improved for this 2015 release in various aspects (Planck Collaboration II 2016; Planck Collaboration VII 2016). We refer the interested reader to Planck Collaboration II (2016) and Planck Collaboration VII (2016) for details, and we describe here two of these improvements. The absolute calibration has been improved using the orbital dipole and more accurate characterization of the *Planck* beams. The calibration discrepancy between *Planck* and WMAP described in Planck Collaboration XXXI (2014) for the 2013 release has now been greatly reduced. At the time of that release, a blind analysis for primordial power spectrum reconstruction described a broad feature at $\ell \approx 1800$ in the temperature power spectrum, which was most prominent in the 217×217 GHz auto-spectra (PCI13). In work done after the *Planck* 2013 data release, this feature was shown to be associated with imperfectly subtracted systematic effects associated with the 4 K cooler lines, which were particularly strong in the first survey. This systematic effect was shown to potentially lead to 0.5σ shifts in the cosmological parameters, slightly increasing n_s and H_0 , similarly to the case in which the 217×217 channel was excised from the likelihood (Planck Collaboration XV 2014; Planck Collaboration XVI 2014). The *Planck* likelihood (Planck Collaboration XI 2016) is based on the full mission data and comprises temperature and polarization data (see Fig. 2).

Planck low- ℓ likelihood

The *Planck* low- ℓ temperature-polarization likelihood uses foreground-cleaned LFI 70 GHz polarization maps together with the temperature map obtained from the *Planck* 30 to 353 GHz channels by the Commander component separation algorithm over 94% of the sky (see Planck Collaboration IX 2016 for further details). The *Planck* polarization map uses the LFI 70 GHz (excluding Surveys 2 and 4) low-resolution maps of Q and U polarization from which polarized synchrotron and thermal dust

emission components have been removed using the LFI 30 GHz and HFI 353 GHz maps as templates, respectively. (See Planck Collaboration XI 2016 for more details.) The polarization map covers the 46% of the sky outside the lowP polarization mask.

The low- ℓ likelihood is pixel-based and treats the temperature and polarization at the same resolution of $3'6$, or HEALpix (Górski et al. 2005) $N_{\text{side}} = 16$. Its multipole range extends from $\ell = 2$ to $\ell = 29$ in TT , TE , EE , and BB . In the 2015 *Planck* papers the polarization part of this likelihood is denoted as “lowP”.⁴ This *Planck* low- ℓ likelihood replaces the *Planck* temperature low- ℓ Gibbs module combined with the WMAP 9-yr low- ℓ polarization module used in the *Planck* 2013 cosmology papers (denoted by WP), which used lower resolution polarization maps at $N_{\text{side}} = 8$ (about $7'3$). With this *Planck*-only low- ℓ likelihood module, the basic *Planck* results presented in this release are completely independent of external information.

The *Planck* low-multipole likelihood alone implies $\tau = 0.067 \pm 0.022$ (Planck Collaboration XI 2016), a value smaller than the value inferred using the WP polarization likelihood, $\tau = 0.089 \pm 0.013$, used in the *Planck* 2013 papers (Planck Collaboration XV 2014). See Planck Collaboration XIII (2016) for the important implications of this decrease in τ for reionization. However, the LFI 70 GHz and WMAP polarization maps are in very good agreement when both are foreground-cleaned

⁴ In this paper we use the conventions introduced in Planck Collaboration XIII (2016). We adopt the following labels for likelihoods: (i) *Planck* TT denotes the combination of the TT likelihood at multipoles $\ell \geq 30$ and a low- ℓ temperature-only likelihood based on the CMB map recovered with Commander; (ii) *Planck* TT-lowT denotes the TT likelihood at multipoles $\ell \geq 30$; (iii) *Planck* TT+lowP further includes the *Planck* polarization data in the low- ℓ likelihood, as described in the main text; (iv) *Planck* TE denotes the likelihood at $\ell \geq 30$ using the TE spectrum; and (v) *Planck* TT, TE, EE+lowP denotes the combination of the likelihood at $\ell \geq 30$ using TT , TE , and EE spectra and the low- ℓ multipole likelihood. The label “ τ prior” denotes the use of a Gaussian prior $\tau = 0.07 \pm 0.02$. The labels “lowT, P” and “lowEB” denote the low- ℓ multipole likelihood and the Q , U pixel likelihood only, respectively.

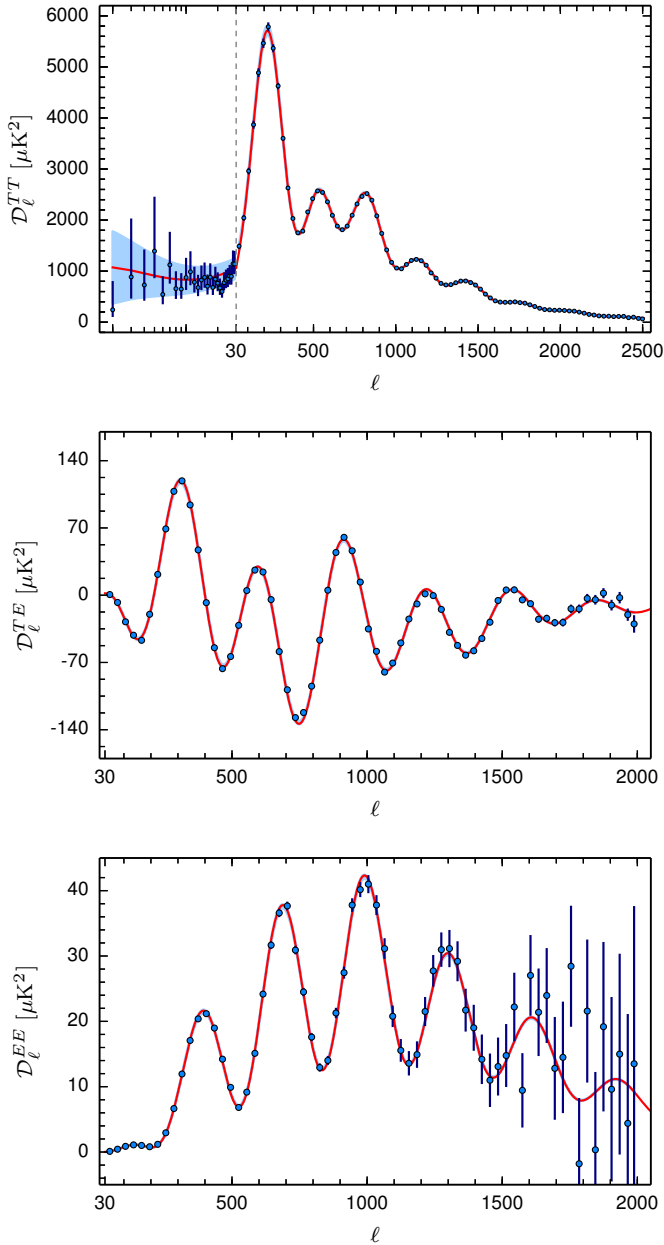


Fig. 2. *Planck* TT (top), high- ℓ TE (centre), and high- ℓ EE (bottom) angular power spectra. Here $\mathcal{D}_\ell \equiv \ell(\ell + 1)C_\ell/(2\pi)$.

using the HFI 353 GHz map as a polarized dust template (see [Planck Collaboration XI 2016](#) for further details). Therefore, it is useful to construct a noise-weighted combination to obtain a joint *Planck*/WMAP low resolution polarization data set, also described in [Planck Collaboration XI \(2016\)](#), using as a polarization mask the union of the WMAP P06 and *Planck* lowP polarization masks and keeping 74% of the sky. The polarization part of the combined low multipole likelihood is called lowP+WP. This combined low multipole likelihood gives $\tau = 0.071^{+0.011}_{-0.013}$ ([Planck Collaboration XI 2016](#)).

Planck high- ℓ likelihood

Following [Planck Collaboration XV \(2014\)](#), and [Planck Collaboration XI 2016](#) for polarization, we use a Gaussian

approximation for the high- ℓ part of the likelihood ($30 < \ell < 2500$), so that

$$-\log \mathcal{L}(\hat{C}|C(\theta)) = \frac{1}{2}(\hat{C} - C(\theta))^T \mathcal{M}^{-1}(\hat{C} - C(\theta)), \quad (12)$$

where a constant offset has been discarded. Here \hat{C} is the data vector, $C(\theta)$ is the model prediction for the parameter value vector θ , and \mathcal{M} is the covariance matrix. For the data vector, we use 100 GHz, 143 GHz, and 217 GHz half-mission cross-power spectra, avoiding the Galactic plane as well as the brightest point sources and the regions where the CO emission is the strongest. We retain 66% of the sky for 100 GHz, 57% for 143 GHz, and 47% for 217 GHz for the T masks, and respectively 70%, 50%, and 41% for the Q , U masks. Following [Planck Collaboration XXX \(2014\)](#), we do not mask for any other Galactic polarized emission. All the spectra are corrected for the beam and pixel window functions using the same beam for temperature and polarization. (For details see [Planck Collaboration XI 2016](#).)

The model for the cross-spectra can be written as

$$C_{\mu,\nu}(\theta) = \frac{C^{\text{cmb}}(\theta) + C_{\mu,\nu}^{\text{fg}}(\theta)}{\sqrt{c_\mu c_\nu}}, \quad (13)$$

where $C^{\text{cmb}}(\theta)$ is the CMB power spectrum, which is independent of the frequency, $C_{\mu,\nu}^{\text{fg}}(\theta)$ is the foreground model contribution for the cross-frequency spectrum $\mu \times \nu$, and c_μ is the calibration factor for the $\mu \times \mu$ spectrum. The model for the foreground residuals includes the following components: Galactic dust, clustered cosmic infrared background (CIB), thermal and kinetic Sunyaev-Zeldovich (tSZ and kSZ) effect, tSZ correlations with CIB, and point sources, for the TT foreground modeling; and for polarization, only dust is included. All the components are modelled by smooth C_ℓ templates with free amplitudes, which are determined along with the cosmological parameters as the likelihood is explored. The tSZ and kSZ models are the same as in 2013 (see [Planck Collaboration XV 2014](#)), although with different priors ([Planck Collaboration XI 2016](#); [Planck Collaboration XIII 2016](#)), while the CIB and tSZ-CIB correlation models use the updated CIB models described in [Planck Collaboration XXX \(2014\)](#). The point source contamination is modelled as Poisson noise with an independent amplitude for each frequency pair. Finally, the dust contribution uses an effective smooth model measured from high frequency maps. Details of our dust and noise modelling can be found in [Planck Collaboration XI \(2016\)](#). The dust is the dominant foreground component for TT at $\ell < 500$, while the point source component, and for 217×217 also the CIB component, dominate at high ℓ . The other foreground components are poorly determined by *Planck*. Finally, our treatment of the calibration factors and beam uncertainties and mismatch are described in [Planck Collaboration XI \(2016\)](#).

The covariance matrix accounts for the correlation due to the mask and is computed following the equations in [Planck Collaboration XV \(2014\)](#), extended to polarization in [Planck Collaboration XI \(2016\)](#) and references therein. The fiducial model used to compute the covariance is based on a joint fit of base Λ CDM and nuisance parameters obtained with a previous version of the matrix. We iterate the process until the parameters stop changing. For more details, see [Planck Collaboration XI \(2016\)](#).

The joint unbinned covariance matrix is approximately of size $23\,000 \times 23\,000$. The memory and speed requirements for dealing with such a huge matrix are significant, so to reduce its

size, we bin the data and the covariance matrix to compress the data vector size by a factor of 10. The binning uses varying bin width with $\Delta\ell = 5$ for $29 < \ell < 100$, $\Delta\ell = 9$ for $99 < \ell < 1504$, $\Delta\ell = 17$ for $1503 < \ell < 2014$, and $\Delta\ell = 33$ for $2013 < \ell < 2509$, and a weighting in $\ell(\ell+1)$ to flatten the spectrum. Where a higher resolution is desirable, we also use a more finely binned version (“bin3”, unbinned up to $\ell = 80$ and $\Delta\ell = 3$ beyond that) as well as a completely unbinned version (“bin1”). We use odd bin sizes, since for an azimuthally symmetric mask, the correlation between a multipole and its neighbours is symmetric, oscillating between positive and negative values. Using the base Λ CDM model and single-parameter classical extensions, we confirmed that the cosmological and nuisance parameter fits with or without binning are indistinguishable.

As discussed in [Planck Collaboration XI \(2016\)](#) and [Planck Collaboration XIII \(2016\)](#), the *TE* and *EE* high- ℓ data are not free of small systematic effects, such as leakage from temperature to polarization. Although the propagated effects of these residual systematics on cosmological parameters are small and do not alter the conclusions of this paper, we mainly refer to *Planck* TT+lowP in combination with the *Planck* lensing or additional data sets as the most reliable results for this release.

Planck CMB bispectrum

We use measurements of the non-Gaussianity amplitude f_{NL} from the CMB bispectrum presented in [Planck Collaboration XVII \(2016\)](#). Non-Gaussianity constraints have been obtained using three optimal bispectrum estimators: separable template fitting (also known as “KSW”), binned, and modal. The maps analysed are the *Planck* 2015 full mission sky maps, both in temperature and in *E* polarization, as cleaned with the four component separation methods SMICA, SEVEM, NILC, and Commander. The map is masked to remove the brightest parts of the Galaxy as well as the brightest point sources and covers approximately 70% of the sky. In this paper we mainly exploit the joint constraints on equilateral and orthogonal non-Gaussianity (after removing the integrated Sachs-Wolfe effect-lensing bias), $f_{\text{NL}}^{\text{equil}} = -16 \pm 70$, $f_{\text{NL}}^{\text{ortho}} = -34 \pm 33$ from *T* only, and $f_{\text{NL}}^{\text{equil}} = -3.7 \pm 43$, $f_{\text{NL}}^{\text{ortho}} = -26 \pm 21$ from *T* and *E* (68% CL). For reference, the constraints on local non-Gaussianity are $f_{\text{NL}}^{\text{local}} = 2.5 \pm 5.7$ from *T* only, and $f_{\text{NL}}^{\text{local}} = 0.8 \pm 5.0$ from *T* and *E* (68% CL). Starting from a Gaussian f_{NL} -likelihood, which is an accurate assumption in the regime of small primordial non-Gaussianity, we use these constraints to derive limits on the sound speed of the inflation fluctuations (or other microscopic parameters of inflationary models; [Planck Collaboration XXIV 2014](#)). The bounds on the sound speed for various models are then used in combination with *Planck* power spectrum data.

Planck CMB lensing data

Some of our analysis includes the *Planck* 2015 lensing likelihood, presented in [Planck Collaboration XV \(2016\)](#), which utilizes the non-Gaussian trispectrum induced by lensing to estimate the power spectrum of the lensing potential, $C_\ell^{\phi\phi}$. This signal is extracted using a full set of temperature- and polarization-based quadratic lensing estimators ([Okamoto & Hu 2003](#)) applied to the SMICA CMB map over approximately 70% of the sky, as described in [Planck Collaboration IX \(2016\)](#). We have used the conservative bandpower likelihood, covering multipoles $40 \leq \ell \leq 400$. This provides a measurement of the

lensing potential power at the 40σ level, giving a 2.5%-accurate constraint on the overall lensing power in this multipole range. The measurement of the lensing power spectrum used here is approximately twice as powerful as the measurement used in our previous 2013 analysis ([Planck Collaboration XXII 2014](#); [Planck Collaboration XVII 2014](#)), which used temperature-only data from the *Planck* nominal mission data set.

3.4. Non-Planck data

BAO data

Baryon acoustic oscillations (BAO) are the counterpart in the late time matter power spectrum of the acoustic oscillations seen in the CMB multipole spectrum ([Eisenstein et al. 2005](#)). Both originate from coherent oscillations of the photon-baryon plasma before these two components become decoupled at recombination. Measuring the position of these oscillations in the matter power spectra at different redshifts constrains the expansion history of the universe after decoupling, thus removing degeneracies in the interpretation of the CMB anisotropies.

In this paper, we combine constraints on $D_V(\bar{z})/r_s$ (the ratio between the spherically-averaged distance scale D_V to the effective survey redshift, \bar{z} , and the sound horizon, r_s) inferred from 6dFGRS data ([Beutler et al. 2011](#)) at $\bar{z} = 0.106$, the SDSS-MGS data ([Ross et al. 2015](#)) at $\bar{z} = 0.15$, and the SDSS-DR11 CMASS and LOWZ data ([Anderson et al. 2014](#)) at redshifts $\bar{z} = 0.57$ and 0.32 . For details see [Planck Collaboration XIII \(2016\)](#).

Joint BICEP2/Keck Array and Planck constraint on r

Since the *Planck* temperature constraints on the tensor-to-scalar ratio are close to the cosmic variance limit, the inclusion of data sets sensitive to the expected *B*-mode signal of primordial gravitational waves is particularly useful. In this paper, we provide results including the joint analysis cross-correlating BICEP2/Keck Array observations and *Planck* (BKP). Combining the more sensitive BICEP2/Keck Array *B*-mode polarization maps in the approximately 400 deg^2 BICEP2 field with the *Planck* maps at higher frequencies where dust dominates allows a statistical analysis taking into account foreground contamination. Using *BB* auto- and cross-frequency spectra between BICEP2/Keck Array (150 GHz) and *Planck* (217 and 353 GHz), BKP find a 95% upper limit of $r_{0.05} < 0.12$.

3.5. Parameter estimation and model comparison

Much of this paper uses a Bayesian approach to parameter estimation, and unless otherwise specified, we assign broad top-hat prior probability distributions to the cosmological parameters listed in Table 1. We generate posterior probability distributions for the parameters using either the Metropolis-Hastings algorithm implemented in CosmoMC ([Lewis & Bridle 2002](#)) or MontePython ([Audren et al. 2013](#)), the nested sampling algorithm MultiNest ([Feroz & Hobson 2008](#); [Feroz et al. 2009, 2013](#)), or PolyChord, which combines nested sampling with slice sampling ([Handley et al. 2015](#)). The latter two also compute the Bayesian evidence needed for model comparison. Nevertheless, χ^2 values are often provided as well (using CosmoMC’s implementation of the BOBYQA algorithm ([Powell 2009](#)) for maximizing the likelihood), and other parts of the paper employ frequentist methods when appropriate.

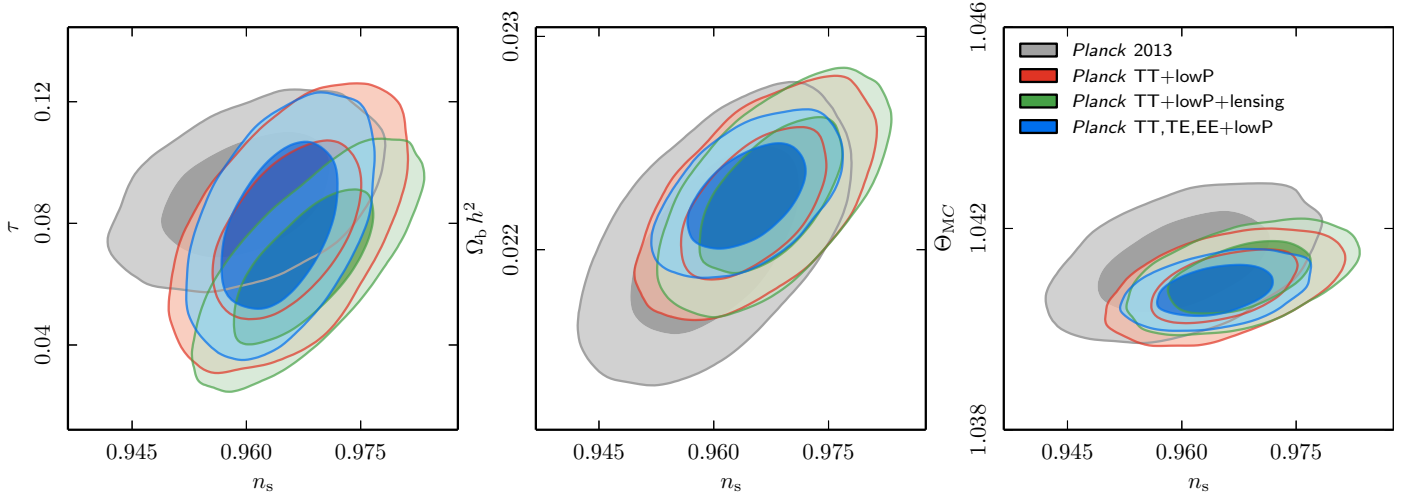


Fig. 3. Comparison of the marginalized joint 68% and 95% CL constraints on (n_s, τ) (left panel), $(n_s, \Omega_b h^2)$ (middle panel), and (n_s, θ_{MC}) (right panel), for *Planck* 2013 (grey contours), *Planck* TT+lowP (red contours), *Planck* TT+lowP+lensing (green contours), and *Planck* TT, TE, EE+lowP (blue contours).

Table 3. Confidence limits on the parameters of the base Λ CDM model, for various combinations of *Planck* 2015 data, at the 68% confidence level.

Parameter	TT+lowP	TT+lowP+lensing	TT+lowP+BAO	TT, TE, EE+lowP
$\Omega_b h^2$	0.02222 ± 0.00023	0.02226 ± 0.00023	0.02226 ± 0.00020	0.02225 ± 0.00016
$\Omega_c h^2$	0.1197 ± 0.0022	0.1186 ± 0.0020	0.1190 ± 0.0013	0.1198 ± 0.0015
$100\theta_{MC}$	1.04085 ± 0.00047	1.04103 ± 0.00046	1.04095 ± 0.00041	1.04077 ± 0.00032
τ	0.078 ± 0.019	0.066 ± 0.016	0.080 ± 0.017	0.079 ± 0.017
$\ln(10^{10} A_s)$	3.089 ± 0.036	3.062 ± 0.029	3.093 ± 0.034	3.094 ± 0.034
n_s	0.9655 ± 0.0062	0.9677 ± 0.0060	0.9673 ± 0.0045	0.9645 ± 0.0049
H_0	67.31 ± 0.96	67.81 ± 0.92	67.63 ± 0.57	67.27 ± 0.66
Ω_m	0.315 ± 0.013	0.308 ± 0.012	0.3104 ± 0.0076	0.3156 ± 0.0091

4. Constraints on the primordial spectrum of curvature perturbations

One of the most important results of the *Planck* nominal mission was the determination of the departure from scale invariance for the spectrum of scalar perturbations at high statistical significance (Planck Collaboration XVI 2014; Planck Collaboration XXII 2014). We now update these measurements with the *Planck* full mission data in temperature and polarization.

4.1. Tilt of the curvature power spectrum

For the base Λ CDM model with a power-law power spectrum of curvature perturbations, the constraint on the scalar spectral index, n_s , with the *Planck* full mission temperature data is

$$n_s = 0.9655 \pm 0.0062 \text{ (68\% CL, Planck TT+lowP)}. \quad (14)$$

This result is compatible with the *Planck* 2013 constraint, $n_s = 0.9603 \pm 0.0073$ (Planck Collaboration XV 2014; Planck Collaboration XVI 2014). See Fig. 3 for the accompanying changes in τ , $\Omega_b h^2$, and θ_{MC} . The shift towards higher values for n_s with respect to the nominal mission results is due to several improvements in the data processing and likelihood which are discussed in Sect. 3, including the removal of the 4 K cooler systematics. For the values of other cosmological parameters in

the base Λ CDM model, see Table 3. We also provide the results for the base Λ CDM model and extended models online.⁵

When the *Planck* high- ℓ polarization is combined with temperature, we obtain

$$n_s = 0.9645 \pm 0.0049 \text{ (68\% CL, Planck TT, TE, EE+lowP)}, \quad (15)$$

together with $\tau = 0.079 \pm 0.017$ (68% CL), which is consistent with the TT+lowP results. The *Planck* high- ℓ polarization pulls τ up to a slightly higher value. When the *Planck* lensing measurement is added to the temperature data, we obtain

$$n_s = 0.9677 \pm 0.0060 \text{ (68\% CL, Planck TT+lowP+lensing)}, \quad (16)$$

with $\tau = 0.066 \pm 0.016$ (68% CL). The shift towards slightly smaller values of the optical depth is driven by a marginal preference for a smaller primordial amplitude, A_s , in the *Planck* lensing data (Planck Collaboration XV 2016). Given that the temperature data provide a sharp constraint on the combination $e^{-2\tau} A_s$, a slightly lower A_s requires a smaller optical depth to reionization.

4.2. Viability of the Harrison-Zeldovich spectrum

Even though the estimated scalar spectral index has risen slightly with respect to the *Planck* 2013 release, the assumption of

⁵ <http://www.cosmos.esa.int/web/planck/pla>

a Harrison-Zeldovich (HZ) scale-invariant spectrum (Harrison 1970; Peebles & Yu 1970; Zeldovich 1972) continues to be disfavoured (with a modest increase in significance, from 5.1σ in 2013 to 5.6σ today), because the error bar on n_s has decreased. The value of n_s inferred from the *Planck* 2015 temperature plus large-scale polarization data lies 5.6 standard deviations away from unity (with a corresponding $\Delta\chi^2 = 29.9$), if one assumes the base Λ CDM late-time cosmological model. If we consider more general reionization models, parameterized by a principal component analysis (Mortonson & Hu 2008) instead of τ (where reionization is assumed to have occurred instantaneously), we find $\Delta\chi^2 = 14.9$ for $n_s = 1$. Previously, simple one-parameter extensions of the base model, such as Λ CDM+ N_{eff} (where N_{eff} is the effective number of neutrino flavours) or Λ CDM+ Y_p (where Y_p is the primordial value of the helium mass fraction), could nearly reconcile the *Planck* temperature data with $n_s = 1$. They now lead to $\Delta\chi^2 = 7.6$ and 9.3 , respectively. For any of the cosmological models that we have considered, the $\Delta\chi^2$ by which the HZ model is penalized with respect to the tilted model has increased since the 2013 analysis (PCI13) thanks to the constraining power of the full mission temperature data. Adding *Planck* high- ℓ polarization data further disfavours the HZ model: in Λ CDM, the χ^2 increases by 57.8, for general reionization we obtain $\Delta\chi^2 = 41.3$, and for Λ CDM+ N_{eff} and Λ CDM+ Y_p we find $\Delta\chi^2 = 22.5$ and 24.0 , respectively.

4.3. Running of the spectral index

The running of the scalar spectral index is constrained by the *Planck* 2015 full mission temperature data to

$$\frac{dn_s}{d\ln k} = -0.0084 \pm 0.0082 \text{ (68\% CL, Planck TT+lowP)}. \quad (17)$$

The combined constraint including high- ℓ polarization is

$$\frac{dn_s}{d\ln k} = -0.0057 \pm 0.0071 \text{ (68\% CL, Planck TT, TE, EE+lowP)}. \quad (18)$$

Adding the *Planck* CMB lensing data to the temperature data further reduces the central value for the running, i.e., $dn_s/d\ln k = -0.0033 \pm 0.0074$ (68% CL, *Planck* TT+lowP+lensing).

The central value for the running has decreased in magnitude with respect to the *Planck* 2013 nominal mission (Planck Collaboration XVI 2014 found $dn_s/d\ln k = -0.013 \pm 0.009$; see Fig. 4), and the improvement of the maximum likelihood with respect to a power-law spectrum is smaller, $\Delta\chi^2 \approx -0.8$. Among the different effects contributing to the decrease in the central value of the running with respect to the *Planck* 2013 result, we mention a change in HFI beams at $\ell \lesssim 200$ (Planck Collaboration XIII 2016). Nevertheless, the deficit of power at low multipoles in the *Planck* 2015 temperature power spectrum contributes to a preference for slightly negative values of the running, but with low statistical significance.

The *Planck* constraints on n_s and $dn_s/d\ln k$ are remarkably stable against the addition of the BAO likelihood. The combination with BAO shifts n_s to slightly higher values and shrinks its uncertainty by about 30% when only high- ℓ temperature is considered, and by only about 15% when high- ℓ temperature and polarization are combined. In slow-roll inflation, the running of the scalar spectral index is connected to the third derivative of the potential (Kosowsky & Turner 1995). As was the case for the nominal mission results, values of the running compatible

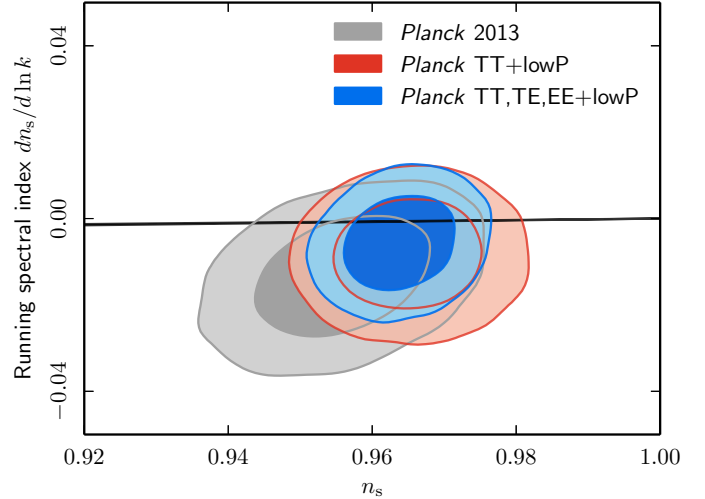


Fig. 4. Marginalized joint 68% and 95% CL for $(n_s, dn_s/d\ln k)$ using *Planck* TT+lowP and *Planck* TT, TE, EE+lowP. Constraints from the *Planck* 2013 data release are also shown for comparison. For comparison, the thin black stripe shows the prediction for single-field monomial chaotic inflationary models with $50 < N_* < 60$.

with the *Planck* 2015 constraints can be obtained in viable inflationary models (Kobayashi & Takahashi 2011).

When the running of the running is allowed to float, the *Planck* TT+lowP (*Planck* TT, TE, EE+lowP) data give:

$$\begin{aligned} n_s &= 0.9569 \pm 0.0077 \text{ (0.9586} \pm 0.0056\text{),} \\ dn_s/d\ln k &= 0.011^{+0.014}_{-0.013} \text{ (0.009} \pm 0.010\text{), (68\% CL)} \\ d^2n_s/d\ln k^2 &= 0.029^{+0.015}_{-0.016} \text{ (0.025} \pm 0.013\text{),} \end{aligned} \quad (19)$$

at the pivot scale $k_* = 0.05 \text{ Mpc}^{-1}$. Allowing for running of the running provides a better fit to the temperature spectrum at low multipoles, such that $\Delta\chi^2 \approx -4.8$ (-4.9) for TT+lowP (TT, TE, EE+lowP), but is not statistically preferred over the simplest Λ CDM model.

Note that the inclusion of small-scale data such as Ly α might further constrain the running of the spectral index and its derivative. The recent analysis of the BOSS one-dimensional Ly α flux power spectrum presented in Palanque-Delabrouille et al. (2015) and Rossi et al. (2015) was optimized for measuring the neutrino mass. It does not include constraints on the spectral index running, which would require new dedicated N -body simulations. Hence we do not include Ly α constraints here.

In Sect. 7 on inflaton potential reconstruction we will show that the data cannot accommodate a significant running but are compatible with a larger running of the running.

4.4. Suppression of power on the largest scales

Although not statistically significant, the trend for a negative running or positive running of the running observed in the last subsection was driven by the lack of power in the *Planck* temperature power spectrum at low multipoles, already mentioned in the *Planck* 2013 release. This deficit could potentially be explained by a primordial spectrum featuring a depletion of power only at large wavelengths. Here we investigate two examples of such models.

Table 4. Constraints on the primordial perturbation parameters for Λ CDM+ r and Λ CDM+ r + $dn_s/d\ln k$ models from *Planck*.

Model	Parameter	<i>Planck</i> TT+lowP	<i>Planck</i> TT+lowP+lensing	<i>Planck</i> TT+lowP+BAO	<i>Planck</i> TT, TE, EE+lowP
Λ CDM+ r	n_s	0.9666 ± 0.0062	0.9688 ± 0.0061	0.9680 ± 0.0045	0.9652 ± 0.0047
	$r_{0.002}$	<0.103	<0.114	<0.113	<0.099
	$-2\Delta \ln \mathcal{L}_{\max}$	0	0	0	0
Λ CDM+ r + $dn_s/d\ln k$	n_s	0.9667 ± 0.0066	0.9690 ± 0.0063	0.9673 ± 0.0043	0.9644 ± 0.0049
	$r_{0.002}$	<0.180	<0.186	<0.176	<0.152
	r	<0.168	<0.176	<0.166	<0.149
	$dn_s/d\ln k$	$-0.0126^{+0.0098}_{-0.0087}$	$-0.0076^{+0.0092}_{-0.0080}$	-0.0125 ± 0.0091	-0.0085 ± 0.0076
	$-2\Delta \ln \mathcal{L}_{\max}$	-0.81	-0.08	-0.87	-0.38

Notes. Constraints on the spectral index and its dependence on the wavelength are given at the pivot scale of $k_* = 0.05 \text{ Mpc}^{-1}$.

We first update the analysis (already presented in [PCI13](#)) of a power-law spectrum multiplied by an exponential cutoff:

$$\mathcal{P}_{\mathcal{R}}(k) = \mathcal{P}_0(k) \left\{ 1 - \exp \left[- \left(\frac{k}{k_c} \right)^{\lambda_c} \right] \right\}. \quad (20)$$

This simple parameterization is motivated by models with a short inflationary stage in which the onset of the slow-roll phase coincides with the time when the largest observable scales exited the Hubble radius during inflation. The curvature spectrum is then strongly suppressed on those scales. We apply top-hat priors on the parameter λ_c , controlling the steepness of the cut-off, and on the logarithm of the cutoff scale, k_c . We choose prior ranges $\lambda_c \in [0, 10]$ and $\ln(k_c/\text{Mpc}^{-1}) \in [-12, -3]$. For *Planck* TT+lowP (*Planck* TT, TE, EE+lowP), the best-fit model has $\lambda_c = 0.50$ (0.53), $\ln(k_c/\text{Mpc}^{-1}) = -7.98$ (-7.98), $n_s = 0.9647$ (0.9649), and improves the effective χ^2 by a modest amount, $\Delta\chi^2 \approx -3.4$ (-3.4).

As a second model, we consider a broken power-law spectrum for curvature perturbations:

$$\mathcal{P}_{\mathcal{R}}(k) = \begin{cases} A_{\text{low}} \left(\frac{k}{k_*} \right)^{n_s-1+\delta} & \text{if } k \leq k_b, \\ A_s \left(\frac{k}{k_*} \right)^{n_s-1} & \text{if } k \geq k_b, \end{cases} \quad (21)$$

with $A_{\text{low}} = A_s(k_b/k_*)^{-\delta}$ to ensure continuity at $k = k_b$. Hence this model, like the previous one, has two parameters, and also suppresses power at large wavelengths when $\delta > 0$. We assume top-hat priors $\delta \in [0, 2]$ and $\ln(k_b/\text{Mpc}^{-1}) \in [-12, -3]$, and standard uniform priors for $\ln(10^{10}A_s)$ and n_s . The best fit to *Planck* TT+lowP (*Planck* TT, TE, EE+lowP) is found for $n_s = 0.9658$ (0.9647), $\delta = 1.14$ (1.14), and $\ln(k_b/\text{Mpc}^{-1}) = -7.55$ (-7.57), with a very small χ^2 improvement of $\Delta\chi^2 \approx -1.9$ (-1.6).

We conclude that neither of these two models with two extra parameters is preferred over the base Λ CDM model. (See also the discussion of a step inflationary potential in Sect. [9.1.1](#))

5. Constraints on tensor modes

In this section, we focus on the *Planck* 2015 constraints on tensor perturbations. Unless otherwise stated, we consider that the tensor spectral index satisfies the standard inflationary consistency condition to lowest order in slow roll, $n_t = -r/8$. We recall that r is defined at the pivot scale $k_* = 0.05 \text{ Mpc}^{-1}$. However, for comparison with other studies, we also report our bounds in terms of the tensor-to-scalar ratio $r_{0.002}$ at $k_* = 0.002 \text{ Mpc}^{-1}$.

5.1. *Planck* 2015 upper bound on r

The constraints on the tensor-to-scalar ratio inferred from the *Planck* full mission data for the Λ CDM+ r model are:

$$r_{0.002} < 0.10 \quad (95\% \text{ CL, } \textit{Planck} \text{ TT+lowP}), \quad (22)$$

$$r_{0.002} < 0.11 \quad (95\% \text{ CL, } \textit{Planck} \text{ TT+lowP+lensing}), \quad (23)$$

$$r_{0.002} < 0.11 \quad (95\% \text{ CL, } \textit{Planck} \text{ TT+lowP+BAO}), \quad (24)$$

$$r_{0.002} < 0.10 \quad (95\% \text{ CL, } \textit{Planck} \text{ TT, TE, EE+lowP}). \quad (25)$$

Table 4 also shows the bounds on n_s in each of these cases.

These results slightly improve over the constraint $r_{0.002} < 0.12$ (95% CL) derived from the *Planck* 2013 temperature data in combination with WMAP large-scale polarization data ([Planck Collaboration XVI 2014](#); [Planck Collaboration XXII 2014](#)). The constraint obtained by *Planck* temperature and polarization on large scales is tighter than the *Planck* B-mode 95% CL upper limit from the 100 and 143 GHz HFI channels, $r < 0.27$ ([Planck Collaboration XI 2016](#)). The constraints on r reported in Table 4 can be translated into upper bounds on the energy scale of inflation at the time when the pivot scale exits the Hubble radius using

$$V_* = \frac{3\pi^2 A_s}{2} r M_{\text{pl}}^4 = (1.88 \times 10^{16} \text{ GeV})^4 \frac{r}{0.10}. \quad (26)$$

This gives an upper bound on the Hubble parameter during inflation of $H_*/M_{\text{pl}} < 3.6 \times 10^{-5}$ (95% CL) for *Planck* TT+lowP.

These bounds are relaxed when allowing for a scale dependence of the scalar and tensor spectral indices. In that case, we assume that the tensor spectral index and its running are fixed by the standard inflationary consistency condition at second order in slow roll. We obtain

$$r_{0.002} < 0.18 \quad (95\% \text{ CL, } \textit{Planck} \text{ TT+lowP}), \quad (27)$$

$$\frac{dn_s}{d\ln k} = -0.013^{+0.010}_{-0.009} \quad (68\% \text{ CL, } \textit{Planck} \text{ TT+lowP}), \quad (28)$$

with $n_s = 0.9667 \pm 0.0066$ (68% CL). At the standard pivot scale, $k_* = 0.05 \text{ Mpc}^{-1}$, the bound is stronger ($r < 0.17$ at 95% CL), because k_* is closer to the scale at which n_s and r decorrelate. The constraint on $r_{0.002}$ in Eq. (27) is 21% tighter than the corresponding *Planck* 2013 constraint. The mean value of the running in Eq. (28) is higher (lower in absolute value) than with *Planck* 2013 by 45%. Figures 5 and 6 clearly illustrate this significant improvement with respect to the previous *Planck* data release. Table 4 shows how bounds on $(r, n_s, dn_s/d\ln k)$ are affected by

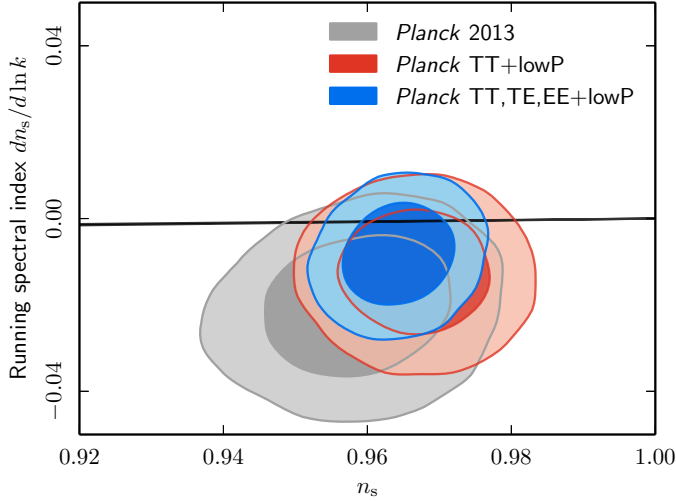


Fig. 5. Marginalized joint confidence contours for $(n_s, dn_s/d\ln k)$, at the 68% and 95% CL, in the presence of a non-zero tensor contribution, and using *Planck* TT+lowP or *Planck* TT, TE, EE+lowP. Constraints from the *Planck* 2013 data release are also shown for comparison. The thin black stripe shows the prediction of single-field monomial inflation models with $50 < N_* < 60$.

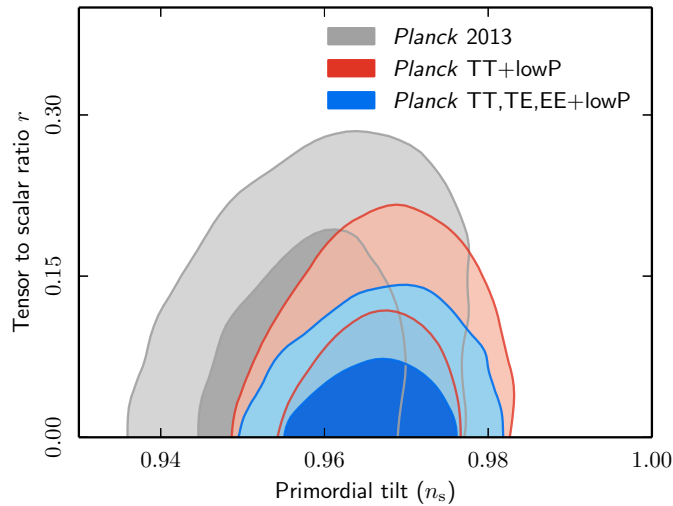


Fig. 6. Marginalized joint confidence contours for (n_s, r) , at the 68% and 95% CL, in the presence of running of the spectral indices, and for the same data combinations as in the previous figure.

the lensing reconstruction, BAO, or high- ℓ polarization data. The tightest bounds are obtained in combination with polarization:

$$r_{0.002} < 0.15 \quad (95\% \text{ CL, } \textit{Planck} \text{ TT, TE, EE+lowP}), \quad (29)$$

$$\frac{dn_s}{d\ln k} = -0.009 \pm 0.008 \quad (68\% \text{ CL, } \textit{Planck} \text{ TT, TE, EE+lowP}), \quad (30)$$

with $n_s = 0.9644 \pm 0.0049$ (68% CL).

Neither the *Planck* full mission constraints in Eqs. (22)–(25) nor those including a running in Eqs. (27) and (29) are compatible with the interpretation of the BICEP2 *B*-mode polarization data in terms of primordial gravitational waves (BICEP2 Collaboration 2014b). Instead they are in excellent agreement with the results of the BICEP2/Keck Array-*Planck* cross-correlation analysis, as discussed in Sect. 13.

5.2. Dependence of the r constraints on the low- ℓ likelihood

The constraints on r discussed above are further tightened by adding WMAP polarization information on large angular scales. The *Planck* measurement of CMB polarization on large angular scales at 70 GHz is consistent with the WMAP 9-year one, based on the *K*, *Q*, and *V*-bands (at 30, 40, and 60 GHz, respectively), once the *Planck* 353 GHz channel is used to remove the dust contamination, instead of the theoretical dust model used by the WMAP team (Page et al. 2007). (For a detailed discussion, see Planck Collaboration XI 2016.) By combining *Planck* TT data with LFI 70 GHz and WMAP polarization data on large angular scales, we obtain a 35% reduction of uncertainty, giving $\tau = 0.074 \pm 0.012$ (68% CL) and $n_s = 0.9660 \pm 0.060$ (68% CL) for the base Λ CDM model. When tensors are added, the bounds become

$$r_{0.002} < 0.09 \quad (95\% \text{ CL, } \textit{Planck} \text{ TT+lowP+WP}), \quad (31)$$

$$n_s = 0.9655 \pm 0.058 \quad (68\% \text{ CL, } \textit{Planck} \text{ TT+lowP+WP}), \quad (32)$$

$$\tau = 0.073^{+0.011}_{-0.013} \quad (68\% \text{ CL, } \textit{Planck} \text{ TT+lowP+WP}). \quad (33)$$

When tensors and running are both varied, we obtain $r_{0.002} < 0.14$ (95% CL) and $dn_s/d\ln k = -0.010 \pm 0.008$ (68% CL) for *Planck* TT+lowP+WP. These constraints are all tighter than those based on *Planck* TT+lowP only.

5.3. The tensor-to-scalar ratio and the low- ℓ deficit in temperature

As noted previously (Planck Collaboration XV 2014; Planck Collaboration XVI 2014; Planck Collaboration XXII 2014), the low- ℓ temperature data display a slight lack of power compared to the expectation of the best-fit tensor-free base Λ CDM model. Since tensor fluctuations add power on small scales, the effect will be exacerbated in models allowing $r > 0$.

In order to quantify this tension, we compare the observed constraint on r to that inferred from simulated *Planck* data. In the simulations, we assume the underlying fiducial model to be tensor-free, with parameters close to the base Λ CDM best-fit values. We limit the simulations to mock temperature power spectra only and fit these spectra with an exact low- ℓ likelihood for $2 \leq \ell \leq 29$ (see Perotto et al. 2006), and a high- ℓ Gaussian likelihood for $30 \leq \ell \leq 2508$ based on the frequency-combined, foreground-marginalized, unbinned *Planck* temperature power spectrum covariance matrix. Additionally, we impose a Gaussian prior of $\tau = 0.07 \pm 0.02$.

Based on 100 simulated data sets, we find a 95% CL upper limit on the tensor-to-scalar ratio of $\bar{r}_{2\sigma} \approx 0.260$. The corresponding constraint from real data (using low- ℓ Commander temperature data, the frequency-combined, foreground-marginalized, unbinned *Planck* high- ℓ TT power spectrum, and the same prior on τ as above) reads $r < 0.123$, confirming that the actual constraint is tighter than what one would have expected. However, the actual constraint is not excessively unusual: out of the 100 simulations, 4 lead to an even tighter bound, corresponding to a significance of about 2σ . Thus, under the hypothesis of the base Λ CDM cosmology, the upper limit on r that we get from the data is not implausible as a chance fluctuation of the low multipole power.

To illustrate the contribution of the low- ℓ temperature power deficit to the estimates of cosmological parameters, we show as an example in Fig. 7 how n_s shifts towards lower values when the $\ell < 30$ temperature information is discarded (we will refer to this case as “*Planck* TT–lowT”). The shift in n_s is approximately

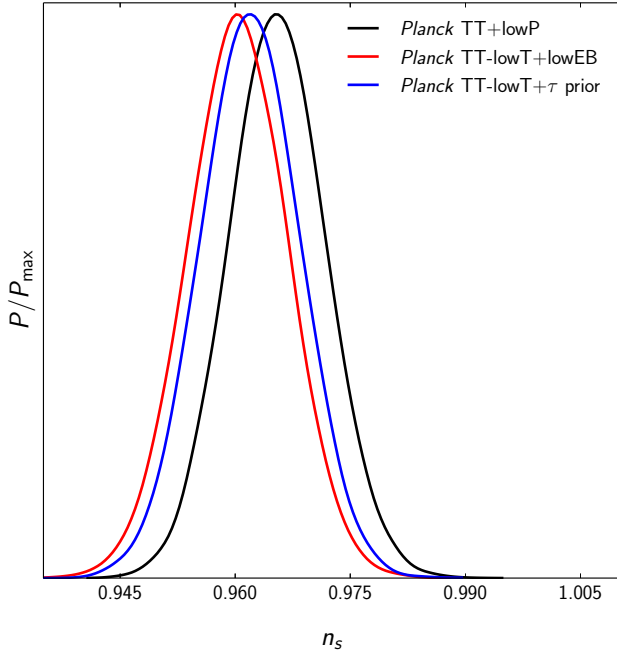


Fig. 7. One-dimensional posterior probabilities for n_s for the base Λ CDM model obtained by excluding temperature multipoles for $\ell < 30$ (“TT–lowT”), while either keeping low- ℓ polarization data, or in addition replacing them with a Gaussian prior on τ .

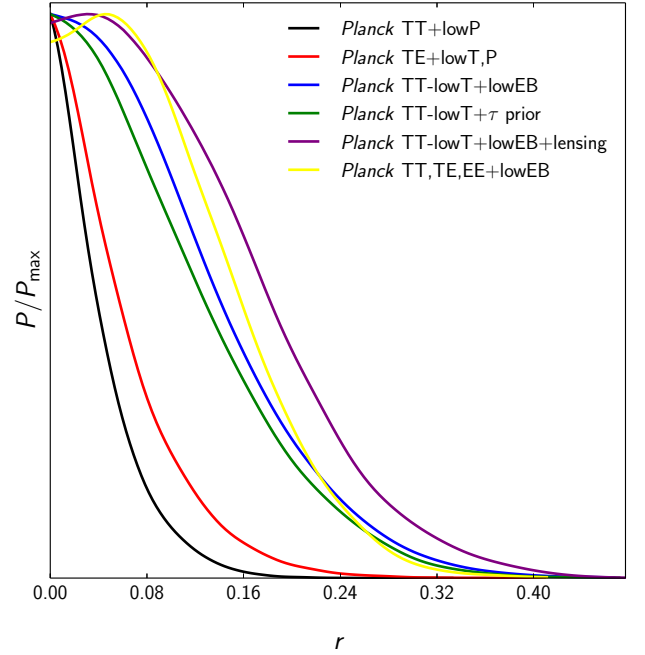


Fig. 8. One-dimensional posterior probabilities for r for various data combinations, either including or not including temperature multipoles for $\ell < 30$, and compared with the baseline choice (*Planck* TT+lowP, black curve).

–0.005 (or –0.003 when the lowP likelihood is replaced by a Gaussian prior $\tau = 0.07 \pm 0.02$). These shifts exceed those found in Sect. 4.4, where a primordial power spectrum suppressed on large scales was fitted to the data.

Figure 8 displays the posterior probability for r for various combinations of data sets, some of which exclude the $\ell < 30$ TT data. This leads to the very conservative bounds $r \lesssim 0.24$ and $r \lesssim 0.23$ at 95% CL when combined with the lowP likelihood or with the Gaussian prior $\tau = 0.07 \pm 0.020$, respectively.

5.4. Relaxing assumptions on the late-time cosmological evolution

As in the *Planck* 2013 release (PCI13), we now ask how robust the *Planck* results on the tensor-to-scalar ratio are against assumptions on the late-time cosmological evolution. The results are summarized in Table 5, and some particular cases are illustrated in Fig. 9. Constraints on r turn out to be remarkably stable for one-parameter extensions of the Λ CDM+ r model, with the only exception the Λ CDM+ r + Ω_K case in the absence of the late time information from *Planck* lensing or BAO data. The weak trend towards $\Omega_K < 0$, i.e., towards a positively curved (closed) universe from the temperature and polarization data alone, and the well-known degeneracy between Ω_K and H_0/Ω_m lead to a slight suppression of the Sachs-Wolfe plateau in the scalar temperature spectrum. This leaves more room for a tensor component.

This further degeneracy when r is added builds on the negative values for the curvature allowed by *Planck* TT+lowP, $\Omega_K = -0.052^{+0.049}_{-0.055}$ at 95% CL (*Planck Collaboration XIII* 2016). The exploitation of the information contained in the *Planck* lensing likelihood leads to a tighter constraint, $\Omega_K = -0.005^{+0.016}_{-0.017}$ at 95% CL, which improves on the *Planck* 2013 results ($\Omega_K = -0.007^{+0.018}_{-0.019}$ at 95% CL). However, due to the remaining degeneracies left by the uncertainties in polarization on large

angular scales, a full appreciation of the improvement due to the full mission temperature and lensing data can be obtained by using lowP+WP, which leads to $\Omega_K = -0.003^{+0.012}_{-0.014}$ at 95% CL. Note that the negative values allowed for the curvature are decreased in magnitude when the running is allowed, suggesting that the low- ℓ temperature deficit is contributing to the estimate of the spatial curvature.

The trend found for Λ CDM+ r + Ω_K is even clearer when spatial curvature and the running of the spectral index are varied at the same time. In this case, the *Planck* temperature plus polarization data are compatible with r values as large as 0.19 (95% CL), at the cost of an almost 4σ deviation from spatial flatness (which, however, disappears as soon as lensing or BAO data are considered).

6. Implications for single-field slow-roll inflation

In this section we study the implications of *Planck* 2015 constraints on standard slow-roll single-field inflationary models.

6.1. Constraints on slow-roll parameters

We first present the *Planck* 2015 constraints on slow-roll parameters obtained through the analytic perturbative expansion in terms of the HFFs ϵ_i for the primordial spectra of cosmological fluctuations during slow-roll inflation (Stewart & Lyth 1993; Gong & Stewart 2001; Leach et al. 2002). When restricting to first order in ϵ_i , we obtain

$$\epsilon_1 < 0.0068 \quad (95\% \text{ CL, } \textit{Planck} \text{ TT+lowP}), \quad (34)$$

$$\epsilon_2 = 0.029^{+0.008}_{-0.007} \quad (68\% \text{ CL, } \textit{Planck} \text{ TT+lowP}). \quad (35)$$

When high- ℓ polarization is included we obtain $\epsilon_1 < 0.0066$ at 95% CL and $\epsilon_2 = 0.030^{+0.007}_{-0.006}$ at 68% CL. When second-order

Table 5. Constraints on extensions of the Λ CDM+ r cosmological model for *Planck* TT+lowP+lensing, *Planck* TT+lowP+BAO, and *Planck* TT, TE, EE+lowP.

Extended model, Λ CDM+ r +	Parameter	<i>Planck</i> TT+lowP +lensing	<i>Planck</i> TT+lowP +BAO	<i>Planck</i> TT, TE, EE +lowP
+general reionization	r	< 0.11	< 0.10	< 0.10
	n_s	0.975 ± 0.006	0.971 ± 0.005	0.968 ± 0.005
+ N_{eff}	r	< 0.14	< 0.12	< 0.11
	n_s	$0.977^{+0.016}_{-0.017}$	0.972 ± 0.009	0.964 ± 0.010
	N_{eff}	$3.24^{+0.30}_{-0.35}$	3.19 ± 0.24	$3.02^{+0.20}_{-0.21}$
+ Y_{He}	r	< 0.14	< 0.12	< 0.12
	n_s	0.975 ± 0.007	0.973 ± 0.009	0.969 ± 0.008
	Y_{He}	0.258 ± 0.022	0.257 ± 0.022	0.252 ± 0.014
+ $\sum m_\nu$	r	< 0.11	< 0.11	< 0.11
	n_s	0.963 ± 0.007	0.967 ± 0.005	0.962 ± 0.005
	$\sum m_\nu$ [eV]	< 0.67	< 0.21	< 0.58
+ Ω_K	r	< 0.15	< 0.11	< 0.15
	n_s	0.971 ± 0.007	0.971 ± 0.007	0.969 ± 0.005
	Ω_K	$-0.008^{+0.010}_{-0.008}$	-0.001 ± 0.003	$-0.045^{+0.016}_{-0.020}$
+ w	r	< 0.14	< 0.11	< 0.12
	n_s	0.969 ± 0.006	0.967 ± 0.006	0.966 ± 0.005
	w	$-1.46^{+0.20}_{-0.40}$	$-1.02^{+0.08}_{-0.07}$	$-1.57^{+0.17}_{-0.37}$
+ $\Omega_K + dn_s/d\ln k$	r	< 0.20	< 0.18	< 0.19
	n_s	0.971 ± 0.007	0.969 ± 0.007	0.969 ± 0.005
	$dn_s/d\ln k$	-0.006 ± 0.009	-0.013 ± 0.009	-0.004 ± 0.008
+ $N_{\text{eff}} + m_{\nu, \text{sterile}}^{\text{eff}}$	Ω_K	$-0.006^{+0.010}_{-0.009}$	-0.001 ± 0.003	$-0.043^{+0.011}_{-0.020}$
	r	< 0.14	< 0.13	< 0.12
	n_s	$0.980^{+0.010}_{-0.014}$	$0.978^{+0.008}_{-0.011}$	$0.968^{+0.006}_{-0.008}$
	$m_{\nu, \text{sterile}}^{\text{eff}}$ [eV]	< 0.59	< 0.55	< 0.83
	N_{eff}	< 3.80	< 3.73	< 3.47

Notes. For each model we quote 68% CL, unless 95% CL upper bounds are reported.

contributions in the HFFs are included, we obtain

$$\epsilon_1 < 0.012 \quad (95\% \text{ CL, } \textit{Planck} \text{ TT+lowP}), \quad (36)$$

$$\epsilon_2 = 0.031^{+0.013}_{-0.011} \quad (68\% \text{ CL, } \textit{Planck} \text{ TT+lowP}), \quad (37)$$

$$-0.41 < \epsilon_3 < 1.38 \quad (95\% \text{ CL, } \textit{Planck} \text{ TT+lowP}). \quad (38)$$

When high- ℓ polarization is included we obtain $\epsilon_1 < 0.011$ at 95% CL, $\epsilon_2 = 0.032^{+0.011}_{-0.009}$ at 68% CL, and $-0.32 < \epsilon_3 < 0.89$ at 95% CL.

The potential slow-roll parameters are obtained as derived parameters by using their exact expressions as function of ϵ_i (Leach et al. 2002; Finelli et al. 2010):

$$\epsilon_V = \frac{V_\phi^2 M_{\text{pl}}^2}{2V^2} = \epsilon_1 \frac{\left(1 - \frac{\epsilon_1}{3} + \frac{\epsilon_2}{6}\right)^2}{\left(1 - \frac{\epsilon_1}{3}\right)^2}, \quad (39)$$

$$\eta_V = \frac{V_{\phi\phi} M_{\text{pl}}^2}{V} = \frac{2\epsilon_1 - \frac{\epsilon_2}{2} - \frac{2\epsilon_1^2}{3} + \frac{5\epsilon_1\epsilon_2}{6} - \frac{\epsilon_2^2}{12} - \frac{\epsilon_2\epsilon_3}{6}}{1 - \frac{\epsilon_1}{3}}, \quad (40)$$

$$\xi_V^2 = \frac{V_{\phi\phi\phi} V_\phi M_{\text{pl}}^4}{V^2} = \frac{1 - \frac{\epsilon_1}{3} + \frac{\epsilon_2}{6}}{\left(1 - \frac{\epsilon_1}{3}\right)^2} \left(4\epsilon_1^2 - 3\epsilon_1\epsilon_2 + \frac{\epsilon_2\epsilon_3}{2} - \epsilon_1\epsilon_2^2 + 3\epsilon_1^2\epsilon_2 - \frac{4}{3}\epsilon_1^3 - \frac{7}{6}\epsilon_1\epsilon_2\epsilon_3 + \frac{\epsilon_2^2\epsilon_3}{6} + \frac{\epsilon_2\epsilon_3^2}{6} + \frac{\epsilon_2\epsilon_3\epsilon_4}{6} \right), \quad (41)$$

where $V(\phi)$ is the inflaton potential, the subscript ϕ denotes the derivative with respect to ϕ , and $M_{\text{pl}} = (8\pi G)^{-1/2}$ is the reduced Planck mass (see also Table 2).

By using Eqs. (39) and (40) with $\epsilon_3 = 0$ and the primordial power spectra to lowest order in the HFFs, the derived constraints for the first two slow-roll potential parameters are:

$$\epsilon_V < 0.0068 \quad (95\% \text{ CL, } \textit{Planck} \text{ TT+lowP}), \quad (42)$$

$$\eta_V = -0.010^{+0.005}_{-0.009} \quad (68\% \text{ CL, } \textit{Planck} \text{ TT+lowP}). \quad (43)$$

When high- ℓ polarization is included we obtain $\epsilon_V < 0.0067$ at 95% CL and $\eta_V = -0.010^{+0.004}_{-0.009}$ at 68% CL. By using Eqs. (39)–(41) with $\epsilon_4 = 0$ and the primordial power spectra to second order in the HFFs, the derived constraints for the slow-roll potential parameters are:

$$\epsilon_V < 0.012 \quad (95\% \text{ CL, } \textit{Planck} \text{ TT+lowP}), \quad (44)$$

$$\eta_V = -0.0080^{+0.0088}_{-0.0146} \quad (68\% \text{ CL, } \textit{Planck} \text{ TT+lowP}), \quad (45)$$

$$\xi_V^2 = 0.0070^{+0.0045}_{-0.0069} \quad (68\% \text{ CL, } \textit{Planck} \text{ TT+lowP}). \quad (46)$$

When high- ℓ polarization is included we obtain $\epsilon_V < 0.011$ at 95% CL, and $\eta_V = -0.0092^{+0.0074}_{-0.0127}$ and $\xi_V^2 = 0.0044^{+0.0037}_{-0.0050}$, both at 68% CL.

In Figs. 10 and 11 we show the 68% CL and 95% CL of the HFFs and the derived potential slow-roll parameters with and without the high- ℓ polarization and compare these values with the *Planck* 2013 results.

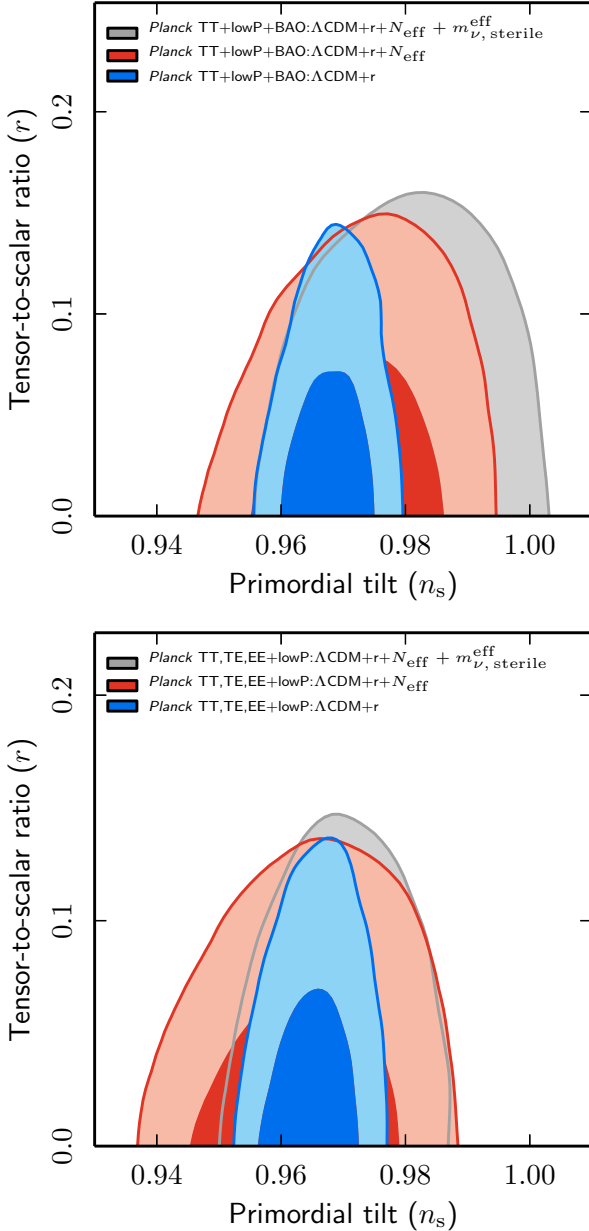


Fig. 9. Marginalized joint 68% and 95% CL for $(n_s, r_{0.002})$ using *Planck* TT+lowP+BAO (upper panel) and *Planck* TT, TE, EE+lowP (lower panel).

6.2. Implications for selected inflationary models

The predictions to lowest order in the slow-roll approximation for (n_s, r) at $k = 0.002 \text{ Mpc}^{-1}$ of a few inflationary models with a representative uncertainty for the entropy generation stage ($50 < N_* < 60$) are shown in Fig. 12. Figure 12 updates Fig. 1 of *PCI13* with the same notation.

In the following we discuss the implications of *Planck* TT+lowP+BAO data for selected slow-roll inflationary models by taking into account the uncertainties in the entropy generation stage. We model these uncertainties by two parameters, as in *PCI13*: the energy scale ρ_{th} by which the Universe has thermalized, and the parameter w_{int} which characterizes the effective equation of state between the end of inflation and the energy scale specified by ρ_{th} . We use the primordial power spectra of cosmological fluctuations generated during slow-roll inflation parameterized by the HFFs, ϵ_i , to

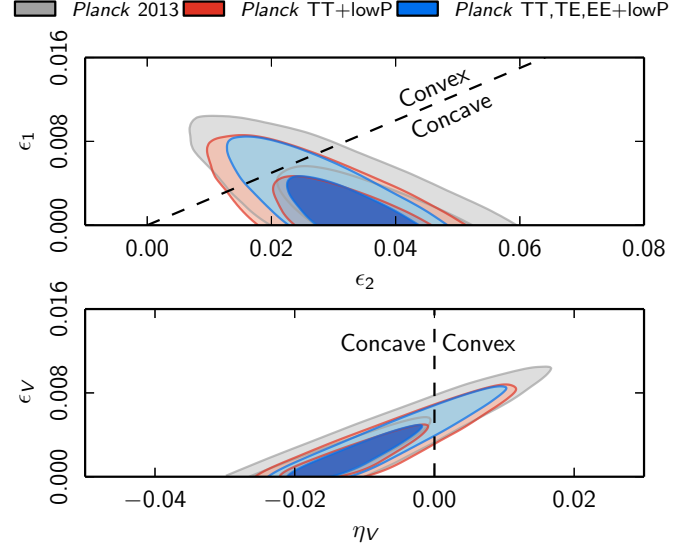


Fig. 10. Marginalized joint 68% and 95% CL regions for (ϵ_1, ϵ_2) (top panel) and (ϵ_V, η_V) (bottom panel) for *Planck* TT+lowP (red contours), *Planck* TT, TE, EE+lowP (blue contours), and compared with the *Planck* 2013 results (grey contours).

Table 6. Priors for cosmological parameters used in the Bayesian comparison of inflationary models.

Parameter range	Prior type
$0.019 < \Omega_b h^2 < 0.025$	uniform
$0.095 < \Omega_c h^2 < 0.145$	uniform
$1.03 < 100\theta_{\text{MC}} < 1.05$	uniform
$0.01 < \tau < 0.4$	uniform

second order, which can be expressed in terms of the number of e -folds to the end of inflation, N_* , and the parameters of the considered inflationary model, using modified routines of the public code ASPIC⁶ (Martin et al. 2014). For the number of e -folds to the end of inflation (Liddle & Leach 2003; Martin & Ringeval 2010) we use the expression (*PCI13*)

$$N_* \approx 67 - \ln\left(\frac{k_*}{a_0 H_0}\right) + \frac{1}{4} \ln\left(\frac{V_*^2}{M_{\text{pl}}^4 \rho_{\text{end}}}\right) + \frac{1 - 3w_{\text{int}}}{12(1 + w_{\text{int}})} \ln\left(\frac{\rho_{\text{th}}}{\rho_{\text{end}}}\right) - \frac{1}{12} \ln(g_{\text{th}}), \quad (47)$$

where ρ_{end} is the energy density at the end of inflation, $a_0 H_0$ is the present Hubble scale, V_* is the potential energy when k_* left the Hubble radius during inflation, w_{int} characterizes the effective equation of state between the end of inflation and the thermalization energy scale ρ_{th} , and g_{th} is the number of effective bosonic degrees of freedom at the energy scale ρ_{th} . We consider the pivot scale $k_* = 0.002 \text{ Mpc}^{-1}$, $g_{\text{th}} = 10^3$, and $\epsilon_{\text{end}} = 1$. We consider the uniform priors for the cosmological parameters listed in Table 6. We also consider a logarithmic prior on $10^{10} A_s$ (over the interval $[(e^{2.5}, e^{3.7})]$) and ρ_{th} (over the interval $[(1 \text{ TeV})^4, \rho_{\text{end}}]$). We consider both the case in which w_{int} is kept fixed at zero and the case in which it is allowed to vary with a uniform prior in the range $-1/3 < w_{\text{int}} < 1/3$.

⁶ <http://cp3.irmp.ucl.ac.be/~ringeval/aspic.html>

Table 7. Results of the inflationary model comparison.

Inflationary model	$\Delta\chi^2$		$\ln B$	
	$w_{\text{int}} = 0$	$w_{\text{int}} \neq 0$	$w_{\text{int}} = 0$	$w_{\text{int}} \neq 0$
$R + R^2/(6M^2)$	+0.8	+0.3	...	+0.7
$n = 2/3$	+6.5	+3.5	-2.4	-2.3
$n = 1$	+6.2	+5.5	-2.1	-1.9
$n = 4/3$	+6.4	+5.5	-2.6	-2.4
$n = 2$	+8.6	+8.1	-4.7	-4.6
$n = 3$	+22.8	+21.7	-11.6	-11.4
$n = 4$	+43.3	+41.7	-23.3	-22.7
Natural	+7.2	+6.5	-2.4	-2.3
Hilltop ($p = 2$)	+4.4	+3.9	-2.6	-2.4
Hilltop ($p = 4$)	+3.7	+3.3	-2.8	-2.6
Double well	+5.5	+5.3	-3.1	-2.3
Brane inflation ($p = 2$)	+3.0	+2.3	-0.7	-0.9
Brane inflation ($p = 4$)	+2.8	+2.3	-0.4	-0.6
Exponential tails	+0.8	+0.3	-0.7	-0.9
SB SUSY	+0.7	+0.4	-2.2	-1.7
Supersymmetric α -model	+0.7	+0.1	-1.8	-2.0
Superconformal ($m = 1$)	+0.9	+0.8	-2.3	-2.2
Superconformal ($m \neq 1$)	+0.7	+0.5	-2.4	-2.6

Notes. We provide $\Delta\chi^2$ with respect to base Λ CDM and Bayes factors with respect to R^2 inflation.

We have validated the slow-roll approach by cross-checking the Bayes factor computations against the fully numerical inflationary mode equation solver *ModeCode* coupled to the *PolyChord* sampler. For each inflationary model we provide in Table 7 and in the main text the $\Delta\chi^2$ value with respect to the base Λ CDM model, computed with the *CosmoMC* implementation of the BOBYQA algorithm for maximizing the likelihood, and the Bayesian evidence with respect to the R^2 inflationary model (Starobinsky 1980), computed by *CosmoMC* connected to *CAMB*, using *MultiNest* as the sampler.

Power law potentials

We first investigate the class of inflationary models with a single monomial potential (Linde 1983):

$$V(\phi) = \lambda M_{\text{pl}}^4 \left(\frac{\phi}{M_{\text{pl}}} \right)^n, \quad (48)$$

in which inflation occurs for large values of the inflaton, $\phi > M_{\text{pl}}$. The predictions for the scalar spectral index and the tensor-to-scalar ratio at first order in the slow-roll approximation are $n_s - 1 \approx -2(n+2)/(4N_* + n)$ and $r \approx 16n/(4N_* + n)$, respectively. By assuming a dust equation of state (i.e., $w_{\text{int}} = 0$) prior to thermalization, the cubic and quartic potentials are strongly disfavoured by $\ln B = -11.6$ and $\ln B = -23.3$, respectively. The quadratic potential is moderately disfavoured by $\ln B = -4.7$. Other values, such as $n = 4/3$, 1, and $2/3$, motivated by axion monodromy (Silverstein & Westphal 2008; McAllister et al. 2010), are compatible with *Planck* data with $w_{\text{int}} = 0$.

Small modifications occur when considering the effective equation of state parameter, $w_{\text{int}} = (n-2)/(n+2)$, defined by averaging over the coherent oscillation regime which follows inflation (Turner 1983). The Bayes factors are slightly modified when w_{int} is allowed to float, as shown in Table 7.

Hilltop models

In hilltop models (Boubekeur & Lyth 2005), with potential

$$V(\phi) \approx \Lambda^4 \left(1 - \frac{\phi^p}{\mu^p} + \dots \right), \quad (49)$$

the inflaton rolls away from an unstable equilibrium. The predictions to first order in the slow-roll approximation are $r \approx 8p^2(M_{\text{pl}}/\mu)^2 x^{2p-2}/(1-x^p)^2$ and $n_s - 1 \approx -2p(p-1)(M_{\text{pl}}/\mu)^2 x^{p-2}/(1-x^p) - 3r/8$, where $x = \phi_*/\mu$. As in PCI13, the ellipsis in Eq. (49) and in what follows indicates higher-order terms that are negligible during inflation but ensure positiveness of the potential.

By sampling $\log_{10}(\mu/M_{\text{pl}})$ within the prior $[0.30, 4.85]$ for $p = 2$, we obtain $\log_{10}(\mu/M_{\text{pl}}) > 1.02$ (1.05) at 95% CL and $\ln B = -2.6$ (-2.4) for $w_{\text{int}} = 0$ (allowing w_{int} to float).

An exact potential which could also apply after inflation, instead of the approximated one in Eq. (49), might be needed for a better comparison among different models. For $\mu/M_{\text{pl}} \gg 1$, hilltop models as defined in Eq. (49) by neglecting the additional terms denoted by the ellipsis lead to $n_s - 1 \approx -3r/8$, the same prediction as for the previously discussed linear potential, $V(\phi) \propto \phi$. By considering a double well potential, $V(\phi) = \Lambda^4[1 - \phi^2/(2\mu^2)]^2$, instead, we obtain a slightly worse Bayes factor than the hilltop $p = 2$ model, $\ln B = -3.1$ (-2.3) for $w_{\text{int}} = 0$ (w_{int} allowed to vary). This different result can be easily understood. Although the double well potential is equal to the hilltop model for $\phi \ll \mu$, it approximates $V(\phi) \propto \phi^2$ for $\mu/M_{\text{pl}} \gg 1$. Since a linear potential is a better fit to *Planck* than ϕ^2 , the fit of the double well potential is therefore worse than the hilltop $p = 2$ case for $\mu/M_{\text{pl}} \gg 1$, and this partially explains the slightly different Bayes factors obtained.

In the $p = 4$ case, we obtain $\log_{10}(\mu/M_{\text{pl}}) > 1.05$ (1.02) at 95% CL and $\ln B = -2.8$ (-2.6) for $w_{\text{int}} = 0$ (allowing w_{int} to float), assuming a prior range $[-2, 2]$ for $\log_{10}(\mu/M_{\text{pl}})$.

Natural inflation

In *natural* inflation (Freese et al. 1990; Adams et al. 1993) a nonperturbative shift symmetry is invoked to suppress radiative corrections leading to the periodic potential

$$V(\phi) = \Lambda^4 \left[1 + \cos\left(\frac{\phi}{f}\right) \right], \quad (50)$$

where f is the scale which determines the curvature of the potential. We sample $\log_{10}(f/M_{\text{pl}})$ within the prior $[0.3, 2.5]$ as in PCI13. We obtain $\log_{10}(f/M_{\text{pl}}) > 0.84$ (>0.83) at 95% CL and $\ln B = -2.4$ (-2.3) for $w_{\text{int}} = 0$ (allowing w_{int} to vary).

Note that the super-Planckian value for f required by observations is not necessarily a problem for this class of models. When several fields ϕ_i with a cosine potential as in Eq. (50) and scales f_i appear in the Lagrangian, an effective single-field inflationary trajectory can be found for a suitable choice of parameters (Kim et al. 2005). In such a setting, the super-Planckian value of the effective scale f required by observations can be obtained even if the original scales satisfy $f_i \ll M_{\text{pl}}$ (Kim et al. 2005).

D-brane inflation

Inflation can arise from physics involving extra dimensions. If the standard model of particle physics is confined to our

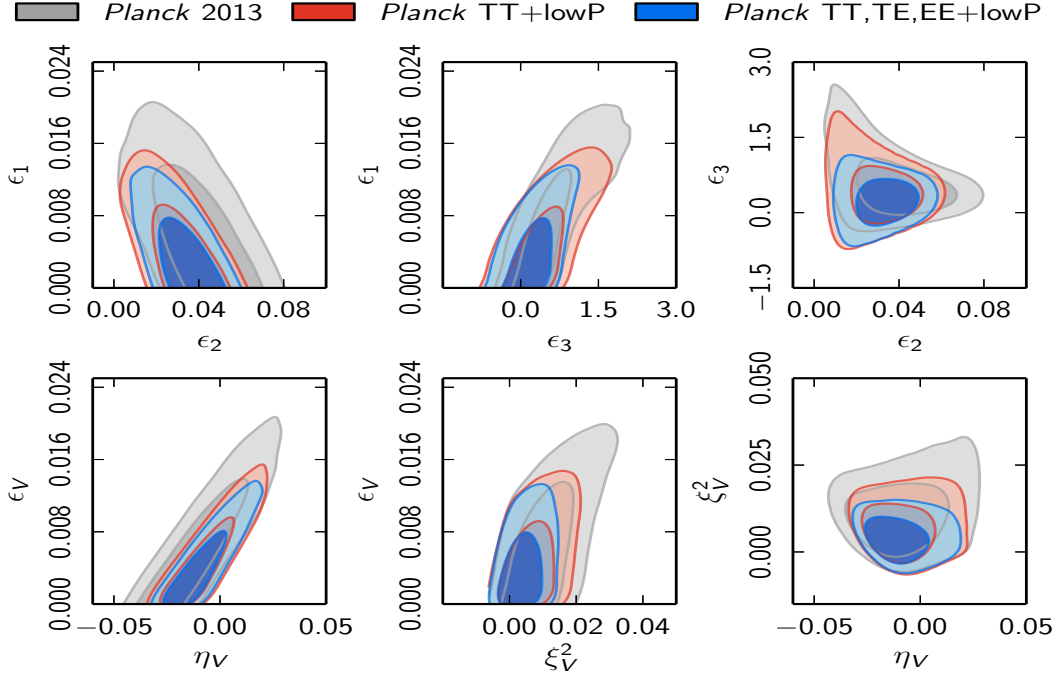


Fig. 11. Marginalized joint 68% and 95% CL regions for $(\epsilon_1, \epsilon_2, \epsilon_3)$ (top panels) and $(\epsilon_V, \eta_V, \xi_V^2)$ (bottom panels) for *Planck* TT+lowP (red contours), *Planck* TT, TE, EE+lowP (blue contours), and compared with the *Planck* 2013 results (grey contours).

3-dimensional brane, the distance between our brane and anti-brane can drive inflation. We consider the following parameterization for the effective potential driving inflation:

$$V(\phi) = \Lambda^4 \left(1 - \frac{\mu^p}{\phi^p} + \dots \right). \quad (51)$$

Sampling $\log_{10}(\mu/M_{\text{pl}})$ using a uniform prior over $[-6, 0.3]$, we consider $p = 4$ (Kachru et al. 2003; Dvali et al. 2001) and $p = 2$ (Garcia-Bellido et al. 2002). The predictions for r and n_s can be obtained from the hilltop case with the substitution $p \rightarrow -p$. These models agree with the *Planck* data with a Bayes factor of $\ln B = -0.4$ (-0.6) and $\ln B = -0.7$ (-0.9) for $p = 4$ and $p = 2$, respectively, for $w_{\text{int}} = 0$ (allowing w_{int} to vary).

Potentials with exponential tails

Exponential potentials are ubiquitous in inflationary models motivated by supergravity and string theory (Goncharov & Linde 1984; Stewart 1995; Dvali & Tye 1999; Burgess et al. 2002; Cicoli et al. 2009). We restrict ourselves to analysing the following class of potentials:

$$V(\phi) = \Lambda^4 \left(1 - e^{-q\phi/M_{\text{pl}}} + \dots \right). \quad (52)$$

As for the hilltop models described earlier, the ellipsis indicates possible higher-order terms that are negligible during inflation but ensure positiveness of the potential. These models predict $r \approx 8q^2 e^{-2q\phi/M_{\text{pl}}} / (1 - e^{-q\phi/M_{\text{pl}}})^2$ and $n_s - 1 \approx -q^2 e^{-q\phi/M_{\text{pl}}} (2 + e^{-q\phi/M_{\text{pl}}}) / (1 - e^{-q\phi/M_{\text{pl}}})^2$ with a slow-roll trajectory characterized by $N \approx f(\phi/M_{\text{pl}}) - f(\phi_{\text{end}}/M_{\text{pl}})$, with $f(x) = (e^{qx} - qx)/q^2$. By sampling $\log_{10}(q/M_{\text{pl}})$ with a uniform prior over $[-3, 3]$, we obtain a Bayes factor of -0.6 for $w_{\text{int}} = 0$ (-0.9 when w_{int} is allowed to vary).

Spontaneously broken SUSY

Hybrid models (Copeland et al. 1994; Linde 1994) predicting $n_s > 1$ are strongly disfavoured by the *Planck* data, as for the first cosmological release (PCI13). An example of a hybrid model predicting $n_s < 1$ is the case in which slow-roll inflation is driven by loop corrections in spontaneously broken supersymmetric (SUSY) grand unified theories (Dvali et al. 1994) described by the potential

$$V(\phi) = \Lambda^4 \left[1 + \alpha_h \log(\phi/M_{\text{pl}}) \right], \quad (53)$$

where $\alpha_h > 0$ is a dimensionless parameter. Note that for $\alpha_h \ll 1$, this model leads to the same predictions as the power-law potential for $p \ll 1$ to lowest order in the slow-roll approximation. By sampling $\log_{10}(\alpha_h)$ on a flat prior $[-2.5, 1]$, we obtain a Bayes factor of -2.2 for $w_{\text{int}} = 0$ (-1.7 when w_{int} is allowed to vary).

R^2 inflation

The first inflationary model proposed (Starobinsky 1980), with action

$$S = \int d^4x \sqrt{-g} \frac{M_{\text{pl}}^2}{2} \left(R + \frac{R^2}{6M^2} \right), \quad (54)$$

still lies within the *Planck* 68% CL constraints, as for the *Planck* 2013 release (PCI13). This model corresponds to the potential

$$V(\phi) = \Lambda^4 \left(1 - e^{-\sqrt{2/3}\phi/M_{\text{pl}}} \right)^2 \quad (55)$$

in the Einstein frame, which leads to the slow-roll predictions $n_s - 1 \approx -2/N$ and $r \approx 12/N^2$ (Mukhanov & Chibisov 1981; Starobinsky 1983).

After the *Planck* 2013 release, several theoretical developments supported the model in Eq. (54) beyond the original motivation of including quantum effects at one-loop

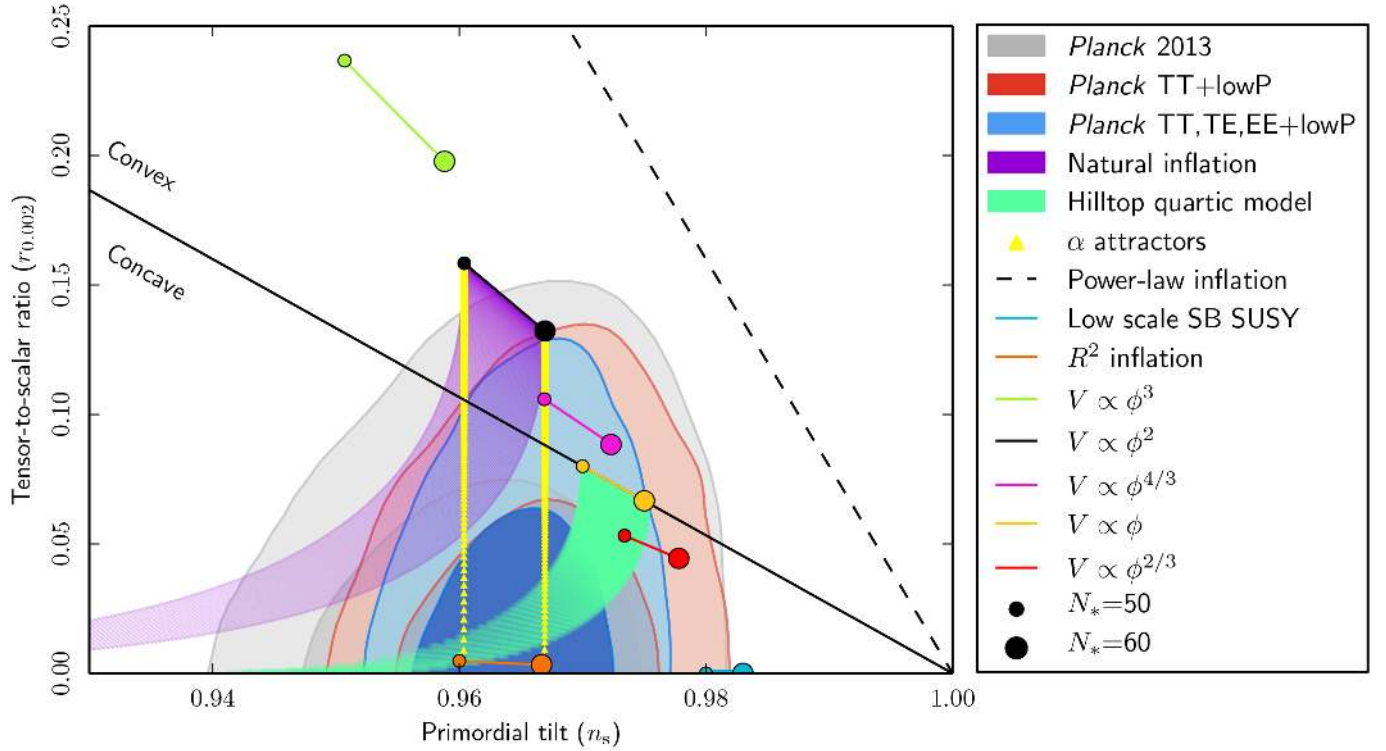


Fig. 12. Marginalized joint 68% and 95% CL regions for n_s and r at $k = 0.002 \text{ Mpc}^{-1}$ from *Planck* compared to the theoretical predictions of selected inflationary models. Note that the marginalized joint 68% and 95% CL regions have been obtained by assuming $dn_s/d\ln k = 0$.

(Starobinsky 1980). No-scale supergravity (Ellis et al. 2013a), the large-field regime of superconformal D -term inflation (Buchmüller et al. 2013), or recent developments in minimal supergravity (Farakos et al. 2013; Ferrara et al. 2013b) can lead to a generalization of the potential in Eq. (55) (see Ketov & Starobinsky 2011 for a previous embedding of R^2 inflation in $F(\mathcal{R})$ supergravity). The potential in Eq. (55) can also be generated by spontaneous breaking of conformal symmetry (Kallosh & Linde 2013b). This inflationary model has $\Delta\chi^2 \approx 0.8$ (0.3) larger than the base ΛCDM model with no tensors for $w_{\text{int}} = 0$ (for w_{int} allowed to vary). We obtain $54 < N_* < 62$ ($53 < N_* < 64$) at 95% CL for $w_{\text{int}} = 0$ (for w_{int} allowed to vary), compatible with the theoretical prediction, $N_* = 54$ (Starobinsky 1980; Vilenkin 1985; Gorbunov & Panin 2011).

α attractors

We now study two classes of inflationary models motivated by recent developments in conformal symmetry and supergravity (Kallosh et al. 2013). The first class has been motivated by considering a vector rather than a chiral multiplet for the inflaton in supergravity (Ferrara et al. 2013a) and corresponds to the potential (Kallosh et al. 2013)

$$V(\phi) = \Lambda^4 \left(1 - e^{-\sqrt{2}\phi/(\sqrt{3}\alpha M_{\text{pl}})} \right)^2. \quad (56)$$

To lowest order in the slow-roll approximation, these models predict $r \approx 64/[3\alpha(1 - e^{-\sqrt{2}\phi/(\sqrt{3}\alpha M_{\text{pl}})})^2]$ and $n_s - 1 \approx -8(1 + e^{-\sqrt{2}\phi/(\sqrt{3}\alpha M_{\text{pl}})})/[3\alpha(1 - e^{-\sqrt{2}\phi/(\sqrt{3}\alpha M_{\text{pl}})})^2]$ based on an inflationary trajectory characterized by $N \approx g(\phi/M_{\text{pl}}) - g(\phi_{\text{end}}/M_{\text{pl}})$ with $g(x) = (3\alpha^4 e^{\sqrt{2}x/\sqrt{3}\alpha} - \sqrt{6}\alpha x)/4$. The relation between N and ϕ can be inverted through the use of the Lambert functions, as carried out for other potentials (Martin et al. 2014). By sampling

$\log_{10}(\alpha^2)$ with a flat prior over $[0, 4]$, we obtain $\log_{10}(\alpha^2) < 1.7$ (2.0) at 95% CL and a Bayes factor of -1.8 (-2) for $w_{\text{int}} = 0$ (for w_{int} allowed to vary).

The second class of models has been called super-conformal α attractors (Kallosh et al. 2013) and can be understood as originating from a different generating function with respect to the first class. This second class is described by the following potential (Kallosh et al. 2013):

$$V(\phi) = \Lambda^4 \tanh^{2m} \left(\frac{\phi}{\sqrt{6}\alpha M_{\text{pl}}} \right). \quad (57)$$

This is the simplest class of models with spontaneous breaking of conformal symmetry, and for $\alpha = m = 1$ reduces to the original model introduced by Kallosh & Linde (2013b). The potential in Eq. (57) leads to the following slow-roll predictions (Kallosh et al. 2013):

$$r \approx \frac{48\alpha m}{4mN^2 + 2Ng(\alpha, m) + 3\alpha m}, \quad (58)$$

$$n_s - 1 \approx -\frac{8mN + 6\alpha m + 2g(\alpha, m)}{4mN^2 + 2Ng(\alpha, m) + 3\alpha m}, \quad (59)$$

where $g(\alpha, m) = \sqrt{3\alpha(4m^2 + 3\alpha)}$. The predictions of this second class of models interpolate between those of a large-field chaotic model, $V(\phi) \propto \phi^{2m}$, for $\alpha \gg 1$ and the R^2 model for $\alpha \ll 1$.

For α we adopt the same priors as for the previous class in Eq. (56). By fixing $m = 1$, we obtain $\log_{10}(\alpha^2) < 2.3$ (2.5) at 95% CL and a Bayes factor of -2.3 (-2.2) for $w_{\text{int}} = 0$ (when w_{int} is allowed to vary). When m is allowed to vary as well with a flat prior in the range $[0, 2]$, we obtain $0.02 < m < 1$ ($m < 1$) at 95% CL for $w_{\text{int}} = 0$ (when w_{int} is allowed to vary).

Non-minimally coupled inflaton

Inflationary predictions are quite sensitive to a non-minimal coupling $\xi R\phi^2$ of the inflaton to the Ricci scalar. One of the most interesting effects due to $\xi \neq 0$ is to reconcile the quartic potential $V(\phi) = \lambda\phi^4/4$ with *Planck* observations, even for $\xi \ll 1$. Non-minimal coupling leads as well to attractor behaviour towards predictions similar to those in R^2 inflation (Kaiser & Sfakianakis 2014; Kallosh & Linde 2013a).

The Higgs inflation model (Bezrukov & Shaposhnikov 2008), in which inflation occurs with $V(\phi) = \lambda(\phi^2 - \phi_0^2)^2/4$ and $\xi \gg 1$ for $\phi \gg \phi_0$, leads to the same predictions as the R^2 model to lowest order in the slow-roll approximation at tree level (see Barvinsky et al. 2008; and Bezrukov & Shaposhnikov 2009 for the inclusion of loop corrections). It is therefore in agreement with the *Planck* constraints, as for the first cosmological data release (PCI13).

We summarize below our findings for *Planck* lowP+BAO.

- Monomial potentials with integral $n > 2$ are strongly disfavoured with respect to R^2 .
- The Bayes factor prefers R^2 over chaotic inflation with monomial quadratic potential by odds of 110:1 under the assumption of a dust equation of state during the entropy generation stage.
- R^2 inflation has the strongest evidence (i.e., the greatest Bayes factor) among the models considered here. However, care must be taken not to overinterpret small differences in likelihood lacking statistical significance.
- The models closest to R^2 in terms of evidence are brane inflation and exponential inflation, which have one more parameter than R^2 . Both brane inflation considered in Eq. (51) and exponential inflation in Eq. (52) approximate the linear potential for a large portion of parameter space (for $\mu/M_{\text{pl}} \gg 1$ and $q \gg 1$, respectively). For this reason these models have a higher Bayesian evidence (although not at a statistically significant level) than those that approximate a quadratic potential, as do α -attractors, for instance.
- In the models considered here, the $\Delta\chi^2$ obtained by allowing w to vary is modest (i.e., less than approximately 1.6 with respect to $w_{\text{int}} = 0$). The gain in the logarithm of the Bayesian evidence is even smaller, since an extra parameter is added.

7. Reconstruction of the potential and analysis beyond slow-roll approximation

7.1. Introduction

In the previous section, we derived constraints on several types of inflationary potentials assumed to account for the inflaton dynamics between the time at which the largest observable scales crossed the Hubble radius during inflation and the end of inflation. The full shape of the potential was used in order to identify when inflation ends, and thus the field value ϕ_* when the pivot scale crosses the Hubble radius.

In Sect. 6 of PCI13, we explored another approach, consisting of reconstructing the inflationary potential within its observable range without making any assumptions concerning the inflationary dynamics outside that range. Indeed, given that the number of e -folds between the observable range and the end of inflation can always be adjusted to take a realistic value, any potential shape giving a primordial spectrum of scalar and tensor perturbations in agreement with observations is a valid candidate. Inflation can end abruptly by a phase transition, or can last

a long time if the potential becomes very flat after the observable region has been crossed. Moreover, there could be a short inflationary stage responsible for the origin of observable cosmological perturbations, and another inflationary stage later on (but before nucleosynthesis), thus contributing to the total N_* .

In Sect. 6 of PCI13, we performed this analysis with a full integration of the inflaton and metric perturbation modes, so that no slow-roll approximation was made. The only assumption was that primordial scalar perturbations are generated by the fluctuations of a single inflaton field with a canonical kinetic term. Since in this approach one is only interested in the potential over a narrow range of observable scales (centred around the field value ϕ_* when the pivot scale crosses the Hubble radius), it is reasonable to test relatively simple potential shapes described by a small number of free parameters.

This approach gave very similar results to calculations based on the standard slow-roll analysis. This agreement can be explained by the fact that the *Planck* 2013 data already preferred a primordial spectrum very close to a power law, at least over most of the observable range. Hence the 2013 data excluded strong deviations from slow-roll inflation, which would either produce a large running of the spectral index or imprint more complicated features on the primordial spectrum. However, this conclusion did not apply to the largest scales observable by *Planck*, for which cosmic variance and slightly anomalous data points remained compatible with significant deviations from a simple power law spectrum. The most striking result in Sect. 6 of PCI13 was that a less restricted functional form for the inflaton potential gave results compatible with a rather steep potential at the beginning of the observable window, leading to a “not-so-slow” roll stage during the first few observable e -folds. This explains the shape of the potential in Fig. 14 of PCI13 for a Taylor expansion at order $n = 4$ and in the region where $\phi - \phi_* \leq -0.2$. However, such features were only partially explored because the method used for potential reconstruction did not allow for an arbitrary value of the inflation velocity $\dot{\phi}$ at the beginning of the observable window. Instead, our code imposed that the inflaton already tracked the inflationary attractor solution when the largest observable modes crossed the Hubble scale.

Given that the *Planck* 2015 data establish even stronger constraints on the primordial power spectrum than the 2013 results, it is of interest to revisit the reconstruction of the potential $V(\phi)$. Section 7.2 presents some new results following the same approach as in PCI13 (explained previously in Lesgourgues & Valkenburg 2007; and Mortonson et al. 2011). But in the present work, we also present some more general results, independent of any assumption concerning the initial field velocity $\dot{\phi}$ when the inflaton enters the observable window. Following previous studies (Kinney 2002; Kinney et al. 2006; Peiris & Easther 2006a,b, 2008; Easther & Peiris 2006; Lesgourgues et al. 2008; Powell & Kinney 2007; Hamann et al. 2008; Norena et al. 2012), we reconstruct the Hubble function $H(\phi)$, which determines both the potential $V(\phi)$ through

$$V(\phi) = 3M_{\text{pl}}^2 H^2(\phi) - 2M_{\text{pl}}^4 [H'(\phi)]^2, \quad (60)$$

and the solution $\phi(t)$ through

$$\dot{\phi} = -2M_{\text{pl}}^2 H'(\phi), \quad (61)$$

with $H'(\phi) = \partial H / \partial \phi$. Note that these two relations are exact. In Sect. 7.3, we fit $H(\phi)$ directly to the data, implicitly including all canonical single-field models in which the inflaton is rolling not very slowly (ϵ not much smaller than unity) just before entering the observable window, and the issue of having to start

Table 8. Numerical reconstruction of the potential slow-roll parameters *beyond* any slow-roll approximation when the potential is Taylor expanded to n th order, using *Planck* TT+lowP+BAO.

n	2	3	4
ϵ_V	<0.0074	<0.010	$0.0072^{+0.0093}_{-0.0069}$
η_V	$-0.007^{+0.014}_{-0.012}$	$-0.020^{+0.021}_{-0.018}$	$0.021^{+0.044}_{-0.042}$
ξ_V^2	...	$0.006^{+0.010}_{-0.010}$	$-0.018^{+0.028}_{-0.027}$
ϖ_V^3	$0.015^{+0.016}_{-0.017}$
τ	$0.083^{+0.036}_{-0.036}$	$0.096^{+0.046}_{-0.044}$	$0.102^{+0.046}_{-0.045}$
n_s	$0.9692^{+0.0094}_{-0.0093}$	$0.9689^{+0.0097}_{-0.0097}$	$0.964^{+0.011}_{-0.011}$
$dn_s/d\ln k$	$-0.00034^{+0.00055}_{-0.00059}$	$-0.013^{+0.019}_{-0.019}$	$0.003^{+0.026}_{-0.026}$
$r_{0.002}$	<0.11	<0.16	$0.11^{+0.16}_{-0.11}$
$\Delta\chi^2$...	$\Delta\chi^2_{3/2} = -1.2$	$\Delta\chi^2_{4/3} = -2.1$
$\Delta\ln B$...	$\Delta\ln B_{3/2} = -4.3$	$\Delta\ln B_{4/3} = -2.9$

Notes. We also show the corresponding bounds on the derived parameters (here n_s , $dn_s/d\ln k$, and $r_{0.002}$ are derived from the numerically computed primordial spectra). All error bars are at the 95% CL. The effective χ^2 value and Bayesian evidence logarithm ($\ln B$) of model n are given relative to the model of next lowest order ($n-1$) (assuming flat priors for ξ_V^2 and ϖ_V^3 in the range $[-1, 1]$).

sufficiently early in order to allow the initial transient to decay is avoided. The only drawback in reconstructing $H(\phi)$ is that one cannot systematically test the simplest analytic forms for $V(\phi)$ in the observable range (for instance, polynomials of order $n = 1, 3, 5, \dots$ in $(\phi - \phi_*)$). But our goal in this section is to explore how much one can deviate from slow-roll inflation in general, independently of the shape of the underlying inflaton potential.

7.2. Reconstruction of a smooth inflaton potential

Following the approach of [PCI13](#), we Taylor expand the inflaton potential around $\phi = \phi_*$ to order $n = 2, 3, 4$. To obtain faster-converging Markov chains, instead of imposing flat priors on the Taylor coefficients $\{V, V_\phi, \dots, V_{\phi\phi\phi}\}$, we sample the potential slow-roll (PSR) parameters $\{\epsilon_V, \eta_V, \xi_V^2, \varpi_V^3\}$ related to the former as indicated in Table 2. We stress that this is just a choice of prior and does not imply any kind of slow-roll approximation in the calculation of the primordial spectra.

The results are given in Table 8 (for *Planck* TT+lowP+BAO) and Fig. 13 (for the same data set and also for *Planck* TT, TE, EE+lowP). The second part of Table 8 shows the corresponding values of the spectral parameters n_s , $dn_s/d\ln k$, and $r_{0.002}$ as measured for each numerical primordial spectrum (at the pivot scales $k = 0.05 \text{ Mpc}^{-1}$ for the scalar and 0.002 Mpc^{-1} for the tensor spectra), as well as the reionization optical depth. We also show in Fig. 14 the derived distribution of each coefficient V_i (with a non-flat prior) and in Fig. 15 the reconstructed shape of the best-fit inflation potentials in the observable window. Finally, the posterior distribution of the derived parameters $r_{0.002}$ and $dn_s/d\ln k$ is displayed in Fig. 16.

Figure 13 shows that bounds are very similar when temperature data are combined with either high- ℓ polarization data or BAO data. This gives a hint of the robustness of these results. For

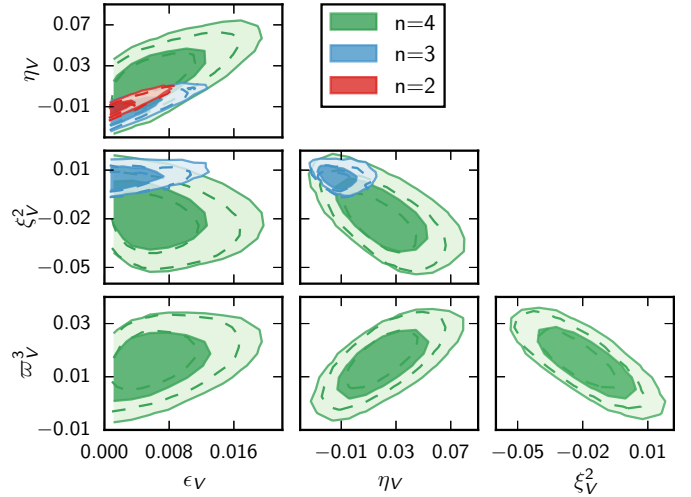


Fig. 13. Posterior distributions for the first four potential slow-roll parameters when the potential is Taylor expanded to n th order using *Planck* TT+lowP+BAO (filled contours) or TT, TE, EE+lowP (dashed contours). The primordial spectra are computed *beyond* the slow-roll approximation.

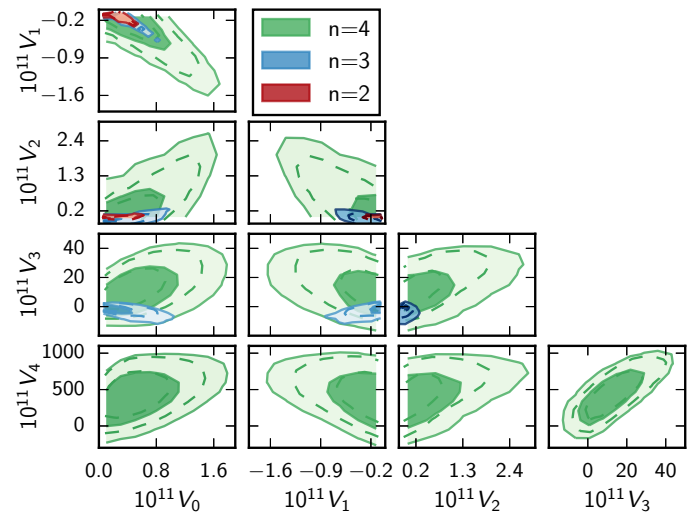


Fig. 14. Posterior distributions for the coefficients of the inflation potential Taylor expanded to n th order (in natural units where $\sqrt{8\pi M_{\text{pl}}} = 1$) reconstructed *beyond* the slow-roll approximation using *Planck* TT+lowP+BAO (filled contours) or TT, TE, EE+lowP (dashed contours). The plot shows only half of the results; the other half is symmetric, with opposite signs for V_ϕ and $V_{\phi\phi\phi}$. Note that, unlike Fig. 13, the parameters shown here do *not* have flat priors, since they are mapped from the slow-roll parameters.

both data sets, the error bars on the PSR parameters are typically smaller by a factor of 1.5 than in [PCI13](#).

Since potentials with $n = 2$ cannot generate a significant running, the bounds on the scalar spectral index and the tensor-to-scalar ratio and the best-fit models are very similar to those obtained with the $\Lambda\text{CDM}+r$ model in Sect. 5 and Table 4. On the other hand, in the $n = 3$ model, results follow the trend of the previous $\Lambda\text{CDM}+r+dn_s/d\ln k$ analysis. The data prefer potentials with V_ϕ and $V_{\phi\phi\phi}$ of the same sign, generating a significant negative running (as can be seen in Fig. 16). This trend for $V_{\phi\phi\phi}$ occurs because a scalar spectrum with negative running reduces the power on large scales, and provides a better fit to

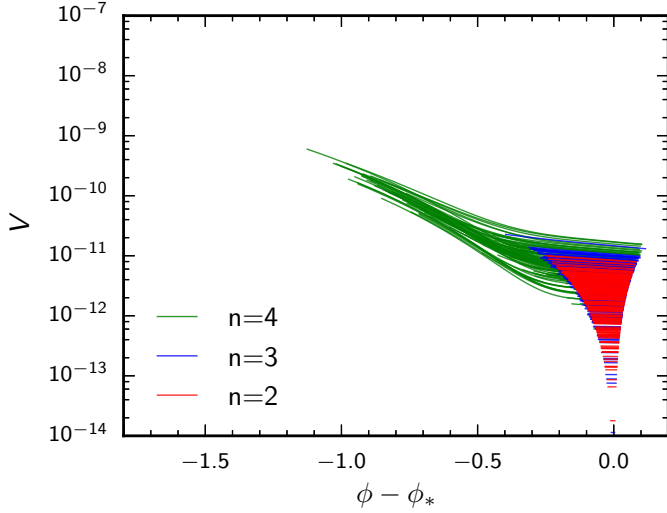


Fig. 15. Observable range of the best-fit inflaton potentials, when $V(\phi)$ is Taylor expanded to the n th order around the pivot value ϕ_* in natural units (where $\sqrt{8\pi}M_{\text{pl}} = 1$) assuming a flat prior on ϵ_V , η_V , ξ_V^2 , and ϖ_V^3 and using *Planck* TT+lowP+BAO. Potentials obtained under the transformation $(\phi - \phi_*) \rightarrow (\phi_* - \phi)$ leave the same observable signature and are also allowed. The sparsity of potentials with a small $V_0 = V(\phi_*)$ is due to our use of a flat prior on ϵ_V rather than on $\ln(V_0)$; in fact, V_0 is unbounded from below in the $n = 2$ and 3 results. The axis ranges are identical to those in Fig. 20, to make the comparison easier.

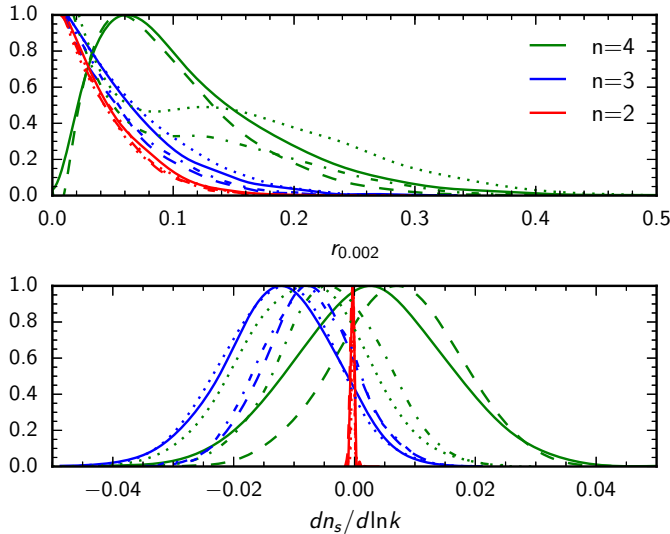


Fig. 16. Posterior distribution for the tensor-to-scalar ratio (at $k = 0.002 \text{ Mpc}^{-1}$) and for the running parameter $dn_s/d\ln k$ (at $k = 0.05 \text{ Mpc}^{-1}$), for the potential reconstructions in Sects. 7.2 and 7.3. The $V(\phi)$ reconstruction gives the solid curves for *Planck* TT+lowP+BAO, or dashed for TT, TE, EE+lowP. The $H(\phi)$ reconstruction gives the dotted curves for *Planck* TT+lowP+BAO, or dashed-dotted for TT, TE, EE+lowP. The tensor-to-scalar ratio appears as a derived parameter, but by taking a flat prior on either ϵ_V or ϵ_H , we implicitly also take a nearly flat prior on r . The same applies to $dn_s/d\ln k$.

low- ℓ temperature multipoles. However, such a running also suppresses power on small scales, so ξ_V^2 cannot be too large.

The $n = 4$ case possesses a new feature. The potential has more freedom to generate complicated shapes which would roughly correspond to a running of the running of the tilt (as studied in Sect. 4). The best-fit models now have V_ϕ and $V_{\phi\phi\phi}$ of opposite sign, and a large positive $V_{\phi\phi\phi\phi}$. The preferred

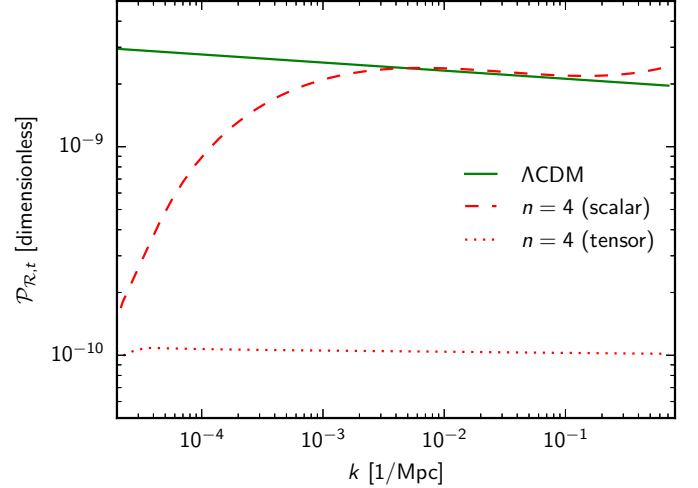


Fig. 17. Primordial spectra (scalar and tensor) of the best-fit $V(\phi)$ model with $n = 4$, for the *Planck* TT, TE, EE+lowP data set, compared to the primordial spectrum (scalar only) of the best-fit base ΛCDM model. The best-fit potential is initially very steep, as can be seen in Fig. 15 (note the typical shape of the green curves). The transition from “marginal slow roll” ($\epsilon_V(\phi)$ between 0.01 and 1) to “full slow roll” ($\epsilon_V(\phi)$ of order 0.01 or smaller) is responsible for the suppression of the large-scale scalar spectrum.

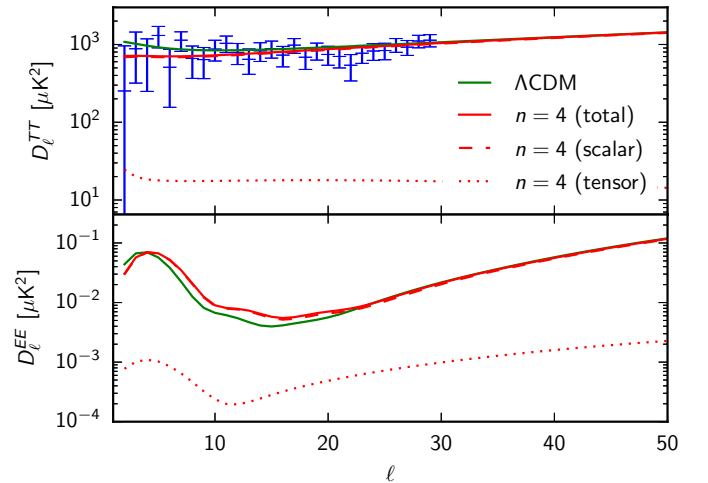


Fig. 18. Temperature and polarization spectra (total, scalar contribution, tensor contribution) of the best-fit $V(\phi)$ model with $n = 4$, for the *Planck* TT, TE, EE+lowP data set, compared to the spectra (scalar contribution only) of the best-fit base model. We also show the *Planck* low- ℓ temperature data, which is driving the small differences between the two best-fit models.

combination of these parameters allows for even more suppression of power on large scales, while leaving small scales nearly unchanged. This can be seen clearly from the shape of the scalar primordial spectrum corresponding to the best-fit models, for both data sets *Planck* TT+lowP+BAO and *Planck* TT, TE, EE+lowP. These two best-fit models are very similar, but in Fig. 17 we show the one for *Planck* TT, TE, EE+lowP, for which the trend is even more pronounced. Interestingly, the preferred models are such that power on large scales is suppressed in the scalar spectrum and balanced by a small tensor contribution, of roughly $r_{0.002} \sim 0.05$. This particular combination gives the best fit to the low- ℓ data, shown in Fig. 18, while leaving the high- ℓ temperature spectrum identical to the best fit base ΛCDM model.

Inflation produces such primordial perturbations with the family of green potentials displayed in Fig. 15. At the beginning of the observable range, the potential is very steep [$\epsilon_V(\phi)$ decreases from $O(1)$ to $O(10^{-2})$], and produces a low amplitude of curvature perturbations (allowing a rather large tensor contribution, up to $r_{0.002} \sim 0.3$). Then there is a transition towards a second region with a much smaller slope, leading to a nearly power-law curvature spectrum with the usual tilt value $n_s \approx 0.96$. In Fig. 15, one can check that the height of the $n = 4$ potentials varies in a definite range, while the $n = 2$ and 3 potentials can have arbitrarily small amplitude at the pivot scale, reflecting the posteriors on ϵ_V or r .

However, the improvement in χ^2 between the base Λ CDM and $n = 4$ models is only 2.2 (for *Planck* TT+lowP+BAO) or 4.3 (for *Planck* TT, TE, EE+lowP). This is marginal and offers no statistically significant evidence in favour of these complicated models. This conclusion is also supported by the calculation of the Bayesian evidence ratios, shown in the last line of Table 8 (under the assumption of flat priors in the range $[-1, 1]$ for ξ_V^2 and ϖ_V^3): the evidence decreases each time that a new free parameter is added to the potential. At the 95% CL, $r_{0.002}$ is still compatible with zero, and so are the higher order PSR parameters ξ_V^2 and ϖ_V^3 . More freedom in the inflaton potential allows fitting the data better, but under the assumption of a smooth potential in the observable range, a simple quadratic form provides the best explanation of the *Planck* observations.

With the *Planck* TT+lowP+BAO and TT, TE, EE+lowP data sets, models with a large running or running of the running can be compatible with an unusually large value of the optical depth, as can be seen in Table 8. Including lensing information helps to break the degeneracy between the optical depth and the primordial amplitude of scalar perturbations. Hence the *Planck* lensing data could be used to strengthen the conclusions of this section.

Since in the $n = 4$ model, slow roll is marginally satisfied at the beginning of observable inflation, the reconstruction is very sensitive to the condition that there is an attractor solution at that time. Hence this case can in principle be investigated in a more conservative way using the $H(\phi)$ reconstruction method of the next section.

7.3. Reconstruction of a smooth Hubble function

In this section, we assume that the shape of the function $H(\phi)$ is well captured within the observable window by a polynomial of order n (corresponding to a polynomial inflaton potential of order $2n$):

$$H(\phi) = \sum_{i=0}^n H_i \frac{\phi^i}{i!}. \quad (62)$$

We vary n between 2 and 4. To avoid parameter degeneracies, as in the previous section we assume flat priors not on the Taylor coefficient H_i , but on the Hubble slow-roll (HSR) parameters, which are related according to

$$\epsilon_H = 2M_{\text{pl}}^2 \left(\frac{H_1}{H_0} \right)^2, \quad \eta_H = 2M_{\text{pl}}^2 \frac{H_2}{H_0}, \quad (63)$$

$$\xi_H^2 = \left(2M_{\text{pl}}^2 \right)^2 \frac{H_1 H_3}{H_0^2}, \quad \varpi_H^3 = \left(2M_{\text{pl}}^2 \right)^3 \frac{H_1^2 H_4}{H_0^3}. \quad (64)$$

This is just a choice of prior. This analysis does not rely on the slow-roll approximation.

Table 9 and Fig. 19 show our results for the reconstructed HSR parameters. Figure 20 shows a representative sample of

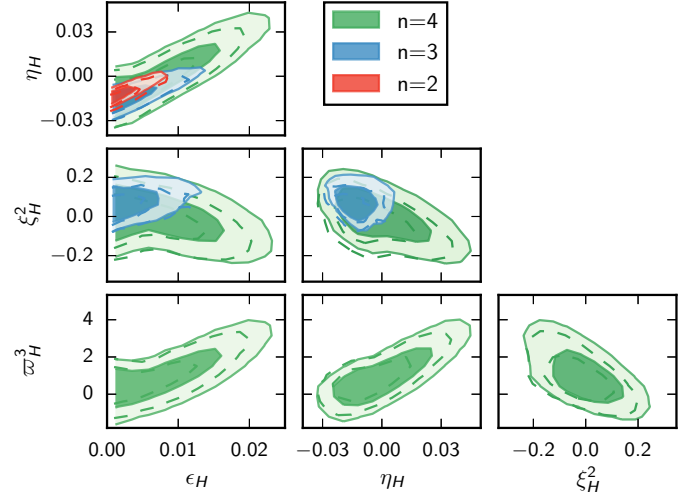


Fig. 19. Posterior distributions for the first four Hubble slow-roll parameters, when $H(\phi)$ is Taylor expanded to n th order, using *Planck* TT+lowP+BAO (filled contours) or TT, TE, EE+lowP (dashed contours). The primordial spectra are computed *beyond* the slow-roll approximation.

Table 9. Numerical reconstruction of the Hubble slow-roll parameters *beyond* the slow-roll approximation, using *Planck* TT+lowP+BAO.

n	2	3	4
ϵ_H	<0.0073	<0.011	<0.020
η_H	$-0.010^{+0.011}_{-0.009}$	$-0.012^{+0.015}_{-0.013}$	$-0.001^{+0.033}_{-0.027}$
ξ_H^2	...	$0.08^{+0.12}_{-0.12}$	$-0.01^{+0.19}_{-0.19}$
ϖ_H^3	$1.0^{+2.3}_{-1.8}$
τ	$0.082^{+0.038}_{-0.036}$	$0.096^{+0.042}_{-0.043}$	$0.096^{+0.042}_{-0.042}$
n_s	$0.9693^{+0.0094}_{-0.0093}$	$0.9680^{+0.0096}_{-0.0096}$	$0.967^{+0.010}_{-0.010}$
$10^3 dn_s/d\ln k$	$-0.251^{+0.41}_{-0.41}$	-13^{+18}_{-19}	-8^{+21}_{-21}
$r_{0.002}$	<0.11	<0.16	<0.32
$\Delta\chi^2$...	$\Delta\chi_{3/2}^2 = -0.6$	$\Delta\chi_{4/3}^2 = -2.3$

Notes. We also show the corresponding bounds on some related parameters (here n_s , $dn_s/d\ln k$, and $r_{0.002}$ are derived from the numerically computed primordial spectra). All error bars are at the 95% CL. The effective χ^2 value of model n is given relative to model $n-1$.

potential shapes $V(\phi - \phi_*)$ derived using Eq. (60), for a sample of models drawn randomly from the chains, for the three cases $n = 2, 3, 4$.

Most of the discussion of Sect. 7.2 also applies to this section, and so will not be repeated. Results for *Planck* TT+lowP+BAO and TT, TE, EE+lowP are still very similar. The $n = 2$ case still gives results close to Λ CDM+ r , and the $n = 3$ case to Λ CDM+ $r+dn_s/d\ln k$. The type of potential preferred in the $n = 4$ case is very similar to the $n = 4$ analysis of the previous section, for the reasons explained in Sect. 7.2. There are, however, small differences, because the range of parametric forms for the potential explored by the two analyses differ. In the $H(\phi)$ reconstruction, the underlying potentials $V(\phi)$ are not polynomials. In the first approximation, they are close to polynomials of order $2n$, but with constraints between the various

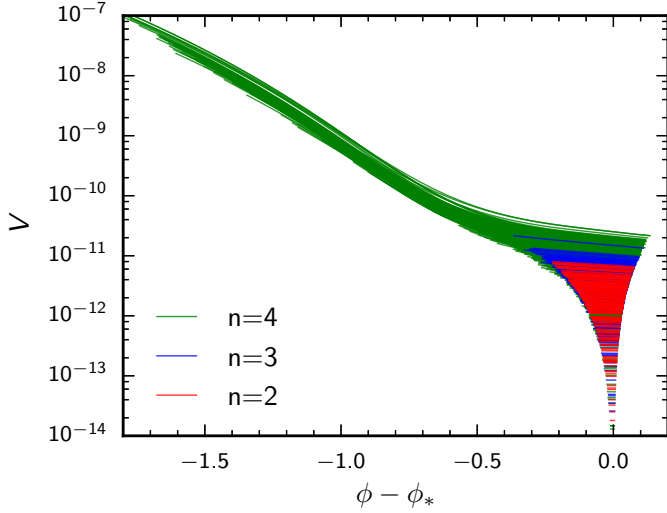


Fig. 20. Same as Fig. 15, when the Taylor expansion to n th order is performed on $H(\phi)$ instead of $V(\phi)$, and the potential is inferred from Eq. (60).

coefficients. The main two differences with respect to the results of Sect. 7.2 are as follows:

- The reconstructed potential shapes for $n = 4$ at the beginning of the observable window differ. Figure 20 shows that even steeper potentials are allowed than for the $V(\phi)$ method, with an even greater excursion of the inflaton field between Hubble crossing for the largest observable wavelengths and the pivot scale. This is because the $H(\phi)$ reconstruction does not rely on attractor solutions and automatically explores all valid potentials regardless of their initial field velocity.
- The best-fit models are different, since they do not explore the same parametric families of potentials. In particular, for $n = 4$, the best-fit models have a negligible tensor contribution, but the distributions still have thick tails towards large tensor-to-scalar ratios, so that the upper bound on $r_{0.002}$ is as high as in the previous $n = 4$ models, $r_{0.002} < 0.32$.

Note that ϖ_H^3 can be significantly larger than unity for $n = 4$. This does not imply violation of slow roll within the observable range. By assumption, for all accepted models, ϵ_H must remain smaller than unity over that range. In fact, for most of the green potentials visible in Fig. 20, we checked that ϵ_H either has a maximum very close to unity near the beginning of the observable range or starts from unity. So the best-fit models (maximizing the power suppression at low multipoles) correspond either to inflation of short duration, or to models nearly violating slow roll just before the observable window. However, such peculiar models are not necessary for a good fit. Table 9 shows that the improvement in χ^2 as n increases is negligible.

In summary, this section further establishes the robustness of our potential reconstruction and two main conclusions. Firstly, under the assumption that the inflaton potential is smooth over the observable range, we showed that the simplest parametric forms (involving only three free parameters including the amplitude $V(\phi_*)$, no deviation from slow roll, and nearly power law primordial spectra) are sufficient to explain the data. No high-order derivatives or deviations from slow roll are required. Secondly, if one allows more freedom in the potential – typically, two more parameters – it is easy to decrease the large-scale primordial spectrum amplitude with an initial stage of “marginal slow roll” along a steep branch of the potential followed by a

transition to a less steep branch. This type of model can accommodate a large tensor-to-scalar ratio, as high as $r_{0.002} \approx 0.3$.

8. $\mathcal{P}(k)$ reconstruction

In PCI13 (Sect. 7) we presented the results of a penalized likelihood reconstruction, seeking to detect any possible deviations from a homogeneous power-law form (i.e., $\mathcal{P}_{\mathcal{R}}(k) \propto k^{n_s-1}$) for the primordial power spectrum (PPS) for various values of a smoothing parameter, λ . (For an extensive set of references to the prior literature concerning the methodology for reconstructing the power spectrum, see PCI13.) In the initial March 2013 preprint version of that paper, we reported evidence for a feature at moderate statistical significance around $k \approx 0.15 \text{ Mpc}^{-1}$. However, in the November 2013 revision we retracted this finding, because subsequent tests indicated that the feature was no longer statistically significant when more aggressive cuts were made to exclude sky survey rings where contamination from electromagnetic interference from the 4 K cooler was largest, as indicated in the November 2013 “Note Added.”

In this section we report on results using the 2015 C_ℓ^{TT} likelihood (Sect. 8.1) using essentially the same methodology as described in PCI13. (See Gauthier & Bucher 2012, and references therein for more technical details.) This method is also extended to include the EE and TE likelihoods in Sect. 8.1.2. As part of this 2015 release, we include the results of two other methods (see Sects. 8.2 and 8.3) to search for features. We find that all three methods yield broadly consistent reconstructions and reach the following main conclusion: there is no statistically significant evidence for any features departing from a simple power-law (i.e., $\mathcal{P}_{\mathcal{R}}(k) \propto k^{n_s-1}$) PPS. Given the substantial differences between these methods, it is satisfying to observe this convergence.

8.1. Method I: penalized likelihood

8.1.1. Update with 2015 temperature likelihood

We repeated the same maximum likelihood analysis used to reconstruct the PPS in PCI13 using the updated *Planck* TT+lowP likelihood. Since we are interested in deviations from the nearly scale-invariant model currently favoured by the parametric approach, we replaced the true PPS $\mathcal{P}_{\mathcal{R}}(k)$ by a fiducial power-law spectrum $\mathcal{P}_{\mathcal{R}}^{(0)}(k) = A_s(k/k_*)^{n_s-1}$, modulated by a small deviation function $f(k)$:

$$\mathcal{P}_{\mathcal{R}}(k) = \mathcal{P}_{\mathcal{R}}^{(0)}(k) \exp[f(k)]. \quad (65)$$

The deviation function $f(k)$ ⁷ was represented by B -spline basis functions parameterized by n_{knot} control points $\mathbf{f} = \{f_i\}_{i=1}^{n_{\text{knot}}}$, which are the values of $f(k)$ along a grid of knot points $\kappa_i = \ln k_i$.

Naively maximizing the *Planck* TT+lowP likelihood with respect to \mathbf{f} results in over-fitting to cosmic variance and noise in the data. Furthermore, due to the limited range of scales over which *Planck* measures the anisotropy power spectrum, the likelihood is very weakly dependent on $f(k)$ at extremely small and large scales. To address these issues, the following two penalty functions were added to the *Planck* likelihood:

$$\begin{aligned} \mathbf{f}^T \mathbf{R}(\lambda, \alpha) \mathbf{f} \equiv & \lambda \int d\kappa \left(\frac{\partial^2 f(\kappa)}{\partial \kappa^2} \right)^2 \\ & + \alpha \int_{-\infty}^{\kappa_{\min}} d\kappa f^2(\kappa) + \alpha \int_{\kappa_{\max}}^{+\infty} d\kappa f^2(\kappa). \end{aligned} \quad (66)$$

⁷ The definition of $f(k)$ used here differs from that of PCI13 in that $\exp(f)$ is used in place of $1 + f$ to ensure that the reconstructed primordial power spectrum is always non-negative.

The first term on the right-hand side of Eq. (66) is a roughness penalty, which disfavours $f(k)$ that “wobble” too much. The last two terms drive $f(k)$ to zero for scales below κ_{\min} and above κ_{\max} . The values of λ and α represent the strengths of the respective penalties. The exact value of α is unimportant as long as it is large enough to drive $f(k)$ close to zero on scales outside $[\kappa_{\min}, \kappa_{\max}]$. However, the magnitude of the roughness penalty λ controls the smoothness of the reconstruction.

Since the anisotropy spectrum depends linearly on the PPS, the Newton-Raphson method is well suited to optimizing with respect to \mathbf{f} . However, a maximum likelihood analysis also has to take into account the cosmological parameters, $\Theta \equiv \{H_0, \Omega_b h^2, \Omega_c h^2\}$ ⁸. These additional parameters are not easy to include in the Newton-Raphson method since it is difficult to evaluate the derivatives $\partial C_\ell / \partial \Theta$, $\partial^2 C_\ell / \partial \Theta^2$, etc., to the accuracy required by the method. Therefore a non-derivative method, such as the downhill simplex algorithm, is best suited to optimization over these parameters. Unfortunately the downhill simplex method is inefficient given the large number of control points in our parameter space. Since each method has its drawbacks, we combined the two methods to draw on their respective strengths. We define the function \mathcal{M} as

$$\mathcal{M}(\Theta) = \min_{\mathbf{f} \in [-1, 1]} \{-2 \ln \mathcal{L}(\Theta, \mathbf{f}) + \mathbf{f}^T \mathbf{R}(\lambda, \alpha) \mathbf{f}\}. \quad (67)$$

Given a set of non-PPS cosmological parameters Θ , \mathcal{M} is the value of the penalized log likelihood, minimized with respect to \mathbf{f} using the Newton-Raphson method. The function \mathcal{M} is in turn minimized with respect to Θ using the downhill simplex method. In contrast to the analysis done in PCI13, the *Planck* low- ℓ likelihood has been modified so that it can be included in the Newton-Raphson minimization. Thus the reconstructions presented here extend to larger scales than were considered in 2013.

Figure 21 shows the best-fit PPS reconstruction using the *Planck* TT+lowP likelihood. The penalties in Eq. (66) introduce a bias in the reconstruction by smoothing and otherwise deforming potential features in the power spectrum. To assess this bias, we define the “minimum reconstructible width” (MRW) to be the minimum width of a Gaussian feature needed so that the integrated squared difference between the feature and its reconstruction is less than 1% of the integrated square of the input Gaussian, which is equivalent to 10% rms. Due to the combination of the roughness and fixing penalties, it is impossible to satisfy the MRW criterion too close to κ_{\min} and κ_{\max} . Wherever the MRW is undefined, the reconstruction is substantially biased and therefore suspect. An MRW cannot be defined too close to the endpoints κ_{\min} and κ_{\max} for two reasons: (1) lack of data; and (2) if a feature is too close to where the fixing penalty has been applied, the fixing penalty distorts the reconstruction. Consequently a larger roughness penalty decreases the range over which an MRW is well defined. The grey shaded areas in Fig. 21 show where the MRW is undefined and thus the reconstruction cannot be trusted. The cutoffs κ_{\min} and κ_{\max} have been chosen to maximize the range over which an MRW is defined for a given value of λ . The 1σ and 2σ error bars in Fig. 21 are estimated using the Hessian of the log-likelihood evaluated at the best-fit PPS reconstruction. More detailed MC investigations suggest that the nonlinear corrections to these error bars are small.

⁸ Due to the high correlation between τ and A_s , τ is not included as a free parameter. Any change in τ can be almost exactly compensated for by a change in A_s . We fix τ to its best-fit fiducial model value.

For the $\lambda = 10^5$ and 10^6 cases of the TT reconstruction, no deviation exceeds 2σ , so we do not comment on the probability of obtaining a worse fit. For the other cases, we use the maximum of the deviation, expressed in σ , of the plotted points as a metric of the quality of fit. Then using Monte Carlo simulations, we compute the p -value, or the probability to obtain a worse fit, according to this metric. For $\lambda = 10^3$ and 10^4 , we obtain p -values of 0.304 and 0.142, respectively, corresponding to 1.03 and 1.47σ . We thus conclude that the observed deviations are not statistically significant.

8.1.2. Penalized likelihood results with polarization

In Fig. 22 the best-fit reconstruction of the PPS from the *Planck* TT, TE, EE+lowP likelihood is shown. We observe that the reconstruction including polarization broadly agrees with the reconstruction obtained using temperature only. For the *Planck* TT, TE, EE+lowP likelihood, we obtain for $\lambda = 10^3$, 10^4 , and 10^5 the p -values 0.166, 0.107, and 0.045, respectively, corresponding to 1.38, 1.61, and 2.00σ , and likewise conclude the absence of any statistically significant evidence for deviations from a simple power-law scalar primordial power spectrum.

8.2. Method II: Bayesian model comparison

In this section we model the PPS $\mathcal{P}_{\mathcal{R}}(k)$ using a nested family of models where $\mathcal{P}_{\mathcal{R}}(k)$ is piecewise linear in the $\ln(\mathcal{P})$ - $\ln(k)$ plane between a number of knots, N_{knots} , that is allowed to vary. The question arises as to how many knots one should use, and we address this question using Bayesian model comparison. A family of priors is chosen where both the horizontal and vertical positions of the knots are allowed to vary. We examine the “Bayes factor” or “Bayesian evidence” as a function of N_{knots} to decide how many knots are statistically justified. A similar analysis has been performed by Vázquez et al. (2012) and Aslanyan et al. (2014). In addition, we marginalize over all possible numbers of knots to obtain an averaged reconstruction weighted according to the Bayesian evidence.

The generic prescription is illustrated in Fig. 23. N_{knots} knots $\{(k_i, \mathcal{P}_i) : i = 1, \dots, N_{\text{knots}}\}$ are placed in the $(k, \mathcal{P}_{\mathcal{R}})$ plane and the function $\mathcal{P}_{\mathcal{R}}(k)$ is constructed by logarithmic interpolation (a linear interpolation in log-log space) between adjacent points. Outside the horizontal range $[k_1, k_N]$ the function is extrapolated using the outermost interval.

Within this framework, base Λ CDM arises when $N_{\text{knots}} = 2$ – in other words, when there are two boundary knots and no internal knots, and the parameters \mathcal{P}_1 and \mathcal{P}_2 (in place of A_s and n_s) parameterize the simple power-law PPS. There are also, of course, the four standard cosmological parameters ($\Omega_b h^2$, $\Omega_c h^2$, $100\theta_{\text{MC}}$, and τ), as well as the numerous foreground parameters associated with the *Planck* high- ℓ likelihood, all of which are unrelated to the PPS. This simplest model can be extended iteratively by successively inserting an additional internal knot, thus requiring with each iteration two more variables to parameterize the new knot position.

We run models for a variety of numbers of internal knots, $N_{\text{int}} = N_{\text{knots}} - 2$, evaluating the evidence for N_{int} . Under the assumption that the prior is justified, the most likely, or preferred, model is the one with the highest evidence. Evidences are evaluated using the PolyChord sampler (Handley et al. 2015) in CAMB and CosmoMC. The use of PolyChord is essential, as the posteriors in this parameterization are often multi-modal. Also, the ordered log-uniform priors on the k_i are easy to implement

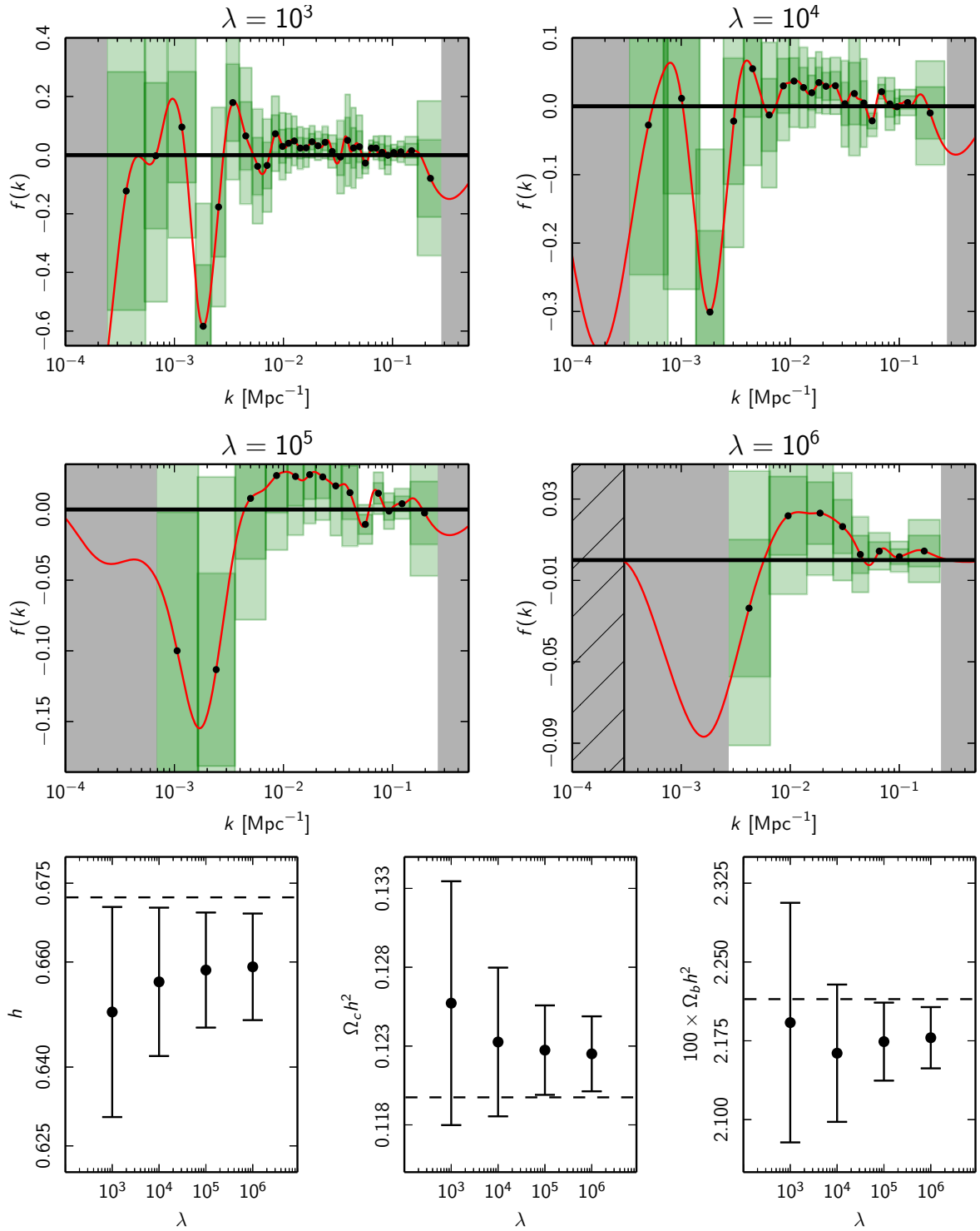


Fig. 21. *Planck* TT+lowP likelihood primordial power spectrum (PPS) reconstruction results. *Top four panels:* reconstruction of the deviation $f(k)$ using four different roughness penalties. The red curves represent the best-fit deviation $f(k)$ using the *Planck* TT+lowP likelihood. $f(k) = 0$ would represent a perfectly featureless spectrum with respect to the fiducial PPS model, which is obtained from the best-fit base Λ CDM model with a power-law PPS. The vertical extent of the dark and light green error bars indicates the $\pm 1\sigma$ and $\pm 2\sigma$ errors, respectively. The width of the error bars represents the minimum reconstructible width (the minimum width for a Gaussian feature so that the mean square deviation of the reconstruction is less than 10%). The grey regions indicate where the minimum reconstructible width is undefined, indicating that the reconstruction in these regions is untrustworthy. The hatched region in the $\lambda = 10^6$ plot shows where the fixing penalty has been applied. These hashed regions are not visible in the other three reconstructions, for which κ_{\min} lies outside the range shown in the plots. For all values of the roughness penalty, all data points are within 2σ of the fiducial PPS except for the deviations around $k \approx 0.002 \text{ Mpc}^{-1}$ in the $\lambda = 10^3$ and $\lambda = 10^4$ reconstructions. *Lower three panels:* $\pm 1\sigma$ error bars of the three non-PPS cosmological parameters included in the maximum likelihood reconstruction. All values are consistent with their respective best-fit fiducial model values indicated by the dashed lines.

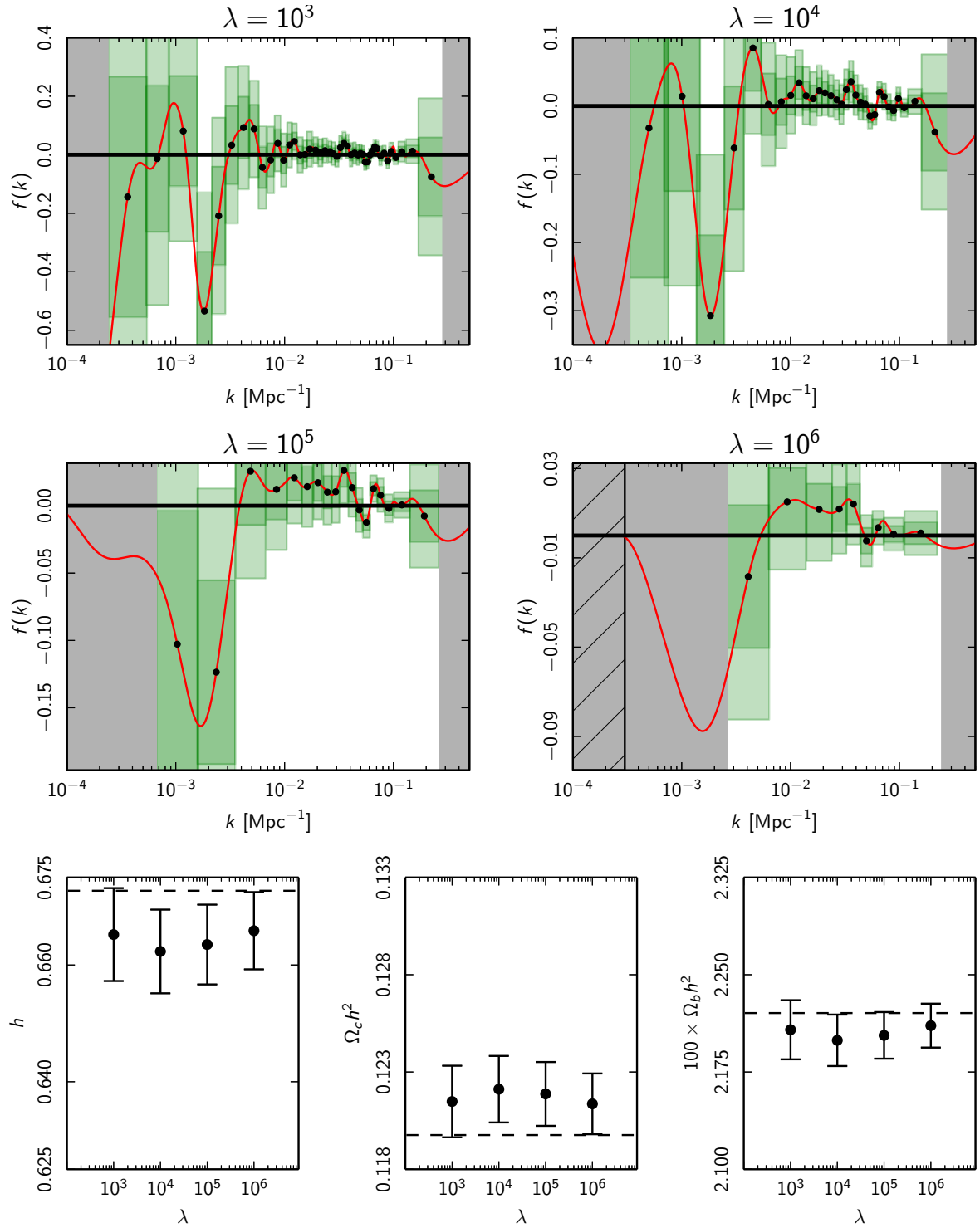


Fig. 22. *Planck* TT, TE, EE+lowP likelihood primordial power spectrum reconstruction results. *Top four panels:* reconstruction of the deviation $f(k)$ using four different roughness penalties. As in Fig. 21, the red curves represent the best-fit deviation $f(k)$ and the height and width of the green error bars represent the error and minimum reconstructible width, respectively. For all values of the roughness penalty, the deviations are consistent with a featureless spectrum. *Lower three panels:* $\pm 1\sigma$ error bars of the three non-PPS cosmological parameters included in the maximum likelihood reconstruction. All values are consistent with their respective best-fit fiducial model values (indicated by the dashed lines).

within the PolyChord framework. All runs were performed with 1000 live points, oversampling the semi-slow and fast parameters by a factor of 5 and 100, respectively.

Priors for the reconstruction parameters are detailed in Table 10. We report evidence ratios with respect to the base Λ CDM case. The cosmological priors remain the same for all

models, and this part of the prior has almost no impact on the evidence ratios. The choice of prior on the reconstruction parameters $\{\mathcal{P}_i\}$ does affect the Bayes factor. CosmoMC, however, puts an implicit prior on all models by excluding parameter choices that render the internal computational approximations in CAMB invalid. The baseline prior for the vertical position of the

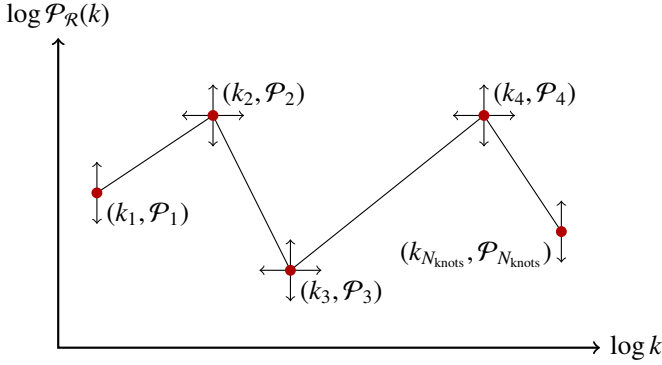


Fig. 23. Linear spline reconstruction. The primordial power spectrum is reconstructed using N_{knots} interpolation points $\{(k_i, \mathcal{P}_i) : i = 1, 2, \dots, N_{\text{knots}}\}$. The end knots are fixed in k but allowed to vary in \mathcal{P} , whereas the internal knots can vary subject to the constraint that $k_1 < k_2 < \dots < k_{N_{\text{knots}}}$. The function $\mathcal{P}_R(k)$ is constructed within the range $[k_1, k_{N_{\text{knots}}}]$ by interpolating logarithmically between adjacent knots (i.e., linearly in log-log space). Outside this range the function is extrapolated logarithmically. The function $\mathcal{P}_R(k; \{k_i, \mathcal{P}_i\})$ thus has $2N_{\text{knots}} - 2$ parameters.

Table 10. Prior for moveable knot positions.

Parameter range	Prior type
$10^{-4} \text{ Mpc}^{-1} = k_1 < k_2 < \dots < k_{N_{\text{knots}}} = 0.3 \text{ Mpc}^{-1}$	log uniform (sorted)
$2 < \ln(10^{10} \mathcal{P}_1), \dots, \ln(10^{10} \mathcal{P}_{N_{\text{knots}}}) < 4$	log uniform
$2 \leq N_{\text{knots}} \leq 10$	integer uniform

Notes. The \mathcal{P}_R positions are distributed in a log-uniform manner across a wide range. The k positions are also log-uniformly distributed across the entire range needed by CosmoMC and are sorted so that $k_1 < \dots < k_{N_{\text{knots}}}$. When we marginalize over the number of knots, N_{knots} , we assume a uniform prior between 2 and 10.

knots includes all of the range allowed by CosmoMC, so slightly increasing this prior range will not affect the evidence ratios. If one were to reduce the prior widths significantly, the evidence ratios would be increased. The allowed horizontal range includes all k -scales accessible to *Planck*. Thus, altering this width would be unphysical.

After completion of an evidence calculation, PolyChord generates a representative set of samples of the posterior for each model, $P(\Theta) \equiv P(\Theta|\text{data}, N_{\text{int}})$. We may use this to calculate a marginalized probability distribution for the PPS:

$$P(\log \mathcal{P}_R | k, N_{\text{int}}) = \int \delta(\log \mathcal{P}_R - \log \mathcal{P}_R(k; \Theta)) P(\Theta) d\Theta. \quad (68)$$

This expression encapsulates our knowledge of \mathcal{P}_R at each value of k for a given number of knots. Plots of this PPS posterior are shown in Fig. 24 using *Planck* TT data.

If one considers the Bayesian evidence of each model, Fig. 25 shows that although no model is preferred over base Λ CDM, the case $N_{\text{int}} = 1$ is competitive. This model is analogous to the broken-power-law spectrum of Sect. 4.4, although the models differ significantly in terms of the priors used. In this case, the additional freedom of one knot allows a reconstruction of the suppression of power at low ℓ . Adding polarization data does not alter the evidences significantly, although $N_{\text{int}} = 1$ is strengthened. We also plot a *Planck* TT run, but with the reduced vertical priors $2.5 < \ln(10^{10} \mathcal{P}_i) < 3.5$. As expected,

this increases the evidence ratios, but does not alter the above conclusion.

For increasing numbers of internal knots, the Bayesian evidence monotonically decreases. Occam’s razor dictates, therefore, that these models should not be preferred, due to their higher complexity. However, there is an intriguing stable oscillatory feature, at $20 \lesssim \ell \lesssim 50$, that appears once there are enough knots to reconstruct it. This is a qualitative feature predicted by several inflationary models (discussed in Sect. 9), and a possible hint of new physics, although its statistical significance is not compelling.

A full Bayesian analysis marginalizes over all models weighted according to the normalized evidence $Z_{N_{\text{int}}}$, so that

$$P(\log \mathcal{P}_R | k) = \sum_{N_{\text{int}}} P(\log \mathcal{P}_R | k, N_{\text{int}}) Z_{N_{\text{int}}}, \quad (69)$$

as indicated in Fig. 26. This reconstruction is sensitive to how model complexity is penalized in the prior distribution.

8.3. Method III: cubic spline reconstruction

In this section we investigate another reconstruction algorithm based on cubic splines in the $\ln(k)$ - $\ln \mathcal{P}_R$ plane, where (unlike for the approach of the previous subsection) the horizontal positions of the knots are uniformly spaced in $\ln(k)$ and fixed. A prior on the vertical positions (described in detail below) is chosen and the reconstructed power spectrum is calculated using CosmoMC for various numbers of knots. This method differs from the method in Sect. 8.1 in that the smoothness is controlled by the number of discrete knots rather than by a continuous parameter of a statistical model having a well-defined continuum limit. With respect to the Bayesian model comparison of Sect. 8.2, the assessment of model complexity differs because here the knots are not movable.

Let the horizontal positions of the n knots be given by k_b , where $b = 1, \dots, n$, spaced so that k_{b+1}/k_b is independent of b . We single out a “pivot knot” $b = p$, so that $k_p = k_* = 0.05 \text{ Mpc}^{-1}$, which is the standard scalar power spectrum pivot scale. For a given number of knots n we choose k_1 and k_n so that the interval of relevant cosmological scales, taken to extend from 10^{-4} Mpc^{-1} to $O(1) \text{ Mpc}^{-1}$, is included. We now define the prior on the vertical knot coordinates. For the pivot point, we define $\ln A_s = \ln \mathcal{P}_R(k_*)$, where $\ln A_s$ has a uniformly distributed prior, and for the other points with $b \neq p$, we define the derived variable

$$q_b \equiv \ln \left(\frac{\mathcal{P}_R(k_b)}{\mathcal{P}_{R,\text{fid}}(k_b)} \right), \quad (70)$$

where $\mathcal{P}_{R,\text{fid}}(k) \equiv A_s (k/k_*)^{n_{s,\text{fid}}-1}$. Here the spectral index $n_{s,\text{fid}}$ is fixed. A uniform prior is imposed on each variable q_b ($b \neq p$) and the constraint $-1 \leq q_b \leq 1$ is also imposed to force the reconstruction to behave reasonably near the endpoints, where it is hardly constrained by the data. The quantity $\ln \mathcal{P}_R(k)$ is interpolated between the knots using cubic splines with natural boundary conditions (i.e., the second derivatives vanish at the first and the last knots). Outside $[k_1, k_n]$ we set $\mathcal{P}_R(k) = e^{q_1} \mathcal{P}_{R,\text{fid}}(k)$ (for $k < k_1$) and $\mathcal{P}_R(k) = e^{q_n} \mathcal{P}_{R,\text{fid}}(k)$ (for $k > k_n$). For most knots, we found that the upper and lower bounds of the q_b prior hardly affect the reconstruction, since the data sharpen the allowed range significantly. However, for super-Hubble scales (i.e., $k \lesssim 10^{-4} \text{ Mpc}^{-1}$) and very small scales (i.e., $k \gtrsim 0.2 \text{ Mpc}^{-1}$), which are only weakly constrained by the cosmological data, the prior dominates the reconstruction. For the results here, a fiducial

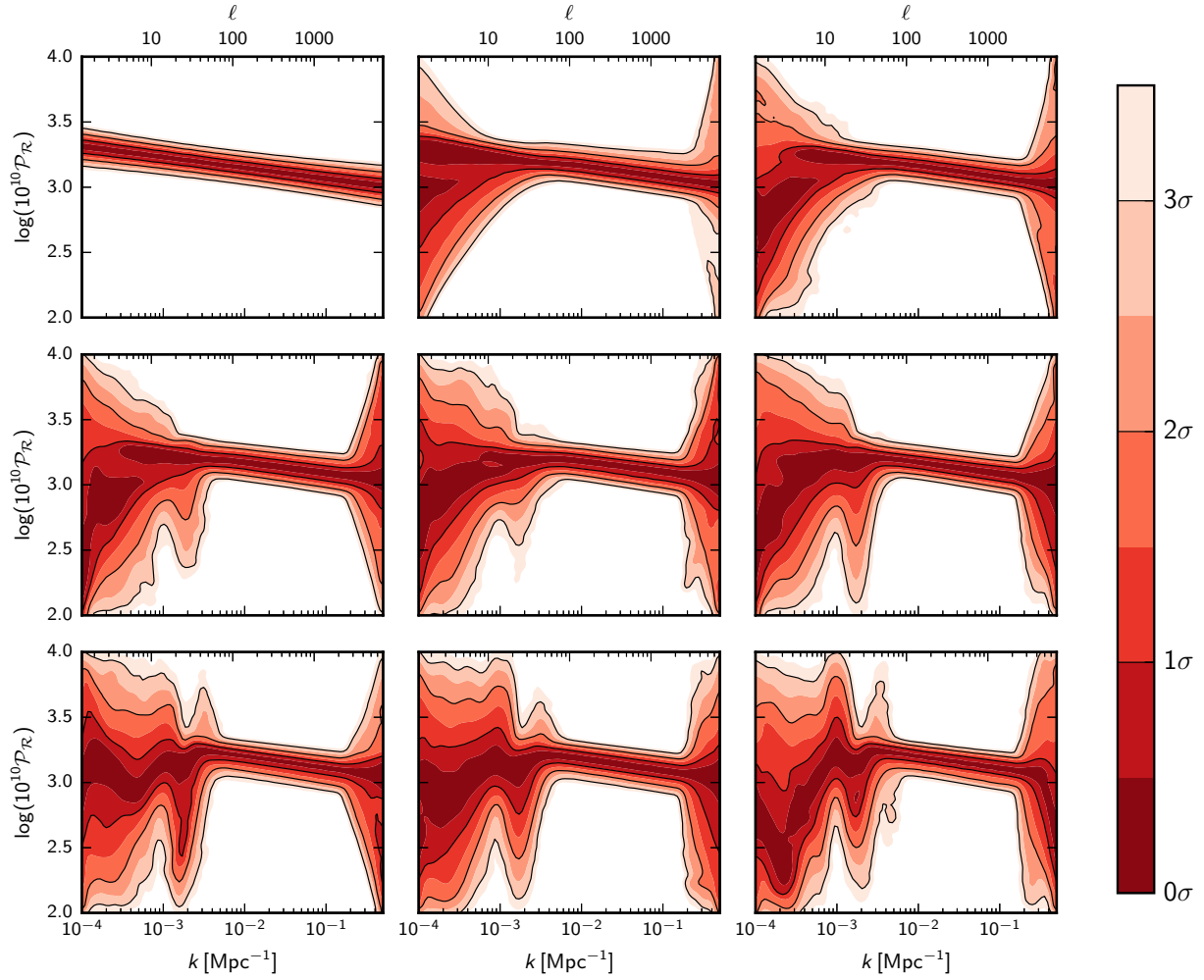


Fig. 24. Bayesian movable knot reconstructions of the primordial power spectrum $\mathcal{P}_{\mathcal{R}}(k)$ using *Planck* TT data. The plots indicate our knowledge of the PPS $P(\mathcal{P}_{\mathcal{R}}(k)|k, N_{\text{int}})$ for a given number of knots. The number of internal knots N_{int} increases (left to right and top to bottom) from 0 to 8. For each k -slice, equal colours have equal probabilities. The colour scale is chosen so that darker regions correspond to lower- σ confidence intervals. 1σ and 2σ confidence intervals are also indicated (black curves). The upper horizontal axes give the approximate corresponding multipoles via $\ell \approx kD_{\text{rec}}$, where D_{rec} is the comoving distance to recombination.

spectral index $n_{s,\text{fid}} = 0.967$ for $\mathcal{P}_{\mathcal{R},\text{fid}}$ was chosen, which is close to the estimate from *Planck* TT+lowP+BAO. A different choice of $n_{s,\text{fid}}$ leads to a trivial linear shift in the q_b .

The possible presence of tensor modes (see Sect. 5) has the potential to bias and introduce additional uncertainty in the reconstruction of the primordial scalar power spectrum as parameterized above. Obviously, in the absence of a detection of tensors at high statistical significance, it is not sensible to model a possible tensor contribution with more than a few degrees of freedom. A complicated model would lead to prior dominated results. We therefore use the power law parameterization, $\mathcal{P}_{\text{t}}(k) = rA_s(k/k_*)^{n_t}$, where the consistency relation $n_t = -r/8$ is enforced as a constraint.

Primordial tensor fluctuations contribute to CMB temperature and polarization angular power spectra, in particular at spatial scales larger than the recombination Hubble length, $k \lesssim (aH)_{\text{rec}} \approx 0.005 \text{ Mpc}^{-1}$. If a large number of knots in $\ln \mathcal{P}_{\mathcal{R}}(k)$ is included over that range, then a modified $\mathcal{P}_{\mathcal{R}}$ can mimic a tensor contribution, leading to a near-degeneracy. This can lead to large uncertainty in the tensor amplitude, r . Once r is measured or tightly constrained in B -mode experiments, this near degeneracy will be broken. As examples here, we do allow r to float, but also show what happens when r is constrained to take the values $r = 0.1$ and $r = 0.01$ in the reconstruction.

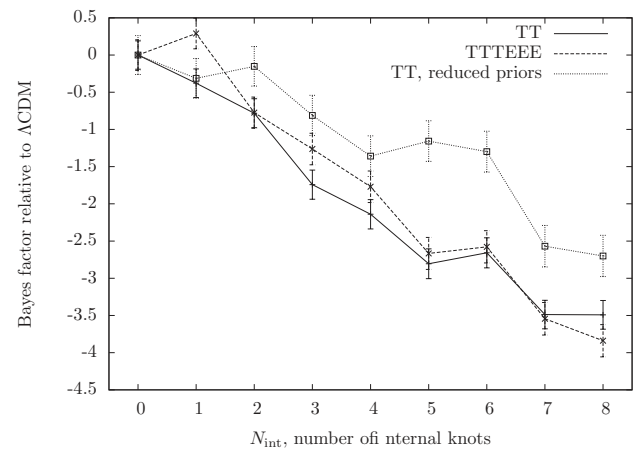


Fig. 25. Bayes factor (relative to the base ΛCDM model) as a function of the number of knots for three separate runs. Solid line: *Planck* TT. Dashed line: *Planck* TT, TE, EE. Dotted line: *Planck* TT, with priors on the \mathcal{P}_i parameters reduced in width by a factor of 2 ($2.5 < \ln(10^{10}\mathcal{P}_i) < 3.5$).

Figure 27 shows the reconstruction obtained using the 2015 *Planck* TT+lowP likelihood, BAO, SNIa, HST, and a $z_{\text{re}} > 6$

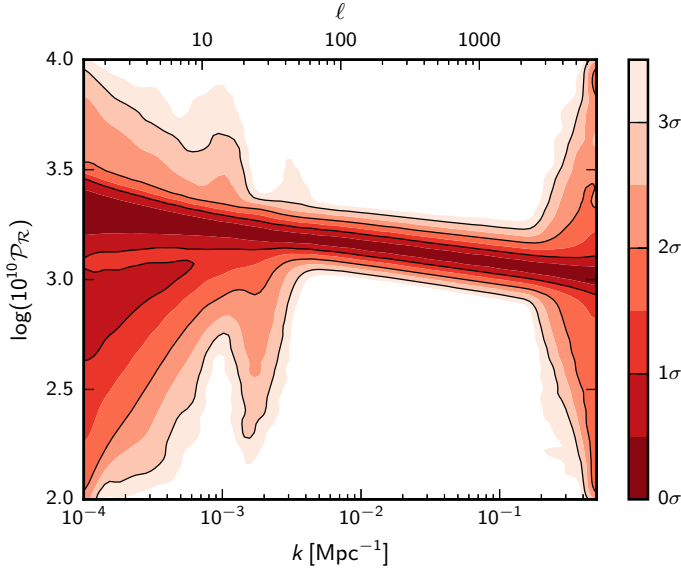


Fig. 26. Bayesian reconstruction of the primordial power spectrum averaged over different values of N_{int} (as shown in Fig. 24), weighted according to the Bayesian evidence. The region $30 < \ell < 2300$ is highly constrained, but the resolution is lacking to say anything precise about higher ℓ . At lower ℓ , cosmic variance reduces our knowledge of $\mathcal{P}_R(k)$. The weights assigned to the lower N_{int} models outweigh those of the higher models, so no oscillatory features are visible here.

prior. Including these ancillary likelihoods improves the constraint on the PPS by helping to fix the cosmological parameters (e.g., H_0 , τ , and the late-time expansion history), which in this context may be regarded as nuisance parameters. These results were obtained by modifying CosmoMC to incorporate the n -knot parameterization of the PPS. Here 12 knots were used and the mean reconstruction as well as the 1σ and 2σ limits are shown. Some 1σ sample trajectories (dashed curves) are also shown to illustrate the degree of correlation or smoothing of the reconstruction. The tensor trajectories are also shown, but, as explained above, have been constrained to be straight lines. In the top panel r is allowed to freely float, and a wide range of r is allowed because of the near-degeneracy with the low- k scalar power. Two illustrative values of fixed r (i.e., $r = 0.1$ and $r = 0.01$) are also shown to give an idea of how much the reconstruction is sensitive to variations in r within the range of presently plausible values.

The reconstructions using the 2013 *Planck* likelihood in place of the 2015 likelihood are broadly consistent with the reconstruction shown in Fig. 27. To demonstrate robustness with respect to the interpolation scheme we tried using linear interpolation instead of cubic splines and found that the reconstruction was consistent provided enough knots (i.e., $n_{\text{knot}} \approx 14$) were used. At intermediate k the reconstruction is consistent with a simple power law, corresponding to a straight line in Fig. 27. We observe that once k drops, so that the effective multipole being probed is below about 60, deviations from a power law appear, but the dispersion in allowed trajectories also rises as a consequence of cosmic variance. The power deficit at $k \approx 0.002 \text{ Mpc}^{-1}$ (i.e., $\ell_k \equiv kD_{\text{rec}} \approx 30$, where D_{rec} is the comoving distance to recombination) is largely driven by the power spectrum anomaly in the $\ell \approx 20$ – 30 range that has been evident since the early spectra from WMAP (Bennett et al. 2011), and verified by *Planck*.

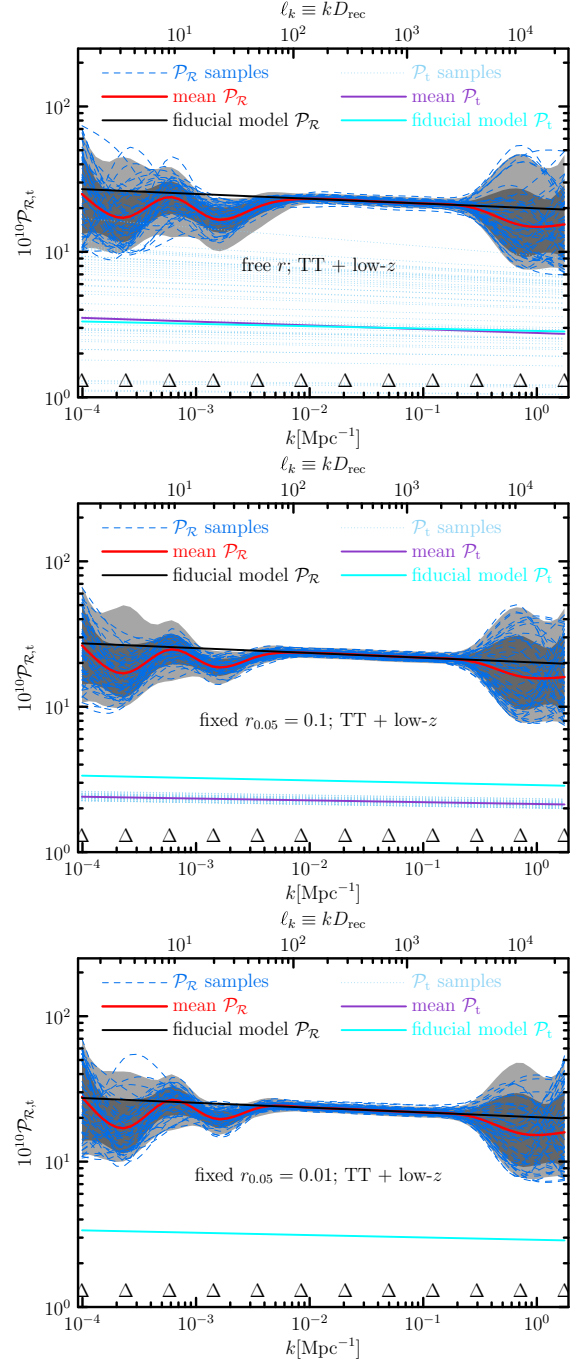


Fig. 27. Reconstructed power spectra applied to the *Planck* 2015 data using 12 knots (with positions marked as Δ at the bottom of each panel) with cubic spline interpolation. Mean spectra as well as sample trajectories are shown for scalars and tensors, and $\pm 1\sigma$ and $\pm 2\sigma$ limits are shown for the scalars. The fiducial tensor spectrum corresponds, arbitrarily, to $r = 0.13$. *Top*: uniform prior, $0 \leq r \leq 1$. *Middle*: fixed, $r = 0.1$. *Bottom*: fixed, $r = 0.01$. Data sets: *Planck* TT+lowP+BAO+SN+HST+ $z_{\text{re}} > 6$ prior. D_{rec} is the comoving distance to recombination.

We also explore the impact of including the *Planck* polarization likelihood in the reconstruction. Figure 28 shows the reconstructed power spectra using various combinations of the polarization and temperature data. The $\ell < 30$ treatments are the same in all cases, so this is mainly a test of the higher k region. What is seen is that, except at high k , the *EE* polarization data also enforce a nearly uniform n_s , consistent with that

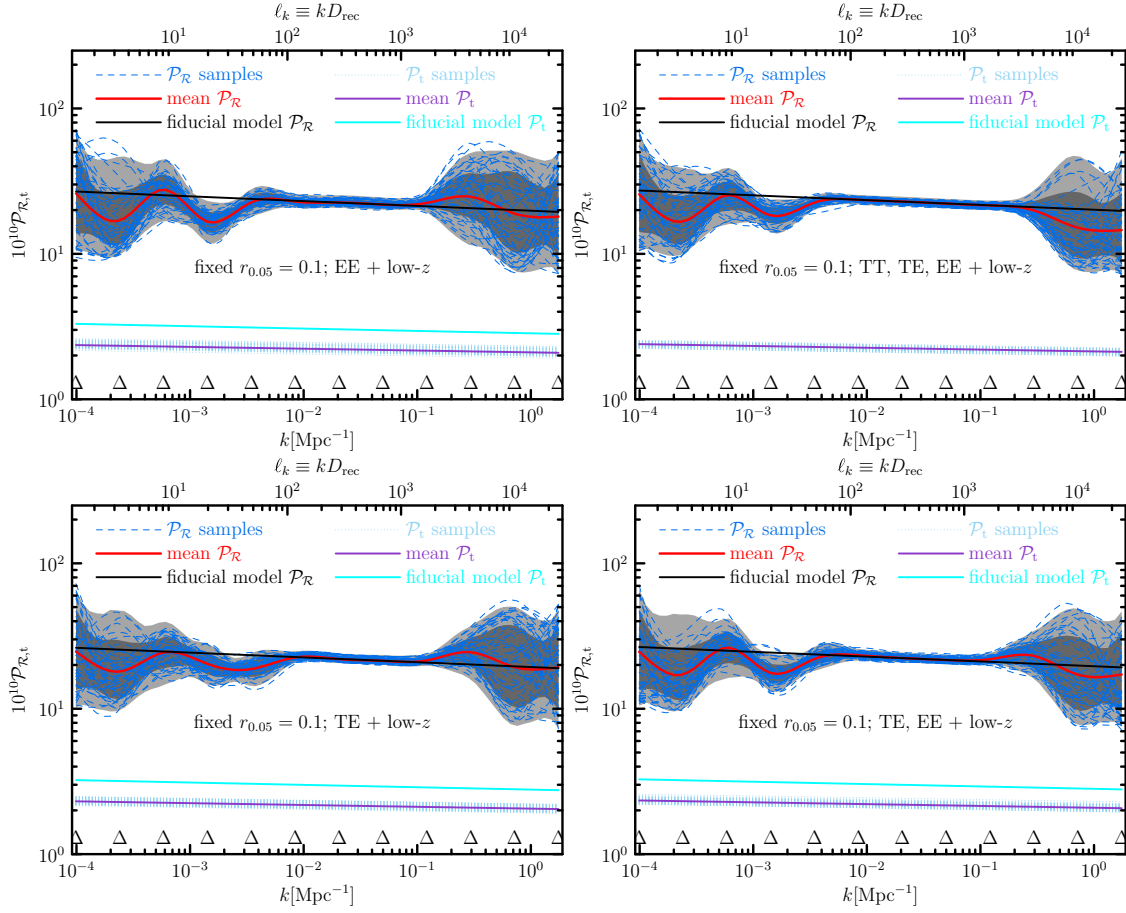


Fig. 28. Reconstructed 12-knot power spectra with polarization included. Data sets in common: lowT+lowP+BAO+SN+HST+ $z_{\text{re}} > 6$ prior.

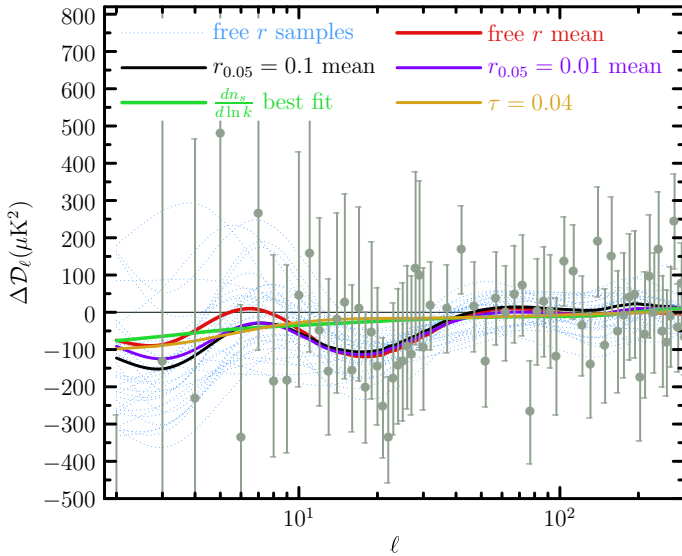


Fig. 29. Reconstructed $\mathcal{D}_\ell^{\text{TT}}$ power spectra with the base ΛCDM best fit subtracted. The mean spectra shown are for the floating r and the two fixed r cases with 12 cubic spline knots. These should be contrasted with the running best-fit mean (green) and the similar looking uniform n_s case in which τ has been lowered from its best-fit base ΛCDM value to 0.04. Data points are the *Planck* 2015 Commander ($\ell < 30$) and *Planck* ($\ell \geq 30$) temperature power spectrum.

from TT , over a broad k -range. When TE is used alone, or TE and EE are used in combination, the result is also very similar.

The upper right panel shows the constraints from all three spectra together, and the errors on the reconstruction are now better than those from TT alone.

It is interesting to examine how the TT power spectrum obtained using the above reconstructions compares to the CMB data, in particular around the range $\ell \approx 20$ – 30 , corresponding roughly to $k_4 \approx 1.5 \times 10^{-3} \text{ Mpc}^{-1}$. In Fig. 29 the differences in $\mathcal{D}_\ell^{\text{TT}}$ from the best-fit simple power-law model are plotted for various assumptions concerning r . We see that a better fit than the power-law model can apparently be obtained around $\ell \approx 20$ – 30 . We quantify this improvement below.

Due to the degeneracy of scalar and tensor contributions to $\mathcal{D}_\ell^{\text{TT}}$, the significance of the low- ℓ anomaly depends on the tensor prior and whether polarization data are used. For $k < 10^{-3} \text{ Mpc}^{-1}$, once more degeneracy appears: the shape of $\mathcal{D}_\ell^{\text{TT}}$ also depends on the reionization optical depth, τ . In Fig. 29 we also show the effect of replacing the best-fit τ for tilted base ΛCDM with a low value, while keeping $A_s e^{-2\tau}$ unchanged. A low τ bends $\mathcal{D}_\ell^{\text{TT}}$ downward at $\ell \lesssim 10$. For the 12-knot (or similar) runs, if τ is allowed to run into the (nonphysically) small values $\tau \lesssim 0.04$, a slight rise in $\mathcal{P}_R(k)$ at $k \approx 3 \times 10^{-4} \text{ Mpc}^{-1}$ is preferred to compensate the low- τ effect. This degeneracy can be broken to a certain extent using low-redshift data: $z_{\text{re}} > 6$ from quasar observations (Becker et al. 2001), BAO (SDSS), Supernova (JLA), and HST.

It is evident that allowing n_s to run is not what the $\mathcal{D}_\ell^{\text{TT}}$ data prefer. The best-fit running is also shown in Fig. 29. The k -space $\mathcal{P}_R(k)$ -response in Fig. 27 shows that running does not capture the shape of the low- ℓ residuals.

Table 11. Reduced χ^2 and p -values for low- k knots (5 knots) and high- k knots (6 knots, pivot knot excluded), with the null hypothesis being the best-fit power-law spectrum.

r prior	low- z data	<i>Planck</i> data	low- k χ^2_{reduced}	low- k p -value	high- k χ^2_{reduced}	high- k p -value	q_3 constraint	q_4 constraint
$0 \leq r \leq 1$	used	TT	0.95	0.45	0.17	0.98	-0.07 ± 0.28	-0.39 ± 0.20
$r = 0.01$	used	TT	1.13	0.34	0.09	0.997	0.01 ± 0.24	-0.23 ± 0.12
$r = 0.01$	not used	TT	0.89	0.49	0.36	0.90	0.10 ± 0.24	-0.23 ± 0.12
$r = 0.1$	used	TT	1.70	0.13	0.12	0.994	-0.04 ± 0.26	-0.28 ± 0.13
$r = 0.1$	not used	TT	1.46	0.20	0.38	0.89	0.05 ± 0.27	-0.28 ± 0.13
$r = 0.1$	used	TT, TE, EE	1.71	0.13	0.17	0.985	-0.02 ± 0.25	-0.30 ± 0.12
$r = 0.1$	used	TE, EE	1.72	0.13	0.38	0.89	0.06 ± 0.25	-0.32 ± 0.15
$r = 0.1$	used	TE	1.80	0.11	0.26	0.95	-0.02 ± 0.27	-0.17 ± 0.16
$r = 0.1$	used	EE	1.78	0.11	0.18	0.98	0.09 ± 0.25	-0.39 ± 0.16
$r = 0.1$	used	TT+lensing	1.54	0.17	0.05	0.9995	0.05 ± 0.25	-0.27 ± 0.13

Notes. Low- z data refers to BAO+SN+HST+ $z_{\text{re}} > 6$ prior. In all cases lowP data are used.

We have shown that the cubic spline reconstruction studied in this section consistently produces a dip in q_4 , corresponding to $k \approx 1.5 \times 10^{-3} \text{ Mpc}^{-1}$. We now turn to the question of whether this result is real or simply the result of cosmic variance. To assess the statistical significance of the departures of the mean reconstruction from a simple power law, we calculate the low- k and high- k reduced χ^2 for the five q_b values for scales below and six q_b values ($b \neq p$) for scales above $50/D_{\text{rec}}$, respectively, indicating the corresponding p -values (i.e., probability to exceed), for various data combinations, in Table 11. The high- k fit is better than expected for reasons that we do not understand, but we attribute this situation to chance. The low- k region shows a poor fit, but in no case does the p -value fall below 10%. Therefore, even though the low- k dip is robust against the various choices made for the reconstruction, we conclude that it is not statistically significant. The plot for the knot position of the dip (corresponding to q_4) in Fig. 30 does not contradict this conclusion.

Because of the r degeneracy associated with the scalar power, it is best when quoting statistics to use the fixed r cases, although for completeness we show the floating r case as well. There is also a smaller effect associated with the τ degeneracy, and the values quoted have restricted the redshift of reionization to exceed 6. The value $z_{\text{re}} = 6.5$ was used in Planck Collaboration XIII (2016). The significance of the low- k anomaly is meaningful only if an explicit r prior and low-redshift constraint on τ have been applied.

Finally, we relate the reconstructed $\mathcal{P}_{\mathcal{R}}(k)$ calculated above to the trajectories of the slow-roll parameter $\epsilon = -\dot{H}/H^2|_{k=aH}$ plotted as a function of k (see Fig. 31). We also plot in Fig. 32 the reconstructed inflationary potential in the region over which the inflationary potential is constrained by the data. Here canonical single-field inflation is assumed, and the value of r enters solely to fix the height of the potential at the pivot scale. This is not entirely self-consistent, but justified by the lack of constraining power on the tensors at present.

8.4. Power spectrum reconstruction summary

The three non-parametric methods for reconstructing the primordial power spectrum explored here support the following two conclusions:

1. Except possibly at low k , over the range of k where the CMB data best constrain the form of the primordial power spectrum, none of the three methods finds any statistically significant evidence for deviations from a simple power-law

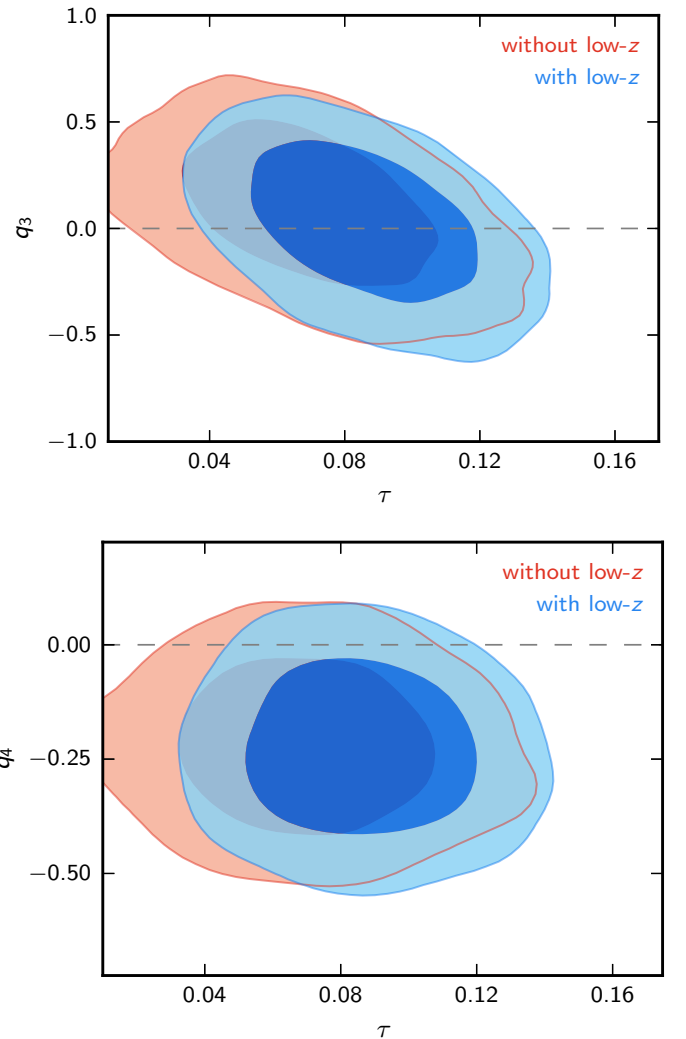


Fig. 30. The degeneracy between τ and the knot variables q_3 and q_4 in the 12-knot case shown in Fig. 27.

form. The fluctuations seen in this regime are entirely consistent with the expectations from cosmic variance and noise.

2. At low k , all three methods reconstruct a power deficit at $k \approx 1.5\text{--}2.0 \times 10^{-3} \text{ Mpc}^{-1}$, which can be linked to the dip in the TT angular power spectrum at $\ell \approx 20\text{--}30$. This

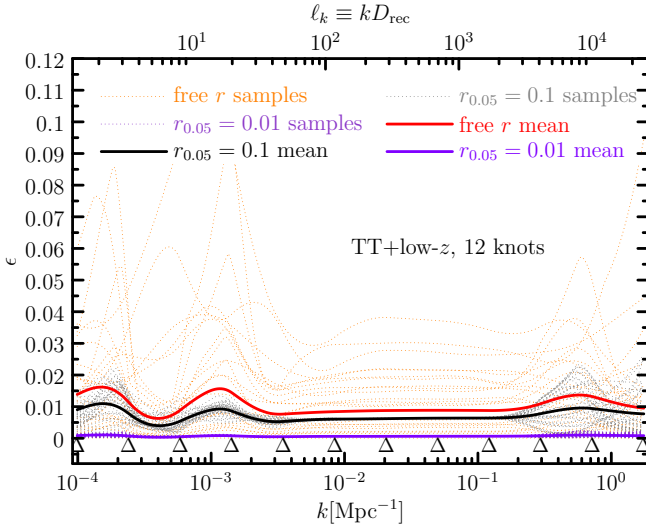


Fig. 31. Slow-roll parameter ϵ for reconstructed trajectories using 12 knots (marked as Δ at the bottom of the figure) with cubic spline interpolation. The mean values are shown for floating r and r fixed to be 0.1 and 0.01. Sample 1σ trajectories shown for the floating r case show wide variability, which is significantly diminished if r is fixed to $r = 0.1$, as shown.

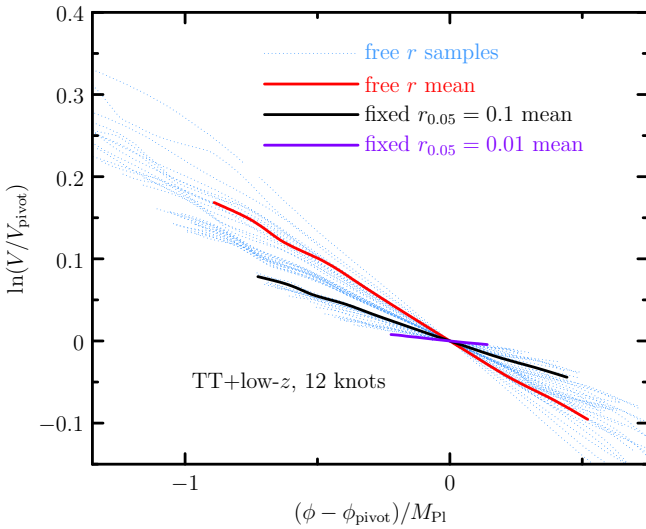


Fig. 32. Reconstructed single-field inflaton potentials from the cubic spline power spectra mode expansion using 12 knots.

agreement suggests that the reconstruction of this “anomaly” is not an artefact of any of the methods, but rather inherent in the CMB data themselves. However, the evidence for this feature is marginal since it is in a region of the spectrum where the fluctuations from cosmic variance are large.

3. We have verified that the power deficit at $\ell = 20\text{--}30$ is not substantially modified (a) by removing from the CMB pattern the hottest and coldest peaks selected by the Kolmogorov-Smirnov test studied in Sects. 4.5.3 and 4.5.4 of Planck Collaboration XVI (2016) or (b) by substituting the anomalously cold region around the Cold Spot with Gaussian constrained realizations.

9. Search for parameterized features

In this section, we explore the possibility of a radical departure from the near-scale-invariant power-law spectrum

$\mathcal{P}_{\mathcal{R}}^0(k) = A_s(k/k_*)^{n_s-1}$ of the standard slow-roll scenario for a selection of theoretically motivated parameterizations of the spectrum (see Chluba et al. 2015 for a recent review).

9.1. Models

9.1.1. Step in the inflaton potential

A sudden, step-like feature in the inflaton potential (Adams et al. 2001) or the sound speed (Achúcarro et al. 2011) leads to a localized oscillatory burst in the scalar primordial power spectrum. A general parameterization describing both a tanh-step in the potential and in the warp term of a DBI model was proposed in Miranda & Hu (2014):

$$\ln \mathcal{P}_{\mathcal{R}}^s(k) = \exp \left[\ln \mathcal{P}_{\mathcal{R}}^0(k) + \mathcal{I}_0(k) + \ln \left(1 + \mathcal{I}_1^2(k) \right) \right], \quad (71)$$

where the first- and second-order terms are given by

$$\mathcal{I}_0 = \left[\mathcal{A}_s \mathcal{W}_1^{(0)}(k/k_s) + \mathcal{A}_2 \mathcal{W}_2^{(0)}(k/k_s) + \mathcal{A}_3 \mathcal{W}_3^{(0)}(k/k_s) \right] \mathcal{D} \left(\frac{k/k_s}{x_s} \right), \quad (72)$$

$$\mathcal{I}_1 = \frac{1}{\sqrt{2}} \left\{ \frac{\pi}{2} (1 - n_s) + \left[\mathcal{A}_s \mathcal{W}_1^{(1)}(k/k_s) + \mathcal{A}_2 \mathcal{W}_2^{(1)}(k/k_s) + \mathcal{A}_3 \mathcal{W}_3^{(1)}(k/k_s) \right] \mathcal{D} \left(\frac{k/k_s}{x_s} \right) \right\}, \quad (73)$$

with window functions

$$\mathcal{W}_1^{(0)}(x) = \frac{1}{2x^3} \left[(18x - 6x^3) \cos 2x + (15x^2 - 9) \sin 2x \right], \quad (74)$$

$$\mathcal{W}_2^{(0)}(x) = \frac{3}{2x^3} \left[\sin(2x) - 2x \cos(2x) - x^2 \sin(2x) \right], \quad (75)$$

$$\mathcal{W}_3^{(0)}(x) = \frac{1}{x^3} \left[6x \cos(2x) + (4x^2 - 3) \sin(2x) \right], \quad (76)$$

$$\mathcal{W}_1^{(1)}(x) = -\frac{1}{x^3} \left\{ 3(x \cos x - \sin x) \left[3x \cos x + (2x^2 - 3) \sin x \right] \right\}, \quad (77)$$

$$\mathcal{W}_2^{(1)}(x) = \frac{3}{x^3} (\sin x - x \cos x)^2, \quad (78)$$

$$\mathcal{W}_3^{(1)}(x) = -\frac{1}{x^3} \left[3 + 2x^2 - (3 - 4x^2) \cos(2x) - 6x \sin(2x) \right], \quad (79)$$

and damping function

$$\mathcal{D}(x) = \frac{x}{\sinh x}. \quad (80)$$

Due to the high complexity of this model, we focus on the limiting case of a step in the potential ($\mathcal{A}_2 = \mathcal{A}_3 = 0$).

9.1.2. Logarithmic oscillations

Logarithmic modulations of the primordial power spectrum generically appear, for example, in models with non-Bunch-Davies initial conditions (Martin & Brandenberger 2001; Danielsson 2002; Bozza et al. 2003), or, approximately, in the axion monodromy model, explored in more detail in Sect. 10. We assume a constant modulation amplitude and use

$$\mathcal{P}_{\mathcal{R}}^{\log}(k) = \mathcal{P}_{\mathcal{R}}^0(k) \left\{ 1 + \mathcal{A}_{\log} \cos \left[\omega_{\log} \ln \left(\frac{k}{k_*} \right) + \varphi_{\log} \right] \right\}. \quad (81)$$

Table 12. Parameters and prior ranges.

Model	Parameter	Prior range
Step	\mathcal{A}_s	[0, 2]
	$\log_{10}(k_s/\text{Mpc}^{-1})$	[-5, 0]
	$\ln x_s$	[-1, 5]
Log osc.	\mathcal{A}_{log}	[0, 0.5]
	$\log_{10} \omega_{\text{log}}$	[0, 2.1]
	φ_{log}	[0, 2π]
Linear osc.	\mathcal{A}_{lin}	[0, 0.5]
	$\log_{10} \omega_{\text{lin}}$	[0, 2]
	n_{lin}	[-1, 1]
	φ_{lin}	[0, 2π]
Cutoff	$\log_{10}(k_c/\text{Mpc}^{-1})$	[-5, -2]

9.1.3. Linear oscillations

A modulation linear in k can be obtained, for example, in boundary effective field theory models (Jackson & Shiu 2013), and is typically accompanied by a scale-dependent modulation amplitude. We adopt the parameterization used in Meerborg & Spergel (2014), which allows for a strong scale dependence of the modulation amplitude:

$$\mathcal{P}_{\mathcal{R}}^{\text{lin}}(k) = \mathcal{P}_{\mathcal{R}}^0(k) \left[1 + \mathcal{A}_{\text{lin}} \left(\frac{k}{k_*} \right)^{n_{\text{lin}}} \cos \left(\omega_{\text{lin}} \frac{k}{k_*} + \varphi_{\text{lin}} \right) \right]. \quad (82)$$

9.1.4. Cutoff model

If today's largest observable scales exited the Hubble radius before the inflaton field reached the slow-roll attractor, the amplitude of the primordial power spectrum is typically strongly suppressed at low k . As an example of such a model, we consider a scenario in which slow roll is preceded by a stage of kinetic energy domination. The resulting power spectrum was derived by Contaldi et al. (2003) and can be expressed as

$$\ln \mathcal{P}_{\mathcal{R}}^c(k) = \ln \mathcal{P}_{\mathcal{R}}^0(k) + \ln \left(\frac{\pi}{16} \frac{k}{k_c} |C_c - D_c|^2 \right), \quad (83)$$

with

$$C_c = \exp \left(\frac{-ik}{k_c} \right) \left[H_0^{(2)} \left(\frac{k}{2k_c} \right) - \left(\frac{k_c}{k} + i \right) H_1^{(2)} \left(\frac{k}{2k_c} \right) \right], \quad (84)$$

$$D_c = \exp \left(\frac{ik}{k_c} \right) \left[H_0^{(2)} \left(\frac{k}{2k_c} \right) - \left(\frac{k_c}{k} - i \right) H_1^{(2)} \left(\frac{k}{2k_c} \right) \right], \quad (85)$$

where $H_n^{(2)}$ denotes the Hankel function of the second kind. The power spectrum in this model is exponentially suppressed for wavenumbers smaller than the cutoff scale k_c and converges to a standard power-law spectrum for $k \gg k_c$, with an oscillatory transition region for $k \gtrsim k_c$.

9.2. Analysis and results

We use MultiNest to evaluate the Bayesian evidence for the models, establish parameter constraints, and roughly identify the global maximum likelihood region of parameter space. The features model best-fit parameters and $\ln \mathcal{L}$ are then obtained with the help of the CosmoMC minimization algorithm taking narrow priors around the MultiNest best fit. We assign flat prior probabilities to the parameters of the features models with prior ranges

Table 13. Improvement in fit and Bayes factors with respect to power-law base Λ CDM for *Planck* TT+lowP and *Planck* TT, TE, EE+lowP data, as well as approximate probability to exceed the observed $\Delta\chi^2$ (p -value), constructed from simulated *Planck* TT+lowP data.

Model	<i>Planck</i> TT+lowP $\Delta\chi^2$	<i>Planck</i> TT, TE, EE+lowP $\ln B$	$\Delta\chi^2$	$\ln B$	PTE
Step	-8.6	-0.3	-7.3	-0.6	0.09
Log osc.	-10.6	-1.9	-10.1	-1.5	0.24
Linear osc.	-8.9	-1.9	-10.9	-1.3	0.50
Cutoff	-2.0	-0.4	-2.2	-0.6	0.12

Notes. Negative Bayes factors indicate a preference for the power-law model.

listed in Table 12. Note that throughout this section for the sake of maximizing sensitivity to very sharp features, the unbinned (“bin1”) versions of the high- ℓ TT and TT, TE, EE likelihoods are used instead of the standard binned versions.

Since the features considered here can lead to broad distortions of the CMB angular power spectrum degenerate with the late time cosmological parameters (Miranda & Hu 2014), in all cases we simultaneously vary primordial parameters and all the Λ CDM parameters, but keep the foreground parameters fixed to their best-fit values for the power-law base Λ CDM model.

We present the Bayes factors with respect to the power-law base Λ CDM model and the improvement in the effective χ^2 over the power-law model in Table 13. For our choice of priors, none of the features models is preferred over a power-law spectrum. The best-fit power spectra are plotted in Fig. 33. While the cutoff and step model best fits reproduce the large-scale suppression at $\ell \approx 20$ –30 also obtained by direct power spectrum reconstruction in Sect. 8, the oscillation models prefer relatively high frequencies beyond the resolution of the reconstruction methods.

In addition to the four features models we also show in Fig. 33 the best fit of a model allowing for steps in both inflaton potential and warp (brown line). Note the strong resemblance to the reconstructed features of the previous section. The effective $\Delta\chi^2$ for this model is -12.1 (-11.5) for *Planck* TT+lowP (*Planck* TT, TE, EE+lowP) data at the cost of adding five new parameters, resulting in a \ln -Bayes factor of -0.8 (-0.4). A similar phenomenology can be also be found for a model with a sudden change in the slope of the inflaton potential (Starobinsky 1992; Choe et al. 2004), which yields a best-fit $\Delta\chi^2 = -4.5$ (-4.9) for two extra parameters.

As shown in Table 14, constraints on the remaining cosmological parameters are not significantly affected when allowing for the presence of features.

For the cutoff and step models, the inclusion of *Planck* small-scale polarization data does not add much in terms of direct sensitivity. The best fits lie in the same parameter region as for *Planck* TT+lowP data, and the $\Delta\chi^2$ and Bayes factors are not subject to major changes. The two oscillation models' *Planck* TT+lowP best fits, on the other hand, also predict a non-negligible signature in the polarization spectra at high ℓ . Therefore, if the features were real, one would expect an additional improvement in $\Delta\chi^2$ for *Planck* TT, TE, EE+lowP. This is not the case here. Though the linear oscillation model's maximum $\Delta\chi^2$ does increase, the local $\Delta\chi^2$ in the *Planck* TT+lowP best-fit regions is in fact reduced for both models, and the global likelihood maxima occur at different frequencies ($\log_{10} \omega_{\text{log}} = 1.25$ and $\log_{10} \omega_{\text{lin}} = 1.02$) compared to their *Planck* TT+lowP counterparts.

Table 14. Best-fit features parameters and parameter constraints on the remaining cosmological parameters for the four features models for *Planck* TT+lowP data.

Parameter	Step	Log osc.	Linear osc.	Cutoff	Power law
100 ω_b	2.23 ± 0.02	2.22 ± 0.02	2.23 ± 0.02	2.23 ± 0.02	2.23 ± 0.02
10 ω_c	1.20 ± 0.02	1.20 ± 0.02	1.20 ± 0.02	1.19 ± 0.02	1.19 ± 0.02
100 θ_{MC}	1.0409 ± 0.0004	1.0409 ± 0.0004	1.0409 ± 0.0004	1.0410 ± 0.0005	1.0409 ± 0.0005
τ	0.083 ± 0.015	0.082 ± 0.015	0.084 ± 0.014	0.086 ± 0.017	0.085 ± 0.016
$\ln(10^{10} A_s)$	3.10 ± 0.03	3.10 ± 0.03	3.10 ± 0.03	3.11 ± 0.03	3.10 ± 0.03
n_s	0.966 ± 0.005	0.970 ± 0.007	0.967 ± 0.004	0.968 ± 0.005	0.968 ± 0.005
\mathcal{A}_s	0.374
$\log_{10}(k_s/\text{Mpc}^{-1})$	-3.10
$\ln x_s$	0.342
\mathcal{A}_{\log}	...	0.0278
$\log_{10} \omega_{\log}$...	1.51
$\varphi_{\log}/2\pi$...	0.634
\mathcal{A}_{lin}	0.0292
$\log_{10} \omega_{\text{lin}}$	1.73
n_{lin}	0.662
$\varphi_{\text{lin}}/2\pi$	0.554
$\log_{10}(k_c/\text{Mpc}^{-1})$	-3.44	...

Notes. The foreground parameters have been fixed to their power-law base Λ CDM best-fit values.

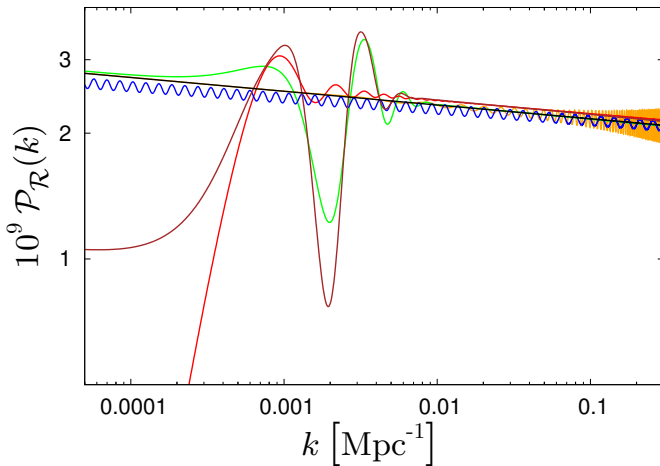


Fig. 33. Best-fit power spectra for the power-law (black curve), step (green), logarithmic oscillation (blue), linear oscillation (orange), and cutoff (red) models using *Planck* TT+lowP data. The brown curve is the best fit for a model with a step in the warp and potential (Eqs. (71)–(80)).

In addition to the Bayesian model comparison analysis, we also approach the matter of the statistical relevance of the features models from a frequentist statistics perspective in order to give the $\Delta\chi^2$ numbers a quantitative interpretation. Assuming that the underlying $\mathcal{P}_{\mathcal{R}}(k)$ was actually a featureless power law, we can ask how large an improvement to $\ln \mathcal{L}$ the different features models would yield on average just by overfitting scatter from cosmic variance and noise. For this purpose, we simulate *Planck* power spectrum data sets consisting of temperature and polarization up to $\ell = 29$ and unbinned temperature for $30 \leq \ell \leq 2508$, taking as input fiducial spectra the power-law base Λ CDM model's best-fit spectra.

For each of these simulated *Planck* data sets, we perform the following procedure: (i) find the power-law Λ CDM model's best-fit parameters with CosmoMC's minimization algorithm;

(ii) fix the non-primordial parameters (ω_b , ω_c , θ_{MC} , τ) to their respective best-fit values; (iii) using MultiNest, find the best fit of the features models;⁹ and (iv) extract the effective $\Delta\chi^2$ between power-law and features models.

The resulting distributions are shown in Fig. 34. Compared to the real data $\Delta\chi^2$ values from Table 13, they are biased towards lower values, since we do not vary the late-time cosmological parameters in the analysis of the simulated data. Nonetheless, the observed improvements in the fit do not appear to be extraordinarily large, with the respective (conservative) p -values ranging between 0.09 and 0.50.

These observations lead to the conclusion that even though some of the peculiarities seen in the residuals of the *Planck* data with respect to a power-law primordial spectrum may be explained in terms of primordial features, none of the simple model templates considered here is required by *Planck* data. The simplicity of the power-law spectrum continues to give it an edge over more complicated initial spectra and the most plausible explanation for the apparent features in the data remains that we are just observing fluctuations due to cosmic variance at large scales and noise at small scales.

10. Implications of *Planck* bispectral constraints on inflationary models

The combination of power spectrum constraints and primordial non-Gaussianity (NG) constraints, such as the *Planck* upper bound on the NG amplitude f_{NL} (Planck Collaboration XVII 2016), can be exploited to limit extensions to the simplest standard single-field models of slow-roll inflation. The next subsection considers inflationary models with a non-standard kinetic term (Garriga & Mukhanov 1999), where the inflaton Lagrangian is a general function of the scalar inflaton field and its first derivative, i.e., $\mathcal{L} = P(\phi, X)$, where $X = -g^{\mu\nu}\partial_\mu\phi\partial_\nu\phi/2$

⁹ Due to the multimodal nature of the posterior, usual minimization routines perform poorly here.

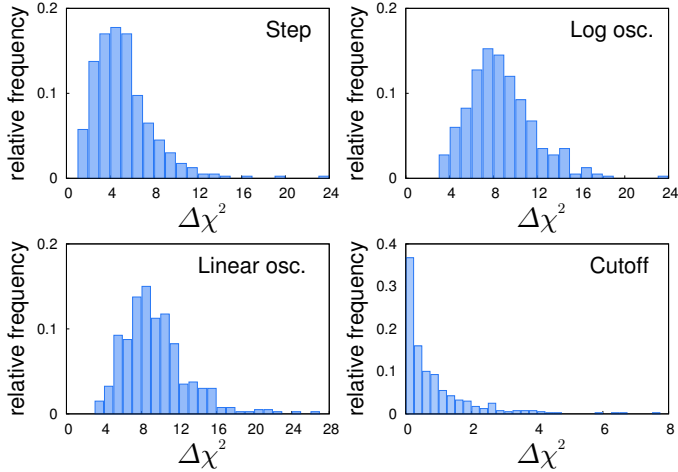


Fig. 34. Distribution of $\Delta\chi^2$ from 400 simulated *Planck* TT+lowP data sets.

(Garriga & Mukhanov 1999; Chen et al. 2007). Section 10.2 focuses on a specific example of a single-field model of inflation with more general higher-derivative operators, the so-called “Galileon inflation”. Section 10.3 presents constraints on axion monodromy inflation. See Planck Collaboration XVII (2016) for the analysis of other interesting non-standard inflationary models, including warm inflation (Berera 1995), whose f_{NL} predictions can be constrained by *Planck*.

10.1. Inflation with a non-standard kinetic term

This class of models includes k -inflation (Armendáriz-Picón 1999; Garriga & Mukhanov 1999) and Dirac-Born-Infeld (DBI) models introduced in the context of brane inflation (Silverstein & Tong 2004; Alishahiha et al. 2004; Chen 2005b,a). In these models inflation can take place despite a steep potential or may be driven by the kinetic term.

Moreover, one of the main predictions of inflationary models with a non-standard kinetic term is that the inflaton perturbations can propagate with a sound speed $c_s < 1$. We show how the *Planck* combined measurement of the power spectrum and the nonlinearity parameter f_{NL} (Planck Collaboration XVII 2016) improves constraints on this class of models by breaking degeneracies between the parameters determining the observable power spectra. Such degeneracies (see, e.g., Peiris et al. 2007; Powell et al. 2009; Lorenz et al. 2008; Agarwal & Bean 2009; Baumann et al. 2015) are evident from the expressions for the power spectra. We adopt the same notation as Planck Collaboration XXIV (2014). At leading order in the slow-roll parameters the scalar power spectrum depends additionally on the sound speed c_s via (Garriga & Mukhanov 1999)

$$A_s \approx \frac{1}{8\pi^2 M_{\text{pl}}^2} \frac{H^2}{c_s \epsilon_1}, \quad (86)$$

which is evaluated at $kc_s = aH$. Correspondingly, the scalar spectral index

$$n_s - 1 = -2\epsilon_1 - \epsilon_2 - s \quad (87)$$

depends on an additional slow-roll parameter $s = \dot{c}_s/(c_s H)$, which describes the running of the sound speed. The usual consistency relation holding for the standard single-field models of

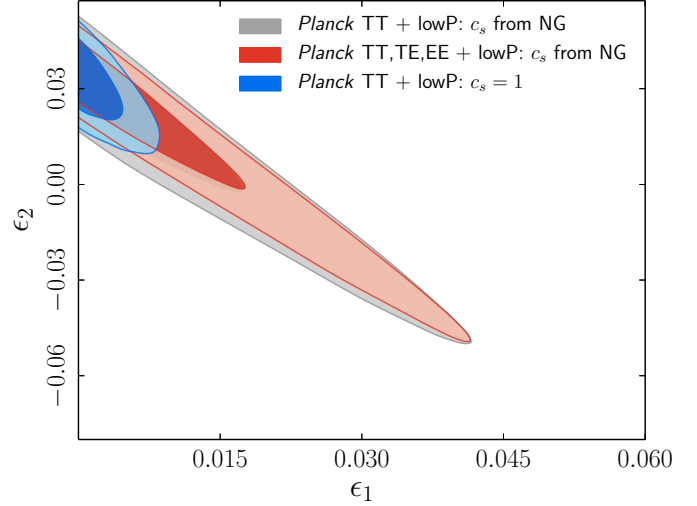


Fig. 35. (ϵ_1, ϵ_2) 68% and 95% CL constraints for *Planck* data comparing the canonical Lagrangian case with $c_s = 1$ to the case of varying c_s with a uniform prior $0.024 < c_s < 1$ derived from the *Planck* NG measurements.

slow-roll inflation ($r = -8n_t$) is modified to $r \approx -8n_t c_s$, with $n_t = -2\epsilon_1$ as usual (Garriga & Mukhanov 1999), potentially allowing models which otherwise would predict a large tensor-to-scalar ratio for the Klein-Gordon case (Unnikrishnan et al. 2012).¹⁰

At lowest order in the slow-roll parameters, there are strong degeneracies between the parameters $(A_s, c_s, \epsilon_1, \epsilon_2, s)$. This makes the constraints on these parameters from the power spectrum alone not very stringent, and for parameters like ϵ_1 and ϵ_2 less stringent compared with the standard case. However, combining the constraints on the power spectra observables with those on f_{NL} can also result in a stringent test for this class of inflationary models. Models where the inflaton field has a non-standard kinetic term predict a high level of primordial NG of the scalar perturbations for $c_s \ll 1$, (see, e.g., Chen et al. 2007). Primordial NG is generated by the higher-derivative interaction terms arising from the expansion of the kinetic part of the Lagrangian, $P(\phi, X)$. There are two main contributions to the amplitude of the NG (i.e., to the nonlinearity parameter f_{NL}), coming from the inflaton field interaction terms $\delta\phi(\nabla\delta\phi)^2$ and $(\delta\phi)^3$ (Chen et al. 2007; Senatore et al. 2010). The NG from the first term scales as c_s^{-2} , while the NG arising from the other term is determined by a second parameter, \tilde{c}_3 (following the notation of Senatore et al. 2010). Each of these two interactions produces bispectrum shapes similar to the so-called *equilateral* shape (Babich et al. 2004) for which the signal peaks for equilateral triangles with $k_1 = k_2 = k_3$. (These two shapes are called, respectively, “EFT1” and “EFT2” in Planck Collaboration XVII 2016). However, the difference between the two shapes is such that the total signal is a linear combination of the two, leading to an “orthogonal” bispectral template (Senatore et al. 2010).

The equilateral and orthogonal NG amplitudes can be expressed in terms of the two “microscopic” parameters, c_s and \tilde{c}_3

¹⁰ We use the more accurate relation

$$r = 16\epsilon_1 c_s^{(1+\epsilon_1)/(1-\epsilon_1)}, \quad (88)$$

accounting for different epochs of freeze-out for the scalar fluctuations (at sound horizon crossing, $kc_s = aH$) and tensor perturbations (at Hubble radius crossing, $k = aH$; Peiris et al. 2007; Powell et al. 2009; Lorenz et al. 2008; Agarwal & Bean 2009; Baumann et al. 2015).

(for more details see [Planck Collaboration XVII 2016](#)), according to

$$f_{\text{NL}}^{\text{equil}} = \frac{1 - c_s^2}{c_s^2} \left[-0.275 - 0.0780c_s^2 - (2/3) \times 0.780\tilde{c}_3 \right], \quad (89)$$

$$f_{\text{NL}}^{\text{ortho}} = \frac{1 - c_s^2}{c_s^2} \left[0.0159 - 0.0167c_s^2 - (2/3) \times 0.0167\tilde{c}_3 \right]. \quad (90)$$

Thus the measurements of $f_{\text{NL}}^{\text{equil}}$ and $f_{\text{NL}}^{\text{ortho}}$ obtained in the companion paper ([Planck Collaboration XVII 2016](#)) provide a constraint on the sound speed, c_s , of the inflaton field. Such constraints allow us to combine the NG information with the analyses of the power spectra, since the sound speed is the NG parameter also affecting the power spectra.

In this subsection we consider three cases. In the first case we perform a general analysis as described above (focusing on the simplest case of a constant sound speed, $s = 0$), improving on [PCI13](#) and [Planck Collaboration XXIV \(2014\)](#) by exploiting the full mission temperature and polarization data. The *Planck* constraints on primordial NG in general single-field models of inflation provide the most stringent bound on the inflaton sound speed ([Planck Collaboration XVII 2016](#)):¹¹

$$c_s \geq 0.024 \quad (95\% \text{ CL}). \quad (91)$$

We then use this information on c_s as a uniform prior $0.024 \leq c_s \leq 1$ in Eq. (88) within the HFF formalism, as in [PCI13](#). Figure 35 shows the joint constraints on ϵ_1 and ϵ_2 . *Planck* TT+lowP yields $\epsilon_1 < 0.031$ at 95% CL. No improvement in the upper bound on ϵ_1 results when using *Planck* TT, TE, EE+lowP. This constraint improves the previous analysis in [PCI13](#) and can be compared with the restricted case of $c_s = 1$, also shown in Fig. 35, with $\epsilon_1 < 0.0068$ at 95% CL. The limits on the sound speed from the constraints on primordial NG are crucial for deriving an upper limit on ϵ_1 , because the relation between the tensor-to-scalar ratio and ϵ_1 also involves the sound speed (see, e.g., Eq. (88)). This breaks the degeneracy in the scalar spectral index.

The other two cases analysed involve DBI models. The degeneracy between the different slow-roll parameters can be broken for $s = 0$ or in the case where $s \propto \epsilon_2$. We first consider models defined by an action of the DBI form

$$P(\phi, X) = -f(\phi)^{-1} \sqrt{1 - 2f(\phi)\dot{X}} + f(\phi)^{-1} - V(\phi), \quad (92)$$

where $V(\phi)$ is the potential and $f(\phi)$ describes the warp factor determined by the geometry of the extra dimensions. We follow an analogous procedure to exploit the NG limits derived in [Planck Collaboration XVII \(2016\)](#) on c_s in the case of DBI models: $c_s \geq 0.087$ (at 95% CL). Assuming a uniform prior, $0.087 \leq c_s \leq 1$, and $s = 0$, *Planck* TT+lowP gives $\epsilon_1 < 0.024$ at 95% CL, a 43% improvement with respect to [PCI13](#). The addition of high- ℓ TE and EE does not improve the upper bound on ϵ_1 for this DBI case.

Next we update the constraints on the particularly interesting case of infrared DBI models ([Chen 2005b,a](#)), where $f(\phi) \approx \lambda/\phi^4$. (For details, see [Silverstein & Tong 2004](#); [Alishahiha et al. 2004](#); [Chen et al. 2007](#), and references therein.)

¹¹ This section uses results based on f_{NL} constraints from T and E ([Planck Collaboration XVII 2016](#)). In [Planck Collaboration XVII \(2016\)](#) it is shown that, although conservatively considered as preliminary, the f_{NL} constraints from T and E are robust, since they pass an extensive battery of validation tests and are in full agreement with T-only constraints.

In these models the inflaton field moves from the IR to the UV side with an inflaton potential

$$V(\phi) = V_0 - \frac{1}{2}\beta H^2 \phi^2. \quad (93)$$

From a theoretical point of view a wide range of values for β is allowed: $0.1 < \beta < 10^9$ ([Bean et al. 2008](#)). [PCI13](#) dramatically restricted the allowed parameter space of these models in the limit where stringy effects can be neglected and the usual field theory computation of the primordial curvature perturbation holds (see [Chen 2005a,c](#); [Bean et al. 2008](#) for more details). In this limit of the IR DBI model, one finds ([Chen 2005c](#); [Chen et al. 2007](#)) $c_s \approx (\beta N_*/3)^{-1}$, $n_s - 1 = -4/N_*$, and $dn_s/d\ln k = -4/N_*$. (In this model one can verify that $s \approx 1/N_* \approx \epsilon_2/3$.) Combining the uniform prior on c_s with *Planck* TT+lowP, we obtain

$$\beta \leq 0.31 \quad (95\% \text{ CL}), \quad (94)$$

and a preference for a high number of e -folds: $78 < N_* < 157$ at 95% CL.

We now constrain the general case of the IR DBI model, including the “stringy” regime, which occurs when the inflaton extends back in time towards the IR side ([Bean et al. 2008](#)). The stringy phase transition is characterized by an interesting phenomenology altering the predictions for cosmological perturbations. A parameterization of the power spectrum of curvature perturbations interpolating between the two regimes is ([Bean et al. 2008](#); see also [Ma et al. 2013](#))

$$\mathcal{P}_{\mathcal{R}}(k) = \frac{A_s}{(N_e^{\text{DBI}})^4} \left[1 - \frac{1}{(1+x)^2} \right], \quad (95)$$

where $A_s = 324\pi^2/(n_B\beta^4)$ is the amplitude of the perturbations which depends on various microscopic parameters (n_B is the number of branes at the B-throat; see [Bean et al. 2008](#) for more details), while $x = (N_e^{\text{DBI}}/N_c)^8$ sets the stringy phase transition taking place at the critical e -fold N_c . (Here N_e^{DBI} is the number of e -folds to the end of IR DBI inflation.) The spectral index and its running are

$$n_s - 1 = \frac{4}{N_e^{\text{DBI}}} \frac{x^2 + 3x - 2}{(x+1)(x+2)}, \quad (96)$$

$$\frac{dn_s}{d\ln k} = \frac{4}{(N_e^{\text{DBI}})^2} \frac{x^4 + 6x^3 - 55x^2 - 96x - 4}{(x+1)^2(x+2)^2}. \quad (97)$$

A prediction for the primordial NG in the stringy regime is not available. We assume the standard field-theoretic result for a primordial bispectrum of the equilateral type with an amplitude $f_{\text{NL}}^{\text{DBI}} = -(35/108)[(\beta^2(N_e^{\text{DBI}})^2/9) - 1]$. By considering the same uniform prior on c_s , we obtain $\beta < 0.77$, $66 < N_e^{\text{DBI}} < 72$, and $x < 0.41$ at 95% CL, which severely limits the general IR DBI model and strongly restricts the allowed parameter space.

10.2. Galileon inflation

As a further example of the implications of the NG constraints on (non-standard) inflationary models we consider Galileon inflation [Burrage et al. \(2011](#); see also [Kobayashi et al. 2010](#); [Mizuno & Koyama 2010](#); [Ohashi & Tsujikawa 2012](#)). This represents a well-defined and well-motivated model of inflation with more general higher derivatives of the inflaton field compared to the

non-standard kinetic term case analysed above. The Galileon models of inflation are based on the so-called “Galilean symmetry” (Nicolis et al. 2009), and enjoy some well understood stability properties (absence of ghost instabilities and protection from large quantum corrections). This makes the theory also very predictive, since observable quantities (scalar and tensor power spectra and higher-order correlators) depend on a finite number of parameters. From this point of view this class of models shares some of the same properties as the DBI inflationary models (Silverstein & Tong 2004; Alishahiha et al. 2004). The Galileon field arises naturally within fundamental physics constructions (e.g., de Rham & Gabadadze 2010b,a). These models also offer an interesting example of large-scale modifications to Einstein gravity.

The Galileon model is based on the action (Deffayet et al. 2009a,b)

$$S = \int d^4x \sqrt{-g} \left(\frac{M_{\text{pl}}^2}{2} R + \sum_{n=0}^3 \mathcal{L}_n \right), \quad (98)$$

where

$$\mathcal{L}_0 = c_2 X, \quad (99)$$

$$\mathcal{L}_1 = -2(c_3/\Lambda^3) X \Box \phi, \quad (100)$$

$$\mathcal{L}_2 = 2(c_4/\Lambda^6) X \left[(\Box \phi)^2 - (\nabla_\mu \nabla_\nu \phi)^2 \right] + (c_4/\Lambda^6) X^2 R, \quad (101)$$

$$\mathcal{L}_3 = -2(c_5/\Lambda^9) X \left[(\Box \phi)^3 - 3\Box \phi (\nabla_\mu \nabla_\nu \phi)^2 + 2(\nabla_\mu \nabla_\nu \phi)^3 \right] + 6(c_5/\Lambda^9) X^2 G_{\mu\nu} \nabla^\mu \nabla^\nu \phi. \quad (102)$$

Here $X = -\nabla_\mu \phi \nabla^\mu \phi / 2$, $(\nabla_\mu \nabla_\nu \phi)^2 = \nabla_\mu \nabla_\nu \phi \nabla^\mu \nabla^\nu \phi$, and $(\nabla_\mu \nabla_\nu \phi)^3 = \nabla_\mu \nabla_\nu \phi \nabla^\mu \nabla^\rho \phi \nabla^\rho \nabla_\nu \phi$. The coupling coefficients c_i are dimensionless and Λ is the cutoff of the theory. The case of interest includes a potential term $V(\phi) = V_0 + \lambda\phi + (1/2)m^2\phi^2 + \dots$ to drive inflation.

The predicted scalar power spectrum at leading order is (Ohashi & Tsujikawa 2012; Burrage et al. 2011; Tsujikawa et al. 2013; see also Kobayashi et al. 2011a; Gao & Steer 2011)¹²

$$\mathcal{P}_{\mathcal{R}} = \frac{H^2}{8\pi^2 M_{\text{pl}}^2 \epsilon_s F c_s} \Big|_{c_s k=aH} = \frac{H^4}{8\pi^2 A (\dot{\phi}_0)^2 c_s^3}, \quad (104)$$

where $F = 1 + \bar{c}_4 (\dot{\phi}_0)^2 / (2H^2 M_{\text{pl}}^2)$ and $c_s^2 = -B/A$ is the sound speed of the Galileon field. ϵ_s is different from the usual slow-roll parameter ϵ_1 and at leading order related according to $\epsilon_s = -2B/(1 + 6\bar{c}_3 + 18\bar{c}_4 + 30\bar{c}_5)\epsilon_1$. The scalar spectral index

$$n_s - 1 = -2\epsilon_1 - \eta_s - s \quad (105)$$

depends on the slow-roll parameters ϵ_1 , $\eta_s = \dot{\epsilon}_s/(H\epsilon_s)$, and $s = \dot{c}_s/(Hc_s)$. As usual the slow-roll parameter s describes the running of the sound speed. In the following we restrict ourselves to the case of a constant sound speed with $s = 0$. The tensor-to-scalar ratio is

$$r = 16\epsilon_s c_s = 16\epsilon_1 \bar{c}_s, \quad (106)$$

¹² For the following expressions it is convenient to define the quantities $A = c_2/2 + 6\bar{c}_3 + 27\bar{c}_4 + 60\bar{c}_5$, $B = -c_2/2 - 4\bar{c}_3 - 13\bar{c}_4 - 24\bar{c}_5$, (103)

where $\bar{c}_i = c_i Z^{i-2}$ for $i = 2$ to 5 , with $Z = H\dot{\phi}_0/\Lambda^3$. In order to have a viable model we require $A > 0$ (no ghosts) and $B < 0$ (no gradient instabilities).

where we have introduced the parameter $\bar{c}_s = -[2B/(1 + 6\bar{c}_3 + 18\bar{c}_4 + 30\bar{c}_5)]c_s$, which is related to the Galileon sound speed. The parameter \bar{c}_s can be either positive or negative. In the negative branch a blue spectral tilt for the primordial gravitational waves is allowed, contrary to the situation for standard slow-roll models of inflation. We introduce such a quantity so that the consistency relation takes the form $r \approx -8n_t \bar{c}_s$, with $n_t = -2\epsilon_1$, analogous to Eq. (88). The measurements of primordial NG constrain \bar{c}_s , which in turn constrains ϵ_1 and η_s in Eq. (105). This is analogous to the constraints on ϵ_1 and η of Eq. (87) in the previous subsection.

Galileon models of inflation predict interesting NG signatures (Burrage et al. 2011; Tsujikawa et al. 2013).¹³ We have verified (see also Creminelli et al. 2011) that bispectra can be generated with the same shapes as the “EFT1” and “EFT2” (Senatore et al. 2010; Chen et al. 2007) constrained in the companion paper (Planck Collaboration XVII 2016), which usually arise in models of inflation with non-standard kinetic terms, with

$$f_{\text{NL}}^{\text{EFT1}} = \frac{17}{972} \left(-\frac{5}{c_s^4} + \frac{30}{c_s^2} - \frac{40}{c_s \bar{c}_s} + 15 \right), \quad (107)$$

$$f_{\text{NL}}^{\text{EFT2}} = \frac{1}{243} \left(\frac{5}{c_s^4} + \frac{30/A - 55}{c_s^2} + \frac{40}{c_s \bar{c}_s} - 320 \frac{c_s}{\bar{c}_s} - \frac{30}{A} + 275 - 225c_s^2 + 280 \frac{c_s^3}{\bar{c}_s} \right). \quad (108)$$

As explained in the previous subsection, the linear combinations of these two bispectra produce both equilateral and orthogonal bispectrum templates. Given Eqs. (104)–(108), we can proceed as in the previous section to exploit the limits on primordial NG in a combined analysis with the power spectra analysis. In Planck Collaboration XVII (2016) the constraint $c_s \geq 0.23$ (95% CL) is obtained based on the constraints on $f_{\text{NL}}^{\text{equil}}$ and $f_{\text{NL}}^{\text{ortho}}$. One can proceed as described in Planck Collaboration XVII (2016) to constrain the parameter \bar{c}_s modifying the consistency relation, Eq. (106). Adopting a log-uniform prior on A in the interval $10^{-4} \leq A \leq 10^4$ and a uniform prior $10^{-4} \leq c_s \leq 1$, the Planck measurements on $f_{\text{NL}}^{\text{equil}}$ and $f_{\text{NL}}^{\text{ortho}}$ constrain \bar{c}_s to be $0.038 \leq \bar{c}_s \leq 100$ (95% CL) (Planck Collaboration XVII 2016). We also explore the possibility of the negative branch (corresponding to a blue tensor spectral index), finding $-100 \leq \bar{c}_s \leq -0.034$ (95% CL) (Planck Collaboration XVII 2016). By allowing a logarithmic prior on \bar{c}_s based on the f_{NL} measurements, Fig. 36 shows the joint constraints on ϵ_1 and η_s for the $n_t < 0$ branch and for the $n_t > 0$ branch. Planck TT+lowP+BAO and the NG bounds on \bar{c}_s constrain $\epsilon_1 < 0.036$ at 95% CL for $n_t < 0$ (and $|\epsilon_1| < 0.041$ for $n_t > 0$).

10.3. Axion monodromy inflation

10.3.1. Introduction

The mechanism of monodromy inflation (Silverstein & Westphal 2008; McAllister et al. 2010; Kaloper et al. 2011; Flauger et al. 2014b) in string theory motivates a broad class of inflationary potentials of the form

$$V(\phi) = \mu^{4-p} \phi^p + \Lambda_0^4 e^{-C_0 \left(\frac{\phi}{\phi_0} \right)^{p_\Lambda}} \cos \left[\gamma_0 + \frac{\phi_0}{f_0} \left(\frac{\phi}{\phi_0} \right)^{p_f+1} \right]. \quad (109)$$

¹³ See also Mizuno & Koyama (2010), Gao & Steer (2011), Kobayashi et al. (2011b), De Felice & Tsujikawa (2013), and Regan et al. (2015).

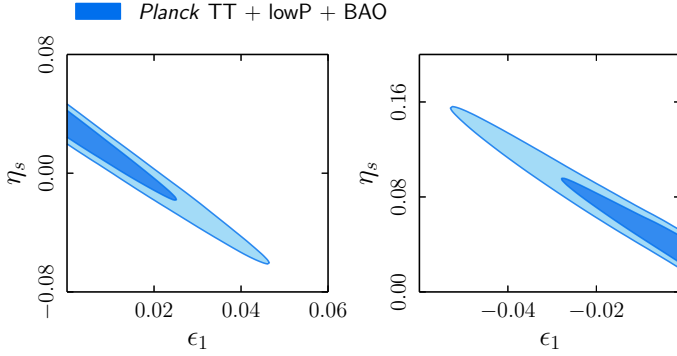


Fig. 36. Marginalized joint 68% and 95% CL for the Galileon parameters (ϵ_1, η_s) for $n_t < 0$ (left panel) and $n_t > 0$ (right panel).

Here μ , Λ_0 , f_0 , and ϕ_0 are constants with the dimension of mass and C_0 , p , p_Λ , p_f , and γ_0 are dimensionless.

In simpler parameterizations used in prior analyses of oscillations from axion monodromy inflation (Peiris et al. 2013; Planck Collaboration XXII 2014; Easther & Flauger 2014; Jackson et al. 2014; Meerburg et al. 2014b,a; Meerburg & Spergel 2014; Meerburg 2014), one assumes $p_\Lambda = p_f = 0$, corresponding to a sinusoidal term with constant amplitude throughout inflation taken to be a periodic function of the canonically-normalized inflaton ϕ . Taking $p_\Lambda \neq 0$ and $p_f \neq 0$ allows the magnitude and frequency, respectively, of the modulation to depend on ϕ . For example, the frequency is always a periodic function of an underlying angular axion field, but its relation to the canonically normalized inflaton field is model-dependent.

The microphysical motivation for $p_\Lambda \neq 0$ and $p_f \neq 0$ is that in string theory additional scalar fields, known as “moduli,” evolve during inflation. The inflationary potential depends on a subset of these fields. Because the magnitude and frequency of modulations are determined by the vacuum expectation values of moduli, both quantities are then naturally functions of ϕ . The case $p_\Lambda = p_f = 0$ corresponds to when these fields are approximately fixed, stabilized strongly by additional terms in the scalar potential. But in other cases, the axion potential that drives inflation also provides a leading term stabilizing the moduli. The exponential dependence of the magnitude in the potential of Eq. (109) arises because the modulations are generated non-perturbatively, e.g., by instantons. For this reason, the modulations can be undetectably small in this framework, although there are interesting regimes where they could be visible.

Specific examples studied thus far yield exponents p , p_Λ , and p_f that are rational numbers of modest size. For example, models with $p = 3, 2, 4/3, 1$, and $2/3$ have been constructed (Silverstein & Westphal 2008; McAllister et al. 2010, 2014), or in another case $p = 4/3$, $p_\Lambda = -1/3$, and $p_f = -1/3$. Following Flauger et al. (2014b), we investigate the effect of a drift in frequency arising from p_f , neglecting a possible drift in the modulation amplitude by setting $p_\Lambda = C_0 = 0$. Even in this restricted model, a parameter exploration using a fully numerical computation of the primordial power spectrum following the methodology of Peiris et al. (2013) is prohibitive, so we follow Flauger et al. (2014b) to study two templates capturing the features of the primordial spectra generated by this potential.

The first template, which we call the “semi-analytic” template, is given by

$$\mathcal{P}_{\mathcal{R}}(k) = \mathcal{P}_{\mathcal{R}}(k_*) \left(\frac{k}{k_*} \right)^{n_s-1} \left\{ 1 + \delta n_s \cos \left[\frac{\phi_0}{f} \left(\frac{\phi_k}{\phi_0} \right)^{p_f+1} + \Delta\phi \right] \right\}.$$

The parameter f is higher than the underlying axion decay constant f_0 of the potential by a few percent, but this difference will be neglected in this analysis. The quantity ϕ_0 is some fiducial value for the scalar field, and ϕ_k is the value of the scalar field at the time when the mode with comoving momentum k exits the Hubble radius. At leading order in the slow-roll expansion, in units where the reduced Planck mass $M_{\text{Pl}} = 1$, $\phi_k = \sqrt{2p(N_0 - \ln(k/k_*))}$, where $N_0 = N_* + \phi_{\text{end}}^2/(2p)$, and ϕ_{end} is the value of the scalar field at the end of inflation.

The second “analytic” template was derived by Flauger et al. (2014b) by expanding the argument of the trigonometric function in Eq. (110) in $\ln(k/k_*)$, leading to

$$\mathcal{P}_{\mathcal{R}}(k) = \mathcal{P}_{\mathcal{R}}(k_*) \left(\frac{k}{k_*} \right)^{n_s-1} \times \left\{ 1 + \delta n_s \cos \left[\Delta\phi + \alpha \left(\ln \left(\frac{k}{k_*} \right) + \sum_{n=1}^2 \frac{c_n}{N_*^n} \ln^{n+1} \left(\frac{k}{k_*} \right) \right) \right] \right\}. \quad (111)$$

The relation between the empirical parameters in the templates and the potential parameters are approximated by $\delta n_s = 3b\sqrt{2\pi}/\alpha$, where

$$\alpha = (1 + p_f) \frac{\phi_0}{2fN_0} \left(\frac{\sqrt{2pN_0}}{\phi_0} \right)^{1+p_f}, \quad (112)$$

and b is the monotonicity parameter defined in Flauger et al. (2014b), providing relations converting bounds on c_n into bounds on the microphysical parameters of the potential. However, the analytic template can describe more general shapes of primordial spectra than just axion monodromy.

As discussed by Flauger et al. (2014b), there is a degeneracy between p (or alternatively n_s) and f . For both templates we fix $p = 4/3$ and also fix the tensor power spectrum to its form in the absence of oscillations. This is an excellent approximation because tensor oscillations are suppressed relative to the scalar oscillations by a factor $\alpha(f/M_{\text{Pl}})^2 \ll 1$. A uniform prior $-\pi < \Delta\phi < \pi$ is adopted for the phase parameter of both templates as well as a prior $0 < \delta n_s < 0.7$ for the modulation amplitude parameter.

In order to specify the semi-analytic template, we assume instantaneous reheating, which for $p = 4/3$ corresponds to $N_* \approx 57.5$ for $k_* = 0.05 \text{ Mpc}^{-1}$. We set $\phi_0 = 12.38 M_{\text{Pl}}$ with $\phi_{\text{end}} = 0.59 M_{\text{Pl}}$. We adopt uniform priors $-4 < \log_{10}(f/M_{\text{Pl}}) < -1$ and $-0.75 < p_f < 1$ for the remaining parameters. The priors $0 < \ln(\alpha) < 6.9$ and $-2 < c_{1,2} < 2$ specify the analytic template. The single-field effective field theory becomes strongly coupled for $\alpha > 200$. However, in principle the string construction remains valid in this regime.

10.3.2. Power spectrum constraints on monodromy inflation

We carry out a Bayesian analysis of axion monodromy inflation using a high-resolution version of CAMB coupled to the PolyChord sampler (see Sect. 8.2). For our baseline analysis we conservatively adopt *Planck* TT+lowP, using the “bin1” high- ℓ TT likelihood. In addition to the primordial template priors specified above, we marginalize over the standard priors for the cosmological parameters, the primordial amplitude, and foreground parameters.

The marginalized joint posterior constraints on pairs of primordial parameters for the analytic and semi-analytic templates are shown in Figs. 37 and 38, respectively.

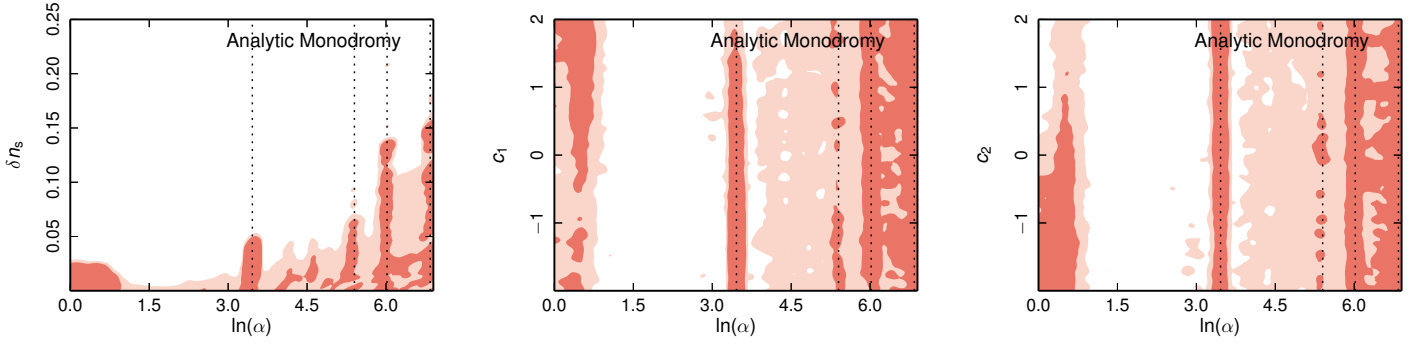


Fig. 37. Constraints on the parameters of the analytic template, showing joint 68% and 95% CL. The dotted lines correspond to the frequencies showing the highest-likelihood improvements (see text).

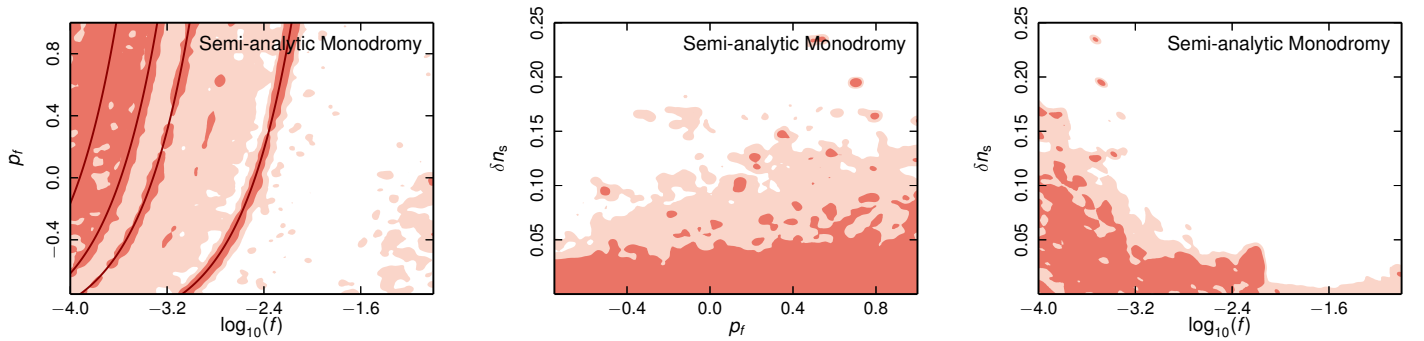


Fig. 38. Constraints on the parameters of the semi-analytic template showing joint 68% and 95% CL. The solid lines on the left-hand panel mark the frequencies showing the highest-likelihood improvements (see text).

The complex structures seen in these plots arise due to degeneracies in the likelihood frequency “beating” between underlying modulations in the data and the model (Easther et al. 2005). Parameter combinations where “beating” occurs over the largest k ranges lead to discrete local maxima in the likelihood. Fortuitous correlations in the observed realization of the C_ℓ can give the same effect.

The four frequencies picked out by these structures, $\ln(\alpha) \approx \{3.5, 5.4, 6.0, 6.8\}$, show improvements of $\Delta\chi^2 \approx \{-9.7, -7.1, -12.2, -12.5\}$ relative to Λ CDM, respectively. These frequencies are marked by dotted lines in Fig. 37, and by solid lines in Fig. 38 using Eq. (112). The semi-analytic and analytic templates lead to self-consistent results as expected, with analogous structures being picked out by the likelihood in each template. There is no evidence for a drifting frequency, $p_f \neq 0$ or $c_n \neq 0$. Thus, these parameters serve to smooth out structures in the marginalized posterior.

The improvement in χ^2 is not compelling enough to suggest a primordial origin. Fitting a modulated model to simulations with a smooth spectrum can give rise to $\Delta\chi^2 \sim -10$ improvements (Flauger et al. 2014b). Furthermore, as the monodromy model contains only a single frequency, at least three of these structures must correspond to spurious fits to the noise. Considering the two models defined by the two templates and the parameter priors specified above, the Bayes factors calculated using PolyChord favours base Λ CDM over both templates by odds of roughly 8:1.

Compared to previous analyses of the linear ($p = 1$) axion monodromy model for WMAP9 (Peiris et al. 2013) and the 2013 *Planck* data (Planck Collaboration XXII 2014; Easther & Flauger 2014) the common frequencies are shifted slightly

upward. The lower frequency in common appears shifted by a factor of order \sqrt{p} from $\alpha \approx 28.9$ to 31.8 and the higher frequency in common from $\alpha \approx 210$ to 223 . Flauger et al. (2014b) suggest that the lower frequency (which had $\Delta\chi^2 = -9$ in PCI13) was associated with the 4 K cooler line systematic effects in the 2013 *Planck* likelihood. However, its presence at similar significance in the 2015 likelihood with improved handling of the cooler line systematics suggests that this explanation is not correct. The second frequency, which appeared with $\Delta\chi^2 \approx -20$ in WMAP9 (Peiris et al. 2013) is still present but with much reduced significance, suggesting that the high multipoles do not give evidence for this frequency. Additionally, two higher frequencies are present, which if interpreted as being of primordial origin, correspond to a regime well beyond the validity of the single-field effective field theory. If one of these frequencies were to be confirmed as primordial, a significantly improved understanding of the underlying string construction would need to be undertaken.

In order to check whether the improvement in fit at these four modulation frequencies is responding to residual foregrounds or other systematics, we examine the frequency residuals. Figure 39 shows the residuals of the data minus the model (including the best-fit foreground model) for the four PLIK frequency combinations binned at $\Delta\ell = 30$ for the lowest modulation frequency, $\ln(\alpha) \approx 3.5$. This plot shows no significant frequency dependence, and thus there is no indication that the fit is responding to frequency dependent systematics. Furthermore, the plot does not show evidence that the improvement for this modulation frequency comes from the feature at $\ell \approx 800$, as suggested by Easther & Flauger (2014). This feature and another at $\ell \approx 1500$ are apparent at all frequency combinations. Similar plots for the

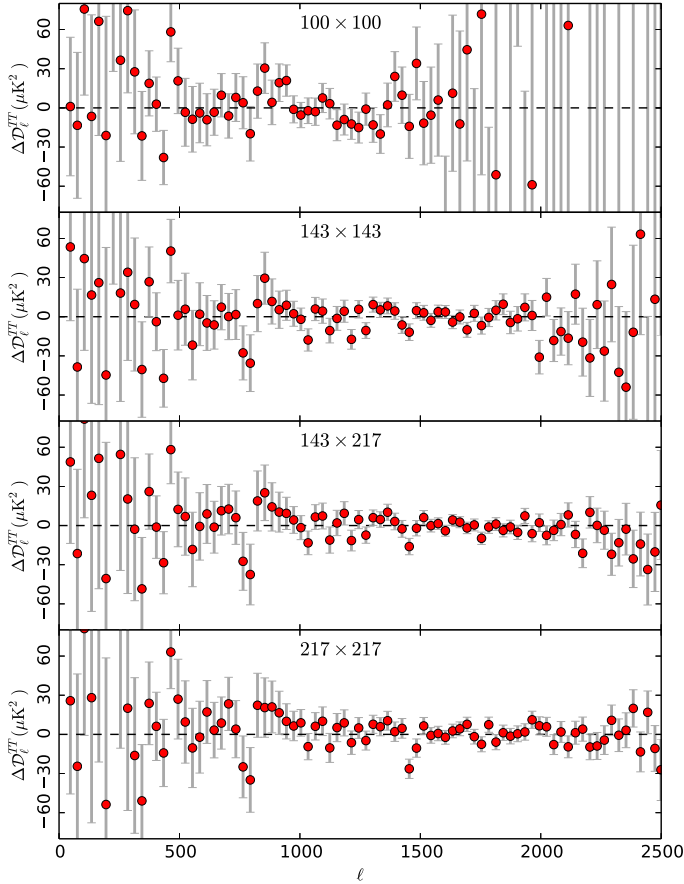


Fig. 39. Frequency residuals for the $\ln(\alpha) \approx 3.5$ likelihood peak, binned at $\Delta\ell = 30$. The $\pm 1\sigma$ errors are given by the square root of the diagonal elements of the covariance matrix.

three other modulation frequencies also do not show indications of frequency dependence.

In order to confirm whether any of the frequencies picked out here is of primordial origin, one can exploit independent information in the polarization data to perform a cross-check of the temperature prediction, thus minimizing the “look-elsewhere” effect (Mortonson et al. 2009). Leaving a complete analysis of the independent information in the polarization for future work, we now check whether the temperature-only result remains stable when high- ℓ polarization is added in the likelihood. In Fig. 40 we show a preliminary analysis using the PLIK temperature and polarization (TT , TE , and EE) “bin1” likelihood plus low- ℓ polarization data. A comparison with the left-hand panels of Figs. 37 and 38 indicates slight differences from the T-only analysis. However, all the four frequencies identified in the temperature are present when high- ℓ polarization is added. There is a maximum $\Delta\chi^2 \approx -8.0$ improvement over Λ CDM. We also repeat the analysis using only the EE polarization “bin1” likelihood plus low- ℓ temperature and polarization data. These results are presented in Fig. 41. The EE -only frequencies are offset with respect to the temperature-only frequencies: the best-fit EE -only frequencies are at $\ln(\alpha) \approx \{3.8, 5.0, 5.4, 5.8, 6.2\}$. The maximum improvement over Λ CDM for this case is $\Delta\chi^2 \approx -12.5$.

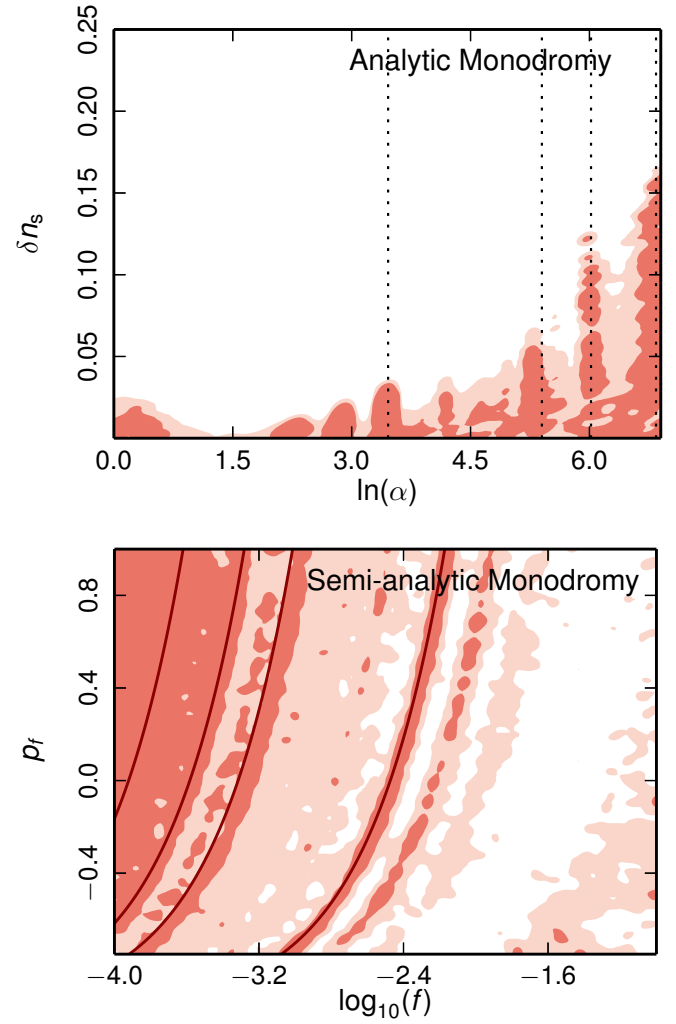


Fig. 40. Constraints on the parameters of the analytic (top) and semi-analytic (bottom) templates with the addition of high- ℓ polarization data in the likelihood, showing joint 68% and 95% CL. The lines mark the frequencies showing the highest-likelihood improvements identified in the baseline temperature-only analysis.

10.3.3. Predictions for resonant non-Gaussianity

The left-hand panel of Fig. 42 presents derived constraints on the parameters of the potential in Eq. (109) calculated using the analytic template. Another cross-check of primordial origin is available since the monodromy model predicts resonant NG, generating a bispectrum whose properties would be strongly correlated with that of the power spectrum (Chen et al. 2008; Flauger & Pajer 2011). Using the mapping

$$f_{\text{NL}}^{\text{res}} = \frac{\delta n_s}{8} \alpha^2, \quad (113)$$

we use the analytic template to derive the posterior probability for the resonant NG signal predicted by constraints from the power spectrum, presented in the middle and right panels of Fig. 42.

Planck Collaboration XVII (2016) use an improved modal estimator to scan for resonant NG. The resolution of this scan is currently limited to $\ln(\alpha) < 3.9$, which potentially can probe the lowest frequency picked out in the power spectrum search. However, the modal estimator’s sensitivity (imposed by cosmic variance) of $\Delta f_{\text{NL}}^{\text{res}} \approx 80$ is significantly greater than the predicted value for this frequency from fits to the power spectrum,

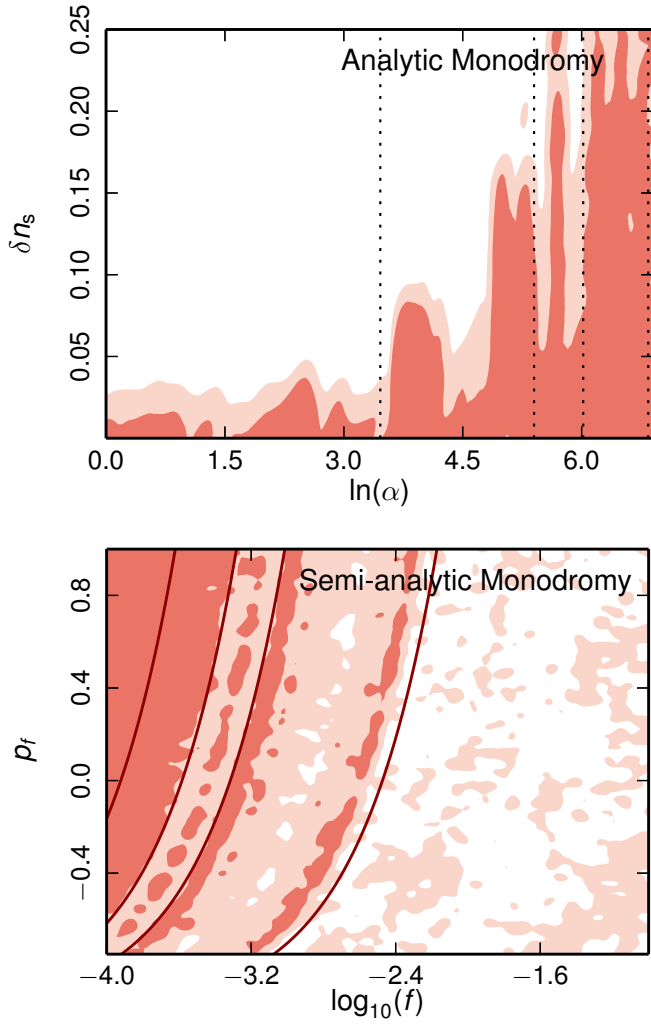


Fig. 41. Constraints on the parameters of the analytic (*top*) and semi-analytic (*bottom*) templates with EE -only high- ℓ polarization data plus low- ℓ temperature and polarization data, showing joint 68% and 95% CL. The lines mark the frequencies showing the highest-likelihood improvements identified in the baseline temperature-only analysis.

$f_{\text{NL}}^{\text{res}} \sim 10$. Efforts to increase the resolution of the modal estimator are ongoing and may allow consistency tests of the significantly higher levels of resonant NG predicted by the higher frequencies in the future.

10.3.4. Power spectrum and bispectrum constraints on axion inflation with a gauge field coupling

We now consider the case where the axion field is coupled to a gauge field. Such a scenario is physically well motivated. From an effective field theory point of view the derivative coupling is natural and must be included since it respects the same shift symmetry that leads to axion models of inflation (Anber & Sorbo 2010; Barnaby & Peloso 2011; Pajer & Peloso 2013). This type of coupling is also ubiquitous in string theory (see, e.g., Barnaby et al. 2012; Linde et al. 2013). The coupling term in the action is (Anber & Sorbo 2010; Barnaby & Peloso 2011; Barnaby et al. 2011)

$$S \supset \int d^4x \sqrt{-g} \left(-\frac{\alpha}{4f} \phi F^{\mu\nu} \tilde{F}_{\mu\nu} \right), \quad (114)$$

where $F_{\mu\nu} = \partial_\mu A_\nu - \partial_\nu A_\mu$, its dual is $\tilde{F}^{\mu\nu} = \epsilon^{\mu\nu\alpha\beta} F_{\alpha\beta}/2$, and α is a dimensionless constant which, from an effective field theory perspective, is expected to be of order one. For the potential of the axion field, we will not investigate further the consequences of the oscillatory part of the potential, focusing on the coupling of the axion field to the U(1) gauge field (effectively setting $\Lambda_0 = 0$).

The coupling of a pseudo-scalar axion with the gauge field has interesting phenomenological consequences, both for density perturbations and primordial gravitational waves (Barnaby & Peloso 2011; Sorbo 2011; Barnaby et al. 2011, 2012; Meerburg & Pajer 2013; Ferreira & Sloth 2014). Gauge field quanta source the axion field via an inverse decay process $\delta A + \delta A \rightarrow \delta\phi$, modifying the usual predictions already at the power spectrum level. Additionally, the inverse decay can generate a high level of primordial NG.

The parameter

$$\xi = \frac{\alpha|\dot{\phi}|}{2fH} \quad (115)$$

characterizes the strength of the inverse decay effects. If $\xi < 1$ the coupling is too small to produce any modifications to the usual predictions of the uncoupled model. For previous constraints on ξ see Barnaby et al. (2011, 2012) and Meerburg & Pajer (2013). Using the slow-roll approximation and neglecting the small oscillatory part of the potential, one can express

$$\xi = M_{\text{Pl}} \frac{\alpha}{f} \sqrt{\frac{p}{8N + 2p}}, \quad (116)$$

where N is, as usual, the number of e -folds to the end of inflation. The scalar power spectrum of curvature perturbations is given by

$$\mathcal{P}_{\mathcal{R}}(k) = \mathcal{P}_* \left(\frac{k}{k_*} \right)^{n_s-1} \left[1 + \mathcal{P}_* \left(\frac{k}{k_*} \right)^{n_s-1} f_2(\xi(k)) e^{4\pi\xi_*} \left(\frac{k}{k_*} \right)^{2\pi\xi_*\epsilon_2} \right], \quad (117)$$

where (Meerburg & Pajer 2013)

$$\xi(k) = \xi_* \left[1 + \frac{\epsilon_2}{2} \ln \left(\frac{k}{k_*} \right) \right]. \quad (118)$$

Here an asterisk indicates evaluation at the pivot scale, $k_* = 0.05 \text{ Mpc}^{-1}$, and $\mathcal{P}_* = H_*^4/(4\pi^2\dot{\phi}_*^2)$ and $n_s - 1 = -2\epsilon_1 - \epsilon_2$ are the amplitude and spectral index, respectively, of the standard slow-roll power spectrum of vacuum-mode curvature perturbations (the usual power spectrum in the absence of the gauge-coupling). By numerically evaluating the function $f_2(\xi)$ (defined in Eq. (3.27) of Barnaby et al. 2011), we created an analytical fit to this function accurate to better than 2% for $0.1 < \xi_* < 7$.¹⁴ In the following, unless stated otherwise, we fix $p = 4/3$ as in the previous subsection and assume instantaneous reheating so that $N_* \approx 57.5$ and the slow-roll parameters ϵ_1 and ϵ_2 are fixed. For the tensor power spectrum we adopt the approximation (Barnaby et al. 2011)

$$\mathcal{P}_t(k) = \mathcal{P}_t \left(\frac{k}{k_*} \right)^{n_t} \left[1 + \frac{\pi^2}{2} \mathcal{P}_{t,L}(\xi(k)) e^{4\pi\xi_*} \left(\frac{k}{k_*} \right)^{n_t+2\pi\epsilon_2\xi_*} \right], \quad (119)$$

¹⁴ The fitting function used is $\exp\{-a - b \ln(\xi) - c [\ln(\xi)]^2 + d [\ln(\xi)]^3 + e [\ln(\xi)]^4\}$, where the coefficients are $a = 10.8$, $b = 4.58$, $c = 0.51$, $d = 0.01$, and $e = 0.02$.

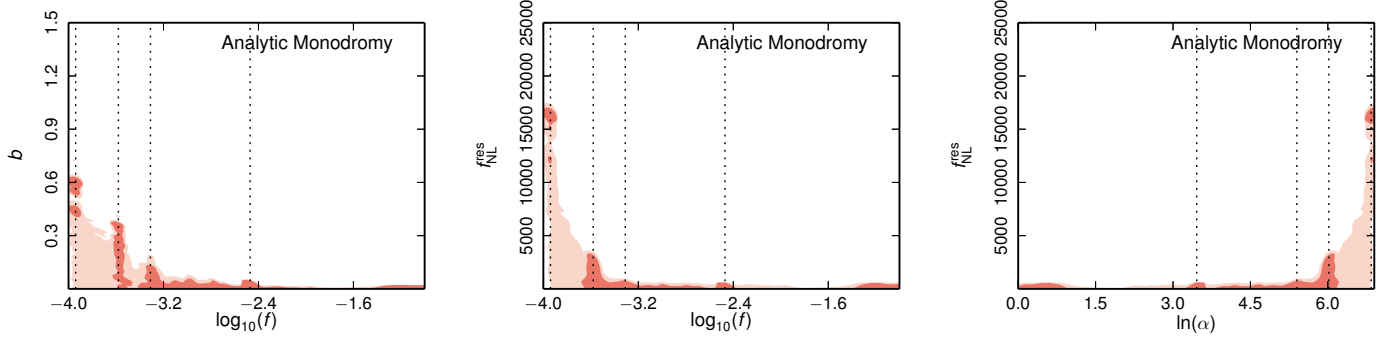


Fig. 42. Derived constraints on the parameters of the potential, Eq. (109), as well as the predicted resonant NG, $f_{\text{NL}}^{\text{res}}$, using the analytic template, showing joint 68% and 95% CL. The dotted lines mark the frequencies showing the highest-likelihood improvements (see text).

where

$$f_{\text{tL}}(\xi(k)) = 2.6 \times 10^{-7} \xi^{-5.7}(k). \quad (120)$$

Here $\mathcal{P}_t = 2H_*^2/(\pi^2 M_{\text{Pl}}^2)$ and $n_t = -2\epsilon_1$ are the “usual” expressions for the tensor amplitude and tensor tilt in standard slow-roll inflation.

The total bispectrum is (Barnaby et al. 2012)

$$B(k_i) = B_{\text{inv.dec.}}(k_i) + B_{\text{res}}(k_i) \quad (121a)$$

$$= f_{\text{NL}}^{\text{inv.dec.}}(\xi) F_{\text{inv.dec.}}(k_i) + B_{\text{res}}(k_i), \quad (121b)$$

where the explicit expression for $F_{\text{inv.dec.}}(k_i)$ (Barnaby et al. 2011; see also Meerburg & Pajer 2013) is reported in Planck Collaboration XVII (2016). This shows that the inverse decay effects and the resonant effects (which arise from the oscillatory part of the potential) simply “add up” in the bispectrum. The nonlinearity parameter is

$$f_{\text{NL}}^{\text{inv.dec.}} = \frac{f_3(\xi_*) \mathcal{P}_*^3 e^{6\pi\xi_*}}{\mathcal{P}_*^2(k_*)}. \quad (122)$$

The function $f_3(\xi_*)$ corresponds to the quantity $f_3(\xi_*; 1, 1)$ defined in Eq. (3.29) of Barnaby et al. (2011). We have computed $f_3(\xi_*)$ numerically and used a fit with an accuracy of better than 2%.¹⁵ We use the observational constraint $f_{\text{NL}}^{\text{inv.dec.}} = 22.7 \pm 25.5$ (68% CL) obtained in Planck Collaboration XVII (2016) from an analysis where only the inverse decay type NG is assumed present. We omit the explicit expression for the resonant bispectrum B_{res} , since it will not be used here.

We carried out an MCMC analysis of constraints on the (scalar and tensor) power spectra predicted by this model with the Planck TT+lowP likelihood, marginalizing over standard priors for the cosmological parameters and foreground parameters with the uniform priors $2.5 \leq \ln[10^{10}\mathcal{P}_*] \leq 3.7$ and $0.1 \leq \xi_* \leq 7.0$.

The power spectrum constraint gives

$$0.1 \leq \xi_* \leq 2.3 \quad (95\% \text{ CL}). \quad (123)$$

Given that $f_{\text{NL}}^{\text{inv.dec.}}$ is exponentially sensitive to ξ , this translates into the prediction (using Eq. (122)) $f_{\text{NL}}^{\text{inv.dec.}} \leq 1.2$, which is significantly tighter than the current bispectrum constraint from Planck Collaboration XVII (2016). Indeed, importance sampling with the likelihood for $f_{\text{NL}}^{\text{inv.dec.}}$, taken to be a Gaussian centred

¹⁵ The fit has the same expression as the one for $f_2(\xi)$ with coefficients $a = 17.0048$, $b = 6.6578$, $c = 0.96479$, $d = 0.0506098$, and $e = 0.039139$.

on the NG estimate $f_{\text{NL}}^{\text{inv.dec.}} = 22.7 \pm 25.5$ (68% CL) (Planck Collaboration XVII 2016), changes the limit on ξ_* only at the second decimal place.

We now derive constraints on model parameters using only the observational constraint on $f_{\text{NL}}^{\text{inv.dec.}}$. The constraints thus derived are applicable for generic p and also to the axion monodromy model discussed in Sect. 10.3, even in the case $\Lambda_0 \neq 0$. We follow the procedure described in Sect. 11 of Planck Collaboration XVII (2016). The likelihood for $f_{\text{NL}}^{\text{inv.dec.}}$ is taken to be a Gaussian centred on the NG estimate $f_{\text{NL}}^{\text{inv.dec.}} = 22.7 \pm 25.5$ (68% CL) (Planck Collaboration XVII 2016). We use the expression of Eq. (122), where $f_3(\xi_*)$ is numerically evaluated. To find the posterior distribution for the parameter ξ_* we choose uniform priors in the intervals $1.5 \times 10^{-9} \leq \mathcal{P}_* \leq 3.0 \times 10^{-9}$ and $0.1 \leq \xi_* \leq 7.0$. This yields 95% CL constraints for ξ_* (for any value of p) of

$$\xi_* \leq 2.5 \quad (95\% \text{ CL}). \quad (124)$$

If we choose a log-constant prior on ξ_* we find

$$\xi_* \leq 2.2 \quad (95\% \text{ CL}). \quad (125)$$

For both cases the results are insensitive to the upper limit chosen for the prior on ξ_* since the likelihood quickly goes to zero for $\xi_* > 3$. As the likelihood for ξ_* is fairly flat, the tighter constraint seen for the log-constant case is mildly prior driven. The constraints from the bispectrum are consistent with, and slightly worse than, the result from the power spectrum alone.

Using a similar procedure and Eq. (116) one can also obtain a constraint on α/f . Adopting a log-constant prior¹⁶ $2 \leq \alpha/f \leq 100$ and uniform priors $50 \leq N_* \leq 70$ and $1.5 \times 10^{-9} \leq \mathcal{P}_* \leq 3.0 \times 10^{-9}$ we obtain the 95% CL constraints

$$\alpha/f \leq 48 M_{\text{Pl}}^{-1} \quad \text{for } p = 1, \quad \alpha/f \leq 35 M_{\text{Pl}}^{-1} \quad \text{for } p = 2, \quad (126)$$

and

$$\alpha/f \leq 42 M_{\text{Pl}}^{-1} \quad \text{for } p = 4/3. \quad (127)$$

For example, for a linear potential, $p = 1$, if $\alpha \sim 1$ as suggested by effective field theory, then the axion decay constant f is constrained to be

$$f \geq 0.020 M_{\text{Pl}} \quad (95\% \text{ CL}), \quad (128)$$

while for a potential with $p = 4/3$ we find

$$f \geq 0.023 M_{\text{Pl}} \quad (95\% \text{ CL}). \quad (129)$$

These limits are complementary to those derived in Sect. 10.3.

¹⁶ We give only the results for a log-constant prior on α/f , which is well-motivated since it corresponds to a log-constant prior on the axion decay constant for some fixed α .

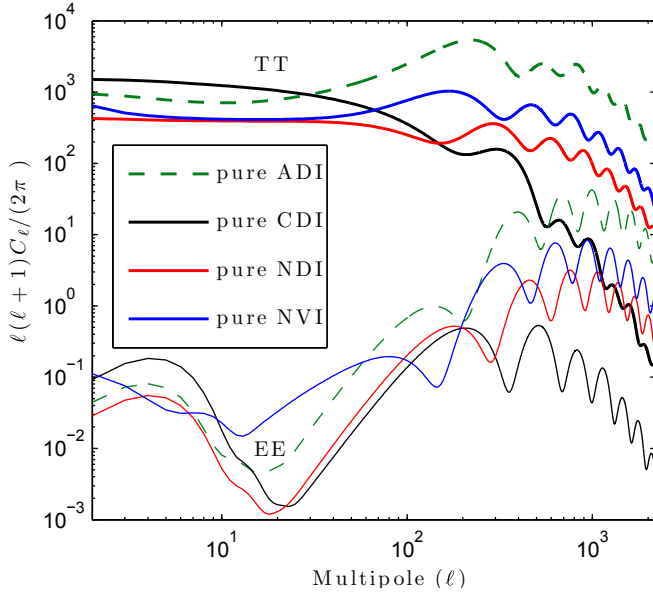


Fig. 43. Angular power spectra for the scale-invariant (i.e., $n_{RR} = 1$) pure adiabatic mode (ADI, green dashed curves) and for the scale invariant ($n_{II} = 1$) pure isocurvature (CDI, NDI, or NVI) modes, with equal primordial perturbation amplitudes. The thick lines represent the temperature auto-correlation (TT) and the thin lines the E-mode polarization auto-correlation (EE).

11. Constraints on isocurvature modes

In [PCI13](#), we presented constraints on a number of simple models featuring a mixture of the adiabatic (ADI) mode and one type of isocurvature mode. We covered the cases of CDM density isocurvature (CDI), neutrino density isocurvature (NDI), and neutrino velocity isocurvature (NVI) modes ([Bucher et al. 2000](#)) with different assumptions concerning the correlation ([Langlois 1999](#); [Amendola et al. 2002](#)) between the primordial adiabatic and isocurvature perturbations. Isocurvature modes, possibly correlated among themselves and with the adiabatic mode, can be generated in multi-field models of inflation; however, at present a mechanism for exciting the neutrino velocity isocurvature mode is lacking. Section 11.2 shows how these constraints have evolved with the new *Planck* TT+lowP likelihoods, how much including the *Planck* lensing likelihood changes the results, and what extra information the *Planck* high- ℓ polarization contributes. A pure isocurvature mode as a sole source of perturbations has been ruled out ([Enqvist et al. 2002](#)), since, as can be seen from Fig. 43, any of the isocurvature modes leads to an acoustic peak structure for the temperature angular power very different from the adiabatic mode, which fits the data very well. The different phases and tilts of the various modes also occur in the polarization spectra, as shown in Fig. 43 for the E mode.¹⁷

¹⁷ The transfer function mapping the primordial CDI mode to C_ℓ^{TT} is suppressed by a factor $(k/k_{eq})^{-2} \sim (\ell/\ell_{eq})^{-2}$ relative to the ADI mode, where k_{eq} is the wavenumber of matter-radiation equality. As seen in Fig. 43, there is a similar damping for the E mode in the CDI versus the ADI case. Therefore, to be observable at high ℓ , a CDI mode should be (highly) blue tilted. So, if the data favoured as small as possible a disturbance by CDI over all scales, then the CDI should have a spectral index, n_{II} , of roughly three. In practice, the lowest- ℓ part of the data has very little weight due to cosmic variance, and thus we expect that the data should favour n_{II} less than three, but significantly larger than one. This should be kept in mind when interpreting the results in the

In Sect. 11.4 we add one extra degree of freedom to the generally-correlated ADI+CDI model by allowing primordial tensor perturbations (assuming the inflationary consistency relation for the tilt of the tensor power spectrum and its running). Our main goal is to explore a possible degeneracy between tensor modes and negatively-correlated CDI modes, tending to tilt the large-scale temperature spectrum in opposite directions. In Sect. 11.5, we update the constraints on three special cases motivated by axion or curvaton scenarios.

The goal of this analysis is to test the hypothesis of adiabaticity and establish the robustness of the base Λ CDM model against different assumptions concerning initial conditions (Sect. 11.3). Adiabaticity is also an important probe of the inflationary paradigm, since any significant detection of isocurvature modes would exclude the possibility that all perturbations in the Universe emerged from quantum fluctuations of a single inflaton field, which can excite only one degree of freedom, the curvature (i.e., adiabatic) perturbation.¹⁸

In this section, theoretical predictions were obtained with a modified version of the CAMB code (version Jul14) while parameter exploration was performed with the MultiNest nested sampling algorithm.

11.1. Parameterization and notation

A general mixture of the adiabatic mode and one isocurvature mode is described by the three functions $\mathcal{P}_{RR}(k)$, $\mathcal{P}_{II}(k)$, and $\mathcal{P}_{RI}(k)$ describing the curvature, isocurvature, and cross-correlation power spectra, respectively. Our sign conventions are such that positive values for \mathcal{P}_{RI} correspond to a positive contribution of the cross-correlation term to the Sachs-Wolfe component of the total temperature spectrum.

As in [PCI13](#), we specify the amplitudes at two scales $k_1 < k_2$ and assume power-law behaviour, so that

$$\mathcal{P}_{ab}(k) = \exp \left[\left(\frac{\ln(k) - \ln(k_2)}{\ln(k_1) - \ln(k_2)} \right) \ln(\mathcal{P}_{ab}^{(1)}) + \left(\frac{\ln(k) - \ln(k_1)}{\ln(k_2) - \ln(k_1)} \right) \ln(\mathcal{P}_{ab}^{(2)}) \right], \quad (130)$$

where $a, b = I, R$ and $I = I_{CDI}, I_{NDI}$, or I_{NVI} . We set $k_1 = 0.002 \text{ Mpc}^{-1}$ and $k_2 = 0.100 \text{ Mpc}^{-1}$, so that $[k_1, k_2]$ spans most of the range constrained by the *Planck* data. The positive definiteness of the initial condition matrix imposes a constraint on its elements at any value of k :

$$[\mathcal{P}_{ab}(k)]^2 \leq \mathcal{P}_{aa}(k)\mathcal{P}_{bb}(k). \quad (131)$$

CDI case, i.e., one cannot expect strong constraints on the *primordial* CDI fraction at small scales, even if the data are purely adiabatic. The imprint of the baryon density isocurvature (BDI) mode in the CMB, at least at linear order, is indistinguishable from the CDI case, and hence we do not consider it separately as it can be described by $\mathcal{I}_{CDI}^{\text{effective}} = \mathcal{I}_{CDI} + (\Omega_b/\Omega_c)\mathcal{I}_{BDI}$. The trispectrum, however, can in principle be used to distinguish the BDI and CDI modes ([Grin et al. 2014](#)).

¹⁸ However, conversely, if no isocurvature was detected, the fluctuations could have been seeded either by single- or multi-field inflation, since later processes easily wash out inflationary isocurvature perturbations ([Mollerach 1990](#); [Weinberg 2004](#); [Beltrán et al. 2005](#)). An example is the curvaton model, in which perturbations can be purely isocurvature at Hubble exit during inflation, but are later converted to ADI if the curvaton or curvaton particles ([Linde & Mukhanov 2006](#)) dominate the energy density at the curvaton's decay. For a summary of various curvaton scenarios, see, e.g., [Gordon & Lewis \(2003\)](#).

We take uniform priors on the positive amplitudes,

$$\mathcal{P}_{\mathcal{R}\mathcal{R}}^{(1)}, \mathcal{P}_{\mathcal{R}\mathcal{R}}^{(2)} \in (10^{-9}, 10^{-8}), \quad (132)$$

$$\mathcal{P}_{\mathcal{I}\mathcal{I}}^{(1)}, \mathcal{P}_{\mathcal{I}\mathcal{I}}^{(2)} \in (0, 10^{-8}). \quad (133)$$

The correlation spectrum can be positive or negative. For $a \neq b$ we apply a uniform prior at large scales (at k_1):

$$\mathcal{P}_{ab}^{(1)} \in (-10^{-8}, 10^{-8}), \quad (134)$$

but reject all parameter combinations violating the constraint in Eq. (131). To ensure that Eq. (131) holds for all k , we restrict ourselves to a scale-independent correlation fraction:

$$\cos \Delta_{ab} \equiv \frac{\mathcal{P}_{ab}}{(\mathcal{P}_{aa}\mathcal{P}_{bb})^{1/2}} \in (-1, 1). \quad (135)$$

Thus $\mathcal{P}_{ab}^{(2)}$ is a derived parameter¹⁹ given by

$$\mathcal{P}_{ab}^{(2)} = \mathcal{P}_{ab}^{(1)} \frac{(\mathcal{P}_{aa}^{(2)}\mathcal{P}_{bb}^{(2)})^{1/2}}{(\mathcal{P}_{aa}^{(1)}\mathcal{P}_{bb}^{(1)})^{1/2}}, \quad (136)$$

which in terms of spectral indices is equivalent to

$$n_{ab} = \frac{1}{2}(n_{aa} + n_{bb}). \quad (137)$$

The conservative baseline likelihood is *Planck* TT+lowP. The results obtained with *Planck* TT, TE, EE+lowP should be interpreted with caution because the data used in the 2015 release are known to contain some low level systematics, in particular arising from *T*-to-*E* leakage, and it is possible that such systematics may be fit by the isocurvature auto-correlation and cross-correlation templates. (See [Planck Collaboration XIII 2016](#) for a detailed discussion.)

In what follows, we quote our results in terms of derived parameters identical to those in [PCI13](#). We define the primordial isocurvature fraction as

$$\beta_{\text{iso}}(k) = \frac{\mathcal{P}_{\mathcal{I}\mathcal{I}}(k)}{\mathcal{P}_{\mathcal{R}\mathcal{R}}(k) + \mathcal{P}_{\mathcal{I}\mathcal{I}}(k)}. \quad (138)$$

Unlike the primordial correlation fraction $\cos \Delta$ defined in Eq. (135), β_{iso} is scale-dependent in the general case. We present bounds on this quantity at $k_{\text{low}} = k_1$, $k_{\text{mid}} = 0.050 \text{ Mpc}^{-1}$, and $k_{\text{high}} = k_2$.

We report constraints on the relative adiabatic ($ab = \mathcal{R}\mathcal{R}$), isocurvature ($ab = \mathcal{I}\mathcal{I}$), and correlation ($ab = \mathcal{R}\mathcal{I}$) components according to their contribution to the observed CMB temperature variance in various multipole ranges:

$$\alpha_{ab}(\ell_{\min}, \ell_{\max}) \equiv \frac{(\Delta T)_{ab}^2(\ell_{\min}, \ell_{\max})}{(\Delta T)_{\text{tot}}^2(\ell_{\min}, \ell_{\max})}, \quad (139)$$

¹⁹ Given our ansatz of power-law primordial spectra, if we treated $\mathcal{P}_{ab}^{(2)}$ as an independent parameter as we do with $\mathcal{P}_{ab}^{(1)}$, Eq. (131) would always be violated somewhere outside $[k_1, k_2]$. In [PCI13](#), we dealt with this by assuming that when maximal (anti-)correlation is reached at some scale, the correlation remains at (-100%) beyond this scale. This introduced a kink in the cross-correlation spectrum, located at a different wavenumber for each model. Even though the range $[k_1, k_2]$ was chosen to span most of the observable scales, this kink tended to impact the smallest (or largest) multipole values used in the analysis. In particular, the kink helped fit the dip in the temperature angular power in the multipole range $\ell \approx 10$ – 40 .

where

$$(\Delta T)_{ab}^2(\ell_{\min}, \ell_{\max}) = \sum_{\ell=\ell_{\min}}^{\ell_{\max}} (2\ell + 1) C_{ab,\ell}^{\text{TT}}. \quad (140)$$

The ranges considered are $(\ell_{\min}, \ell_{\max}) = (2, 20)$, $(21, 200)$, $(201, 2500)$, and $(2, 2500)$, where the last range describes the total contribution to the observed CMB temperature variance. Here $\alpha_{\mathcal{R}\mathcal{R}}$ measures the adiabaticity of the temperature angular power spectrum, a value of unity meaning “fully adiabatic initial conditions”. Values less than unity mean that some of the observed power comes from the isocurvature or correlation spectrum, while values larger than unity mean that some of the power is “cancelled” by a negatively-correlated isocurvature contribution. The relative non-adiabatic contribution can be expressed as $\alpha_{\text{non-adi}} \equiv 1 - \alpha_{\mathcal{R}\mathcal{R}} = \alpha_{\mathcal{I}\mathcal{I}} + \alpha_{\mathcal{R}\mathcal{I}}$.

11.2. Results for generally-correlated adiabatic and one isocurvature mode (CDI, NDI, or NVI)

Results are reported as 2D and 1D marginalized posterior probability distributions. Numerical 95% CL intervals or upper bounds are tabulated in Table 16.

Figure 44 shows the *Planck* 68% and 95% CL contours for various 2D combinations of the primordial adiabatic and isocurvature amplitude parameters at large scales ($k_1 = 0.002 \text{ Mpc}^{-1}$) and small scales ($k_2 = 0.100 \text{ Mpc}^{-1}$) for (a) the generally-correlated ADI+CDI; (b) ADI+NDI; and (c) ADI+NVI models. Overall, the results using *Planck* TT+lowP are consistent with the nominal mission results in [PCI13](#), but slightly tighter. In the first panels of Figs. 44a–c we also show the constraints on the curvature perturbation power in the pure adiabatic case. Comparing the generally-correlated isocurvature case to the pure adiabatic case with the same data combination summarizes neatly what the data tell us about the initial conditions. If the contours in the $\mathcal{P}_{\mathcal{R}\mathcal{R}}^{(1)}\text{--}\mathcal{P}_{\mathcal{R}\mathcal{R}}^{(2)}$ plane were shifted significantly relative to the pure adiabatic case, the missing power could come either from the isocurvature and positive correlation contributions, or the extra adiabatic power could be cancelled by a negative correlation contribution. We can see that these shifts are small. The low- ℓ temperature data continue to mildly favour a negative correlation (see in particular the bottom middle panel for each of the three models), since compared to the prediction of the best-fit adiabatic base ΛCDM model, the TT angular power at multipoles $\ell \lesssim 40$ is somewhat low. But the dotted grey shaded contours in the three middle top panels show that for *Planck* TT+lowP, the posterior peaks at values $(\mathcal{P}_{\mathcal{I}\mathcal{I}}^{(1)}, \mathcal{P}_{\mathcal{I}\mathcal{I}}^{(2)})$ entirely consistent with $(0, 0)$, i.e., the pure adiabatic case is preferred. The best-fit values of $(\mathcal{P}_{\mathcal{I}\mathcal{I}}^{(1)}, \mathcal{P}_{\mathcal{I}\mathcal{I}}^{(2)})$ are $(1.4 \times 10^{-11}, 4.7 \times 10^{-13})$ for CDI, $(1.2 \times 10^{-12}, 4.6 \times 10^{-10})$ for NDI, and $(1.6 \times 10^{-12}, 2.3 \times 10^{-10})$ for NVI, while $(\mathcal{P}_{\mathcal{R}\mathcal{R}}^{(1)}, \mathcal{P}_{\mathcal{R}\mathcal{R}}^{(2)}) \approx (2.4 \times 10^{-9}, 2.1 \times 10^{-9})$. It may appear from the bottom-centre panels of Fig. 44 that there is nonzero posterior probability for $\mathcal{P}_{\mathcal{R}\mathcal{I}}^{(1)} \neq 0$ when $\mathcal{P}_{\mathcal{I}\mathcal{I}}^{(1)} = 0$, which would violate the positivity constraint, Eq. (131). However, the leftmost pixels of the plots are actually evaluated at values of $\mathcal{P}_{\mathcal{I}\mathcal{I}}^{(1)}$ large enough that the constraint is satisfied.

Including the *Planck* lensing likelihood does not significantly affect the non-adiabatic primordial powers, except for tightening the constraints on the adiabatic power (see the blue versus black contours in the first panels of Figs. 44a–c). Including the lensing ($C_{\ell}^{\phi\phi}$) likelihood constrains the optical

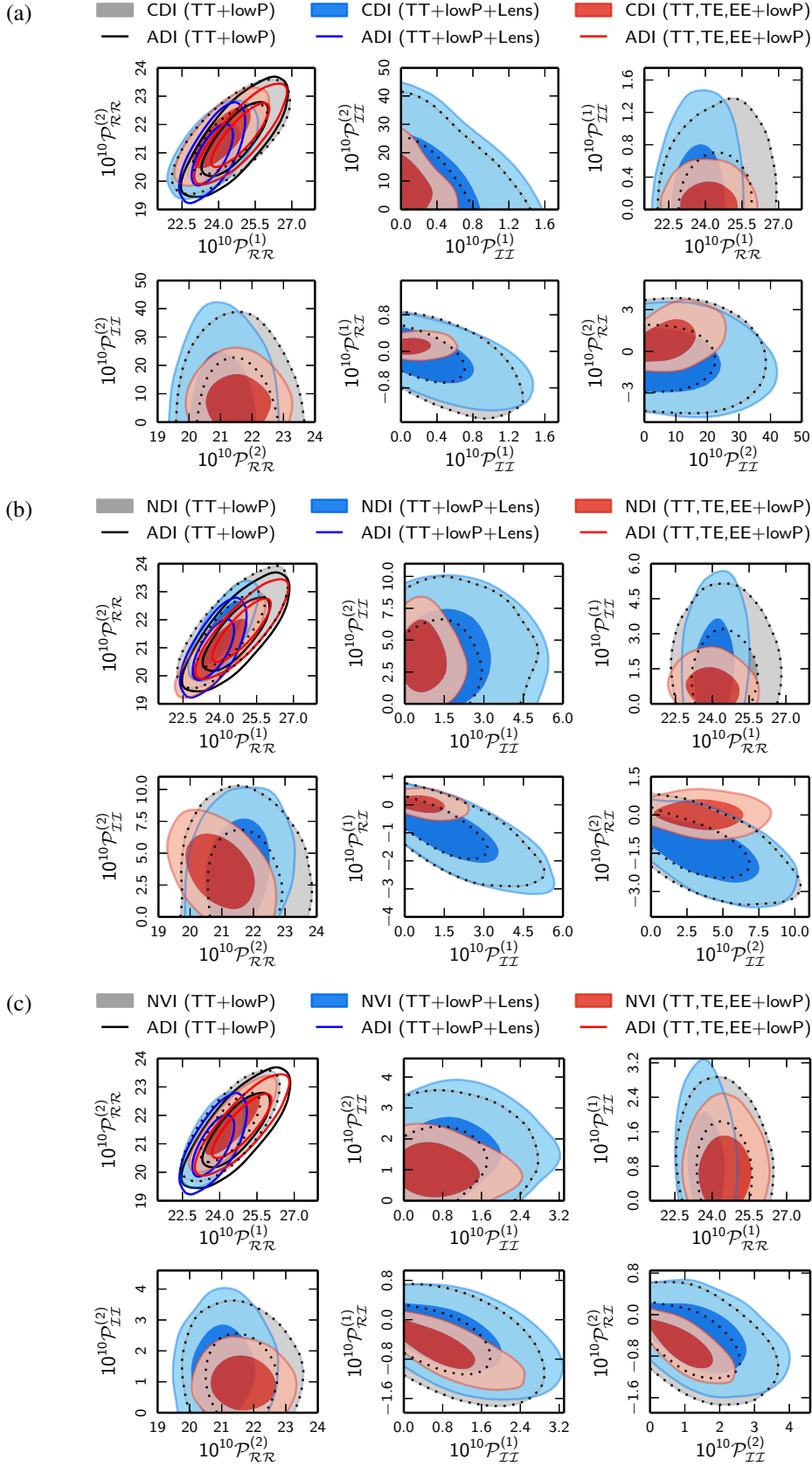


Fig. 44. 68% and 95% CL constraints on the primordial perturbation power in general mixed ADI+CDI **a**); ADI+NDI **b**); and ADI+NVI **c**) models at two scales, $k_1 = 0.002 \text{ Mpc}^{-1}$ (1) and $k_2 = 0.100 \text{ Mpc}^{-1}$ (2), for *Planck* TT+lowP (grey regions highlighted by dotted contours), *Planck* TT+lowP+lensing (blue), and *Planck* TT, TE, EE+lowP (red). In the first panels, we also show contours for the pure adiabatic base ΛCDM model with the corresponding colours of solid lines.

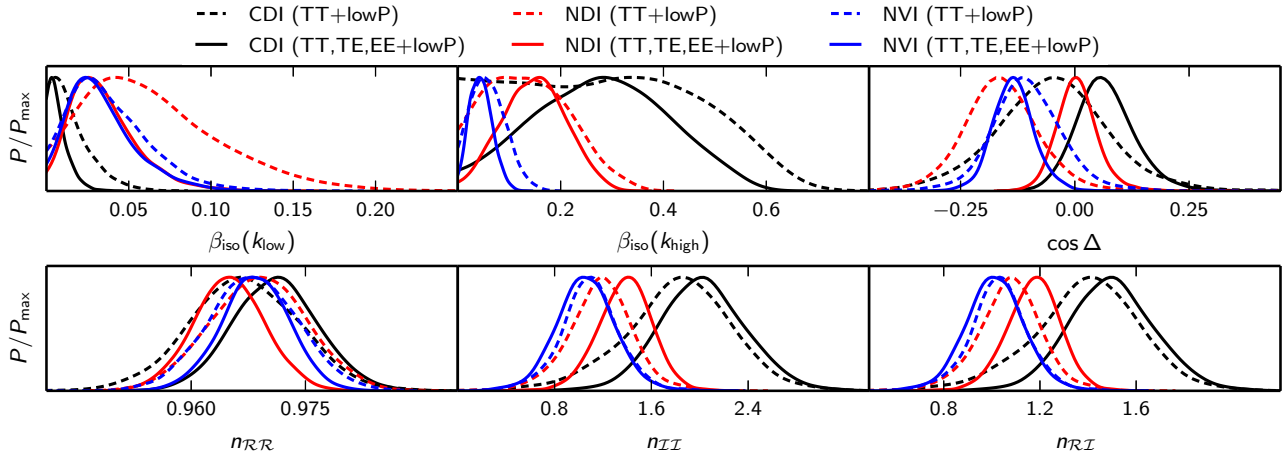


Fig. 45. Constraints on the primordial isocurvature fraction, β_{iso} , at $k_{\text{low}} = 0.002 \text{ Mpc}^{-1}$ and $k_{\text{high}} = 0.100 \text{ Mpc}^{-1}$, the primordial correlation fraction, $\cos \Delta$, the adiabatic spectral index, n_{RR} , the isocurvature spectral index, n_{II} , and the correlation spectral index, $n_{\text{RI}} = (n_{\text{RR}} + n_{\text{II}})/2$, with *Planck* TT+lowP data (dashed curves) and TT, TE, EE+lowP data (solid curves), for the generally-correlated mixed ADI+CDi (black), ADI+NDi (red), and ADI+NVi (blue) models. All these parameters are derived, and the distributions shown here result from a uniform prior on the primary parameters, as detailed in Eqs. (132)–(134). However, the effect of the non-flat derived-parameter priors is negligible for all parameters except for n_{II} (and n_{RI}) where the prior biases the distribution toward one. With TT+lowP, the flatness of $\beta_{\text{iso}}(k_{\text{high}})$ in the CDi case up to a “threshold” value of about 0.5 is a consequence of the $(k/k_{\text{eq}})^{-2}$ damping of its transfer function as explained in Footnote 17.

depth τ more tightly than the high- ℓ temperature and low- ℓ polarization alone (Planck Collaboration XIII 2016). As there is a strong degeneracy between τ and the primordial (adiabatic) perturbation power \mathcal{P}_{RR} (denoted in the other sections of this paper by A_s), it is natural that adding the lensing data leads to stronger constraints on \mathcal{P}_{RR} . Moreover, replacing the low- ℓ likelihood *Planck* lowP by *Planck* lowP+WP constrains τ better (Planck Collaboration XIII 2016). In the ADI+CDi case the effect of this replacement was very similar to adding the *Planck* lensing data (see also Table 16). Although the *Planck* lensing data do not directly constrain the isocurvature contribution,²⁰ they can shift and tighten the constraints on some derived isocurvature parameters by affecting the favoured values of the standard parameters (present even in the pure adiabatic model). However this effect is small as confirmed in Table 16. Therefore, in the figures we do not show 1D posteriors of the derived isocurvature parameters for *Planck* TT+lowP+lensing, since they would be (almost) indistinguishable from *Planck* TT+lowP, as we see in Fig. 44 for the primary non-adiabatic parameters.

In contrast, the high- ℓ polarization data significantly tighten the bounds on isocurvature and cross-correlation parameters, as seen by comparing the dotted grey and red contours in Fig. 44. The significant negative correlation previously allowed by the temperature data in the ADI+CDi and ADI+NDi models is now disfavoured. This is also clearly visible in the 1D posteriors of primordial and observable isocurvature and cross-correlation fractions shown, respectively, in Figs. 45 and 46. Note how the $\cos \Delta$ and α_{RI} parameters are driven towards zero by the inclusion of the high- ℓ TE, EE data (from the dashed to the solid lines) in the ADI+CDi and ADI+NDi cases. We also observed that when the lowP data are replaced by a simple Gaussian prior on the reionization optical depth ($\tau = 0.078 \pm 0.019$), the trend is similar. The high- ℓ ($\ell \geq 30$) *Planck* TT data allow a large negative correlation, while the high- ℓ *Planck* TE, EE data prefer positive correlation. This is clearly seen in Fig. 47 for the ADI+CDi case. The best-fit values show an even more dramatic

effect. We find $\cos \Delta = -0.55$ with TT+lowP, and $+0.15$ with TT, TE, EE+lowP.

Hence there is a competition between the temperature and polarization data that balances out and yields almost symmetric results about zero correlation (except in the ADI+NVi case). The isocurvature auto-correlation amplitude is also strongly reduced, especially in the ADI+CDi case. The best-fit values are slightly offset from $(\mathcal{P}_{\text{II}}^{(1)}, \mathcal{P}_{\text{II}}^{(2)}) = (0, 0)$, but the pure adiabatic model still lies inside the 68% CL (for ADI+CDi and ADI+NDi) or 95% CL (for ADI+NVi) regions. In summary, the high- ℓ polarization data exhibit a strong preference for adiabaticity, although one should keep in mind the possibility of unaccounted systematic effects in the polarization data, possibly leading to artificially strong constraints. For example, the tendency for polarization to shift the constraints towards positive correlation may be due to particular systematic effects that mimic modified acoustic peak structure, as we discussed in Sect. 11.1.

We also performed a parameter extraction with the *Planck* TT, TE, EE+lowP+lensing data, but this combination did not provide interesting new constraints. We found only a tightening of bounds on the standard adiabatic parameters as in the *Planck* TT+lowP+lensing case.

We provide 95% CL upper limits or ranges for β_{iso} , $\cos \Delta$, and α_{RR} in Table 16. With *Planck* TT+lowP, the constraints on the non-adiabatic contribution to the temperature variance, $1 - \alpha_{\text{RR}}(2, 2500)$, are $(-1.5\%, 1.9\%)$, $(-4.0\%, 1.4\%)$, and $(-2.3\%, 2.4\%)$ in the ADI+CDi, ADI+NDi, and ADI+NVi cases, respectively.²¹ With *Planck* TT, TE, EE+lowP these tighten to $(0.1\%, 1.5\%)$, $(-0.1\%, 2.2\%)$, and $(-2.0\%, 0.8\%)$. In the ADI+CDi case, zero is not in the 95% CL interval, but this should not be considered a detection of non-adiabaticity. For example, as mentioned above, $(\mathcal{P}_{\text{II}}^{(1)}, \mathcal{P}_{\text{II}}^{(2)}) = (0, 0)$ is in the 68% CL region, and the best-fit values are $(\mathcal{P}_{\text{II}}^{(1)}, \mathcal{P}_{\text{II}}^{(2)}) = (1.0 \times 10^{-13}, 3.5 \times 10^{-9})$. Moreover,

²⁰ This is expected, since already with *Planck* TT+lowP, the allowed isocurvature fraction is so small that it hardly affects the lensing potential spectrum, C_ℓ^{dip} .

²¹ These numbers can be positive even if the correlation contribution is negative. This happens whenever $\alpha_{\text{II}} > |\alpha_{\text{RI}}|$. Thus in the observational non-adiabaticity estimator $1 - \alpha_{\text{RR}}(2, 2500)$, the negative numbers are not as pronounced as in the primordial correlation fraction $\cos \Delta$.

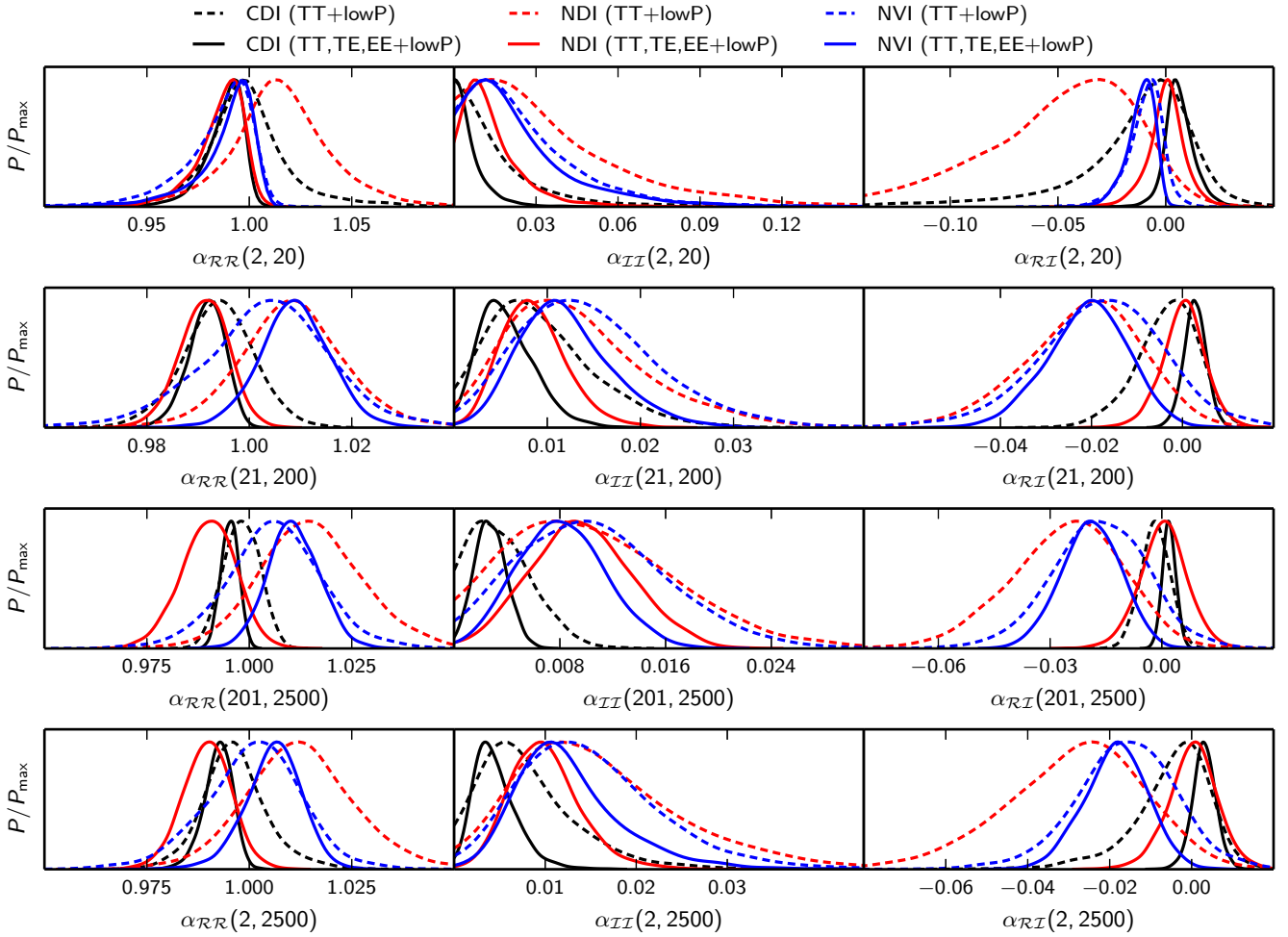


Fig. 46. Constraints on the fractional contribution of the adiabatic (\mathcal{RR}), isocurvature (\mathcal{II}), and correlation (\mathcal{RI}) components to the CMB temperature variance in various multipole ranges, as defined in Eq. (139), with *Planck* TT+lowP data (dashed curves) and with *Planck* TT, TE, EE+lowP data (solid curves). These are shown for the generally-correlated mixed ADI+CDI (black), ADI+NDI (red), or ADI+NVI (blue) models.

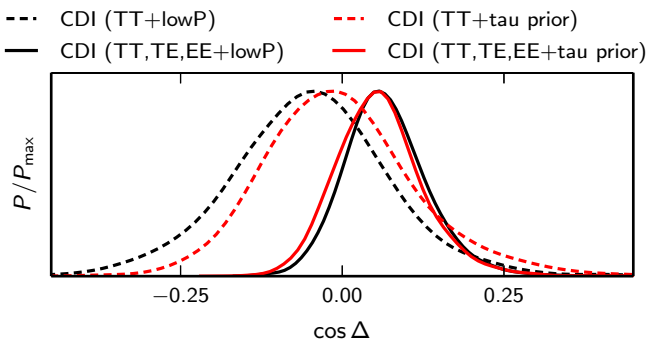


Fig. 47. Constraints on the primordial correlation fraction, $\cos \Delta$, in the mixed ADI+CDI model with *Planck* TT+lowP data (dashed black curve) compared to the case where *Planck* lowP data are not used, but replaced by a Gaussian prior $\tau = 0.078 \pm 0.019$ (dashed red curve). The same exercise is repeated with *Planck* TT, TE, EE data (solid curves) demonstrating that to a great extent the preferred value of $\cos \Delta$ is driven by the high- ℓ data.

Planck TT+lowP it does not even exceed the number of extra degrees of freedom, which is three (see Table 16).

Finally, we checked whether there is any Bayesian evidence for the presence of generally-correlated adiabatic and isocurvature modes. In all cases and with all data combinations studied, the Bayesian model comparison supports the null hypothesis, i.e., adiabaticity. Indeed, the logarithm of the evidence ratio is $\ln B = \ln(P_{\text{ISO}}/P_{\text{ADI}}) < -5$ (i.e., odds of much greater than 150:1 in favour of pure adiabaticity within *Planck*'s accuracy and given the parameterization and prior ranges used in our analysis), except for ADI+NDI with *Planck* TT+lowP+lensing, for which the evidence ratio is slightly larger, -4.6 , corresponding to odds of 1:100 for the ADI+NDI model compared to the pure adiabatic model.

11.3. Robustness of the determination of standard cosmological parameters

Another outcome of our analysis is the robustness of the determination of the standard cosmological parameters against assumptions on initial conditions. Figure 48 shows the 1D marginalized posteriors for several cosmological parameters (not all independent of each other) with the *Planck* TT+lowP data alone. For the first time, we observe that in the presence of

the improvement in χ^2 with respect to the adiabatic model is only 5.3 with 3 extra parameters, so this is not a significant improvement of fit. Indeed, for all generally-correlated mixed models the improvement in χ^2 is very small. In particular, with

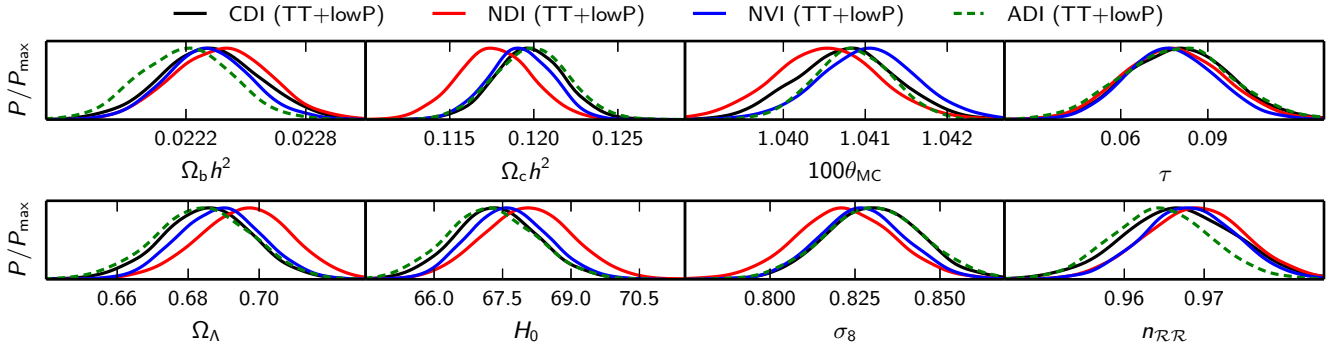


Fig. 48. Constraints on selected “standard” cosmological parameters with *Planck* TT+lowP data for the generally-correlated ADI+CDI (black), ADI+NDI (red), and ADI+NVI (blue) models compared to the pure adiabatic case (ADI, green dashed curves).

one generally-correlated isocurvature mode (CDI, NDI, or NVI), predictions for these parameters remain very stable with respect to the pure adiabatic case. Except for the ADI+NDI case, the posteriors neither broaden nor shift significantly. A small broadening is only observed in the sound horizon angle θ_{MC} , which is naturally the most sensitive parameter to tiny disturbances of the acoustic peak structure. In the ADI+NDI case, the peak of the posterior distribution for some parameters shifts slightly, but the largest shift (for $\Omega_c h^2$) is less than 1σ .

It is striking that a scale-invariant adiabatic spectrum ($n_{RR} = 1$) is excluded at many σ even when isocurvature modes are allowed: at 4.7σ (ADI+CDI), 5.0σ (ADI+NDI), and 5.4σ (ADI+NVI). This illustrates how much the constraining power of the CMB has improved. With WMAP data, there was still a strong degeneracy between, for example, the primordial isocurvature fraction and the adiabatic spectral index (Valiviita & Giannantonio 2009; Savelainen et al. 2013). This degeneracy nearly disappears with *Planck* TT+lowP, and even more so with *Planck* TT, TE, EE+lowP, as shown in the upper panel of Fig. 49. Contours in the $(n_{RR}, \cos \Delta)$ space also shrink considerably, with some correlation remaining between these parameters in the ADI+CDI and ADI+NVI cases (Fig. 49, lower panel).

11.4. CDI and primordial tensor perturbations

A primordial tensor contribution adds extra temperature angular power at low multipoles, where the adiabatic base Λ CDM model predicts slightly more power than seen in the data. Hence allowing for a nonzero tensor-to-scalar ratio r might tighten the constraints on positively-correlated isocurvature, but degrade them in negatively-correlated models. We test how treating r as a free parameter affects the constraints on isocurvature and how allowing for the generally-correlated CDI mode affects the constraints on r . These cases are denoted as “CDI+ r ”. For comparison, we examine the pure adiabatic case in the same parameterization, and call it “ADI+ r ”. We also consider another approach where we fix $r = 0.1$. These cases are named “CDI+ $r = 0.1$ ” and “ADI+ $r = 0.1$ ”.

In the pure adiabatic case (where the curvature and tensor perturbations stay constant on super-Hubble scales), the primordial r is the same as the tensor-to-scalar ratio at the Hubble radius exit of perturbations during inflation, which we call \tilde{r} . However, in the presence of an isocurvature component, \mathcal{P}_{RR} is not constant in time even on super-Hubble scales (García-Bellido & Wands 1996). Instead, the isocurvature component may source \mathcal{P}_{RR} , for example if the background trajectory in the field space is curved between Hubble exit and the end of inflation (Langlois 1999; Langlois & Riazuelo 2000; Gordon et al. 2001; Amendola et al. 2002). As a result, we will have at the primordial time

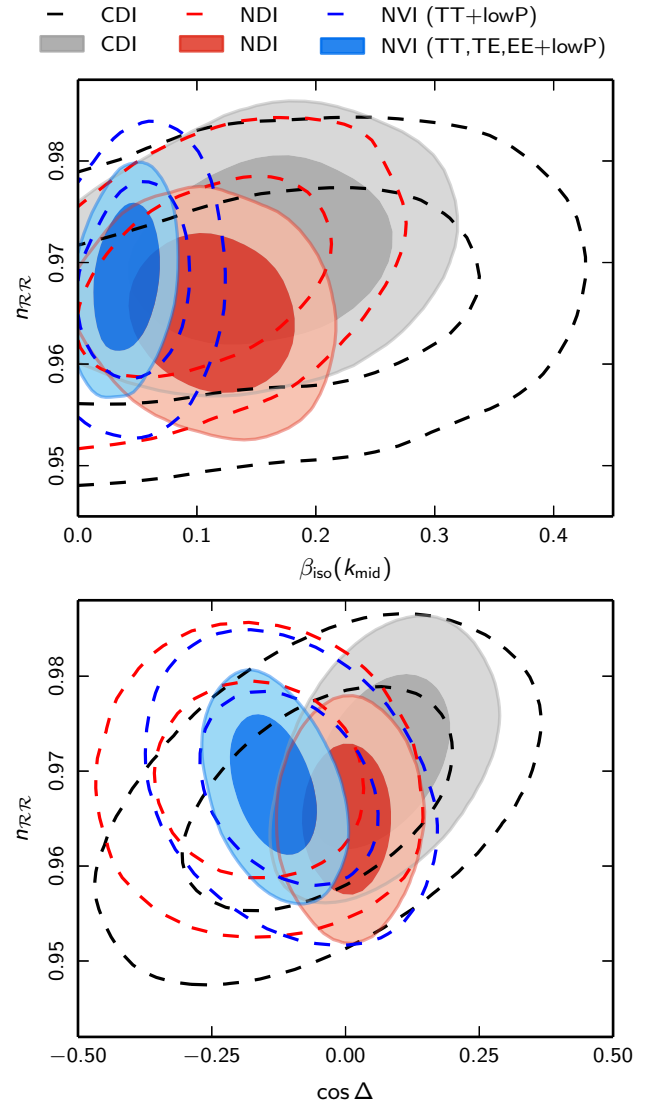


Fig. 49. Dependence of the determination of the adiabatic spectral index n_{RR} (called n_s in the other sections of this paper) on the primordial isocurvature fraction β_{iso} and correlation fraction $\cos \Delta$, with *Planck* TT+lowP data (dashed contours) and with *Planck* TT, TE, EE+lowP data (shaded regions).

$\mathcal{P}_{RR} = \tilde{\mathcal{P}}_{RR}/(1 - \cos^2 \Delta)$, where $\tilde{\mathcal{P}}_{RR}$ is the curvature power at Hubble exit. That is, by the primordial time the curvature perturbation power is larger than at the Hubble radius exit time

(Bartolo et al. 2001; Wands et al. 2002; Byrnes & Wands 2006). Thus we find a relation (Savelainen et al. 2013; Valiviita et al. 2012; Kawasaki & Sekiguchi 2008):

$$r = (1 - \cos^2 \Delta) \tilde{r}, \quad (141)$$

i.e., the tensor-to-scalar ratio at the primordial time (r) is smaller than the ratio at the Hubble radius exit time (\tilde{r}).

The derivation of Eq. (141) assumes that the adiabatic and isocurvature perturbations are uncorrelated at Hubble radius exit ($\cos \tilde{\Delta} = 0$), and that all the possible primordial correlation ($\cos \Delta \neq 0$) appears from the evolution of super-Hubble perturbations between Hubble exit and the primordial time. This is true to leading order in the slow-roll parameters, but inflationary models that break slow roll might produce perturbations that are strongly correlated already at the Hubble radius exit time. In these cases the correlation would depend on the details of the particular model, such as the detailed shape of the potential and the interactions of the fields. However, a generic prediction of slow-roll inflation is that, at Hubble radius exit, the cross-correlation $\tilde{\mathcal{P}}_{RI}$ is very weak, and indeed is of the order of the slow-roll parameters compared to the auto-correlations $\tilde{\mathcal{P}}_{RR}$ and $\tilde{\mathcal{P}}_{II}$ (see, e.g., Byrnes & Wands 2006). Thus, for slow-roll models, $|\cos \tilde{\Delta}| = \mathcal{O}(\text{slow-roll parameters}) \ll 1$.

In our analysis, we fix the tensor spectral index by the leading-order inflationary consistency relation, which now reads (Wands et al. 2002)

$$n_t = -\frac{\tilde{r}}{8} = -\frac{r}{8(1 - \cos^2 \Delta)}. \quad (142)$$

Assuming a uniform prior for r would lead to huge negative n_t whenever $\cos^2 \Delta$ was close to one. Therefore, when studying the CDI+ r case we assume a uniform prior on \tilde{r} at $k = 0.05 \text{ Mpc}^{-1}$ (for details, see Savelainen et al. 2013).

Surprisingly, allowing for a generally-correlated CDI mode (i.e., three extra parameters) hardly changes the constraints on r from those obtained in the pure adiabatic model. In Fig. 50 we demonstrate this in a “standard” plot of $r_{0.002}$ versus adiabatic spectral index.

From Table 16 we notice that, with *Planck* TT+lowP and TT, TE, EE+lowP, fixing r to 0.1 tightens constraints on the primordial isocurvature fraction at large scales. This is as we expected, since both tensor and isocurvature perturbations add power at low ℓ , and the data do not prefer this. However, the shapes of the tensor spectrum and correlation spectrum are such that negative correlation cannot efficiently cancel the unwanted extra power over all scales produced by tensor perturbations (at $\ell \lesssim 70$). Therefore, the correlation fraction $\cos \Delta$ is almost unaffected. However, when we allow r to vary, the cancellation mechanism works to some degree when using *Planck* TT+lowP data, leading to more negative $\cos \Delta$ than without r : with varying r we have $\cos \Delta$ in the range $(-0.43, 0.20)$, while without r it is in $(-0.30, 0.20)$, at 95% CL. As there is now some cancellation of power at large scales, the constraint on $\beta_{\text{iso}}(k_{\text{low}})$ weakens slightly from 0.041 without r to 0.043 with r . On the other hand, the high- ℓ polarization data constrain the correlation to be so close to zero that with *Planck* TT, TE, EE+lowP the results for $\cos \Delta$ with and without r are almost identical.

The mean value of $\cos \Delta$ in the CDI+ r cases is -0.071 (TT+lowP) and -0.076 (TT, TE, EE+lowP). Therefore, $1 - \cos^2 \Delta \approx 0.99$, and so we do not expect a large difference between the primordial r and the Hubble radius exit value \tilde{r} . The smallness of the difference is evident in Table 15. To summarize, CDI hardly affects the determination of r from the *Planck* data,

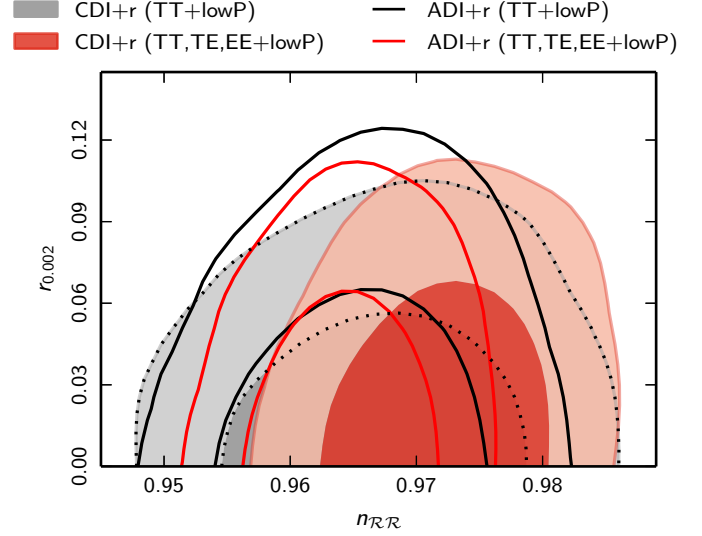


Fig. 50. 68% and 95% CL constraints on the primordial adiabatic spectral index n_{RR} and the primordial tensor-to-scalar ratio r (more accurately, in the CDI+ r model, the primordial tensor-to-curvature power ratio) at $k = 0.002 \text{ Mpc}^{-1}$. Filled contours are for generally-correlated ADI+CDI and solid contours for the pure adiabatic model.

Table 15. 95% CL upper bounds on the tensor-to-scalar ratio (actually the tensor-to-curvature power ratio) at the primordial time, r , and earlier, at the Hubble radius exit time during inflation, \tilde{r} , at $k = 0.05 \text{ Mpc}^{-1}$.

Model (and data)	$r_{0.05}$	$\tilde{r}_{0.05}$	$C_{10}^{\text{tens}}/C_{10}^{\text{scal}}$
CDI+ r (TT+lowP)	0.086	0.089	0.041
ADI+ r (TT+lowP)	0.101	0.101	0.048
CDI+ r (TT, TE, EE+lowP)	0.092	0.092	0.043
ADI+ r (TT, TE, EE+lowP)	0.094	0.094	0.044

Notes. In the pure adiabatic case r and \tilde{r} are equal. In the last column $C_{10}^{\text{tens}}/C_{10}^{\text{scal}}$ indicates the tensor contribution to the temperature angular power at $\ell = 10$ relative to the temperature power from scalar perturbations ($C_{10}^{\text{scal}} = C_{10}^{\text{RR}} + C_{10}^{\text{RI}} + C_{10}^{\text{IR}} + C_{10}^{\text{II}}$).

and allowing for tensor perturbations hardly affects the determination of the non-adiabaticity parameters.

11.5. Special CDI cases

Next we study three one-parameter CDI extensions to the adiabatic model. In all these extensions the isocurvature mode modifies only the largest angular scales, since we either fix n_{II} to unity (“axion”) or to the adiabatic spectral index (“curvaton I/II”). As can be seen from Fig. 43, the polarization E mode at multipoles $\ell \gtrsim 200$ will not be significantly affected by this type of CDI mode. Therefore, these models are much less sensitive to residual systematic effects in the high- ℓ polarization data than the generally-correlated models.

11.5.1. Uncorrelated ADI+CDI (“Axion”)

We start with an uncorrelated mixture of adiabatic and CDI modes ($\mathcal{P}_{RI} = 0$) and make the additional assumption that $\mathcal{P}_{II}^{(2)} = \mathcal{P}_{II}^{(1)}$, i.e., we assume unit isocurvature spectral index, $n_{II} = 1$. Constraints in the $(n_{RR}, \beta_{\text{iso}})$ plane are presented in

Table 16. Constraints on mixed adiabatic and isocurvature models.

Model (and data)	$100\beta_{\text{iso}}(k_{\text{low}})$	$100\beta_{\text{iso}}(k_{\text{mid}})$	$100\beta_{\text{iso}}(k_{\text{high}})$	$100 \cos \Delta$	$100\alpha_{\mathcal{RR}}(2, 2500)$	Δn	$\Delta\chi^2$	$\ln B$
General models:								
CDI (TT+lowP)	4.1	35.4	56.9	[−30:20]	[98.1:101.5]	3	−2.1	−8.8
CDI (TT+lowP+WP)	4.2	35.5	57.2	[−31:23]	[97.9:101.4]	3	−1.8	−9.1
CDI (TT, TE, EE+lowP)	2.0	[3.4:28.1]	[3.1:51.8]	[−6:20]	[98.5:99.9]	3	−5.3	−8.8
CDI (TT, TE, EE+lowP+WP)	2.1	[2.3:28.4]	[2.6:52.1]	[−7:21]	[98.5:99.9]	3	−5.5	−8.2
CDI (TT+lowP+lensing)	4.5	37.9	59.4	[−28:17]	[98.1:101.1]	3	−1.2	−8.8
NDI (TT+lowP)	14.3	22.4	27.4	[−33:1]	[98.6:104.0]	3	−2.0	−5.3
NDI (TT, TE, EE+lowP)	7.3	[3.4:19.3]	[3.5:26.7]	[−9:10]	[97.8:100.1]	3	−5.5	−5.5
NDI (TT+lowP+lensing)	15.8	[1.4:24.1]	[0.3:28.4]	[−32:0]	[98.6:104.0]	3	−2.8	−4.6
NVI (TT+lowP)	8.3	[0.1:10.2]	11.9	[−26:6]	[97.6:102.3]	3	−2.8	−6.3
NVI (TT, TE, EE+lowP)	7.4	[0.9:7.4]	[0.4:8.8]	[−22:−4]	[99.2:102.0]	3	−6.2	−6.5
NVI (TT+lowP+lensing)	9.7	[0.4:11.6]	13.1	[−23:7]	[97.1:102.0]	3	−2.5	−6.5
General models + r :								
CDI+ $r=0.1$ (TT+lowP)	3.4	38.7	63.9	[−33:24]	[98.1:101.4]	3	−5.4	−8.9
CDI+ $r=0.1$ (TT, TE, EE+lowP)	1.6	[4.4:31.7]	[6.9:59.2]	[−6:22]	[98.6:99.9]	3	−6.3	−8.1
CDI+ r (TT+lowP)	4.3	34.9	56.2	[−43:20]	[97.9:102.4]	3	−3.3	−7.7
CDI+ r (TT, TE, EE+lowP)	1.7	[3.9:29.0]	[5.8:53.8]	[−5:21]	[98.6:99.9]	3	−5.1	−7.2
Special CDI cases:								
Uncorrelated, $n_{II} = 1$								
“axion” (TT+lowP)	3.3	3.7	3.8	0	[98.5:100]	1	0.0	−5.2
“axion” (TT, TE, EE+lowP)	3.5	3.8	3.9	0	[98.4:100]	1	−0.2	−4.9
“axion” (TT+lowP+lensing)	3.9	4.3	4.4	0	[98.3:100]	1	0.0	−5.0
Fully correlated, $n_{II} = n_{\mathcal{RR}}$								
“curvaton I” (TT+lowP)	0.18	0.18	0.18	100	[97.5:100.0]	1	−0.1	−8.1
“curvaton I” (TT, TE, EE+lowP)	0.13	0.13	0.13	100	[97.8:99.9]	1	0.0	−7.8
“curvaton I” (TT+lowP+lensing)	0.22	0.22	0.22	100	[97.3:99.7]	1	0.0	−8.5
Fully anti-correlated, $n_{II} = n_{\mathcal{RR}}$								
“curvaton II” (TT+lowP)	0.64	0.64	0.64	−100	[100.5:105.1]	1	−1.1	−5.4
“curvaton II” (TT, TE, EE+lowP)	0.08	0.08	0.08	−100	[100.1:101.8]	1	0.0	−8.9
“curvaton II” (TT+lowP+lensing)	0.52	0.52	0.52	−100	[100.4:104.4]	1	−0.6	−6.3

Notes. For each mixed model, we report 95% CL bounds on the fractional primordial contribution of isocurvature modes at three comoving wavenumbers ($k_{\text{low}} = 0.002 \text{ Mpc}^{-1}$, $k_{\text{mid}} = 0.050 \text{ Mpc}^{-1}$, and $k_{\text{high}} = 0.100 \text{ Mpc}^{-1}$), as well as the scale-independent primordial correlation fraction, $\cos \Delta$. The fractional adiabatic contribution to the observed temperature variance is denoted by $\alpha_{\mathcal{RR}}(2, 2500)$, and from this the nonadiabatic contribution can be calculated as $\alpha_{\text{non-adi}} = 1 - \alpha_{\mathcal{RR}}(2, 2500)$. The number of extra parameters compared with the corresponding pure adiabatic model is denoted by Δn , and $\Delta\chi^2$ is the difference between the χ^2 of the best-fitting mixed and pure adiabatic models. (A negative $\Delta\chi^2$ means that the mixed model is a better fit to the data.) In the last column we give the difference between the logarithm of Bayesian evidences. (A negative $\ln B = \ln(P_{\text{ISO}}/P_{\text{ADI}})$ means that Bayesian model comparison disfavors the mixed model. With our settings of MultiNest the uncertainty in these numbers is about ± 0.5 .)

Fig. 51. This model is the only case for which our new results do not improve over bounds from PCI13. At $k_{\text{mid}} = 0.050 \text{ Mpc}^{-1}$, we find $\beta_{\text{iso}} < 0.038$ (95% CL, TT, TE, EE+lowP; see Table 16), compared with $\beta_{\text{iso}} < 0.039$ using *Planck* 2013 and low- ℓ WMAP data. This is not surprising, since fixing n_{II} to unity implies that bounds are dominated by measurements on very large angular scales, $\ell \lesssim 30$, as can easily be understood from Fig. 43. Hence the results are insensitive to the addition of better high- ℓ temperature data, or new high- ℓ polarization data.

We summarized in PCI13 why an uncorrelated CDI mode with $n_{II} \approx 1$ can be produced in axion models under a number of restrictive assumptions: the Peccei-Quinn symmetry should be broken before inflation; it should not be restored by quantum fluctuations of the inflaton or by thermal fluctuations when the Universe reheats; and axions produced through the misalignment angle should contribute to a sizable fraction (or all) of the dark matter. Under all of these assumptions, limits on β_{iso} can be used

to infer a bound on the energy scale of inflation, using Eq. (73) of PCI13. This bound is strongest when all the dark matter is assumed to be in the form of axions. In that case, the limit on $\beta_{\text{iso}}(k_{\text{mid}})$ for *Planck* TT, TE, EE+lowP gives

$$H_{\text{inf}} < 0.86 \times 10^7 \text{ GeV} \left(\frac{f_a}{10^{11} \text{ GeV}} \right)^{0.408} \quad (95\% \text{ CL}), \quad (143)$$

where H_{inf} is the expansion rate at Hubble radius exit of the scale corresponding to $k_{\text{mid}} = 0.050 \text{ Mpc}^{-1}$ and f_a is the Peccei-Quinn symmetry-breaking energy scale.

11.5.2. Fully correlated ADI+CDI (“Curvaton I”)

Another interesting special case of mixed adiabatic and CDI (or BDI) perturbations is a model where these perturbations are primordially fully correlated and their power spectra have the same shape. These cases are obtained by setting $\mathcal{P}_{\mathcal{RI}}^{(1)} = (\mathcal{P}_{\mathcal{RR}}^{(1)} \mathcal{P}_{II}^{(1)})^{1/2}$,

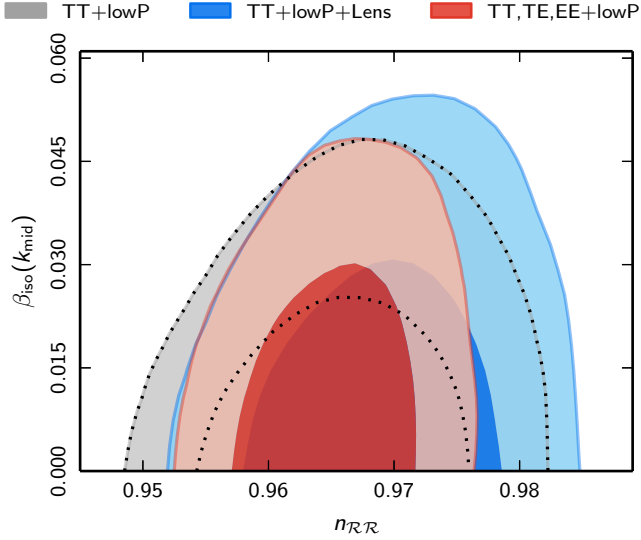


Fig. 51. Uncorrelated ADI+CDI with $n_{II} = 1$ (“axion”).

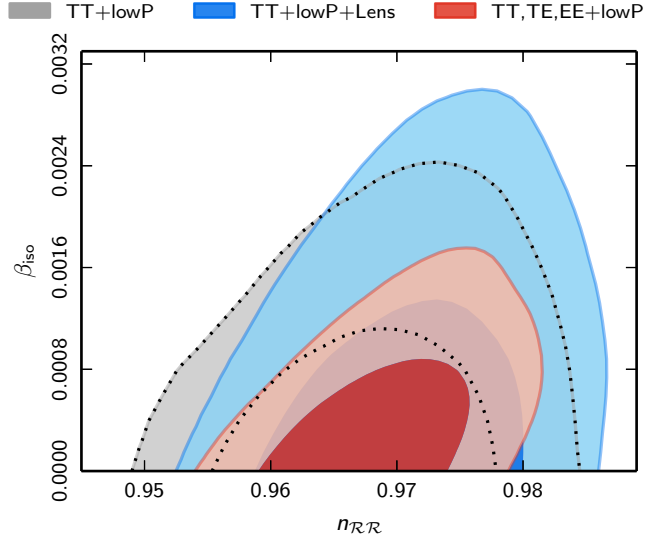


Fig. 52. Fully correlated ADI+CDI with $n_{II} = n_{RR}$ (“curvaton I”). Since the spectral indices are equal, the primordial isocurvature fraction β_{iso} is scale-independent.

which, by condition (136), implies that the corresponding statement holds at scale k_2 and indeed at any scale. In addition, we set $\mathcal{P}_{II}^{(2)} = (\mathcal{P}_{RR}^{(2)}/\mathcal{P}_{RR}^{(1)})\mathcal{P}_{II}^{(1)}$, i.e., $n_{II} = n_{RR}$. From this it follows that β_{iso} is scale-independent. Therefore, this model has only one primary non-adiabaticity parameter, $\mathcal{P}_{II}^{(1)}$.

A physically motivated example of this type of model is the curvaton model (Mollerach 1990; Linde & Mukhanov 1997; Enqvist & Sloth 2002; Moroi & Takahashi 2001; Lyth & Wands 2002; Lyth et al. 2003) with the following assumptions. (1) The average curvaton field value $\bar{\chi}_*$ is sufficiently below the Planck mass when cosmologically interesting scales exit the Hubble radius during inflation. (2) At Hubble radius exit, the curvature perturbation from the inflaton is negligible compared to the perturbation caused by the curvaton. (3) The same is true for any inflaton decay products after reheating. This means that, after reheating, the Universe is homogeneous, except for the spatially varying entropy (i.e., isocurvature perturbation) due to the curvaton field perturbations. (4) Later, CDM is created from the curvaton decay and baryon number after curvaton decay. This corresponds to case 4 presented in Gordon & Lewis (2003). (5) The curvaton contributes a significant amount to the energy density of the Universe at the time of the curvaton’s decay to CDM, i.e., the curvaton decays late enough. (6) The energy density of curvaton particles possibly produced during reheating should be sufficiently low (Bartolo & Liddle 2002; Linde & Mukhanov 2006). (7) The small-scale variance of curvaton perturbations, $\Delta_s^2 = \langle \delta\chi^2 \rangle_s / \bar{\chi}^2$, is negligible, so that it does not significantly contribute to the average energy density on CMB scales; see Eq. (102) in Sasaki et al. (2006). The last two conditions are necessary in order to have an almost-Gaussian curvature perturbation, as required by the *Planck* observations. Indeed, if they are not valid, a large f_{NL}^{local} follows, as discussed below. The conditions (6) and (7) are related, since curvaton particles would add a homogeneous component to the average energy density on large scales, and hence we can describe their effect by $\Delta_s^2 = \rho_{\chi, particles} / \rho_{\bar{\chi}, field}$, where $\rho_{\bar{\chi}, field}$ is the average energy density of the classical curvaton field on large scales; see Eq. (98) in Sasaki et al. (2006). Then the total energy density carried by the curvaton will be $\bar{\rho}_\chi = \rho_{\bar{\chi}, field} + \rho_{\chi, particles}$.

The amount of isocurvature and non-Gaussianity present after curvaton decay depends on the “curvaton decay fraction”

$$r_D = \frac{3\bar{\rho}_\chi}{3\bar{\rho}_\chi + 4\bar{\rho}_{radiation}} \quad (144)$$

evaluated at curvaton decay time. If conditions (6) and (7) do not hold, then the isocurvature perturbation disappears.²²

The curvaton scenario presented here is one of the simplest to test against observations. It should be noted that at least the conditions (1)–(5) listed at the beginning of this subsection should be satisfied simultaneously. Indeed, if we relax some of these conditions, almost any type of correlation can be produced. For example, the relative correlation fraction can be written as $\cos \Delta = \sqrt{\lambda/(1+\lambda)}$, where $\lambda = (8/9)r_D^2\epsilon_*(M_{Pl}/\bar{\chi}_*)^2$. Therefore, the model is fully correlated only if $\lambda \gg 1$. If the slow-roll parameter ϵ_* is very close to zero or the curvaton field value $\bar{\chi}_*$ is large compared to the Planck mass, this model leads to almost uncorrelated perturbations.

As seen in Fig. 52 and Table 16, the upper bound on the primordial isocurvature fraction in the fully-correlated ADI+CDI model weakens slightly when we add the *Planck* lensing data to *Planck* TT+lowP, whereas adding high- ℓ TE, EE tightens the upper bound moderately. With all of these three data combinations, the pure adiabatic model gives an equally good best-fit χ^2 as the fully-correlated ADI+CDI model. Bayesian model comparison strengthens the conclusion that the data disfavour this model with respect to the pure adiabatic model.

The isocurvature fraction is connected to the curvaton decay fraction in Eq. (144) by

$$\beta_{iso} \approx \frac{9(1-r_D)^2}{r_D^2 + 9(1-r_D)^2} \quad (145)$$

(see case 4 in Gordon & Lewis 2003). We can convert the constraints on β_{iso} from Table 16 into constraints on r_D and further

²² Indeed, if curvaton particles are produced during reheating, they can be expected to survive and outweigh other particles at the moment of curvaton decay, but by how much depends on the details of the model. As the curvaton field (during its oscillations) and the curvaton particles have the same equation of state and they decay simultaneously, no isocurvature perturbations are produced.

into the non-Gaussianity parameter assuming a quadratic potential for the curvaton and instantaneous decay²³(Sasaki et al. 2006):

$$f_{\text{NL}}^{\text{local}} = (1 + \Delta_s^2) \frac{5}{4r_D} - \frac{5}{3} - \frac{5r_D}{6}. \quad (146)$$

If conditions (6) and (7) hold, i.e., $\Delta_s^2 = 0$, as implicitly assumed, e.g., in Bartolo et al. (2004a,b), then the smallest possible value of $f_{\text{NL}}^{\text{local}}$ is $-5/4$, which is obtained when $r_D = 1$, and Eqs. (145) and (146) yield for the various *Planck* data sets (at 95% CL):²⁴

$$\begin{aligned} \text{TT+lowP: } \beta_{\text{iso}} < 0.0018 &\Rightarrow 0.9860 < r_D \leq 1 \\ &\Rightarrow -1.250 \leq f_{\text{NL}}^{\text{local}} < -1.220, \end{aligned} \quad (147)$$

$$\begin{aligned} \text{TT+lowP+lensing: } \beta_{\text{iso}} < 0.0022 &\Rightarrow 0.9845 < r_D \leq 1 \\ &\Rightarrow -1.250 \leq f_{\text{NL}}^{\text{local}} < -1.217, \end{aligned} \quad (148)$$

$$\begin{aligned} \text{TT, TE, EE+lowP: } \beta_{\text{iso}} < 0.0013 &\Rightarrow 0.9882 < r_D \leq 1 \\ &\Rightarrow -1.250 \leq f_{\text{NL}}^{\text{local}} < -1.225. \end{aligned} \quad (149)$$

Thus the results for the simplest curvaton model remain unchanged from those presented in PCI13. In order to produce almost purely adiabatic perturbations, the curvaton should decay when it dominates the energy density of the Universe ($r_D > 0.98$), and the non-Gaussianity parameter is constrained to close to its smallest possible value ($-5/4 < f_{\text{NL}}^{\text{local}} < -1.21$), which is consistent with the result $f_{\text{NL}}^{\text{local}} = 2.5 \pm 5.7$ (68% CL, from *T* only) found in Planck Collaboration XVII (2016).

11.5.3. Fully anticorrelated ADI+CDI (“Curvaton II”)

The curvaton scenario or some other mechanism could also produce 100% anticorrelated perturbations, with $n_{\text{II}} = n_{\text{RR}}$. The constraints in the $(n_{\text{RR}}, \beta_{\text{iso}})$ plane are presented in Fig. 53. Examples of this kind of model are provided by cases 2, 3, and 6 in Gordon & Lewis (2003). These lead to a fixed, large amount of isocurvature, e.g., in case 2 to $\beta_{\text{iso}} = 9/10$, and are hence excluded by the data at very high significance. However, case 9 in Gordon & Lewis (2003), with a suitable r_D (i.e., $r_D > R_c$, where $R_c = \rho_c/(\rho_c + \rho_b)$), leads to fully-anticorrelated perturbations and might provide a good fit to the data. In this case CDM is produced by curvaton decay while baryons are created earlier from inflaton decay products and do not carry a curvature perturbation. We obtain a very similar expression to Eq. (145), namely

$$\beta_{\text{iso}} \approx \frac{9(1 - r_D/R_c)^2}{r_D^2 + 9(1 - r_D/R_c)^2}. \quad (150)$$

²³ The formula $f_{\text{NL}}^{\text{local}} = 5/(4r_D)$ is often quoted or utilized, particularly in the older curvaton literature. This result, which follows from considering only squares of first order perturbations, is valid when r_D is close to zero (i.e., when $f_{\text{NL}}^{\text{local}}$ is very large). However, when r_D is close to unity or $f_{\text{NL}}^{\text{local}} \lesssim 10$, which is the case with the *Planck* measurements, the second and third terms of Eq. (146) are crucial. These follow from second order perturbation theory calculations. Coincidentally, if one erroneously uses the expression $5/(4r_D)$ in the limit $r_D \rightarrow 1$, one obtains the result $+5/4$, whereas the correct formula (146) with $\Delta_s^2 = 0$ leads to $-5/4$ when $r_D \rightarrow 1$.

²⁴ However, if Δ_s^2 was non-negligible, then all the constraints on $f_{\text{NL}}^{\text{local}}$ would shift upward. For example, with $\Delta_s^2 = 1$, our constraints on β_{iso} would translate to $0 \leq f_{\text{NL}}^{\text{local}} \leq 0.03$. On the other hand, the *Planck* constraint of $f_{\text{NL}}^{\text{local}}$ can be converted to an upper bound $\Delta_s^2 = \rho_{\chi, \text{particles}}/\rho_{\chi, \text{field}} < 8.5$ (95% CL from *T* only) as shown in Planck Collaboration XVII (2016).

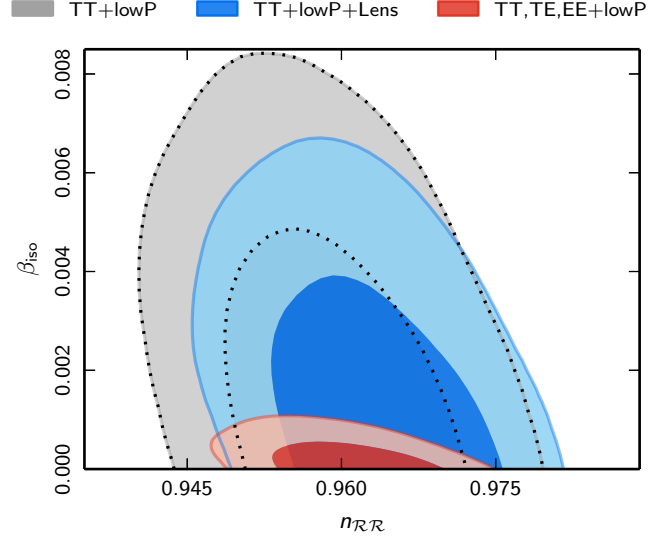


Fig. 53. Fully anticorrelated ADI+CDI with $n_{\text{II}} = n_{\text{RR}}$ (“curvaton II”).

We convert this to an approximate constraint on r_D by fixing R_c to its best-fit value, $R_c = 0.8437$ (*Planck* TT+lowP), within this model. The results for the various *Planck* data sets are:

$$\begin{aligned} \text{TT+lowP: } \beta_{\text{iso}} < 0.0064 &\Rightarrow 0.8437 < r_D < 0.8632 \\ &\Rightarrow -0.9379 < f_{\text{NL}}^{\text{local}} < -0.8882, \end{aligned} \quad (151)$$

$$\begin{aligned} \text{TT+lowP+lensing: } \beta_{\text{iso}} < 0.0052 &\Rightarrow 0.8437 < r_D < 0.8612 \\ &\Rightarrow -0.9329 < f_{\text{NL}}^{\text{local}} < -0.8882, \end{aligned} \quad (152)$$

$$\begin{aligned} \text{TT, TE, EE+lowP: } \beta_{\text{iso}} < 0.0008 &\Rightarrow 0.8437 < r_D < 0.8505 \\ &\Rightarrow -0.9056 < f_{\text{NL}}^{\text{local}} < -0.8882. \end{aligned} \quad (153)$$

After all the tests conducted in this section, both for the generally-correlated CDI, NDI, and NVI cases as well as for the special CDI cases, we conclude that within the spatially flat base Λ CDM model, the initial conditions of perturbations are consistent with the hypothesis of pure adiabaticity, a conclusion that is also supported by the Bayesian model comparison. Moreover, Planck Collaboration XVII (2016) reports a null detection of *isocurvature non-Gaussianity*, with polarization improving constraints significantly.

12. Statistical anisotropy and inflation

A key prediction of standard inflation, which in the present context includes all single field models of inflation as well as many multi-field models, is that the stochastic process generating the primordial cosmological perturbations is completely characterized by its power spectrum, constrained by statistical isotropy to depend only on the multipole number ℓ . This statement applies at least to the accuracy that can be probed using the CMB given the limitations imposed by cosmic variance, since all models exhibit *some* level of non-Gaussianity. Nevertheless, more general Gaussian stochastic processes can be envisaged for which one or more special directions on the sky are singled out, so that the expectation values for the temperature multipoles take the form

$$\langle a_{\ell m}^T (a_{\ell' m'}^T)^* \rangle = C_{\ell m; \ell' m'}^{\text{TT}}, \quad (154)$$

rather than the very special form

$$\langle a_{\ell m}^T (a_{\ell' m'}^T)^* \rangle = C_{\ell}^{\text{TT}} \delta_{\ell, \ell'} \delta_{m, m'}, \quad (155)$$

which is the only possibility consistent with statistical isotropy.

The most general form for a Gaussian stochastic process on the sphere violating the hypothesis of statistical isotropy in Eq. (154) is too broad to be useful, given that we have only one sky to analyse. For $\ell < \ell_{\max}$, there are $O(\ell_{\max}^2)$ multipole expansion coefficients, compared with $O(\ell_{\max}^4)$ model parameters. Therefore, in order to make some progress on testing the hypothesis of statistical isotropy, we must restrict ourselves to examining only the simplest models violating statistical isotropy, for which the available data can establish meaningful constraints and for which one can hope to find a simple theoretical motivation.

12.1. Asymmetry: observations versus model building

In one simple class of statistically anisotropic models, we start with a map produced by a process respecting statistical isotropy, which becomes modulated by another field in the following manner to produce the observed sky map:

$$\delta T_{\text{sky}}(\hat{\Omega}) = (1 + M(\hat{\Omega})) \delta T_{\text{s-i}}(\hat{\Omega}), \quad (156)$$

where $\hat{\Omega}$ denotes a position on the celestial sphere and $\delta T_{\text{s-i}}(\hat{\Omega})$ is the outcome of the underlying statistically isotropic process before modulation. Roughly speaking, where the modulating field $M(\hat{\Omega})$ is positive, power on scales smaller than the scale of variation of $M(\hat{\Omega})$ is enhanced, whereas where $M(\hat{\Omega})$ is negative, power is suppressed. We refer to this as a “power asymmetry.” If $M(\hat{\Omega}) = A \hat{d} \cdot \hat{\Omega}$, we have a model of dipolar modulation with amplitude A and direction \hat{d} , but higher-order or mixed modulation may also be considered, such as a quadrupole modulation or modulation by a scale-invariant field $M(\hat{\Omega})$, to name just a few special cases. Alternatively, and more closely tied to physical models, we can consider modulations of the position- or k -space fluctuations.

In Planck Collaboration XXIII (2014) and Planck Collaboration XVI (2016), the details of constructing efficient estimators for statistical anisotropy, in particular in the presence of realistic data involving sky cuts and possibly incompletely removed foreground contamination, are considered in depth. In addition, the question of the statistical significance of any detected “anomalies” from the expectations of base Λ CDM is examined in detail. Importantly, in the *absence* of a particular inflationary model for such an observed anomaly, the significance should be corrected for the “multiplicity of tests” that *could* have resulted in similarly-significant detections (i.e., for the “look elsewhere effect”), although applying such corrections can be ambiguous. In this paper, however, we consider only forms of statistical anisotropy that are predicted by specific inflationary models, and hence such corrections will not be necessary.

Several important questions can be posed regarding the link between statistical isotropy and inflation. In particular, we can ask the following questions. (1) Does a statistically significant finding of a violation of statistical isotropy falsify inflation? (2) If not, what sort of non-standard inflation could produce the required departure from statistical isotropy? (3) What other perhaps non-inflationary models could also account for the violation of statistical isotropy? In this section, we begin to address these questions by assessing the viability of an inflationary model for dipolar asymmetry, as well as by placing new limits on the presence of quadrupolar power asymmetry.

For the case of the observed dipolar asymmetry examined in detail in Planck Collaboration XVI (2016), there are two aspects that make inflationary model building difficult. First is the

problem of obtaining a significant amplitude of dipole modulation. In Planck Collaboration XVI (2016) the asymmetry was found to have amplitude $A \approx 6\text{--}7\%$ on scales $2 \leq \ell \leq 64$. This compares with the expected value of $A = 2.9\%$ on these scales due to cosmic variance in statistically isotropic skies. One basic strategy for incorporating the violation of statistical isotropy into inflation is to consider some form of multi-field inflation and use one of the directions orthogonal to the direction of slow roll as the field responsible for the modulation. Obtaining the required modulation is problematic because most extra fields in multi-field inflation become disordered in a nearly scale-invariant way, just like the fluctuations in the field parallel to the direction of slow roll. What is needed resembles a pure gradient with no fluctuations of shorter wavelength. In Liddle & Cort s (2013) it was proposed that such a field could be produced using the supercurvature mode of open inflation. (See however the discussion in Kanno et al. 2013.) Also, in order to respect the f_{NL} constraints, one must avoid that the modulating field leave a direct imprint on the temperature anisotropy.

The second aspect which makes model building difficult for dipolar asymmetry is that the measured amplitude is strongly scale dependent, and on scales $\ell \gtrsim 100$ no significant detection of a dipolar modulation amplitude is made (Planck Collaboration XVI 2016), once our proper motion has been taken into account (Planck Collaboration XXVII 2014). On the other hand, the simplest models are scale-free and produce statistical anisotropy of the type described by the ansatz in Eq. (156), for which the bulk of the statistical weight should be detected at the resolution of the survey. To resolve this difficulty, Erickcek et al. (2009) proposed modulating CDI fluctuations generated within the framework of a curvaton scenario, because, unlike adiabatic perturbations, CDI perturbations entering the Hubble radius before last scattering contribute negligibly to the CMB fluctuations (recall Fig. 43).

The situation for the quadrupolar power asymmetry is different from the dipolar case in that no detection is currently claimed. Model building is easier than the dipolar case since no pure gradient modes are required, but also more difficult in that anisotropy during inflation is needed. While the isotropy of the recent expansion of the Universe (i.e., since the CMB fluctuations were first imprinted) is tightly constrained, bounds on a possible anisotropic expansion at early times are much weaker. Ackerman et al. (2007) proposed using constraints on the quadrupolar statistical anisotropy of the CMB to probe the isotropy of the expansion during inflation – that is, during the epoch when the perturbations now seen in the CMB first exited the Hubble radius. Assuming an anisotropic expansion during inflation, Ackerman et al. (2007) computed its impact on the three-dimensional power spectrum on super-Hubble scales by integrating the mode functions for the perturbations during inflation and beyond. Several sources of such anisotropy have been proposed, such as vector fields during inflation (Dimastrogiovanni et al. 2010; Soda 2012; Maleknejad et al. 2013; Schmidt & Hui 2013; Bartolo et al. 2013; Naruko et al. 2015), or an inflating solid or elastic medium (Bartolo et al. 2013).

12.2. Scale-dependent modulation and idealized estimators

The ansatz in Eq. (156) expressed in angular space may be rewritten in terms of the multipole expansion and generalized to include scale-dependent modulation by means of Wigner $3j$ symbols:

$$\langle a_{\ell m}^T a_{\ell' m'}^T \rangle = \sum_{L=0}^{\infty} \sum_{M=-L}^{+L} C_{\ell; \ell'; L, M}^{\text{TT}} \begin{pmatrix} \ell & \ell' & L \\ m & m' & M \end{pmatrix}. \quad (157)$$

Because of the symmetry of the left-hand side, the coefficients $C_{\ell;\ell';L,M}^{\text{TT}}$ acquire a phase $(-1)^{\ell+\ell'+L}$ under interchange of ℓ and ℓ' . This is the most general form consistent with the hypothesis of Gaussianity. The usual isotropic power spectrum, which is the generic prediction of simple models of inflation, includes only the $L = 0$ term, where $C_{\ell;\ell';0,0}^{\text{TT}} = C_{\ell}^{\text{TT}}$ and the Wigner $3j$ symbol provides the $\delta_{\ell,\ell'}\delta_{m,m'}$ factor. The coefficients $C_{\ell;\ell';L,M}^{\text{TT}}$ with $L > 0$ introduce statistical anisotropy.

If we assume that there is a common vector (corresponding to $L = 1$ on the celestial sphere) that defines the direction of the anisotropy of the power spectrum for all the terms of $L = 1$, we may adopt a more restricted ansatz for the bipolar modulation, so that

$$C_{\ell;\ell';1,M}^{\text{TT}} = C_{\ell,\ell'}^1 X_M^{(1)}, \quad (158)$$

where we assume that X_M is normalized (i.e., $\sum_M X_M X_M^* = 1$). In such a model, supposing that $C_{\ell,\ell'}^1$ is theoretically determined, but the orientation of the unit vector X_M is random and isotropically distributed on the celestial sphere, we may construct the following quadratic estimator for the direction:

$$X_M^{(L)} = \sum_{\ell,m} \sum_{\ell',m'} \frac{w_{\ell,\ell';L}}{(2L+1)(C_{\ell})^{1/2} (C_{\ell'})^{1/2}} \times \begin{pmatrix} \ell & \ell' & L \\ m & m' & M \end{pmatrix} a_{\ell m}^T a_{\ell' m'}^T, \quad (159)$$

where the weights for the unbiased minimum variance estimator are given by

$$w_{\ell,\ell';L} = C_{\ell,\ell'}^L \left(\sum_{\ell,\ell'} C_{\ell,\ell'}^L \right)^{-1}. \quad (160)$$

This construction, which for the $L = 1$ case may be found in [Moss et al. \(2011\)](#) and [Planck Collaboration XVI \(2016\)](#), may be readily generalized to $L > 1$ in the above way.

12.3. Constraining inflationary models for dipolar asymmetry

In this section, we confront with *Planck* data the modulated curvaton model of [Erickcek et al. \(2009\)](#), which attempts to explain the observed large-scale power asymmetry via a gradient in the background curvaton field. In this model, the curvaton decays after CDM freeze out, which results in a nearly-scale-invariant isocurvature component between CDM and radiation. In the viable version of this scenario, the curvaton contributes negligibly to the CDM density. A long-wavelength fluctuation in the curvaton field initial value σ_* is assumed, with amplitude $\Delta\sigma_*$ across our observable volume. This modulates the curvaton isocurvature fluctuations according to $S_{\sigma\gamma} \approx 2\delta\sigma_*/\sigma_*$. The curvaton produces all of the final CDI fluctuations, which are nearly scale invariant, as well as a component of the final adiabatic fluctuations. Hence both of these components will be modulated, and the parameter space of the model will be constrained by observations of the power asymmetry on large and small scales, as well as the full-sky CDI fraction. In practice, the very tight constraints on small scale power asymmetry obtained in [Planck Collaboration XVI \(2016\)](#) imply a small curvaton adiabatic component, which implies that the CDI and adiabatic fluctuations are only weakly correlated. This model easily satisfies constraints due to the CMB dipole, quadrupole, and non-Gaussianity ([Erickcek et al. 2009](#)).

There are two main parameters that we constrain for this model. First, the fraction of adiabatic fluctuations due to the curvaton ξ is defined as

$$\xi \equiv \frac{\Sigma_{\sigma}^2 \mathcal{P}_{\sigma}}{\mathcal{P}_{\mathcal{R}_{\text{inf}}} + \Sigma_{\sigma}^2 \mathcal{P}_{\sigma}}. \quad (161)$$

Here, $\mathcal{P}_{\mathcal{R}_{\text{inf}}}$ and \mathcal{P}_{σ} are the inflaton and curvaton primordial power spectra, respectively, and Σ_{σ} is the coupling from curvaton isocurvature to adiabatic fluctuations. (Up to a sign, ξ is equal to the correlation parameter.) Next, the coupling of curvaton to CDI, $M_{\text{CDI}\sigma}$, is determined by the constant $\kappa \equiv M_{\text{CDI}\sigma}/R \gtrsim -1$, where

$$R \equiv \frac{3\Omega_{\sigma}}{4\Omega_{\gamma} + 3\Omega_{\sigma} + 3\Omega_{\text{CDM}}} \quad (162)$$

and all density parameters are evaluated just prior to curvaton decay. The isocurvature fraction can be written in terms of these two parameters by

$$\beta_{\text{iso}} = \frac{9\kappa^2 \xi}{1 + 9\kappa^2 \xi}. \quad (163)$$

These parameters determine the modulation of the CMB temperature fluctuations via $\Delta C_{\ell}/C_{\ell} = 2K_{\ell}\Delta\sigma_*/\sigma_*$, where ([Erickcek et al. 2009](#))

$$K_{\ell} \equiv \xi \frac{C_{\ell}^{\text{ad}} + 9\kappa^2 C_{\ell}^{\text{iso}} + 3\kappa C_{\ell}^{\text{cor}}}{C_{\ell}^{\text{ad}} + \xi (9\kappa^2 C_{\ell}^{\text{iso}} + 3\kappa C_{\ell}^{\text{cor}})}. \quad (164)$$

Here C_{ℓ}^{ad} , C_{ℓ}^{iso} , and C_{ℓ}^{cor} are the adiabatic, CDI, and correlated power spectra calculated for unity primordial spectra.

Note that this modulated curvaton model contains some simple special cases. For $\kappa = 0$, we have a purely adiabatic (i.e., scale-invariant) modulation. This is equivalent to a modulation of the scalar amplitude, A_s . On the other hand, if we take the limit $\kappa \rightarrow \infty$, with fixed $\kappa^2 \xi$ (i.e., with fixed isocurvature fraction β_{iso}), we obtain a pure CDI modulation. For $\kappa = \xi = 0$ we have no modulation, i.e., we recover base Λ CDM. Therefore this model is particularly useful for examining a range of possible modulations within the context of a concrete framework.

In order to constrain this model, we use a formalism which was developed to determine the signatures of potential gradients in physical parameters in the CMB ([Moss et al. 2011](#)), and which is used to examine dipolar modulation and described in detail in [Planck Collaboration XVI \(2016\)](#). This approach is well-suited to testing the modulated curvaton model since it can accommodate scale-dependent modulations. Briefly, we write the temperature anisotropy covariance given a gradient ΔX_M in a parameter X as

$$C_{\ell m \ell' m'} = C_{\ell} \delta_{\ell \ell'} \delta_{m m'} + (-1)^m \frac{\delta C_{\ell \ell'}}{2} [(2\ell+1)(2\ell'+1)]^{1/2} \times \begin{pmatrix} \ell & \ell' & 1 \\ 0 & 0 & 0 \end{pmatrix} \sum_M \Delta X_M \begin{pmatrix} \ell & \ell' & 1 \\ -m & m' & M \end{pmatrix}, \quad (165)$$

where $\delta C_{\ell \ell'} \equiv dC_{\ell}/dX + dC_{\ell'}/dX$. Note that this covariance takes the form of Eqs. (157) and (158), with

$$C_{\ell;\ell'}^1 = \frac{\delta C_{\ell \ell'}}{2} [(2\ell+1)(2\ell'+1)]^{1/2} \begin{pmatrix} \ell & \ell' & 1 \\ 0 & 0 & 0 \end{pmatrix}. \quad (166)$$

We then construct a maximum likelihood estimator for the gradient components. We use C^{-1} filtered data (Planck Collaboration XV 2016) and perform a mean-field subtraction, giving

$$\Delta\hat{X}_M = \frac{3}{f_{1M}} \sum_{\ell m \ell' m'} (-1)^m C_{\ell; \ell'}^1 \begin{pmatrix} \ell & \ell' & 1 \\ -m & m' & M \end{pmatrix} \times (T_{\ell m} T_{\ell' m'}^* - \langle T_{\ell m} T_{\ell' m'}^* \rangle) \left[\sum_{\ell \ell'} (C_{\ell; \ell'}^1)^2 F_\ell F_{\ell'} \right]^{-1}. \quad (167)$$

Here f_{1M} is a normalization correction due to the applied mask, $M(\Omega)$, and is given by

$$f_{1M} \equiv \int d\Omega Y_{1M}^*(\Omega) M(\Omega). \quad (168)$$

The $T_{\ell m}$ are the filtered data and $F_\ell \equiv \langle T_{\ell m} T_{\ell m}^* \rangle$. Note that the lack of aberration in the *Planck* Full Focal Plane simulations (Planck Collaboration XII 2016) is expected to have negligible effect on this analysis and on that of the quadrupolar modulation in the next subsection, since the CDI modulation is heavily suppressed for $\ell \gtrsim 500$, whereas the effect of aberration has a very different ℓ dependence and will bias the modulation signal for $\ell \lesssim 1000$ at an insignificant level.

In practice, exploring the parameter space of the model is sped up dramatically by binning the estimator defined in Eq. (167) into bins of width $\Delta\ell = 1$, which means that the estimators only need to be calculated once (Planck Collaboration XVI 2016). Finally, for the modulated curvaton model we identify

$$\frac{dC_\ell}{dX} = 2K_\ell C_\ell. \quad (169)$$

Note that for our constraints we fix the curvaton gradient to its maximum value, $\Delta\sigma_*/\sigma_* = 1$. Therefore, our constraints are conservative, since smaller $\Delta\sigma_*/\sigma_*$ would only reduce the modulation that this model could produce.

The temperature anisotropies measured by *Planck* constrain the modulated curvaton parameters κ and ξ via Eqs. (164) and (167). Figure 54 shows the constraints in this parameter space evaluating the estimator to $\ell_{\max} = 1000$. The maximum likelihood region corresponds to a band at $\kappa \gtrsim 3$. For parameters in this region, the model produces a large-scale asymmetry via a mainly-CDI modulation. However, the *amplitude* of this large-scale asymmetry is lower than the 6–7% actually observed (Planck Collaboration XVI 2016). The reason is that, had a CDI modulation produced all of the large-scale asymmetry, the consequent small-scale asymmetry (due to the shape of the scale-invariant CDI spectrum) would be larger than the *Planck* observations allow. The allowed CDI modulation is further reduced by the *Planck* 95% upper limit on an uncorrelated, scale-invariant (“axion”-type) isocurvature component, $\beta_{\text{iso}} < 0.033$, from Sect. 11. Imposing this constraint reduces the available parameter space in the κ - ξ plane via Eq. (163), as illustrated in Fig. 54.

The best fit in Fig. 54 corresponds to $\Delta\chi^2 = -6.8$ relative to base Λ CDM, for two extra parameters. In order to assess how likely such an improvement would be in statistically isotropic skies, we note that the best-fit CDI modulation amplitude is very close to the mean amplitude expected due to cosmic variance, as calculated directly from Eq. (167). More precisely, since the amplitude is χ^2 distributed with three degrees of freedom, i.e., Maxwell-Boltzmann distributed, we conclude that about 44% of statistically isotropic skies will exhibit a measured

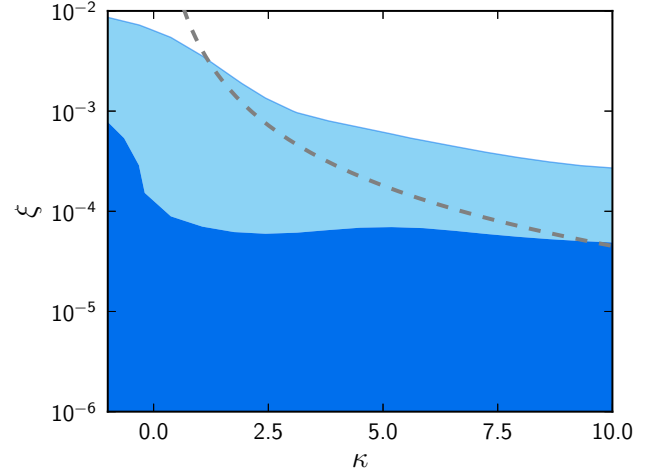


Fig. 54. 68% and 95% CL regions in the modulated isocurvature model parameter space using the *Planck* temperature data up to $\ell_{\max} = 1000$ (contours). The region above the dashed curve is ruled out by the *Planck* constraint on an uncorrelated, scale-invariant isocurvature component.

(via Eq. (167)) isocurvature modulation larger than that of the actual sky.

To summarize, the modulated curvaton model can only produce a small part of the observed large-scale asymmetry, and what it can produce is entirely consistent with cosmic variance in a statistically isotropic sky. Hence we must favour the base Λ CDM model over this model. Finally, note that further generalizing the model (e.g., to allow non-scale-invariant CDI spectra) may allow more large-scale asymmetry to be produced and hence result in an improved $\Delta\chi^2$, at the expense of more parameters. On the other hand, the neutrino isocurvature modes are not expected to fit the observed asymmetry well due to their approximate scale invariance (see Fig. 43).

12.4. Constraints on quadrupolar asymmetry generated during inflation

In this section we assume a quadrupolar directional dependence of the primordial scalar power spectrum about some axis $\pm\hat{\mathbf{d}}$ and having a scale-dependent amplitude $g(k)$. More specifically, we assume

$$\mathcal{P}_{\mathcal{R}}(\mathbf{k}) = \mathcal{P}_{\mathcal{R}}^0(k) \left\{ 1 + g(k) \left[(\hat{\mathbf{k}} \cdot \hat{\mathbf{d}})^2 - \frac{1}{3} \right] \right\}, \quad (170)$$

which can be rewritten as

$$\mathcal{P}_{\mathcal{R}}(\mathbf{k}) = \mathcal{P}_{\mathcal{R}}^0(k) \left[1 + \sum_M g_{2M}(k) Y_{2M}(\hat{\mathbf{k}}) \right], \quad (171)$$

where

$$g_{2M}(k) \equiv \frac{8\pi}{15} g(k) Y_{2M}^*(\hat{\mathbf{d}}), \quad (172)$$

with $g_{2M}(k)$ satisfying $g_{2,-M}(k) = (-1)^M g_{2M}^*(k)$. In this analysis, we will treat the modulation scale dependence as a power law, $g(k) = g_*(k/k_*)^q$, and consider five values of the spectral index, namely $q = -2, -1, 0, 1$, and 2 . Importantly, for $q \neq 0$ our constraints on g_* will depend on the pivot scale, chosen as $k_* = 0.05 \text{ Mpc}^{-1}$ as elsewhere in this paper. Models have been proposed predicting both positive and negative g_* (see, e.g. Tsujikawa 2014), so we keep the sign of g_* free.

Often in the literature the term $-g(k)/3$ is not included in the modulated power spectrum, Eq. (170). Our form sets the modulation monopole to zero, so that there is no correction to the isotropic power spectrum dependent on $g(k)$. We do this because for large $|q|$ the correction would require a joint analysis with the isotropic power spectrum likelihood. Inflationary models have been proposed which predict both forms. For example, the model in Ohashi et al. (2013) includes the modulation monopole, while the model in Libanov & Rubakov (2010) does not. For $q = 0$ our results apply to both forms due to the degeneracy of a scale-independent correction to $\mathcal{P}_{\mathcal{R}}^0(k)$ with the scalar amplitude, A_s . However, for nonzero tilt a joint analysis would yield tighter constraints on g_* when the monopole correction is present, in which case our results will be conservative.

Given the anisotropic power spectrum of Eq. (171), the statistically anisotropic part of the CMB temperature fluctuations has the following expectation value (Ma et al. 2011):

$$C_{\ell, \ell'; 2, M} = i^{\ell - \ell'} D_{\ell \ell'} g_{2M}(k) \left[\frac{5(2\ell + 1)(2\ell' + 1)}{4\pi} \right]^{\frac{1}{2}} \times \begin{pmatrix} 2 & \ell & \ell' \\ 0 & 0 & 0 \end{pmatrix}, \quad (173)$$

where $D_{\ell \ell'} \equiv 4\pi \int d\ln k \Delta_{\ell, T}^s(k) \Delta_{\ell', T}^s(k) \mathcal{P}_{\mathcal{R}}^0(k) (k/k_*)^q$ and $\Delta_{\ell, T}^s(k)$ denotes the temperature radiation transfer function.

The analysis is carried out using the foreground-cleaned CMB temperature maps Commander, NILC, SEVEM, and SMICA, where we apply the extended common mask UT76. The implementation details of the optimal estimator can be found in Sect. 5.3 of Planck Collaboration XVI (2016). However, here we apply an inverse variance weighted filter that assumes a simple white noise component, but optimally accounts for the mask in the same manner as Planck Collaboration XVII (2014) and Sects. 6.3 and 6.6 of Planck Collaboration XVI (2016). We estimate g_{2M} from the data at multipoles $2 \leq \ell \leq 1200$. The range of multipoles is chosen such that the impact of foreground residuals on the conclusions is insignificant. Neglecting very small scales, however, sacrifices little constraining power because those scales are noise dominated. This conclusion was based on realistic simulations containing residual foregrounds. Moreover, we estimate the statistical uncertainty in g_{2M} with various ℓ_{\max} values using simulations.

Once we have obtained estimates for the five g_{2M} coefficients, we must determine values for the model parameters of interest, namely g_* and $\hat{\mathbf{d}}$. We assume the g_{2M} coefficients to be Gaussian distributed due to cosmic variance. We have explicitly checked this hypothesis with simulations. Hence the likelihood function is

$$\mathcal{L} \propto |G|^{-1/2} \times \exp \left[-\frac{1}{2} (\hat{g}_{2M} - g_{2M}(g_*, \hat{\mathbf{d}}))^T G^{-1} (\hat{g}_{2M} - g_{2M}(g_*, \hat{\mathbf{d}})) \right], \quad (174)$$

where G is the g_{2M} covariance matrix, which is estimated using isotropic simulations. One approach to determining the model parameters would be to use this likelihood to calculate marginalized posterior distributions for g_* , from which mean values and errors could be determined. However, we find that g_* is so poorly constrained that the means and widths thus calculated strongly depend on the prior for g_* . Two sensible priors are uniform in g_* or proportional to g_*^2 [i.e., uniform in the Cartesian components of $(g_*, \hat{\mathbf{d}})$]. In addition, we find that the posterior means are

much closer to zero than the widths, which is due to the approximate degeneracy between a modulation ($g_*, \hat{\mathbf{d}}$) and modulation ($-g_*, \hat{\mathbf{d}}'$), where $\hat{\mathbf{d}}'$ is orthogonal to $\hat{\mathbf{d}}$. In such a situation the degree of consistency between the measured value of g_* and the expectations of cosmic variance in statistically isotropic skies is unclear.

Instead we determine best-fit values for g_* and $\hat{\mathbf{d}}$ by maximizing the likelihood over the three parameters using a grid approach. To characterize how unexpected our best-fit values are in statistically isotropic skies, we repeat the procedure replacing our estimates for g_{2M} from the data with estimates from 1000 isotropic simulations. We finally calculate p -values, which give the fraction of simulations with a larger value of $|g_*|$ than the actual data. Note that from the Bayesian perspective the maximum-likelihood values amount to maximizing the posterior for g_* given a uniform prior on g_* , so that these values will change with a different prior. However, we have checked that the p -values depend only very weakly on the choice of prior.

Table 17 shows the g_* values obtained by minimizing χ^2 as well as the p -values for the data compared to statistically isotropic simulations. Note that the constraints on g_* are strongest for the most negative values of the exponent q . This is because for fixed g_* the largest asymmetry over the range of observable scales occurs for $q = -2$, at the largest scales, due to the location of the pivot scale, k_* . Our limits provide a stringent test of rotational symmetry during inflation. We find no sign of deviation from statistical isotropy.²⁵

13. Combination with BICEP2/Keck Array-Planck cross-correlation

In this section we discuss the implications of the recent constraints on the primordial B -mode polarization from the cross-correlation of the BICEP2 and Keck Array data at 150 GHz with the *Planck* maps at higher frequencies to characterize and remove the contribution from polarized thermal dust emission from our Galaxy (BKP). On its own, the BKP likelihood leads to a 95% CL upper limit of $r < 0.12$, compatible with and independent of the constraints obtained using the 2015 *Planck* temperature and large angular scale polarization in Sect. 5. (Note, however, that the BKP likelihood uses the Hamimeche-Lewis approximation (Hamimeche & Lewis 2008), which requires the assumption of a fiducial model.) The BKP results are also compatible with the *Planck* 2013 Results (Planck Collaboration XVI 2014; Planck Collaboration XXII 2014). The posterior probability distribution for r obtained by BKP peaks away from zero at $r \approx 0.05$, but the region of large posterior probability includes $r = 0$.

Here we combine the baseline two-parameter BKP likelihood using the lowest five B -mode bandpowers with the *Planck* 2015 likelihoods. The two BKP nuisance parameters are the B -mode amplitude and frequency spectral index of the polarized thermal dust emission. The combined analysis yields the following constraint on the tensor-to-scalar ratio:

$$r_{0.002} < 0.08 \quad (95\% \text{ CL, Planck TT+lowP+BKP}), \quad (175)$$

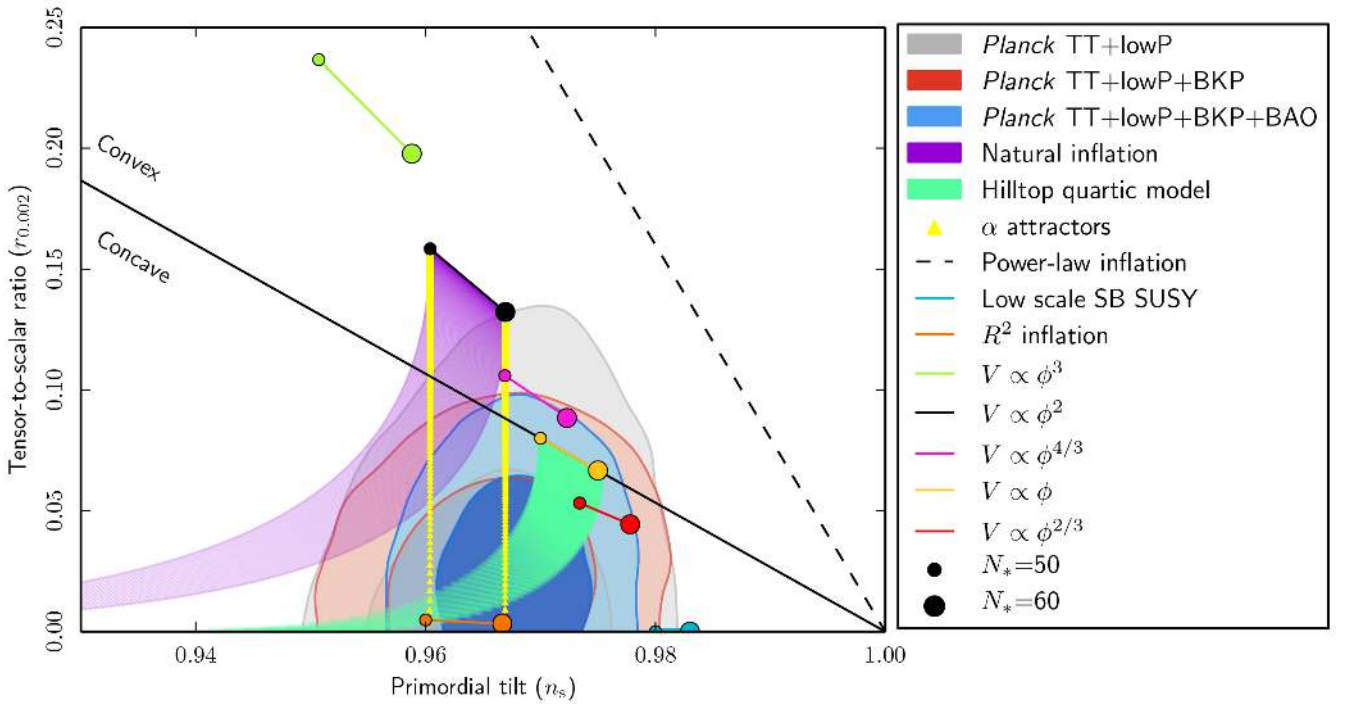
further improving on the upper limits obtained from the different data combinations presented in Sect. 5.

²⁵ The constraints on the *Planck* 2013 data by Kim & Komatsu (2013) should be multiplied by a factor of $\sqrt{2}$ in our normalization.

Table 17. Minimum- χ^2 g_* values for quadrupolar modulation, determined from the Commander, NILC, SEVEM, and SMICA foreground-cleaned maps.

q	Commander		NILC		SEVEM		SMICA	
	g_*	p -value [%]	g_*	p -value [%]	g_*	p -value [%]	g_*	p -value [%]
-2 ...	-7.39×10^{-5}	79.2	-7.66×10^{-5}	79.8	-7.43×10^{-5}	80.6	-7.52×10^{-5}	80.2
-1 ...	5.99×10^{-3}	97.3	6.65×10^{-3}	95.8	6.27×10^{-3}	97.2	6.22×10^{-3}	96.9
0 ...	-2.79×10^{-2}	12.5	-2.38×10^{-2}	26.9	-2.56×10^{-2}	20.7	-2.56×10^{-2}	20.0
1 ...	-2.15×10^{-2}	8.2	-1.79×10^{-2}	23.7	-1.93×10^{-2}	17.8	-1.93×10^{-2}	16.7
2 ...	-1.28×10^{-2}	9.7	-1.07×10^{-2}	23.7	-1.13×10^{-2}	20.4	-1.15×10^{-2}	18.1

Notes. Also given are p -values, defined as the fraction of simulations with larger $|g_*|$ than the data. These results demonstrate that the data are consistent with cosmic variance in statistically isotropic skies.

**Fig. 55.** Marginalized joint 68% and 95% CL regions for n_s and r at $k = 0.002 \text{ Mpc}^{-1}$ from *Planck* alone and in combination with its cross-correlation with BICEP2/Keck Array and/or BAO data compared with the theoretical predictions of selected inflationary models. Note that the marginalized joint 68% and 95% CL regions have been obtained by assuming $dn_s/d\ln k = 0$.

By directly constraining the tensor mode, the BKP likelihood removes degeneracies between the tensor-to-scalar ratio and other parameters. Adding tensors and running, we obtain

$$r_{0.002} < 0.10 \quad (95\% \text{ CL, Planck TT+lowP+BKP}), \quad (176)$$

which constitutes almost a 50% improvement over the *Planck* TT+lowP constraint quoted in Eq. (27). These limits on tensor modes are more robust than the limits using the shape of the C_ℓ^{TT} spectrum alone because scalar perturbations cannot generate B modes irrespective of the shape of the scalar spectrum.

13.1. Implications of BKP on selected inflationary models

Using the BKP likelihood further strengthens the constraints on the inflationary parameters and models discussed in Sect. 6, as seen in Fig. 55. If we set $\epsilon_3 = 0$, the first slow-roll parameter is constrained to $\epsilon_1 < 0.0055$ at 95% CL by

Planck TT+lowP+BKP. With the same data combination, concave potentials are preferred over convex potentials with $\ln B = 3.8$, which improves on the $\ln B = 2$ result obtained from the *Planck* data alone.

Combining with the BKP likelihood strengthens the constraints on the selected inflationary models studied in Sect. 6. Using the same methodology as in Sect. 6 and adding the BKP likelihood gives a Bayes factor preferring R^2 over chaotic inflation with monomial quadratic potential and natural inflation by odds of 403:1 and 270:1, respectively, under the assumption of a dust equation of state during the entropy generation stage. The combination with the BKP likelihood further penalizes the double-well model compared to R^2 inflation. However, adding BKP reduces the Bayes factor of the hilltop models compared to R^2 , because these models can predict a value of the tensor-to-scalar ratio that better fits the statistically insignificant peak at $r \approx 0.05$. See Table 18 for the $\Delta\chi^2$ and the Bayes factors of inflationary models with the same two cases of post-inflationary

Table 18. Results of inflationary model comparison using the cross-correlation between BICEP2/Keck Array and *Planck*.

Inflationary model	$\Delta\chi^2$		$\ln B_{0X}$	
	$w_{\text{int}} = 0$	$w_{\text{int}} \neq 0$	$w_{\text{int}} = 0$	$w_{\text{int}} \neq 0$
$R + R^2/(6M^2)$	+2.1	+1.6	...	+0.3
$n = 2/3$	+3.4	+3.0	-1.9	-1.2
$n = 1$	+5.1	+5.1	-1.6	-1.8
$n = 4/3$	+7.1	+6.6	-2.1	-2.5
$n = 2$	+12.3	+11.8	-6.0	-5.6
$n = 3$	+29.7	+29.6	-16.0	-15.6
$n = 4$	+58.1	+58.0	-30.1	-29.9
Natural	+6.0	+5.2	-5.6	-5.0
Hilltop ($p = 2$)	+1.6	+1.2	-0.7	-0.4
Hilltop ($p = 4$)	+1.5	+1.0	-0.6	-0.9
Double well	+3.2	+3.1	-4.3	-4.2
Brane inflation ($p = 2$)	+2.3	+2.2	+0.2	0.0
Brane inflation ($p = 4$)	+2.2	+2.2	+0.1	-0.1
Exponential tails	+2.2	+1.4	-0.1	0.0
SB SUSY	+3.4	+1.6	-1.8	-1.5
Supersymmetric α -model	+1.6	+1.1	-1.1	+0.1
Superconformal ($m = 1$)	+1.8	+1.3	-1.9	-1.4
Superconformal ($m \neq 1$)	+1.8	+0.9	-2.5	-2.2

Notes. This table is similar to Table 7, which did not use the BKP likelihood. Note, however, that the $\Delta\chi^2$ are computed with respect to the best fit of baseline + tensors, unlike in Table 7.

evolution studied in Sect. 6. Note, however, that the $\Delta\chi^2$ are computed with respect to the best fit of baseline + tensors, unlike in Table 7.

13.2. Implications of BKP on scalar power spectrum

The presence of tensors would, at least to some degree, require an enhanced suppression of the scalar power spectrum on large scales to account for the low- ℓ deficit in the C_ℓ^{TT} spectrum. We therefore repeat the analysis of an exponential cutoff studied in Sect. 4.4 with tensor perturbations included and the standard tensor tilt (i.e., $n_t = -r/8$). Allowing tensors does not significantly degrade the $\Delta\chi^2$ improvement found in Sect. 4.4 for *Planck* TT+lowP with a best fit at $r \approx 0$. When the BKP likelihood is combined, we obtain $\Delta\chi^2 = -4$ with respect to the base ΛCDM model with a best fit at $r \approx 0.04$. However, since this model contains 3 additional parameters, it is not preferred over base ΛCDM .

In Fig. 56 we show how the scalar primordial power spectrum reconstruction discussed in Sect. 8.3 is modified when the BKP likelihood is also included. While the power spectrum reconstruction hardly varies given the uncertainties in the method, the trajectories of the slow-roll parameters are significantly closer to slow roll. When the 12-knot reconstruction is carried out, the upper bound on the tensor-to-scalar ratio is $r < 0.11$ at 95% CL. The χ^2 per degree of freedom for the 5 low- k and 6 high- k knots are 1.14 and 0.22, respectively, corresponding to p -values of 0.33 and 0.97.

13.3. Relaxing the standard single-field consistency condition

We now relax the consistency condition (i.e., $n_t = -r/8$) and allow the tensor tilt to be independent of the tensor-to-scalar ratio. This fully phenomenological analysis with the BKP likelihood

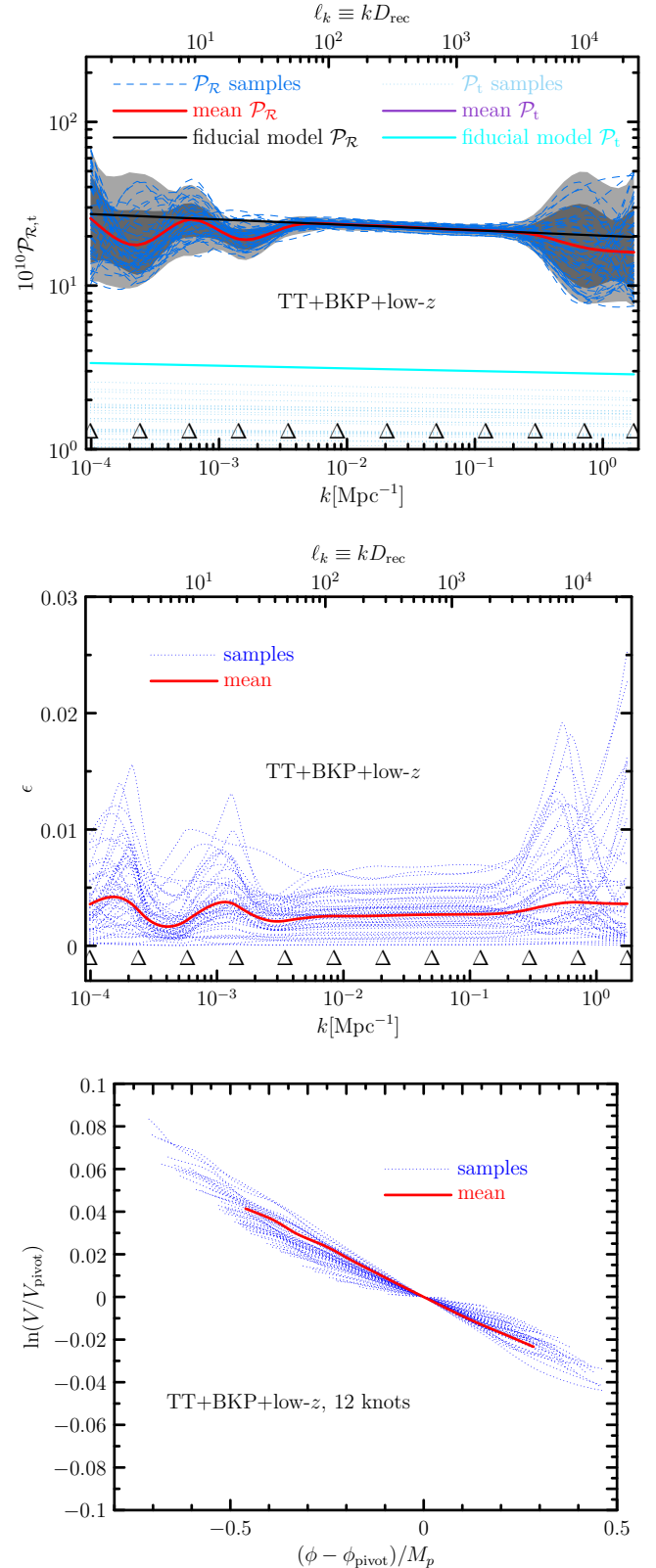


Fig. 56. Impact of BKP likelihood on scalar primordial power spectrum reconstruction. We show how including the BKP likelihood affects the reconstruction in Sect. 8.3. The *top panel* is to be compared with the reconstructions in Fig. 27, and we observe that including BKP has a minimal impact given the uncertainty in the reconstruction. The *middle panel* is to be compared with Fig. 31, and here we notice that including BKP excludes the trajectories with large values of ϵ . The *bottom panel* shows how the inflationary potential reconstructions are modified by BKP (to be compared with Fig. 32).

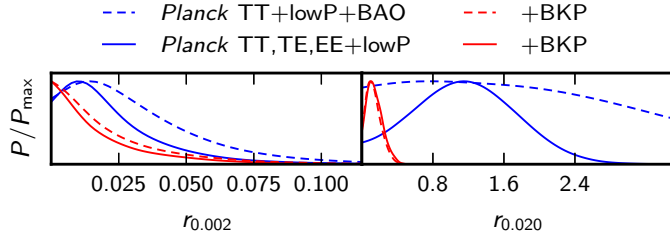


Fig. 57. Posterior probability density of the tensor-to-scalar ratio at two different scales. The inflationary consistency relation is relaxed and $r_{0.002}$ and $r_{0.020}$ are used as sampling parameters, assuming a power-law spectrum for primordial tensor perturbations. When the BKP likelihood is included in the analysis, the results with *Planck* TT+lowP+BAO and *Planck* TT, TE, EE+lowP coincide (dashed and solid red curves, respectively).

is complementary to the study of inflationary models with generalized Lagrangians in Sect. 10, which also predict modifications to the consistency condition $n_t = -r/8$ for a nearly scale-invariant spectrum of tensor modes. In this subsection we adopt a phenomenological approach, thereby including radical departures from $n_t \lesssim 0$, including values which are predicted in alternative models to inflation (Gasperini & Veneziano 1993; Boyle et al. 2004; Brandenberger et al. 2007). In Sect. 10 we folded in the *Planck* f_{NL} constraints (Planck Collaboration XVII 2016), whereas here we consider *Planck* and BKP likelihoods only. Complementary probes such as pulsar timing, direct detection of gravitational waves, and nucleosynthesis bounds could be used to constrain blue values for the tensor spectral index (Stewart & Brandenberger 2008), but here we are primarily interested in what CMB data can tell us.

We caution the reader that in the absence of a clear detection of a tensor component, joint constraints on r and n_t depend strongly on priors, or equivalently on the choice of parameterization. Nevertheless, the BKP likelihood has some constraining power over a range of scales more than a decade wide around $k \approx 0.01 \text{ Mpc}^{-1}$, so the results are not entirely prior driven.

The commonly used (r, n_t) parameterization suffers from pathological behaviour around $r = 0$, which could be problematic for statistical sampling. We therefore use a parameterization specifying r at two different scales, (r_{k_1}, r_{k_2}) (analogous to the treatment of primordial isocurvature in Sect. 11) as well as the more familiar (r, n_t) parameterization. We present results based on $k_1 = 0.002 \text{ Mpc}^{-1}$ and $k_2 = 0.02 \text{ Mpc}^{-1}$, also quoting the amplitude at $k = 0.01 \text{ Mpc}^{-1}$ for both parameterizations. This scale is close to the decorrelation scale for (r, n_t) for the *Planck*+BKP joint constraints. We obtain $r_{0.002} < 0.07$ (0.06) and $r_{0.02} < 0.29$ (0.31) at 95% CL from the two-scale parameterization with *Planck* TT+lowP+BAO+BKP (TT, TE, EE+lowP+BKP). Figure 57 illustrates the impact of the BKP likelihood on the one-dimensional posterior probabilities for these two parameters. The derived constraint at $k = 0.01 \text{ Mpc}^{-1}$ is $r_{0.01} < 0.12$ (0.12) at 95% CL with *Planck* TT+lowP+BAO+BKP (TT, TE, EE+lowP+BKP). The upper panel of Fig. 58 shows the relevant 2D contours for the tensor-to-scalar ratios at the two scales and the improvement due to the combination with the BKP likelihood. The lower panel shows the 2D contours in $(r_{0.01}, n_t)$ obtained by sampling with the two-scale parameterization. Figure 59 shows the 2D contours in $(r_{0.01}, n_t)$ obtained by the $(r_{0.002}, n_t)$ parameterization.

We conclude that positive values of the tensor tilt, n_t , are not statistically significantly preferred by the BKP joint measurement of B -mode polarization in combination with

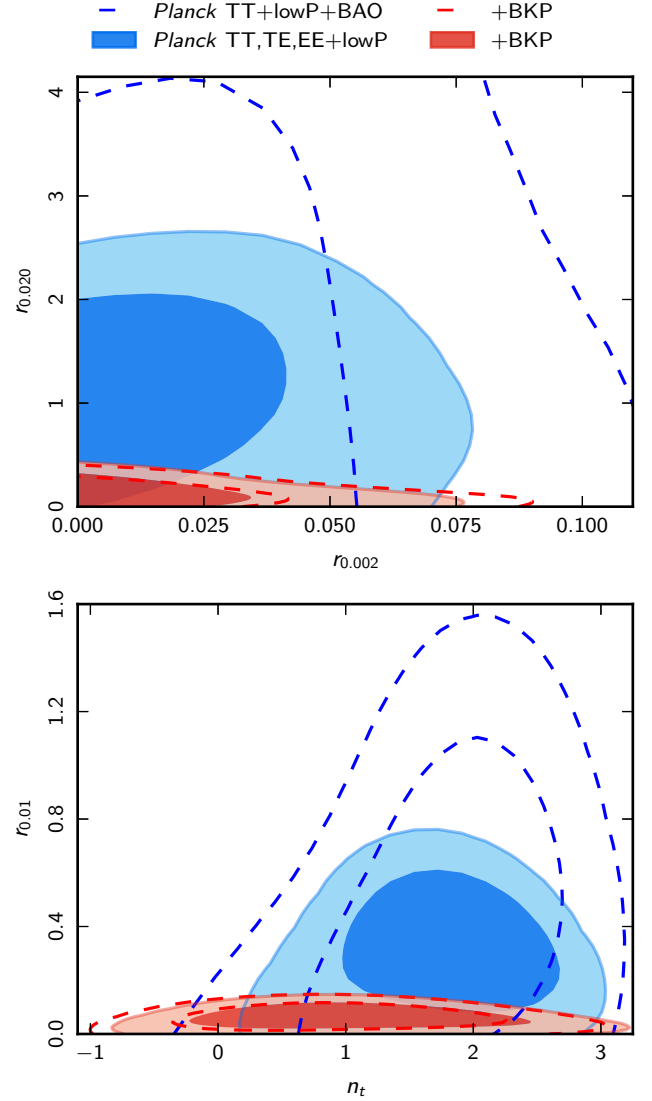


Fig. 58. 68% and 95% CL constraints on tensors when the inflationary consistency relation is relaxed, with *Planck* TT+lowP+BAO (blue dashed contours) and TT, TE, EE+lowP (blue shaded regions). The red colours are for the same data plus the BKP joint likelihood. The upper panel shows our independent primary parameters $r_{0.002}$ and $r_{0.020}$. The lower panel shows the derived parameters n_t and $r_{0.01}$. The scale $k = 0.01 \text{ Mpc}^{-1}$ is near the decorrelation scale of (n_t, r) for the *Planck*+BKP data.

Planck data, a conclusion at variance with results reported using the BICEP2 data (Gerbino et al. 2014). However, the now firmly established contamination by polarized dust emission easily explains the discrepancy. Values of tensor tilt consistent with the standard single-field inflationary consistency relation are compatible with the *Planck*+BKP constraints.

14. Conclusions

The *Planck* full mission temperature and polarization data are consistent with the spatially flat base Λ CDM model whose perturbations are Gaussian and adiabatic with a spectrum described by a simple power law, as predicted by the simplest inflationary models. For this release, the basic *Planck* results do not rely on external data. The first *Planck* polarization release at large

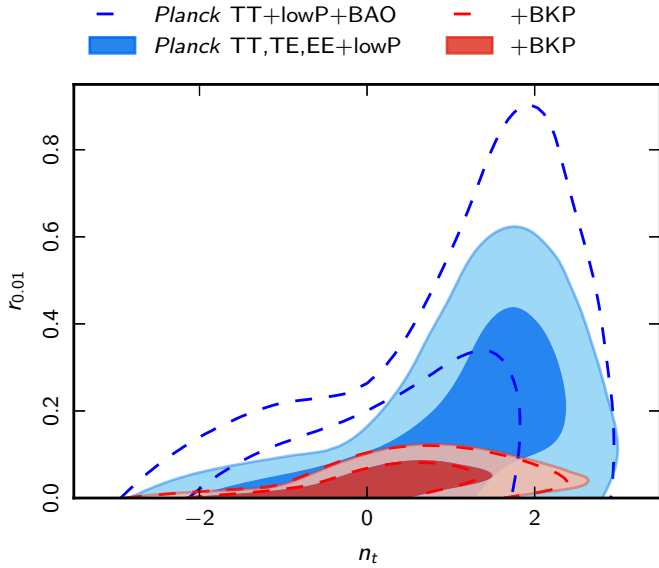


Fig. 59. The same as Fig. 58 lower panel, but using n_t and $r_{0.002}$ as primary parameters.

angular scales from the LFI 70 GHz channel determines an optical depth of $\tau = 0.067 \pm 0.022$ (68% CL, *Planck* low multipole likelihood), a value smaller than the previous *Planck* 2013 result based on the WMAP9 polarization likelihood as delivered by the WMAP team. This *Planck* value of τ is consistent with an analysis of WMAP9 polarization data cleaned for polarized dust emission using the *Planck* 353 GHz data (*Planck Collaboration XV 2014; Planck Collaboration XI 2016*). The estimates of cosmological parameters from the full mission temperature data and polarization on large angular scales are consistent with those of the *Planck* 2013 release. The TE and EE spectra at $\ell \geq 30$ together with the lensing power spectrum lead to cosmological constraints in agreement with those obtained from temperature.

The *Planck* full mission temperature and large-angular-scale polarization data rule out an exactly scale-invariant spectrum of curvature perturbations at 5.6σ . For the base Λ CDM model, the spectral index is measured to be $n_s = 0.965 \pm 0.006$ (68% CL, *Planck* TT+lowP). No evidence for a running of the spectral index is found, with $dn_s/d\ln k = -0.008 \pm 0.008$ (68% CL, *Planck* TT+lowP). By considering *Planck* TT+lowP+lensing we obtain $n_s = 0.968 \pm 0.006$ and $dn_s/d\ln k = -0.003 \pm 0.007$, both at 68% CL.

The *Planck* full mission data improve the upper bound on the tensor-to-scalar ratio to $r_{0.002} < 0.10$ (95% CL, *Planck* TT+lowP), a bound that changes only slightly when including the *Planck* lensing likelihood, the high- ℓ polarization likelihood, or the likelihood from the WMAP large-angular-scale polarization map (dust-cleaned with the *Planck* 353 GHz map). We showed how the low- ℓ deficit in temperature contributes to the *Planck* upper bound on $r_{0.002}$, but this deficit is not a statistically significant anomaly within the base Λ CDM cosmology. Using the full mission *Planck* data, we find the upper bound on $r_{0.002}$ stable, even when extended cosmological models or models with CDM isocurvature are considered. The *Planck* bound on $r_{0.002}$ is consistent with the recent result $r_{0.002} < 0.12$ at 95% CL obtained by the BICEP2/Keck Array-*Planck* cross-correlation analysis (BKP) which provides an estimate for the contamination from polarized dust emission (*Planck Collaboration XXX 2014*). By combining *Planck* TT+lowP with the BKP cross-correlation likelihood, we obtain $r_{0.002} < 0.08$ at 95% CL.

The increased precision of the *Planck* full mission data reduces the area enclosed by the 95% confidence contour in the (n_s, r) plane by 29%. We performed a Bayesian model comparison with the same methodology as in *PCI13*, taking into account reheating uncertainties by marginalizing over two extra parameters: the energy scale at thermalization, ρ_{th} , and the parameter w_{int} characterizing the average equation of state between the end of inflation and thermalization. Among the models considered using this approach, the R^2 inflationary model proposed by *Starobinsky (1980)* is the most favoured. Due to its high tensor-to-scalar ratio, the quadratic model is now strongly disfavoured with respect to R^2 inflation for *Planck* TT+lowP in combination with BAO data. By further including the BKP likelihood, this conclusion is confirmed, and natural inflation is also disfavoured.

We reconstructed the inflaton potential and the Hubble parameter evolution during the observable part of inflation using a Taylor expansion of the inflaton potential or $H(\phi)$. This analysis did not rely on the slow-roll approximation, nor on any assumption about the end of inflation. When higher-order terms were allowed, both reconstructions led to a change in the slope of the potential at the beginning of the observable range, thus better fitting the low- ℓ temperature deficit by turning on a non-zero running of running and accommodating $r_{0.002} \approx 0.2$. These models, however, are not significantly favoured compared to lower-order parameterizations that lead to slow-roll evolution at all times.

Three distinct methods were used to reconstruct the primordial power spectrum. All three methods strongly constrain deviations from a featureless power spectrum over the range of scales $0.008 \text{ Mpc}^{-1} \leq k \leq 0.1 \text{ Mpc}^{-1}$. More interestingly, they also independently find common patterns in the primordial power spectrum of curvature perturbations $\mathcal{P}_{\mathcal{R}}(k)$ at $k \leq 0.008 \text{ Mpc}^{-1}$. These patterns are related to the dip at $\ell \approx 20\text{--}40$ in the temperature power spectrum. This deviation from a simple power-law spectrum has weak statistical significance due to the large cosmic variance at low ℓ .

This direct reconstruction of the power spectrum is complemented by a search for parameterized features in physically motivated models. The models considered range from the minimal case of a kinetic-energy-dominated phase preceding a short inflationary stage (with just one extra parameter), to a model with a step-like feature in the potential and in the sound speed (with five extra parameters). As with the *Planck* 2013 nominal mission data, these templates lead to an improved fit, up to $\Delta\chi^2 \approx 12$. However, neither Bayesian model comparison nor a frequentist-simulation-based analysis shows any statistically significant preference over a simple power law.

We have updated the analysis that combines power spectrum constraints with those derived from the f_{NL} parameters (*Planck Collaboration XVII 2016*). New limits on the sound speed inferred from the full mission temperature and polarization data further constrain the slow-roll parameters for generalized models, including DBI inflation. For the first time, we derived combined constraints on Galileon inflation, including the region of parameter space in which the predicted spectrum of gravitational waves has a blue spectral index.

Several models motivated by the axion monodromy mechanism in string theory predict oscillatory modulations and corresponding non-Gaussianities, potentially detectable by *Planck*. A TT-only analysis picks up four possible modulation frequencies, which remain present when the high- ℓ polarization likelihood is included. An inspection of frequency residuals in the high- ℓ TT likelihood does not reveal evidence of foreground-related systematics at similar frequencies. However, a Bayesian model comparison analysis prefers the smooth base Λ CDM model over

modulated models, suggesting that the latter could simply be fitting the noise in the data. The monodromy model predicts resonant non-Gaussian features correlated to power spectrum features. A partial analysis beyond the power spectrum was presented. We also constrained a possible pseudo-coupling of the axion to gauge fields by requiring that non-Gaussianities induced by inverse decay satisfy the *Planck* bounds on f_{NL} .

Section 11 reports on a search for possible deviations from purely adiabatic initial conditions by studying a range of models including isocurvature modes as well as possible correlations with the adiabatic mode. The *Planck* full mission temperature data are consistent with adiabaticity. The *Planck* TT data place tight constraints on three-parameter extensions to the flat adiabatic base Λ CDM model, allowing arbitrarily-correlated mixtures of the adiabatic mode with one isocurvature mode (of either the CDM, baryon, neutrino density, or neutrino velocity type). Adding the high- ℓ TE and EE polarization data further squeezes the constraints, since polarization spectra contain additional shape and phase information on acoustic oscillations. The likelihood with polarization included is in agreement with adiabatic initial conditions. However, the tightening of the constraints after including polarization must be interpreted with caution because of possible systematic effects. For this reason we emphasize the more conservative *Planck* TT+lowP bounds in Table 16. The constraints on the six base- Λ CDM cosmological model parameters remain stable when correlated isocurvature modes are allowed. The largest shifts occur for the neutrino density mode, but these shifts are not significant (i.e., are below 1σ). The constraints on the tensor-to-scalar ratio also remain stable when isocurvature modes are allowed.

Finally we examined the connection between inflation and statistical isotropy, a key prediction of the simplest inflationary models. We tested separately the two lowest moments of an anisotropic modulation of the primordial curvature power spectrum. We found that a modulated curvaton model proposed to explain the observed large-scale dipolar power asymmetry cannot account for all of the asymmetry, and hence is not preferred over statistically isotropic base Λ CDM. The full mission temperature data place the tightest constraints to date on a quadrupolar modulation of curvature perturbations.

Acknowledgements. The Planck Collaboration acknowledges the support of: ESA; CNES and CNRS/INSU-IN2P3-INP (France); ASI, CNR, and INAF (Italy); NASA and DoE (USA); STFC and UKSA (UK); CSIC, MINECO, JA, and RES (Spain); Tekes, AoF, and CSC (Finland); DLR and MPG (Germany); CSA (Canada); DTU Space (Denmark); SER/SSO (Switzerland); RCN (Norway); SFI (Ireland); FCT/MCTES (Portugal); ERC and PRACE (EU). A description of the Planck Collaboration and a list of its members, indicating which technical or scientific activities they have been involved in, can be found at <http://www.cosmos.esa.int/web/planck/planck-collaboration>. This research used resources of the National Energy Research Scientific Computing Center, a DOE Office of Science User Facility supported by the Office of Science of the US Department of Energy under Contract No. DE-AC02-05CH11231. Part of this work was undertaken at the STFC DiRAC HPC Facilities at the University of Cambridge, funded by UK BIS National E-infrastructure capital grants. We gratefully acknowledge the IN2P3 Computer Center (<http://cc.in2p3.fr>) for providing a significant amount of the computing resources and services needed for this work.

References

Achúcarro, A., Gong, J.-O., Hardeman, S., Palma, G. A., & Patil, S. P. 2011, *JCAP*, 1101, 030
 Ackerman, L., Carroll, S. M., & Wise, M. B. 2007, *Phys. Rev. D*, 75, 083502
 Adams, F. C., Bond, J. R., Freese, K., Frieman, J. A., & Olinto, A. V. 1993, *Phys. Rev. D*, 47, 426
 Adams, J. A., Cresswell, B., & Easther, R. 2001, *Phys. Rev. D*, 64, 123514

Agarwal, N., & Bean, R. 2009, *Phys. Rev. D*, 79, 023503
 Alishahiha, M., Silverstein, E., & Tong, D. 2004, *Phys. Rev. D*, 70, 123505
 Amendola, L., Gordon, C., Wands, D., & Sasaki, M. 2002, *Phys. Rev. Lett.*, 88, 211302
 Anber, M. M., & Sorbo, L. 2010, *Phys. Rev. D*, 81, 043534
 Anderson, L., Aubourg, E., Bailey, S., et al. 2014, *MNRAS*, 441, 24
 Armendáriz-Picón, C., Damour, T., & Mukhanov, V. 1999, *Phys. Lett. B*, 458, 209
 Aslanyan, G., Price, L. C., Abazajian, K. N., & Easther, R. 2014, *JCAP*, 08, 052
 Audren, B., Lesgourgues, J., Benabed, K., & Prunet, S. 2013, *JCAP*, 1302, 001
 Barnaby, N., & Peloso, M. 2011, *Phys. Rev. Lett.*, 106, 181301
 Barnaby, N., Pajer, E., & Peloso, M. 2012, *Phys. Rev. D*, 85, 023525
 Bartolo, N., Matarrese, S., Peloso, M., & Ricciardone, A. 2013, *JCAP*, 1308, 022
 Bartolo, N., Matarrese, S., & Riotto, A. 2001, *Phys. Rev. D*, 64, 123504
 Bartolo, N., Matarrese, S., & Riotto, A. 2004a, *Phys. Rev. Lett.*, 93, 231301
 Babich, D., Creminelli, P., & Zaldarriaga, M. 2004, *JCAP*, 8, 9
 Barnaby, N., Namba, R., & Peloso, M. 2011, *JCAP*, 4, 9
 Bartolo, N., & Liddle, A. R. 2002, *Phys. Rev. D*, 65, 121301
 Bartolo, N., Matarrese, S., & Riotto, A. 2004b, *Phys. Rev. D*, 69, 043503
 Barvinsky, A. O., Kamenshchik, A. Y., & Starobinsky, A. A. 2008, *JCAP*, 0811, 021
 Baumann, D., Green, D., & Porto, R. A. 2015, *JCAP*, 1, 16
 Bean, R., Chen, X., Peiris, H., & Xu, J. 2008, *Phys. Rev. D*, 77, 023527
 Becker, R. H., Fan, X., White, R. L., et al. 2001, *AJ*, 122, 2850
 Beltrán, M., García-Bellido, J., Lesgourgues, J., & Viel, M. 2005, *Phys. Rev. D*, 72, 103515
 Bennett, C. L., Hill, R. S., Hinshaw, G., et al. 2011, *ApJS*, 192, 17
 Berera, A. 1995, *Phys. Rev. Lett.*, 75, 3218
 Beutler, F., Blake, C., Colless, M., et al. 2011, *MNRAS*, 416, 3017
 Bezrukov, F., & Shaposhnikov, M. 2008, *Phys. Lett. B*, 659, 703
 Bezrukov, F., & Shaposhnikov, M. 2009, *JHEP*, 07, 089
 BICEP2 Collaboration. 2014a, *ApJ*, 792, 62
 BICEP2 Collaboration. 2014b, *Phys. Rev. Lett.*, 112, 241101
 BICEP2/Keck Array and Planck Collaborations. 2015, *Phys. Rev. Lett.*, 114, 101301
 Binétruy, P., Kiritsis, E., Mabilard, J., Pieroni, M., & Rosset, C. 2015, *J. Cosmol. Astropart. Phys.*, 2015, 33
 Blas, D., Lesgourgues, J., & Tram, T. 2011, *JCAP*, 1107, 034
 Boubekur, L., & Lyth, D. 2005, *JCAP*, 0507, 010
 Boyle, L. A., Steinhardt, P. J., & Turok, N. 2004, *Phys. Rev. D*, 69, 127302
 Bozza, V., Giovannini, M., & Veneziano, G. 2003, *JCAP*, 0305, 001
 Brandenberger, R. H., Nayeri, A., Patil, S. P., & Vafa, C. 2007, *Phys. Rev. Lett.*, 98, 231302
 Bucher, M. 2015, *Int. J. Mod. Phys. D*, 24, 1530004
 Bucher, M., Moodley, K., & Turok, N. 2000, *Phys. Rev. D*, 62, 083508
 Bucher, M., Moodley, K., & Turok, N. 2001, *Phys. Rev. Lett.*, 87, 191301
 Buchmüller, W., Domcke, V., & Kamada, K. 2013, *Phys. Lett.*, B726, 467
 Burgess, C., Martineau, P., Quevedo, F., Rajesh, G., & Zhang, R. 2002, *JHEP*, 0203, 052
 Burrage, C., de Rham, C., Seery, D., & Tolley, A. J. 2011, *JCAP*, 1, 14
 Byrnes, C. T., & Wands, D. 2006, *Phys. Rev. D*, 74, 043529
 Casadio, R., Finelli, F., Kamenshchik, A., Luzzi, M., & Venturi, G. 2006, *JCAP*, 0604, 011
 Chen, X. 2005a, *JHEP*, 8, 45
 Chen, X. 2005b, *Phys. Rev. D*, 71, 063506
 Chen, X. 2005c, *Phys. Rev. D*, 72, 123518
 Chen, X., Huang, M.-X., Kachru, S., & Shiu, G. 2007, *JCAP*, 1, 2
 Chen, X., Easther, R., & Lim, E. A. 2008, *JCAP*, 0804, 010
 Chluba, J., Hamann, J., & Patil, S. P. 2015, *Int. J. Mod. Phys. D*, 24, 1530023
 Choe, J., Gong, J.-O., & Stewart, E. D. 2004, *JCAP*, 0407, 012
 Cicoli, M., Burgess, C., & Quevedo, F. 2009, *JCAP*, 0903, 013
 Contaldi, C. R., Peloso, M., Kofman, L., & Linde, A. D. 2003, *JCAP*, 0307, 002
 Copeland, E. J., Liddle, A. R., Lyth, D. H., Stewart, E. D., & Wands, D. 1994, *Phys. Rev. D*, 49, 6410
 Creminelli, P., D'Amico, G., Musso, M., Noreña, J., & Trincherini, E. 2011, *JCAP*, 2, 6
 Danielsson, U. H. 2002, *Phys. Rev. D*, 66, 023511
 De Felice, A., & Tsujikawa, S. 2013, *JCAP*, 3, 30
 de Rham, C., & Gabadadze, G. 2010a, *Phys. Rev. D*, 82, 044020
 de Rham, C., & Gabadadze, G. 2010b, *Phys. Lett. B*, 693, 334
 Deffayet, C., Deser, S., & Esposito-Farèse, G. 2009a, *Phys. Rev. D*, 80, 064015
 Deffayet, C., Esposito-Farèse, G., & Vikman, A. 2009b, *Phys. Rev. D*, 79, 084003
 Dimastrogiovanni, E., Bartolo, N., Matarrese, S., & Riotto, A. 2010, *Adv.*

- Astron.*, 752670
- Dvali, G., & Tye, S. H. 1999, *Phys. Lett. B*, 450, 72
- Dvali, G. R., Shafi, Q., & Schaefer, R. K. 1994, *Phys. Rev. Lett.*, 73, 1886
- Dvali, G., Shafi, Q., & Solganik, S. 2001, ArXiv e-prints [[arXiv:hep-th/0105203](#)]
- Easther, R., & Flauger, R. 2014, *JCAP*, 1402, 037
- Easther, R., & Peiris, H. 2006, *JCAP*, 0609, 010
- Easther, R., & Peiris, H. V. 2012, *Phys. Rev. D*, 85, 103533
- Easther, R., Kinney, W. H., & Peiris, H. 2005, *JCAP*, 0505, 009
- Eisenstein, D. J., Zehavi, I., Hogg, D. W., et al. 2005, *ApJ*, 633, 560
- Ellis, J., Nanopoulos, D. V., & Olive, K. A. 2013a, *Phys. Rev. Lett.*, 111, 111301
- Ellis, J., Nanopoulos, D. V., & Olive, K. A. 2013b, *JCAP*, 1310, 009
- Enqvist, K., & Sloth, M. S. 2002, *Nucl. Phys. B*, 626, 395
- Enqvist, K., Kurki-Suonio, H., & Valiviita, J. 2002, *Phys. Rev. D*, 65, 043002
- Erickcek, A. L., Hirata, C. M., & Kamionkowski, M. 2009, *Phys. Rev. D*, 80, 083507
- Farakas, F., Kehagias, A., & Riotto, A. 2013, *Nucl. Phys. B*, 876, 187
- Feroz, F., & Hobson, M. 2008, *MNRAS*, 384, 449
- Feroz, F., Hobson, M., & Bridges, M. 2009, *MNRAS*, 398, 1601
- Feroz, F., Hobson, M., Cameron, E., & Pettitt, A. 2013, ArXiv e-prints [[arXiv:1306.2144](#)]
- Ferrara, S., Kallosh, R., Linde, A., & Porrati, M. 2013a, *Phys. Rev. D*, 88, 085038
- Ferrara, S., Kallosh, R., & Van Proeyen, A. 2013b, *JHEP*, 1311, 134
- Ferreira, R. Z., & Sloth, M. S. 2014, *JHEP*, 12, 139
- Finelli, F., Hamann, J., Leach, S. M., & Lesgourgues, J. 2010, *JCAP*, 1004, 011
- Flauger, R., Hill, J. C., & Spergel, D. N. 2014a, *JCAP*, 1408, 039
- Flauger, R., & Pajer, E. 2011, *JCAP*, 1101, 017
- Flauger, R., McAllister, L., Silverstein, E., & Westphal, A. 2014b, ArXiv e-prints [[arXiv:1412.1814](#)]
- Freese, K., Frieman, J. A., & Olinto, A. V. 1990, *Phys. Rev. Lett.*, 65, 3233
- Gao, X., & Steer, D. A. 2011, *JCAP*, 12, 19
- Garcia-Bellido, J., & Roest, D. 2014, *Phys. Rev. D*, 89, 103527
- García-Bellido, J., & Wands, D. 1996, *Phys. Rev. D*, 53, 5437
- Garcia-Bellido, J., Rabadan, R., & Zamora, F. 2002, *JHEP*, 0201, 036
- Garriga, J., & Mukhanov, V. F. 1999, *Phys. Lett. B*, 458, 219
- Gasperini, M., & Veneziano, G. 1993, *Astropart. Phys.*, 1, 317
- Gauthier, C., & Bucher, M. 2012, *JCAP*, 1210, 050
- Gerbino, M., Marchini, A., Pagano, L., et al. 2014, *Phys. Rev. D*, 90, 047301
- Goncharov, A., & Linde, A. D. 1984, *Sov. Phys. JETP*, 59, 930
- Gong, J.-O., & Stewart, E. D. 2001, *Phys. Lett. B*, 510, 1
- Gorbunov, D., & Panin, A. 2011, *Phys. Lett. B*, 700, 157
- Gordon, C., & Lewis, A. 2003, *Phys. Rev. D*, 67, 123513
- Gordon, C., Wands, D., Bassett, B. A., & Maartens, R. 2001, *Phys. Rev. D*, 63, 023506
- Górski, K. M., Hivon, E., Banday, A. J., et al. 2005, *ApJ*, 622, 759
- Grin, D., Hanson, D., Holder, G. P., Doré, O., & Kamionkowski, M. 2014, *Phys. Rev. D*, 89, 023006
- Guth, A. H., Kaiser, D. I., & Nomura, Y. 2014, *Phys. Lett. B*, 733, 112
- Habib, S., Heitmann, K., Jungman, G., & Molina-Paris, C. 2002, *Phys. Rev. Lett.*, 89, 281301
- Hamann, J., Lesgourgues, J., & Valkenburg, W. 2008, *JCAP*, 0804, 016
- Hamimeche, S., & Lewis, A. 2008, *Phys. Rev. D*, 77, 103013
- Handley, W. J., Hobson, M. P., & Lasenby, A. N. 2015, *MNRAS*, 450, L61
- Harrison, E. R. 1970, *Phys. Rev. D*, 1, 2726
- Hu, W., Seljak, U., White, M. J., & Zaldarriaga, M. 1998, *Phys. Rev. D*, 57, 3290
- Hu, W., & White, M. J. 1997, *Phys. Rev. D*, 56, 596
- Ijjas, A., Steinhardt, P. J., & Loeb, A. 2013, *Phys. Lett. B*, 723, 261
- Ijjas, A., Steinhardt, P. J., & Loeb, A. 2014, *Phys. Lett. B*, 736, 142
- Jackson, M. G., & Shiu, G. 2013, *Phys. Rev. D*, 88, 123511
- Jackson, M. G., Wandelt, B., & Bouchet, F. 2014, *Phys. Rev. D*, 89, 023510
- Kachru, S., Kallosh, R., Linde, A. D., et al. 2003, *JCAP*, 0310, 013
- Kaiser, D. I., & Sfakianakis, E. I. 2014, *Phys. Rev. Lett.*, 112, 011302
- Kallosh, R., & Linde, A. 2013a, *JCAP*, 1310, 033
- Kallosh, R., & Linde, A. 2013b, *JCAP*, 1306, 028
- Kallosh, R., Linde, A., & Roest, D. 2013, *JHEP*, 1311, 198
- Kaloper, N., Lawrence, A., & Sorbo, L. 2011, *JCAP*, 1103, 023
- Kamionkowski, M., Kosowsky, A., & Stebbins, A. 1997, *Phys. Rev. D*, 55, 7368
- Kanno, S., Sasaki, M., & Tanaka, T. 2013, *Progr. Theor. Exp. Phys.*, 2013, 111E01
- Kawasaki, M., & Sekiguchi, T. 2008, *Prog. Theor. Phys.*, 120, 995
- Ketov, S. V., & Starobinsky, A. A. 2011, *Phys. Rev. D*, 83, 063512
- Kim, J., & Komatsu, E. 2013, *Phys. Rev. D*, 88, 101301
- Kim, J. E., Nilles, H. P., & Peloso, M. 2005, *JCAP*, 0501, 005
- Kinney, W. H. 2002, *Phys. Rev. D*, 66, 083508
- Kinney, W. H., Kolb, E. W., Melchiorri, A., & Riotto, A. 2006, *Phys. Rev. D*, 74, 023502
- Kobayashi, T., & Takahashi, F. 2011, *JCAP*, 1101, 026
- Kobayashi, T., Yamaguchi, M., & Yokoyama, J. 2010, *Phys. Rev. Lett.*, 105, 231302
- Kobayashi, T., Yamaguchi, M., & Yokoyama, J. 2011a, *Progr. Theor. Phys.*, 126, 511
- Kobayashi, T., Yamaguchi, M., & Yokoyama, J. 2011b, *Phys. Rev. D*, 83, 103524
- Kosowsky, A., & Turner, M. S. 1995, *Phys. Rev. D*, 52, 1739
- Langlois, D. 1999, *Phys. Rev. D*, 59, 123512
- Langlois, D., & Riazuelo, A. 2000, *Phys. Rev. D*, 62, 043504
- Leach, S. M., Liddle, A. R., Martin, J., & Schwarz, D. J. 2002, *Phys. Rev. D*, 66, 023515
- Lesgourgues, J. 2011, ArXiv e-prints [[arXiv:1104.2932](#)]
- Lesgourgues, J., & Valkenburg, W. 2007, *Phys. Rev. D*, 75, 123519
- Lesgourgues, J., Polarski, D., Prunet, S., & Starobinsky, A. A. 2000, *Astron. Astrophys.*, 359, 414
- Lesgourgues, J., Starobinsky, A. A., & Valkenburg, W. 2008, *JCAP*, 0801, 010
- Lewis, A., & Bridle, S. 2002, *Phys. Rev. D*, 66, 103511
- Libanov, M., & Rubakov, V. 2010, *JCAP*, 1011, 045
- Liddle, A. R., & Cortés, M. 2013, *Phys. Rev. Lett.*, 111, 111302
- Linde, A. 2014, ArXiv e-prints [[arXiv:1402.0526](#)]
- Linde, A. D. 1983, *Phys. Lett. B*, 129, 177
- Linde, A. D. 1994, *Phys. Rev. D*, 49, 748
- Linde, A. D., & Mukhanov, V. 2006, *JCAP*, 0604, 009
- Linde, A. D., & Mukhanov, V. F. 1997, *Phys. Rev. D*, 56, 535
- Liddle, A. R., & Leach, S. M. 2003, *Phys. Rev. D*, 68, 103503
- Linde, A., Mooij, S., & Pajer, E. 2013, *Phys. Rev. D*, 87, 103506
- Lorenz, L., Martin, J., & Ringeval, C. 2008, *Phys. Rev. D*, 78, 083513
- Lyth, D. H. 2013, *JCAP*, 1308, 007
- Lyth, D. H., & Wands, D. 2002, *Phys. Lett. B*, 524, 5
- Lyth, D. H., Ungarelli, C., & Wands, D. 2003, *Phys. Rev. D*, 67, 023503
- Ma, C.-P., & Bertschinger, E. 1995, *ApJ*, 455, 7
- Ma, Y.-Z., Efstathiou, G., & Challinor, A. 2011, *Phys. Rev. D*, 83, 083005
- Ma, Y.-Z., Huang, Q.-G., & Zhang, X. 2013, *Phys. Rev. D*, 87, 103516
- Maleknejad, A., Sheikh-Jabbari, M., & Soda, J. 2013, *Phys. Rept.*, 528, 161
- Martin, J., & Brandenberger, R. H. 2001, *Phys. Rev. D*, 63, 123501
- Martin, J., & Ringeval, C. 2010, *Phys. Rev. D*, 82, 023511
- Martin, J., & Schwarz, D. J. 2003, *Phys. Rev. D*, 67, 083512
- Martin, J., Ringeval, C., & Vennin, V. 2014, *Phys. Dark Univ.*, 5-6, 75
- McAllister, L., Silverstein, E., & Westphal, A. 2010, *Phys. Rev. D*, 82, 046003
- McAllister, L., Silverstein, E., Westphal, A., & Wrase, T. 2014, *JHEP*, 1409, 123
- Meerburg, P. D. 2014, *Phys. Rev. D*, 90, 063529
- Meerburg, P. D., & Pajer, E. 2013, *JCAP*, 2, 17
- Meerburg, P. D., & Spergel, D. N. 2014, *Phys. Rev. D*, 89, 063537
- Meerburg, P. D., Spergel, D. N., & Wandelt, B. D. 2014a, ArXiv e-prints [[arXiv:1406.0548](#)]
- Meerburg, P. D., Spergel, D. N., & Wandelt, B. D. 2014b, *Phys. Rev. D*, 89, 063536
- Miranda, V., & Hu, W. 2014, *Phys. Rev. D*, 89, 083529
- Mizuno, S., & Koyama, K. 2010, *Phys. Rev. D*, 82, 103518
- Mollerach, S. 1990, *Phys. Rev. D*, 42, 313
- Moroi, T., & Takahashi, T. 2001, *Phys. Lett. B*, 522, 215
- Mortonson, M. J., & Hu, W. 2008, *ApJ*, 672, 737
- Mortonson, M. J., Dvorkin, C., Peiris, H. V., & Hu, W. 2009, *Phys. Rev. D*, 79, 103519
- Mortonson, M. J., Peiris, H. V., & Easther, R. 2011, *Phys. Rev. D*, 83, 043505
- Mortonson, M. J., & Seljak, U. 2014, *JCAP*, 1410, 035
- Moss, A., Scott, D., Zibin, J. P., & Battye, R. 2011, *Phys. Rev. D*, 84, 023014
- Mukhanov, V. 2013, *Eur. Phys. J. C*, 73, 2486
- Mukhanov, V. F., & Chibisov, G. 1981, *JETP Lett.*, 33, 532
- Naruko, A., Komatsu, E., & Yamaguchi, M. 2015, *J. Cosmol. Astropart. Phys.*, 2015, 45
- Nicolis, A., Rattazzi, R., & Trincherini, E. 2009, *Phys. Rev. D*, 79, 064036
- Norena, J., Wagner, C., Verde, L., Peiris, H. V., & Easther, R. 2012, *Phys. Rev. D*, 86, 023505
- Ohashi, J., & Tsujikawa, S. 2012, *JCAP*, 10, 35
- Ohashi, J., Soda, J., & Tsujikawa, S. 2013, *Phys. Rev. D*, 87, 083520
- Okamoto, T., & Hu, W. 2003, *Phys. Rev. D*, 67, 083002
- Page, L., Hinshaw, G., Komatsu, E., et al. 2007, *ApJS*, 170, 335
- Pajer, E., & Peloso, M. 2013, *Class. Quant. Grav.*, 30, 214002
- Palanque-Delabrouille, N., Yèche, C., Lesgourgues, J., et al. 2015, *J. Cosmol. Astropart. Phys.*, 2015, 45
- Peebles, P., & Yu, J. 1970, *ApJ*, 162, 815
- Peiris, H., & Easther, R. 2006a, *JCAP*, 0607, 002

- Peiris, H., & Easther, R. 2006b, *JCAP*, **0610**, 017
- Peiris, H. V., & Easther, R. 2008, *JCAP*, **0807**, 024
- Peiris, H. V., Komatsu, E., Verde, L., et al. 2003, *ApJS*, **148**, 213
- Peiris, H., Baumann, D., Friedman, B., & Cooray, A. 2007, *Phys. Rev. D*, **76**, 103517
- Peiris, H., Easther, R., & Flauger, R. 2013, *JCAP*, **1309**, 018
- Perotto, L., Lesgourgues, J., Hannestad, S., Tu, H., & Wong, Y. Y. 2006, *JCAP*, **0610**, 013
- Planck Collaboration XV. 2014, *A&A*, **571**, A15
- Planck Collaboration XVI. 2014, *A&A*, **571**, A16
- Planck Collaboration XVII. 2014, *A&A*, **571**, A17
- Planck Collaboration XXII. 2014, *A&A*, **571**, A22
- Planck Collaboration XXIII. 2014, *A&A*, **571**, A23
- Planck Collaboration XXIV. 2014, *A&A*, **571**, A24
- Planck Collaboration XXV. 2014, *A&A*, **571**, A25
- Planck Collaboration XXVI. 2014, *A&A*, **571**, A26
- Planck Collaboration XXVII. 2014, *A&A*, **571**, A27
- Planck Collaboration XXX. 2014, *A&A*, **571**, A30
- Planck Collaboration XXXI. 2014, *A&A*, **571**, A31
- Planck Collaboration I. 2016, *A&A*, **594**, A1
- Planck Collaboration II. 2016, *A&A*, **594**, A2
- Planck Collaboration III. 2016, *A&A*, **594**, A3
- Planck Collaboration IV. 2016, *A&A*, **594**, A4
- Planck Collaboration V. 2016, *A&A*, **594**, A5
- Planck Collaboration VI. 2016, *A&A*, **594**, A6
- Planck Collaboration VII. 2016, *A&A*, **594**, A7
- Planck Collaboration VIII. 2016, *A&A*, **594**, A8
- Planck Collaboration IX. 2016, *A&A*, **594**, A9
- Planck Collaboration X. 2016, *A&A*, **594**, A10
- Planck Collaboration XI. 2016, *A&A*, **594**, A11
- Planck Collaboration XII. 2016, *A&A*, **594**, A12
- Planck Collaboration XIII. 2016, *A&A*, **594**, A13
- Planck Collaboration XIV. 2016, *A&A*, **594**, A14
- Planck Collaboration XV. 2016, *A&A*, **594**, A15
- Planck Collaboration XVI. 2016, *A&A*, **594**, A16
- Planck Collaboration XVII. 2016, *A&A*, **594**, A17
- Planck Collaboration XVIII. 2016, *A&A*, **594**, A18
- Planck Collaboration XIX. 2016, *A&A*, **594**, A19
- Planck Collaboration XX. 2016, *A&A*, **594**, A20
- Planck Collaboration XXI. 2016, *A&A*, **594**, A21
- Planck Collaboration XXII. 2016, *A&A*, **594**, A22
- Planck Collaboration XXIII. 2016, *A&A*, **594**, A23
- Planck Collaboration XXIV. 2016, *A&A*, **594**, A24
- Planck Collaboration XXV. 2016, *A&A*, **594**, A25
- Planck Collaboration XXVI. 2016, *A&A*, **594**, A26
- Planck Collaboration XXVII. 2016, *A&A*, **594**, A27
- Planck Collaboration XXVIII. 2016, *A&A*, **594**, A28
- Planck Collaboration Int. XIX. 2015, *A&A*, **576**, A104
- Planck Collaboration Int. XX. 2015, *A&A*, **576**, A105
- Planck Collaboration Int. XXI. 2015, *A&A*, **576**, A106
- Planck Collaboration Int. XXII. 2015, *A&A*, **576**, A107
- Planck Collaboration Int. XXX. 2016, *A&A*, **586**, A133
- Polarski, D., & Starobinsky, A. A. 1996, *Class. Quant. Grav.*, **13**, 377
- Powell, B. A., & Kinney, W. H. 2007, *JCAP*, **0708**, 006
- Powell, B. A., Tzirakis, K., & Kinney, W. H. 2009, *JCAP*, **4**, 19
- Powell, M. J. D. 2009, The BoBYQA algorithm for bound constrained optimization without derivatives
- Regan, D., Anderson, G. J., Hull, M., & Seery, D. 2015, *J. Cosmol. Astropart. Phys.*, **2015**, 15
- Ross, A. J., Samushia, L., Howlett, C., et al. 2015, *MNRAS.*, **449**, 835
- Rossi, G., Yèche, C., Palanque-Delabrouille, N., & Lesgourgues, J. 2015, *Phys. Rev. D*, **92**, 063505
- Sasaki, M., Valiviita, J., & Wands, D. 2006, *Phys. Rev. D*, **74**, 103003
- Savelainen, M., Valiviita, J., Walia, P., Rusak, S., & Kurki-Suonio, H. 2013, *Phys. Rev. D*, **88**, 063010
- Schmidt, F., & Hui, L. 2013, *Phys. Rev. Lett.*, **110**, 011301
- Seljak, U., & Zaldarriaga, M. 1997, *Phys. Rev. Lett.*, **78**, 2054
- Senatore, L., Smith, K. M., & Zaldarriaga, M. 2010, *JCAP*, **1**, 28
- Silverstein, E., & Tong, D. 2004, *Phys. Rev. D*, **70**, 103505
- Silverstein, E., & Westphal, A. 2008, *Phys. Rev. D*, **78**, 106003
- Soda, J. 2012, *Class. Quant. Grav.*, **29**, 083001
- Sorbo, L. 2011, *JCAP*, **6**, 3
- Starobinsky, A. 1983, *Sov. Astron. Lett.*, **9**, 302
- Starobinsky, A. A. 1980, *Phys. Lett. B*, **91**, 99
- Starobinsky, A. A. 1992, *JETP Lett.*, **55**, 489
- Stewart, A., & Brandenberger, R. 2008, *JCAP*, **0808**, 012
- Stewart, E. D. 1995, *Phys. Rev. D*, **51**, 6847
- Stewart, E. D., & Lyth, D. H. 1993, *Phys. Lett. B*, **302**, 171
- Tsujikawa, S. 2014, *PTEP*, **2014**, 06B104
- Tsujikawa, S., Ohashi, J., Kuroyanagi, S., & De Felice, A. 2013, *Phys. Rev. D*, **88**, 023529
- Turner, M. S. 1983, *Phys. Rev. D*, **28**, 1243
- Unnikrishnan, S., Sahni, V., & Toporensky, A. 2012, *JCAP*, **1208**, 018
- Valiviita, J., & Giannantonio, T. 2009, *Phys. Rev. D*, **80**, 123516
- Valiviita, J., Savelainen, M., Talvitie, M., Kurki-Suonio, H., & Rusak, S. 2012, *ApJ*, **753**, 151
- Vázquez, J. A., Bridges, M., Hobson, M. P., & Lasenby, A. N. 2012, *JCAP*, **6**, 6
- Vilenkin, A. 1985, *Phys. Rev. D*, **32**, 2511
- Wands, D., Bartolo, N., Matarrese, S., & Riotto, A. 2002, *Phys. Rev. D*, **66**, 043520
- Weinberg, S. 2004, *Phys. Rev. D*, **70**, 083522
- White, M., Scott, D., & Silk, J. 1994, *Ann. Rev. Ast. Astro*, **32**, 319
- Zaldarriaga, M., & Seljak, U. 1997, *Phys. Rev. D*, **55**, 1830
- Zeldovich, Y. 1972, *MNRAS*, **160**, 1P
- ¹ APC, AstroParticule et Cosmologie, Université Paris Diderot, CNRS/IN2P3, CEA/Irfu, Observatoire de Paris, Sorbonne Paris Cité, 10 rue Alice Domon et Léonie Duquet, 75205 Paris Cedex 13, France
 - ² Aalto University Metsähovi Radio Observatory and Dept of Radio Science and Engineering, PO Box 13000, 00076 Aalto, Finland
 - ³ African Institute for Mathematical Sciences, 6–8 Melrose Road, Muizenberg, 7945 Cape Town, South Africa
 - ⁴ Agenzia Spaziale Italiana Science Data Center, via del Politecnico snc, 00133 Roma, Italy
 - ⁵ Aix-Marseille Université, CNRS, LAM (Laboratoire d'Astrophysique de Marseille) UMR 7326, 13388 Marseille, France
 - ⁶ Astrophysics Group, Cavendish Laboratory, University of Cambridge, J J Thomson Avenue, Cambridge CB3 0HE, UK
 - ⁷ Astrophysics & Cosmology Research Unit, School of Mathematics, Statistics & Computer Science, University of KwaZulu-Natal, Westville Campus, Private Bag X54001, 4000 Durban, South Africa
 - ⁸ Atacama Large Millimeter/submillimeter Array, ALMA Santiago Central Offices, Alonso de Cordova 3107, Vitacura, 763 0355 Casilla, Santiago, Chile
 - ⁹ CGEE, SCS Qd 9, Lote C, Torre C, 4° andar, Ed. Parque Cidade Corporate, CEP 70308-200 Brasília, DF, Brazil
 - ¹⁰ CITA, University of Toronto, 60 St. George St., Toronto, ON M5S 3H8, Canada
 - ¹¹ CNRS, IRAP, 9 Av. colonel Roche, BP 44346, 31028 Toulouse Cedex 4, France
 - ¹² CRANN, Trinity College, Dublin 2, Ireland
 - ¹³ California Institute of Technology, Pasadena, CA 91125, USA
 - ¹⁴ Centre for Theoretical Cosmology, DAMTP, University of Cambridge, Wilberforce Road, Cambridge CB3 0WA, UK
 - ¹⁵ Centro de Estudios de Física del Cosmos de Aragón (CEFCA), Plaza San Juan, 1, planta 2, 44001 Teruel, Spain
 - ¹⁶ Computational Cosmology Center, Lawrence Berkeley National Laboratory, Berkeley, CA 94720, USA
 - ¹⁷ Consejo Superior de Investigaciones Científicas (CSIC), 28049 Madrid, Spain
 - ¹⁸ DSM/Irfu/SPP, CEA-Saclay, 91191 Gif-sur-Yvette Cedex, France
 - ¹⁹ DTU Space, National Space Institute, Technical University of Denmark, Elektrovej 327, 2800 Kgs. Lyngby, Denmark
 - ²⁰ Département de Physique Théorique, Université de Genève, 24 quai E. Ansermet, 1211 Genève 4, Switzerland
 - ²¹ Dark Cosmology Centre, Niels Bohr Institute, University of Copenhagen, Juliane Maries Vej 30, 2100 Copenhagen, Denmark
 - ²² Departamento de Astrofísica, Universidad de La Laguna (ULL), 38206 La Laguna, Tenerife, Spain
 - ²³ Departamento de Física, Universidad de Oviedo, Avda. Calvo Sotelo s/n, 33007 Oviedo, Spain
 - ²⁴ Department of Astronomy and Astrophysics, University of Toronto, 50 Saint George Street, Toronto, Ontario, ON M5S 3H41, Canada
 - ²⁵ Department of Astrophysics/IMAPP, Radboud University Nijmegen, PO Box 9010, 6500 GL Nijmegen, The Netherlands

- ²⁶ Department of Physics & Astronomy, University of British Columbia, 6224 Agricultural Road, Vancouver, British Columbia, Canada
- ²⁷ Department of Physics and Astronomy, Dana and David Dornsife College of Letter, Arts and Sciences, University of Southern California, Los Angeles, CA 90089, USA
- ²⁸ Department of Physics and Astronomy, University College London, London WC1E 6BT, UK
- ²⁹ Department of Physics and Astronomy, University of Sussex, Brighton BN1 9QH, UK
- ³⁰ Department of Physics, Florida State University, Keen Physics Building, 77 Chieftan Way, Tallahassee, Florida, USA
- ³¹ Department of Physics, Gustaf Hållströmin katu 2a, University of Helsinki, 00560 Helsinki, Finland
- ³² Department of Physics, Princeton University, Princeton, NJ 08540, USA
- ³³ Department of Physics, University of California, Berkeley, CA 94720, USA
- ³⁴ Department of Physics, University of California, Santa Barbara, California, USA
- ³⁵ Department of Physics, University of Illinois at Urbana-Champaign, 1110 West Green Street, Urbana, Illinois, USA
- ³⁶ Dipartimento di Fisica e Astronomia G. Galilei, Università degli Studi di Padova, via Marzolo 8, 35131 Padova, Italy
- ³⁷ Dipartimento di Fisica e Astronomia, ALMA MATER STUDIORUM, Università degli Studi di Bologna, viale Berti Pichat 6/2, 40127 Bologna, Italy
- ³⁸ Dipartimento di Fisica e Scienze della Terra, Università di Ferrara, via Saragat 1, 44122 Ferrara, Italy
- ³⁹ Dipartimento di Fisica, Università La Sapienza, P.le A. Moro 2, 00133 Roma, Italy
- ⁴⁰ Dipartimento di Fisica, Università degli Studi di Milano, via Celoria, 16, 00133 Milano, Italy
- ⁴¹ Dipartimento di Fisica, Università degli Studi di Trieste, via A. Valerio 2, 00133 Trieste, Italy
- ⁴² Dipartimento di Matematica, Università di Roma Tor Vergata, via della Ricerca Scientifica, 1, 00133 Roma, Italy
- ⁴³ Discovery Center, Niels Bohr Institute, Blegdamsvej 17, 1165 Copenhagen, Denmark
- ⁴⁴ Discovery Center, Niels Bohr Institute, Copenhagen University, Blegdamsvej 17, 1165 Copenhagen, Denmark
- ⁴⁵ European Southern Observatory, ESO Vitacura, Alonso de Cordova 3107, Vitacura, Casilla 19001, Santiago, Chile
- ⁴⁶ European Space Agency, ESAC, Planck Science Office, Camino bajo del Castillo, s/n, Urbanización Villafranca del Castillo, 28691 Villanueva de la Cañada, Madrid, Spain
- ⁴⁷ European Space Agency, ESTEC, Keplerlaan 1, 2201 AZ Noordwijk, The Netherlands
- ⁴⁸ Gran Sasso Science Institute, INFN, viale F. Crispi 7, 67100 L'Aquila, Italy
- ⁴⁹ HGSFP and University of Heidelberg, Theoretical Physics Department, Philosophenweg 16, 69120 Heidelberg, Germany
- ⁵⁰ Helsinki Institute of Physics, Gustaf Hållströmin katu 2, University of Helsinki, 00560 Helsinki, Finland
- ⁵¹ INAF-Osservatorio Astronomico di Padova, Vicolo dell'Osservatorio 5, 35131 Padova, Italy
- ⁵² INAF-Osservatorio Astronomico di Roma, via di Frascati 33, 00040 Monte Porzio Catone, Italy
- ⁵³ INAF-Osservatorio Astronomico di Trieste, via G.B. Tiepolo 11, 34127 Trieste, Italy
- ⁵⁴ INAF/IASF Bologna, via Gobetti 101, 40127 Bologna, Italy
- ⁵⁵ INAF/IASF Milano, via E. Bassini 15, 20133 Milano, Italy
- ⁵⁶ INFN, Sezione di Bologna, via Irnerio 46, 40126 Bologna, Italy
- ⁵⁷ INFN, Sezione di Roma 1, Università di Roma Sapienza, P.le Aldo Moro 2, 00185 Roma, Italy
- ⁵⁸ INFN, Sezione di Roma 2, Università di Roma Tor Vergata, via della Ricerca Scientifica, 1, 00185 Roma, Italy
- ⁵⁹ INFN/National Institute for Nuclear Physics, via Valerio 2, 34127 Trieste, Italy
- ⁶⁰ IPAG: Institut de Planétologie et d'Astrophysique de Grenoble, Université Grenoble Alpes, IPAG, 38000 Grenoble, France; CNRS, IPAG, 38000 Grenoble, France
- ⁶¹ IUCAA, Post Bag 4, Ganeshkhind, Pune University Campus, 411 007 Pune, India
- ⁶² Imperial College London, Astrophysics group, Blackett Laboratory, Prince Consort Road, London, SW7 2AZ, UK
- ⁶³ Infrared Processing and Analysis Center, California Institute of Technology, Pasadena, CA 91125, USA
- ⁶⁴ Institut Néel, CNRS, Université Joseph Fourier Grenoble I, 25 rue des Martyrs, 38042 Grenoble, France
- ⁶⁵ Institut Universitaire de France, 103 bd Saint-Michel, 75005 Paris, France
- ⁶⁶ Institut d'Astrophysique Spatiale, CNRS, Univ. Paris-Sud, Université Paris-Saclay, Bât. 121, 91405 Orsay Cedex, France
- ⁶⁷ Institut d'Astrophysique de Paris, CNRS (UMR 7095), 98bis boulevard Arago, 75014 Paris, France
- ⁶⁸ Institut für Theoretische Teilchenphysik und Kosmologie, RWTH Aachen University, 52056 Aachen, Germany
- ⁶⁹ Institute for Space Sciences, Bucharest-Magurale, Romania
- ⁷⁰ Institute of Astronomy, University of Cambridge, Madingley Road, Cambridge CB3 0HA, UK
- ⁷¹ Institute of Theoretical Astrophysics, University of Oslo, Blindern, 0371 Oslo, Norway
- ⁷² Instituto de Astrofísica de Canarias, C/Vía Láctea s/n, 28205 La Laguna, Tenerife, Spain
- ⁷³ Instituto de Física de Cantabria (CSIC-Universidad de Cantabria), Avda. de los Castros s/n, 39005 Santander, Spain
- ⁷⁴ Istituto Nazionale di Fisica Nucleare, Sezione di Padova, via Marzolo 8, 35131 Padova, Italy
- ⁷⁵ Jet Propulsion Laboratory, California Institute of Technology, 4800 Oak Grove Drive, Pasadena, California, USA
- ⁷⁶ Jodrell Bank Centre for Astrophysics, Alan Turing Building, School of Physics and Astronomy, The University of Manchester, Oxford Road, Manchester, M13 9PL, UK
- ⁷⁷ Kavli Institute for Cosmological Physics, University of Chicago, Chicago, IL 60637, USA
- ⁷⁸ Kavli Institute for Cosmology Cambridge, Madingley Road, Cambridge, CB3 0HA, UK
- ⁷⁹ Kazan Federal University, 18 Kremlyovskaya St., 420008 Kazan, Russia
- ⁸⁰ LAL, Université Paris-Sud, CNRS/IN2P3, Orsay, France
- ⁸¹ LERMA, CNRS, Observatoire de Paris, 61 avenue de l'Observatoire, 75000 Paris, France
- ⁸² Laboratoire AIM, IRFU/Service d'Astrophysique – CEA/DSM – CNRS – Université Paris Diderot, Bât. 709, CEA-Saclay, 91191 Gif-sur-Yvette Cedex, France
- ⁸³ Laboratoire Traitement et Communication de l'Information, CNRS (UMR 5141) and Télécom ParisTech, 46 rue Barrault 75634 Paris Cedex 13, France
- ⁸⁴ Laboratoire de Physique Subatomique et Cosmologie, Université Grenoble-Alpes, CNRS/IN2P3, 53 rue des Martyrs, 38026 Grenoble Cedex, France
- ⁸⁵ Laboratoire de Physique Théorique, Université Paris-Sud 11 & CNRS, Bâtiment 210, 91405 Orsay, France
- ⁸⁶ Lawrence Berkeley National Laboratory, Berkeley, California, USA
- ⁸⁷ Lebedev Physical Institute of the Russian Academy of Sciences, Astro Space Centre, 84/32 Profsoyuznaya st., 117997 Moscow, GSP-7, Russia
- ⁸⁸ Leung Center for Cosmology and Particle Astrophysics, National Taiwan University, 10617 Taipei, Taiwan
- ⁸⁹ Max-Planck-Institut für Astrophysik, Karl-Schwarzschild-Str. 1, 85741 Garching, Germany
- ⁹⁰ McGill Physics, Ernest Rutherford Physics Building, McGill University, 3600 rue University, Montréal, QC, H3A 2T8, Canada
- ⁹¹ National University of Ireland, Department of Experimental Physics, Maynooth, Co. Kildare, Ireland
- ⁹² Nicolaus Copernicus Astronomical Center, Bartycka 18, 00-716 Warsaw, Poland

- ⁹³ Niels Bohr Institute, Blegdamsvej 17, 1165 Copenhagen, Denmark
- ⁹⁴ Niels Bohr Institute, Copenhagen University, Blegdamsvej 17, 1165 Copenhagen, Denmark
- ⁹⁵ Nordita (Nordic Institute for Theoretical Physics), Roslagstullsbacken 23, 106 91 Stockholm, Sweden
- ⁹⁶ Optical Science Laboratory, University College London, Gower Street, London, UK
- ⁹⁷ SISSA, Astrophysics Sector, via Bonomea 265, 34136 Trieste, Italy
- ⁹⁸ SMARTTEST Research Centre, Università degli Studi e-Campus, via Isimbardi 10, 22060 Novedrate (CO), Italy
- ⁹⁹ School of Physics and Astronomy, Cardiff University, Queens Buildings, The Parade, Cardiff, CF24 3AA, UK
- ¹⁰⁰ School of Physics and Astronomy, University of Nottingham, Nottingham NG7 2RD, UK
- ¹⁰¹ Simon Fraser University, Department of Physics, 8888 University Drive, Burnaby BC, Canada
- ¹⁰² Sorbonne Université-UPMC, UMR 7095, Institut d'Astrophysique de Paris, 98bis boulevard Arago, 75014 Paris, France
- ¹⁰³ Space Research Institute (IKI), Russian Academy of Sciences, Profsoyuznaya Str, 84/32, 117997 Moscow, Russia
- ¹⁰⁴ Space Sciences Laboratory, University of California, Berkeley, CA 94720, USA
- ¹⁰⁵ Special Astrophysical Observatory, Russian Academy of Sciences, Nizhnij Arkhyz, Zelenchukskiy region, 369167 Karachai-Cherkessian Republic, Russia
- ¹⁰⁶ Stanford University, Dept of Physics, Varian Physics Bldg, 382 via Pueblo Mall, Stanford, California, USA
- ¹⁰⁷ Sub-Department of Astrophysics, University of Oxford, Keble Road, Oxford OX1 3RH, UK
- ¹⁰⁸ Sydney Institute for Astronomy, School of Physics A28, University of Sydney, NSW 2006, Australia
- ¹⁰⁹ The Oskar Klein Centre for Cosmoparticle Physics, Department of Physics, Stockholm University, AlbaNova, 106 91 Stockholm, Sweden
- ¹¹⁰ Theory Division, PH-TH, CERN, 1211 Geneva 23, Switzerland
- ¹¹¹ UPMC Univ Paris 06, UMR7095, 98bis boulevard Arago, 75014 Paris, France
- ¹¹² Université de Toulouse, UPS-OMP, IRAP, 31028 Toulouse Cedex 4, France
- ¹¹³ Universities Space Research Association, Stratospheric Observatory for Infrared Astronomy, MS 232-11, Moffett Field, CA 94035, USA
- ¹¹⁴ University of Granada, Departamento de Física Teórica y del Cosmos, Facultad de Ciencias, 18071 Granada, Spain
- ¹¹⁵ University of Granada, Instituto Carlos I de Física Teórica y Computacional, 18071 Granada, Spain
- ¹¹⁶ Warsaw University Observatory, Aleje Ujazdowskie 4, 00-478 Warszawa, Poland